UNIVERSIDADE D
COIMBRA

Ricardo Fernando Santos Amorim

MitoBULLET: Antioxidant Targeting of Mitochondria to Prevent Non-Alcoholic Fatty Liver Disease-induced Oxidative Stress

Tese no âmbito do Doutoramento em Biologia Experimental e Biomedicina, ramo de especialização em Biologia Molecular, Celular e do Desenvolvimento, orientada pelo Professor Doutor Paulo Jorge Gouveia Simões da Silva Oliveira, pela Professora Doutora Maria Fernanda Martins Borges e pelo Doutor José Carlos Santos Teixeira e apresentada ao Instituto de Investigação Interdisciplinar da Universidade de Coimbra.

Janeiro de 2022

Instituto de Investigação Interdisciplinar
da Universidade de Coimbra

MITOBULLET: ANTIOXIDANT TARGETING OF MITOCHONDRIA TO PREVENT NON-ALCOHOLIC FATTY LIVER DISEASE-INDUCED OXIDATIVE STRESS

Ricardo Fernando Santos Amorim

Tese no âmbito do Doutoramento em Biologia Experimental e Biomedicina, ramo de especialização em Biologia Molecular, Celular e do Desenvolvimento, orientada pelo Professor Doutor Paulo Jorge Gouveia Simões da Silva Oliveira, pela Professora Doutora Maria Fernanda Martins Borges e pelo Doutor José Carlos Santos Teixeira e apresentada ao Instituto de Investigação Interdisciplinar da Universidade de Coimbra.

Janeiro de 2022

UNIVERSIDADE D
COIMBRA

This work was performed at Center for Neuroscience and Cell Biology, University of Coimbra, Portugal, under the supervision of Doctor Paulo Jorge Oliveira, PhD and at Chemistry Research Center, University of Porto, Porto, under the supervision of Doctor Maria Fernanda Borges

This work was funded by FEDER funds through the Operational Programme Competitiveness Factors - COMPETE and national funds by Foundation for Science and Technology (FCT) to the author (SFRH/BD/131070/2017), by the research grants PTDC/DTPFTO/2433/2014, POCI-01-0145-FEDER-028607, PTDC/ASP-HOR/29152/2017 and POCI-01-0145-FEDER-029152 to Doctor Paulo Jorge Oliveira and the research grants PTDC/BIA-MOL/28607/2017 and POCI-01-0145-FEDER-029391 to Doctor Maria Fernanda Borges and by the institutional grants UIDB/04539/2020, CENTRO-07-ST24-FEDER-002008 and UIDB/00081/2020.

This work also supported by funding from the European Union's Horizon 2020 Research and Innovation programme under the Marie Skłodowska-Curie Grant Agreement No. 734719 (mtFOIE GRAS).

PUBLICATIONS

Part of the work included in this thesis is already published to international peer-reviewed scientific journals, as follows:

Manuscripts in international peer-review journals indexed at Journal Citation Reports from ISI Web of Knowledge

Ricardo Amorim; Inês C.M. Simões; Caroline Veloso; Adriana Carvalho; Rui F. Simões; Francisco B. Pereira; Theresa Thiel; Andrea Normann; Catarina Morais; Amália S. Jurado;, Mariusz R. Wieckowski; José Teixeira; Paulo J. Oliveira. Exploratory Data Analysis of Cell and Mitochondrial High-Fat, High-Sugar Toxicity on Human HepG2 Cells (2021). *Nutrients* 13, no. 5: 1723. doi.org/10.3390/nu13051723.

Ricardo Amorim, Fernando Cagide, Ludgero C Tavares, Rui F Simões, Pedro Soares, Sofia Benfeito, Inês Baldeiras, John G Jones, Fernanda Borges, Paulo J Oliveira, José Teixeira. Mitochondriotropic antioxidant based on caffeic acid AntiOxCIN$_4$ activates Nrf2-dependent antioxidant defenses and quality control mechanisms to antagonize oxidative stress-induced cell damage. Free Radic Biol Med. (2021) Dec 22;179:119-132. doi: 10.1016/j.freeradbiomed.2021.12.304.

Book Chapter

Ricardo Amorim, Sofia Benfeito, José Teixeira, Fernando Cagide, Paulo J. Oliveira and Fernanda Borges. Targeting Mitochondria: The Road to Mitochondriotropic Antioxidants and Beyond (2018). In: Oliveira P. (eds) *Mitochondrial Biology and Experimental Therapeutics.* Springer, Cham. https://doi.org/10.1007/978-3-319-73344-9_16.

Other manuscripts in international peer-review journals indexed at Journal Citation Reports from ISI Web of Knowledge with participation of phD candidate Ricardo Amorim from 2017-2021.

Inês C.M. Simões; **Ricardo Amorim**; José Teixeira; Agnieszka Karkucinska-Wieckowska;, Adriana Carvalho; Susana P. Pereira; Rui F. Simões; Sylwia Szymanska; Michał Dąbrowski; Justyna Janikiewicz; Agnieszka Dobrzyń; Paulo J. Oliveira; Yaiza Potes; Mariusz R. Wieckowski (2021). "The Alterations of Mitochondrial Function during NAFLD

Progression—An Independent Effect of Mitochondrial ROS Production" *Int. J. Mol. Sci.* 22, no. 13: 6848. https://doi.org/10.3390/ijms22136848.

José Teixeira , Farhan Basit, Peter H G M Willems, Jori A Wagenaars, Els van de Westerlo, **Ricardo Amorim**, Fernando Cagide, Sofia Benfeito, Catarina Oliveira, Fernanda Borges, Paulo J Oliveira, Werner J H Koopman. Mitochondria-targeted phenolic antioxidants induce ROS-protective pathways in primary human skin fibroblasts (2021). *Free Radic Biol Med.* 1;163:314-324. doi: 10.1016/j.freeradbiomed.2020.12.023.

Catarina Oliveira, Donatella Bagetta, Fernando Cagide, José Teixeira, **Ricardo Amorim**, Tiago Silva, Jorge Garrido, Fernando Remião, Eugenio Uriarte, Paulo J. Oliveira, Stefano Alcaro, Francesco Ortuso and Fernanda Borges. Benzoic acid-derived nitrones: A new class of potential acetylcholinesterase inhibitors and neuroprotective agents (2019). *Eur J Med Chem*. 174:116-129. doi: 10.1016/j.ejmech.2019.04.026.

Sofia Benfeito, Catarina Oliveira, Carlos Fernandes, Fernando Cagide, José Teixeira, **Ricardo Amorim,** Jorge Garrido, Cláudia Martins, Bruno Sarmento, Renata Silva, Fernando Remião, Eugenio Uriarte, Paulo J. Oliveira and Fernanda Borges. Fine-tuning the neuroprotective and blood-brain barrier permeability profile of multi-target agents designed to prevent progressive mitochondrial dysfunction (2019). *Eur J Med Chem*. 167: 525-545.DOI: 10.1016/j.ejmech.2019.01.055.

Carlos Fernandes, Sofia Benfeito, **Ricardo Amorim**, José Teixeira, Paulo J. Oliveira, Fernando Remião and Fernanda Borges. Desrisking the Cytotoxicity of a Mitochondriotropic Antioxidant Based on Caffeic Acid by a PEGylated Strategy (2018). *Bioconjug Chem*.15;29(8):2723-2733. DOI: 10.1021/acs.bioconjchem.8b00383.

Catarina Oliveira, Fernando Cagide, José Teixeira, **Ricardo Amorim**, Lisa Sequeira, Francesco Mesiti, Tiago Silva, Jorge Garrido, Fernando Remião, Santiago Vilar, Eugenio Uriarte, Paulo J. Oliveira and Fernanda Borges (2018). Hydroxybenzoic Acid Derivatives as Dual-Target Ligands: Mitochondriotropic Antioxidants and Cholinesterase Inhibitors. *Front Chem*. ; 6:126. DOI: 10.3389/fchem.2018.00126.

José Teixeira, Catarina Oliveira, Fernando Cagide, **Ricardo Amorim**, Jorge Garrido, Fernanda Borges and Paulo J. Oliveira. Discovery of a new mitochondria

permeability transition pore (mPTP) inhibitor based on gallic acid (2018). *J Enzyme Inhib Med Chem*. 33(1):567-576. DOI: 10.1080/14756366.2018.1442831.

José Teixeira, **Ricardo Amorim**, Katia Santos, Pedro Soares, Sandipan Datta, Gino A. Cortopassi, Teresa L. Serafim, Vilma A. Sardão, Jorge Garrido, Fernanda Borges and Paulo J.Oliveira. Disruption of mitochondrial function as mechanism for anti-cancer activity of a novel mitochondriotropic menadione derivative (2018). *Toxicology*. *Acta* 393:123-139. DOI: 10.1016/j.tox.2017.11.014.

The results presented in this thesis were presented in national and international scientific meetings in the form of oral and poster communications:

Oral communications

Ricardo Amorim; Inês Simões; José Teixeira; Yaiza Potes; Pedro Soares; Adriana Carvalho; Ludgero Tavares; Fernando Cagide; Sofia Benfeito; Susana Pereira; Rui Simõesa; A Karkucinska-Wieckowska; Ivan Viegas; S Szymanskaf; M Dąbrowskid; J Janikiewiczd; A Dobrzyńd; J Jonesa; Fernanda Borges; Mariuz Wieckowskid and Paulo J. Oliveira. Mitochondria-targeted antioxidant based on caffeic acid AntiOxCIN$_4$. In NAFLD summit, September 16-17, 2021

Ricardo Amorim; José Teixeira; Sofia Benfeito; Fernando Cagide; Fernanda Borges; Paulo J. Oliveira. Decrypting the Nrf2-dependent antioxidant mechanism of action behind the beneficial effects of the mitochondriotropic cinnamic acid AntiOxCIN$_4$. In 55th *ESCI Annual Scientific Meeting*, June 9-11, 2021.

Inês Simões; **Ricardo Amorim**; José Teixeira; A. Karkucinska-Wieckowska; Paulo J. Oliveira; Yaiza Potes; Mariuz Wieckowski. Time dependent effect of western diet on mitochondrial physiology in a mouse model of non-alcoholic fatty liver disease. In 55th *ESCI Annual Scientific Meeting*, June 9-11, 2021.

Ricardo Amorim, Inês Simões, Caroline Veloso, Adriana Carvalho, Rui F. Simões, Theresa Thiel, Catarina M. Morais, Amália Jurado, Mariuz R. Wieckwoski, José Teixeira and Paulo J. Oliveira. High fat vs High sugar: the role of mitochondria on time-dependent

hepatocellular cytotoxic effects. 54th *Annual Meeting of the European Society for Clinical Investigation*, 20-30th, 2020.

Ricardo Amorim, José Teixeira, Sofia Benfeito, Fernando Cagide,Paulo J. Oliveira, Fernanda Borges. Mitochondriotropic Cinnamic Acid Antioxidant Improves Cellular Resistance to Stress. In 4th *Annual Meeting of COST Action CA15135* – Izmir (Turkey) March 5-6, 2020.

Ricardo Amorim, José Teixeira, Ludgero C. Tavares, John G. Jones, Sofia Benfeito, Fernando Cagide, Fernanda Borges, Paulo J. Oliveira – Antioxdant, hormetic-like properties of AntiOxCIN$_4$, a novel hydroxycinnamic acid-based mitochondria-targeted agent. In 10th *Targeting Mitochondria Congress*, October 27-29, 2019, Berlin, Germany.

André Barbosa, **Ricardo Amorim**, Caroline Veloso, Sofia Benfeito, Catarina Oliveira, Fernanda Borges, Paulo J. Oliveira, José Teixeira – Targeting Phenolic Dietary Antioxidants to Mitochondria to Modulate Redox Signaling and Metabolism. In *Sociedade Portuguesa de Farmacologia (SPF) Meeting* at University of Porto, February 6-8, 2019, Porto, Portugal.

Ricardo Amorim, José Teixeira, Caroline Veloso, Sofia Benfeito, Fernando Cagide, Fernanda Borges and Paulo J. Oliveira. Mitochondria-targeted antioxidants in human hepatic cells: a conceivable therapy for non-alcoholic fatty liver disease. In 9th *World Congress on Targeting Mitochondria*, Berlin, October 23-25, 2018.

Ricardo Amorim, José Teixeira, Sofia Benfeito, Fernando Cagide, Jorge Garrido, Paulo J. Oliveira, Fernanda Borges – Mitochondriotropic antioxidants based on cinnamic acid derivatives increase celular stress responses in HepG2 cells. In *MuTaLig COST action*, Universidad de la Laguna, March 15-16, 2018, Tenerife, Spain.

Ricardo Amorim; Inês Simões; José Teixeira; Yaiza Potes; Pedro Soares; Adriana Carvalho; Ludgero Tavares; Fernando Cagide; Sofia Benfeito; Susana Pereira; Rui Simõesa; A Karkucinska-Wieckowska; Ivan Viegas; S Szymanskaf; M Dąbrowskid; J Janikiewiczd; A Dobrzyńd; J Jonesa; Fernanda Borges; Mariuz Wieckowskid and Paulo J. Oliveira. Mitochondria-targeted antioxidant based on caffeic acid AntiOxCIN$_4$. In *NAFLD summit* September 16-17, 2021

Ricardo Amorim; José Teixeira; Sofia Benfeito; Fernando Cagide; Fernanda Borges; Paulo J. Oliveira. Decrypting the Nrf2-dependent antioxidant mechanism of action behind the beneficial effects of the mitochondriotropic cinnamic acid AntiOxCIN$_4$. In 55th *ESCI Annual Scientific Meeting*, June 9-11, 2021.

Inês Simões; **Ricardo Amorim**; José Teixeira; A. Karkucinska-Wieckowska; Paulo J. Oliveira; Yaiza Potes; Mariuz Wieckowski. Time dependent effect of western diet on mitochondrial physiology in a mouse model of non-alcoholic fatty liver disease. In 55th *ESCI Annual Scientific Meeting*, June 9-11, 2021.

Ricardo Amorim, Inês Simões, Caroline Veloso, Adriana Carvalho, Rui F. Simões, Theresa Thiel, Catarina M. Morais, Amália Jurado, Mariuz R. Wieckwoski, José Teixeira and Paulo J. Oliveira. High fat vs High sugar: the role of mitochondria on time-dependent hepatocellular cytotoxic effects. 54th *Annual Meeting of the European Society for Clinical Investigation*, 20-30th September 2020, 2019, COVID Edition Abstract published in the Eur. J. Clin. Inves., 50 (S1):25

Ricardo Amorim, José Teixeira, Sofia Benfeito, Fernando Cagide, Fernando Borges and Paulo J. Oliveira. Effects of mitochondria-targeted antioxidants in human hepatic cells: a possible therapy for hepatic steatosis? In 3rd *Annual Meeting of COST Action CA15135* – La Valletta (Malta) October 18-19 2018.

Ricardo Amorim, José Teixeira, Inês Baldeias, Sofia Benfeito, Fernando Cagide, Jorge Garrido, Paulo J. Oliveira, Fernanda Borges. Mitochondriotropic cinnamic acid antioxidants increase cellular stress responses in HepG2 cells: involvement of (mt)ROS signaling? 2nd *MitoPORTO*, July 13, 2018, Porto, Portugal.

José Teixeira, **Ricardo Amorim**, Sofia Benfeito, Fernando Cagide, Paulo J. Oliveira, Fernanda Borges. Mitochondriotropic cinnamic acid antioxidants improves steatosis in a Non-Alcoholic Fatty Liver Disease (NAFLD) cell model. 2nd *MitoPORTO*, July 13, 2018, Porto, Portugal.

José Teixeira, **Ricardo Amorim**, Rodrigo Carreira, Sofia Benfeito, Fernando Cagide, Paulo J. Oliveira, Fernanda Borges – Mitochondria-targeted cinnamic antioxidants incresae celular stress response through modulation of mitochondria

function/activity. In *MuTaLig COST action*, Universidad de la Laguna, March 15-16, 2018, Tenerife, Spain.

AUTHOR'S DECLARATION

The author states to have afforded a major contribution to the conceptual design, technical execution of the work, interpretation of the results and manuscript preparation of the works included in this thesis

ACKNOWLEDGMENTS/ AGRADECIMENTOS

Escreverei esta seção na língua de Camões porque acredito que a nossa língua expressa melhor todo o sentimento que pretendo enaltecer aqui.

Um doutoramento é um *roller coaster* de emoções. Durantes estes 4 anos de muito trabalho foram imensos os momentos de frustação, desilução, dúvida mas também de esforço, dedicação e, acima de tudo, superação. Em 2017, mudei-me de "armas e bagagens" para um terra que, até então, pouco conhecia. Cantanhede fez-me relembrar o sossego e a humanidade da minha terra Natal, Arouca. Mais do que isso, deu-me a oportunidade de conhecer pessoas fantásticas, que mais do que nunca merecem ser referidas.

Um doutoramento nunca é um trabalho solitário, e por tudo isso, quero endereçar um agradecimento às pessoas e às instituições que permitiram a realização desta tese:

À Fundação para a Ciência e Tecnologia, pelo suporte financeiro não só através dos projetos que foram imprescindíveis para a realização do trabalho experimental, como também por me ter concedido uma bolsa de Doutoramento (SFRH/BD/131070/2017), que durante 4 anos me permitiu completar mais uma etapa importante da minha vida.

Ao Programa Doutoral em Biologia Experimental e Biomedicina (PDBEB), por me permitir embarcar neste projeto e, por fomentar uma multidisciplinariedade de conteúdos aos seus doutorandos.

Aos meus orientadores, pelo papel importante que tiveram na condução do meu doutoramento e pela sua dedicação ao meu trabalho:

Ao Doutor Paulo Oliveira, por ser um modelo do ponto de vista professional mas também do ponto de vista humano. A solidariedade e a capacidade de reconhecer esforço, mesmo nas situaçãos mais difíceis, são essenciais no processo científico. O Doutor Paulo Oliveira é um exemplo positivo dessa dourina. Sou extremamente grato pela oportunidade que me deu desde o ínicio, pelo incansável incentivo e orientação ao

longo de todos estes anos de trabalho, contribuindo em grande parte para o meu desenvolvimento como cientista. Sinto que cresci imenso como investigador, muito graças à liberdade de pensamento que reina sob a orientação do Dr Paulo Oliveira. O grupo MitoXT tem sido ao longo dos anos uma referência no diz respeito ao ambiente saudável no trabalho e, para isso, muito contribuiu a incansável disponibilidade do Dr Paulo em promover atividades extra-laboratoriais.

À Professora Doutora Fernanda Borges, por me acompanhar neste trajecto desde a minha tese de Mestrado. Por se ter lembrado de mim, quando já questionava se deveria continuar na ciência. A professora Doutora Fernanda Broges tem mostrado ao longo do tempo uma assinável amizade com todos os seus estudandes. São poucos os grupos que mantêm os seus colaboradores tanto tempo como o que se tem verificado no grupo da Dra Fernanda Borges. Do ponto de vista científico, a Dra Fernanda Borges é uma referência nacional e internacional e é, com muito orgulho, que a considero a minha "mãe" da ciência.

Ao Doutor José Teixeira, por aceitado disponibilizar tempo do seu doutoramento para "aturar" aquele aluno de mestrado em 2013 e lhe ter incutido o gosto pelas mitocôndrias. O doutor José Teixeira é um jovem cientista em ascensão que muito admiro e respeito. Agradeço o facto de ter sido sempre o meu apoio laboratorial e por nunca me ter suprimido a criatividade. Agradeço ainda as inúmeras e longas discussões saudáveis e sugestões que me orientaram neste caminho. A sua sensatez e serenidade foram preponderantes para que tenha conseguido ultrapassar todos os desafios enontrados ao longo do tempo. Não menos importante, obrigada pela grande amizade que mantemos e que tornou muitas vezes o caminho ao longo destes anos muito mais fácil.

Aos meu colegas do Grupo de Química Medicinal da Universidade do Porto (UP), nomeadamente ao Doutor Fernando Cagide, à Doutora Sofia Benfeito, ao Doutor Pedro Santos, ao Doutor Carlos Fernandes, à Doutor Catarina Oliveira e todos os outros pela síntese química e cedência do composto usado neste trabalho mas, acima de tudo, pela amizade e pelos bons momentos partilhados.

A todos os meus colegas do MitoXT - Mitochondrial Toxicology and Experimental Therapeutics Laboratory, com quem tive a oportunidade de trabalhar e privar no laboratório, em especial ao Luís Grilo, à Ana Duarte e à Vilma Sardão. Independentemente da relação mais ou menos duradoura, agradeço os conselhos científicos e não cientificos que me ajudaram a evoluir. À Susana Pereira e à Cláudia Deus, que conheço desde o meu mestrado, quero agradeço a sincera amizade e ajuda durante todo o percurso.

À Ana Raquel, ao Rui Simões, à Adriana Carvalho e à Rafaela Ferrão por terem sido o meu suporte ao longo do doutoramento. A amizade que criamos e todos os momentos que partilhamos no laboratório, e fora dele, tornaram esta experiência muita mais rica e sinto que ganhei amigos para a vida.

Aos meus ex-colegas do MitoXT - Mitochondrial Toxicology and Experimental Therapeutics Laboratory, em especial à Luciana Ferreira, ao João Martins, à Caroline Veloso, à Inês Simões e ao Ludgero Tavares. Agradeço por tudo o que ensinaram ao longo do tempo em que privamos no laboratório, mas principalmente pela amizade que mantemos desde então.

A todos os funcionários do UC-Biotech, em especial à Rute, à D. Alda, à D. Adelaide, à Filipa e à D. Isabel pelo bom humor, pela disponibilidade em ajudar em todas as situações. No geral, por fazerem o trabalho invisível e, muitas vezes esquecido, .mas indispensável para todo o processo científico.

Aos meus amigos de sempre, o Pedro Feiteira, o Diogo Costa, o Cláudio Oliveira, o Marcelo Feiteira, o Bruno Martins e todos os outros, que de uma ou outra forma contribuíram para a realização da minha tese. A vossa amizade é um refúgio indispensável para mim. Agradeço a paciência e a compreensão pelos momentos em que não pude estar presente.

Aos meus pais, aos meus avós e à minha irmã, que são a minha eterna “casa” e razão primordial da minha existência, quero agradececer a compreensão, o carinho e entusiasmo que me transmitiram para chegar até aqui. Agradeço que tenham sido sempre uma ponte e , nunca um muro, na procura dos meus sonhos.

À Joana, à minha Joana, pela amizade, pela compreensão e, especialmente, pelo amor. Por teres sempre uma palavra encourajadora e um abraço sentido. Por seres a mulher amável, forte e independente que tanto admiro. Obrigado por me fazeres perceber que a felicidade só é real quando partilhada.

A todos aqueles que de uma ou de outra forma, com as suas sugestões, criticas e ideias me ajudaram e encorajaram na realização desta tese.

A todos, o meu sincero obrigado.

Dedico esta Tese ao meus pais, por todo o apoio que sempre
me prestaram e por todos os sacrifícios que suportaram por mim.

Ao meu avô Augusto, por em vida me ter incentivado a procurar o conhecimento.
Espero que o meu percurso esteja à altura daquilo que ele idealizou.

Para a Joana, por todos os momentos
em que não pude estar contigo.

“The good thing about science is that

it's true whether or not you believe in it”

Neil deGrasse Tyson

GENERAL INDEX

LIST OF FIGURES

LIST OF TABLES

ABBREVIATIONS

4-HNE	4-hydroxy-2-nonenal
6-OHDA	6-hydroxydopamine
8-OH-dG	8-oxo-2'-deoxyguanosine
8-OH-G	8-hydroxyguanosine
AA	antimycin A
ABTS	2,2'-azino-bis (3-ethylbenzothiazoline-6-sulfonic acid)
ACC	acetyl-CoA carboxylase
ADP	adenosine diphosphate
AIF	apoptosis-inducing factor 1
AKT	protein kinase B complex
ALCAT1	lysocardiolipin acyltransferase 1
ALT	alanine aminotransferase
AMP	Adenosine monophosphate
AMPK	AMP-activated protein kinase
Apaf-1	apoptotic protease activating factor 1
ARE	antioxidant responsive element
ASK1	apoptosis signal-regulated kinase 1
AST	aspartate aminotransferase
ATG	autophagy-related
ATP	adenosine triphosphate
BAK	BCL-2-homologous antagonist/killer
BAX	BCL-2-associated protein
BCA	bicinchoninic acid
BCL-2	B-cell lymphoma 2
BH	BCL-2-homology domain
Bid	BH-3 interacting domain death agonist
BMI	body mass index
BNIP3	BCL2 interacting protein 3
BSA	bovine serum albumin
CAT	catalase
CDAA	choline deficient, defined amino acid
CE	cholesteryl esters
Chol	free cholesterol
CHOP	CCAAT-enhancer-binding protein homologous protein
CMA	chaperone-mediated autophagy
CoA	coenzyme A
CPT	carnitine palmitoyltransferase
CR	caloric restriction

CVD	cardiovascular diseases
CYP	cytochrome P450
DAG	diacylglycerols
DAMPs	damage-associated molecular patterns
DMSO	dimethyl sulfoxide
DNA	deoxyribonucleic acid
DNL	*de novo* lipogenesis
DNP	dinitrophenol
DRP1	dynamin-1-like protein
DTNB	5,5'-dithio-bis-(2-nitrobenzoic acid)
DTT	dithiothreitol
EGCG	epigallocatechin-3-gallate
ER	endoplasmic reticulum
ERK	extracellular signal-regulated kinase
ETC	electron transport chain
FAO	fatty acid oxidation
FAs	fatty acids
FAS	fatty acid synthase
FasL	Fas ligand
FBS	fetal bovine serum
FCCP	carbonyl cyanide-4-(trifluoromethoxy)phenylhydrazone
FET	forward electron transport
FFAs	free fatty acids
FMN	flavin mononucleotide
G6PC	glucose-6-phosphatase
GAPDH	glyceraldehyde 3-phosphate dehydrogenase
GLUT	glucose transporter
GPX	glutathione peroxidase
GR	glutathione reductase
GSH	reduced glutathione
GSSG	glutathione disulfide
H&E	hematoxylin & eosin
HCAs	hydroxycinnamic acids
HDL	high-density lipoprotein
HF	high fat
HFD	high-fat diet
HFHS	High fat and high sugar
HIFα	hypoxia inducible factor α
HMOX1	Heme oxygenase 1
IMM	inner mitochondrial membrane
IMS	intermembrane space

IR	insulin resistance
JNK	c-Jun N-terminal kinase
KEAP1	kelch-like ECH-associated protein 1
LAMP2	lysosome-associated membrane protein 2
LCFA	long chain fatty acid
LC-MS/MS	liquid chromatography with tandem mass spectrometry
LD	lipid droplets
MAPK	mitogen-activated protein kinase
MAS	mitochondrial assay solution
MCD	methionine-choline deficient
MDA	malondialdehyde
MDA	malondialdehyde
MEN	menadione
MFN	mitofusin
mPTP	mitochondrial permeability transition pore
MRC	mitochondrial respiratory chain
MRI	magnetic resonance imaging
MS	mass spectrometry
MST1	macrophage stimulating 1
MTBE	methyl *tert*-butyl ether
mtDNA	mitochondrial DNA
mTOR	mammalian target of rapamycin complex
mtROS	mitochondrial reactive oxygen species
mtROS	mitochondrial reactive oxygen species
NAD^+	nicotinamide adenine dinucleotide, oxidized form
NADH	nicotinamide adenine dinucleotide, reduced form
NADPH	nicotinamide-adenine dinucleotide phosphate
NAFLD	non-alcoholic fatty liver disease
NAS	NAFLD score
NASH	non-alcoholic steatohepatitis
NLRP3	NLR family pyrin domain containing 3
NMR	nuclear magnetic resonance
NOX	NADPH Oxidase
NQO1	NAD(P)H dehydrogenase (quinone) 1
NRF1	nuclear respiratory factor 1
Nrf2	nuclear factor erythroid 2-related factor 2
OA	oleic acid
OCR	oxygen consumption rate

Olig	oligomycin
OMM	outer mitochondrial membrane
OXPHOS	oxidative phosphorylation
OxS	oxidative stress
PA	palmitic acid
PBS	phosphate buffered saline
PC	phosphatidylcholine
PCA	principal component analysis
PCK2	phosphoenolpyruvate carboxykinase
PCX	pyruvate carboxylase
PE	phosphatidylethanolamine
PGC-1α	peroxisome proliferator-activated receptor-gamma coactivator 1 alpha
PGK2	phosphoglycerate kinase 2
PHSF	primary human skin fibroblasts
PINK1	PTEN-induced kinase 1
PL	phospholipids
PP2A	protein phosphatase 2
PRx	peroxiredoxin
PTM	post-translational modification
PTP1B	protein tyrosine phosphatase 1B
PUFA	polyunsaturated fatty acids
qPCR	quantitative polymerase chain reaction
RCR	respiratory control ratio
RCT	randomized controlled trial
RET	reverse electron transport
ROS	reactive oxygen species
ROT	rotenone
SD	standard diet
SDH	succinate dehydrogenase
SDS-PAGE	sodium dodecyl sulfate polyacrylamide gel electrophoresi
SFAs	saturated fatty acids
SIRT	sirtuin
SNPs	single nucleotide polymorphisms
SOD	superoxide dismutase
STZ	streptozotocin
T2DM	type 2 diabetes
***t*BHP**	*tert*-butylhydroperoxide
TCA	tricarboxylic acid
TFAM	transcription factor A, mitochondrial

TG	triglycerides
TIM	translocase of the inner membrane
TLC	thin layer chromatography
TMPD	N,N,N',N'-tetramethyl-p-phenylenediamine
TMRM	tetramethylrhodamine methyl ester
TNB	2-nitro-5-thiobenzoate acid
TNF	tumor necrosis factor
TOM	translocase of the outer membrane
TPP^+	triphenylphosphonium cation
TRAIL	tumor necrosis factor-related apoptosis-inducing ligand
Trx	thioredoxin
UCP	uncoupling protein
UPS	ubiquitin-proteasome system
VDAC	voltage dependent anion channel
VLDL	very-low-density lipoprotein
WD	western diet
XIAP	inhibitor of apoptosis protein
$\Delta\Psi m$	mitochondrial transmembrane electric potential

ABSTRACT

Non-alcoholic fatty liver disease (NAFLD) is a public health concern affecting 24% of the population worldwide. Non-alcoholic steatohepatitis (NASH), one of the deleterious stages of non-alcoholic fatty liver disease, remains a significant cause of liver-related morbidity and mortality worldwide. NAFLD is a multifactorial disease and is considered the hepatic component of metabolic syndrome. Although mechanisms underlying disease pathophysiology are not fully clarified, mitochondrial dysfunction and oxidative stress (OxS) are potential key players. Mitochondria are key organelles involved in cellular survival, differentiation, and death induction. In this regard, mitochondrial morphology and/or function alterations are involved in stress-induced adaptive pathways, priming mitochondria for mitophagy or apoptosis induction.

In this context and driven by the lack of effective pharmacological therapies, we propose a new approach using a mitochondria-targeted antioxidant ($AntiOxCIN_4$) to prevent non-alcoholic fatty liver (NAFL) development.

Previously studies shown that the mitochondriotropic antioxidant $AntiOxCIN_4$ (100 µM; 48 h) presented significant cytoprotective effect without affecting the viability of human hepatoma-derived (HepG2) cells. Moreover, $AntiOxCIN_4$ (12.5 µM; 72 h) caused a mild increase of reactive oxygen species (ROS) levels without toxicity to primary human skin fibroblasts (PHSF). As Nrf2 is a master regulator of the OxS response inducing antioxidant-encoding gene expression, we hypothesized that $AntiOxCIN_4$ could increase the resistance of human hepatoma-derived HepG2 to oxidative by Nrf2-dependent mechanisms, in a process mediated by mitochondrial ROS (mtROS). In fact, in chapter 7, we showed that after an initial decrease in oxygen consumption paralleled by a moderate increase in superoxide anion levels, $AntiOxCIN_4$ led to a time-dependent Nrf2 translocation to the nucleus. This was followed later by an increase in basal respiration (150 %) and extracellular acidification (120 %). $AntiOxCIN_4$ treatment enhanced mitochondrial quality by triggering the clearance of defective organelles by autophagy and/or mitophagy, coupled with increased mitochondrial biogenesis. $AntiOxCIN_4$ also up-regulated the cellular antioxidant defense system. $AntiOxCIN_4$ seems to have the ability to maintain hepatocyte redox homeostasis, regulating the

electrophilic/nucleophilic tone, and preserve cellular physiological functions. The obtained data in chapter 7 opened a new avenue to explore the effects of AntiOxCIN$_4$ in the context of preserving hepatic mitochondrial function in disorders, such as NASH/NAFLD and type II diabetes.

In agreement with that hypothesis, we next characterized the human HepG2 cells as an *in vitro* model for steatosis (chapter 8), in order to screen mitochondriotropic antioxidants lipid lowering ability. Using an exploratory data analysis, we investigate time-dependent cellular and mitochondrial effects of different supra-physiological fatty acids (FA) overload strategies, in the presence or absence of fructose (F), on human hepatoma-derived HepG2 cells. We measured intracellular neutral lipid content and reactive oxygen species (ROS) levels, mitochondrial respiration and morphology, and caspases activity and cell death. FA-treatments induced a time-dependent increase in neutral lipid content, which was paralleled by an increase in ROS. Fructose, by itself, did not increase intracellular lipid content nor aggravated the effects of palmitic acid (PA) or free fatty acids mixture (FFA), although it led to an increased expression of hepatic fructokinase. Instead, F decreased mitochondrial phospholipid content, as well as OXPHOS subunits levels. Increased lipid accumulation and ROS in FA-treatments preceded mitochondrial dysfunction, comprising altered mitochondrial membrane potential ($\Delta\Psi m$) and morphology, and decreased oxygen consumption rates, especially with PA. Consequently, supra-physiological PA alone or combined with F prompted the activation of caspase pathways leading to a time-dependent decrease in cell viability. Exploratory data analysis methods support this conclusion by clearly identifying the effects of FA treatments. Unsupervised learning algorithms created homogeneous and cohesive clusters, with a clear separation between PA and FFA treated samples to identify a minimal subset of critical mitochondrial markers in order to attain a feasible model to predict cell death in NAFLD or for high throughput screening of possible therapeutic agents, with particular focus in measuring mitochondrial function.

Finally, to validate the beneficial effects of hydroxycinnamic-derived mitochondriotropic antioxidant AntiOxCIN$_4$, C57BL/6J mice daily supplemented with 2.5 mg AntiOxCIN$_4$ were fed with standard diet (SD) or Western diet (WD) (30% high-fat, 30% high-sucrose) for 16 weeks to induce simple steatosis *in vivo*. Additionally, we treated HepG2 cells with AntiOxCIN$_4$ (100 µM, 48 h) before the exposure to bovine serum albumin (BSA)

alone or free fatty acids (FFAs) mixture (250 µM, 24 h) to induce lipid accumulation *in vitro* (chapter 9). In WD-fed mice, AntiOxCIN$_4$ supplementation decreased body (by 43 %), liver weight (by 39 %) and plasma hepatocyte damage markers. The improvement in hepatic-related parameters was associated with a reduction of fat liver accumulation (600 %) and the remodeling of fatty acyl chain composition compared with the WD-fed group. Data on human HepG2 cells confirmed a lower lipid accumulation by the evident reduction of lipid droplets size and number in AntiOxCIN$_4$-treated cells. AntiOxCIN$_4$ supplementation induced mitochondrial metabolism remodeling by upregulating oxidative phosphorylation (OXPHOS) subunits, mediated by the PGC-1α-SIRT3. Accordingly, human HepG2 data corroborated that AntiOxCIN$_4$ pre-treatment stimulated fatty acid oxidation-linked oxygen consumption rates and OXPHOS gene expression remodeling. AntiOxCIN$_4$ also upregulated hepatic antioxidant defense system in WD-fed mice and counteracted cellular ROS exacerbation in FFA-treated human HepG2 cells. Finally, AntiOxCIN$_4$ supplementation prevented lipid accumulation-driven autophagic flux impairment, by increasing lysosomal proteolytic capacity as observed both *in vivo* and *in vitro*

Overall, the results obtained in this dissertation added novel and relevant knowledge by showing that AntiOxCIN$_4$ improved NAFL *in vivo*, via three main mechanisms: a) increasing mitochondrial function (fatty acid oxidation); b) regulating antioxidant capacity (enzymatic and non-enzymatic) and; c) preventing the impairment in autophagy. Together, the findings support the potential use of AntiOxCIN$_4$ in the prevention/ treatment of NAFLD.

Keywords: Dietary antioxidants; Caffeic acid; Mitochondria; Mitochondria-targeted antioxidants; Nrf2; Antioxidant defenses; Non-alcoholic fatty liver disease (NAFLD); Oxidative stress; Mitochondria dys(function); Mitophagy

RESUMO

A síndrome do fígado gordo não-alcoólico (FíGNA) é um problema de saúde pública que afeta 24% da população mundial. A esteatohepatite não-alcoólica (EHNA), um dos estadios nefastos da síndrome do fígado gordo não-alcoólico, é uma causa significativa de morbidade e mortalidade relacionadas com fígado em todo o mundo. A FíGNA é uma doença multissistémica, sendo considerada o componente hepático da síndrome metabólica. Embora os mecanismos subjacentes à fisiopatologia da doença não sejam totalmente conhecidos, a disfunção mitocondrial e o *stress* oxidativo (OxS) são importantes mediadores. As mitocôndrias são organelos envolvidos na sobrevivência celular, diferenciação e indução de morte. De facto, a morfologia mitocondrial e/ou alterações nas sua função estão envolvidas em vias adaptativas induzidas por *stress*, direccionando as mitocôndrias para a indução de mitofagia ou apoptose.

Nesse contexto, e impulsionado pela falta de terapias farmacológicas eficazes, propomos uma nova abordagem usando um antioxidante direcionado à mitocôndria (AntiOxCIN$_4$) para prevenir o síndrome do fígado gordo não-alcoólico (FíGNA).

Estudos anteriores mostraram que o antioxidante mitocondriotrópico AntiOxCIN$_4$ (100 µM; 48 h) tem efeito protector significativo sem afetar a viabilidade das células derivadas do hepatoma humano (HepG2). Além disso, o AntiOxCIN$_4$ (12,5 µM; 72 h) aumentou ligeiramente os níveis de espécies reactivas de oxigénio (ERO) sem provocar toxicidade em fibroblastos primários da pele humana (FPPH). Uma vez que o Nrf2 é um regulador crucial na indução da expressão de genes que codificam para proteínas antioxidantes, formulamos a hipótese de que AntiOxCIN$_4$ poderia aumentar a resistência as células HepG2 à oxidação através de mecanismos dependentes do Nrf2, num processo mediado por ERO mitocondriais (mtROS). De fato, no capítulo 7, mostramos que, após uma diminuição inicial no consumo de oxigénio, acompanhada por um aumento moderado nos níveis do anião superóxido, o AntiOxCIN$_4$ levou a uma translocação, em função do tempo, do Nrf2 para o núcleo. A isto foi juntou-se um aumento na respiração basal (150%) e na acidificação extracelular (120%). A incubação com o AntiOxCIN$_4$ melhorou a qualidade mitocondrial em células HepG2 ao desencadear

a eliminação de organelos disfuncionais por autofagia e/ou mitofagia, juntamente com um acréscimo na biogénese mitocondrial. O AntiOxCIN$_4$ também regulou positivamente o sistema de defesa antioxidante celular. O AntiOxCIN$_4$ parece ter a capacidade de manter a homeostase redox dos hepatócitos, regular o potencial eletrofílico/nucleofílico e preservar as funções fisiológicas celulares. Os dados obtidos no capítulo 7 abriram um novo caminho para explorar os efeitos do AntiOxCIN$_4$ no contexto da preservação da função mitocondrial hepática em doenças, como a FíGNA e a diabetes tipo II.

De acordo com essa hipótese, caracterizamos a seguir as células HepG2 como um modelo *in vitro* para a esteatose (capítulo 8), a fim de rastrear a capacidade de redução de lipídios dos antioxidantes mitocondriotrópicos. Usando uma análise exploratória de dados, investigamos os efeitos celulares e mitocondriais em função do tempo de diferentes ácidos gordos em concentrações suprafisiológicos, na presença ou ausência de frutose (F), em células derivadas de hepatoma humano HepG2. Nesta secção do trabalho, medimos o conteúdo intracelular de lipídos neutros, os níveis de ERO, a respiração mitocondrial e a sua morfologia, a atividade das caspases e a morte celular. Os tratamentos com ácidos gordos induziram a um aumento em função do tempo do teor de lipídos neutros, que foi acompanhado por um aumento nas ERO. A frutose, por si só, não aumentou o conteúdo lipídico intracelular, nem agravou os efeitos do ácido palmítico (PA) ou da mistura de ácidos gordos livres (FFA), embora tenha levado a uma expressão aumentada da frutocinase hepática. Em vez disso, a fructose diminuiu o conteúdo de fosfolipídios mitocondriais, bem como os níveis de subunidades da cadeia fosforilativa mitocondrial (OXPHOS). A acumulação lipídica e dos níveis de ERO em tratamentos com FA precedeu a disfunção mitocondrial, caracterizada pela alteração do potencial de membrana mitocondrial ($\Delta\Psi m$) e da morfologia mitocondrial, assim como taxas de consumo de oxigénio diminuídas, especialmente com o PA. Consequentemente, concentrações suprafisiológicas de PA, por si só, ou em combinação com o F induziu a activação da via das caspases, levando a uma diminuição em função do tempo da viabilidade celular. Métodos de análise exploratória de dados apoiam esta conclusão ao identificar claramente os efeitos dos tratamentos com FA. Na verdade, algoritmos de aprendizagem não supervisionados criaram clusters homogéneos e coesos, com uma separação clara entre amostras tratadas com PA e FFA para identificar um subconjunto mínimo de marcadores mitocondriais críticos, a fim de

atingir um modelo credível para prever a morte celular em NAFLD ou para selecção de possíveis agentes terapêuticos, com particular foco na medição da função mitocondrial.

Finalmente, para validar os efeitos benéficos do antioxidante mitocondriotrópico derivado do ácido hidroxicinámico AntiOxCIN$_4$, ratinhos C57BL/6J suplementados diariamente com 2,5 mg de AntiOxCIN$_4$ foram alimentados com dieta normal (SD) ou dieta ocidental (WD) [com alto teor de gordura (30 %) e sacarose (30 %)] durante 16 semanas para induzir esteatose simples nos ratinhos. Além disso, incubamos células HepG2 com AntiOxCIN$_4$ (100 µM, 48 h) antes da exposição a albumina sérica bovina (BSA) ou à mistura de ácidos gordos livres (FFA) (250 µM, 24 h) como forma de induzir a acumulação lipídica nas células (capítulo 9). Nos ratinhos alimentados com WD, a suplementação com AntiOxCIN$_4$ diminuiu o peso corporal (cerca de 43%) do animal, assim com o peso do fígado (cerca de 39 %), e dos marcadores de dano hepático no plasma. A melhoria nos parâmetros hepáticos caracterizou-se por uma redução na acumulação de gordura no fígado (600 %) e à remodelação da composição da cadeia de ácidos gordos livres em comparação com o grupo alimentado apenas com WD. Os dados em células HepG2 confirmaram uma menor acumulação lipidíca, evidenciada pela redução clara do tamanho e do número de gotículas lipídicas em células incubadas com AntiOxCIN$_4$. A suplementação com o AntiOxCIN$_4$ induziu a remodelação do metabolismo mitocondrial pela regulação positiva das subunidades da OXPHOS, mediada pela via PGC-1α-SIRT3. Consequentemente, os dados em células HepG2 corroboraram que a pré-incubação com AntiOxCIN$_4$ estimula as taxas de consumo de oxigénio associado à oxidação de ácidos gordos e à remodelação da expressão de genes da OXPHOS. AntiOxCIN$_4$ também regulou positivamente o sistema de defesa antioxidante hepático em ratinhos alimentados com WD e neutralizou a exacerbação de espécies reativas de oxigénio (ERO) em células HepG2 incubadas com FFA. Finalmente, a suplementação com AntiOxCIN$_4$ evitou o bloqueio do fluxo autofágico impulsionado pela acumulação lipídica, devido a um aumento da capacidade proteolítica lisossomal tanto *in vivo*, como *in vitro.*

No geral, os resultados obtidos nesta dissertação agregaram novo e, relevante, conhecimento ao mostrar que o AntiOxCIN$_4$ melhora o fenótipo de simples esteatose em ratinhos maioriatariamente por três mecanismos: a) aumentando da função mitocondrial (oxidação de ácidos gordos); b) regulação da capacidade antioxidante

(enzimática e não enzimática) e; c) prevenção do bloqueio do fluxo autofáfico. Juntos, os resultados apoiam o uso potencial de AntiOxCIN$_4$ na prevenção/tratamento da FíGNA.

Palavras-chave: Antioxidantes da dieta; Ácido cafeico; Mitocôndria; Antioxidantes mitocondriotrópicos; Nrf2; Defesas antioxidantes; síndrome do fígado gordo não-alcoólico (FíGNA); *Stress* oxidativo; Dis(função) mitocondrial; Mitofagia

PART I

General Introduction

1. Chapter
Non-alcoholic Fatty Liver Disease (NAFLD)

1.1. Historical background

Non-alcoholic fatty liver disease (NAFLD) is a spectrum of fatty liver syndromes that do not result from excessive alcohol intake (≤ 30 g alcohol/day in men; ≤ 20 g alcohol/day in women), viral, autoimmune, drug exposure-related, or genetic etiologies**.**

Liver Steatosis, a pathological accumulation of intra-hepatic fat content, was initially mentioned in 1836 by Thomas Addison [1]. Carrol Leevy later graded steatosis seriousness in different categories: normal - total liver fat <5%; irregular but no clinically meaningful - 5–9%; mild steatosis - 10–30%; moderate steatosis - 30–70% and severe fatty live - >70% [2]. Subsequently, in 1964, Mario Dianzani described the pathogenesis of fat accumulation in the liver [1, 3]. An association between fatty liver with inflammation, fibrosis or cirrhosis, unrelated to alcohol but associated with diabetes or obesity, was then reported by Michael Adler and Fenton Schaffner in 1979 [4]. Soon after, Jurgen Ludwig and colleagues introduced in 1980 the denomination non-alcoholic steatohepatitis (NASH) for the first time [5], but the terminology nonalcoholic fatty liver disease was only accepted by the scientific community in 1986 [6]. In 1999, Christi Matteoni reported a histological spectrum of NAFLD severity comprising grading of steatosis, lobular inflammation, ballooning degeneration and Mallory hyaline (inclusion of damaged intermediate filaments within the liver cells) or fibrosis [7]. In the same year, Elizabeth Brunt created a consistent histological grading and staging method for NASH diagnosis [8]. Alongside, Helena Cortez-Pinto and Picard Marceau related NAFL with the metabolic syndrome [9, 10]. Hilla Knobler stated a high potential for fatty liver reversibility through dietary interventions [11]. Three years later, Stefano Romeo reported increased NAFLD susceptibility from genetic variations in the PNPLA3 allele [12]. More recently, due to common fatty liver-associated metabolic dysfunction a new term was suggested – metabolic dysfunction associated with disease (MAFLD) [13]. However, NAFLD will still be the standard denomination in this document.

1.2. Epidemiology

NAFLD englobes a spectrum of diseases, ranging from non-alcoholic fatty liver (NAFL) or simple steatosis, a more benign stage, to non-alcoholic steatohepatitis (NASH), which can evolve to cirrhosis and hepatocellular carcinoma (HCC) [14, 15]. The progression through stages is a slow process and can take many years. Patients diagnosticated with simples steatosis take on average 14.3 years to reach the fibrosis stage, while NASH patients take 7.1 years [16].

The incidence and prevalence of NAFLD are alarmingly rising worldwide. Statistically, the global prevalence of NAFLD is around 25-29%, with the lowest rate in Africa (13%) and the highest in Southeast Asia (42%) [17, 18]. In Europe, the prevalence of NAFLD is approximately 24%, with notorious higher rates in Southern Europe compared with Northern Europe [19], peaking at 41% in Greece [20]. Additionally, a time-dependent uptrend in NAFLD prevalence is documented [from 25% between 1999 and 2005, to 28 % between 2006 and 2011, and 34% between 2012 and 2017] [20]. In Portugal, the incidence is around 17% [21]. NAFLD incidence is higher in men than in women (37% vs. 23%) and rising in older populations (age ≥45 years) than in younger populations (age <45 years; 32% vs 27%) [20].

Although NAFLD is strongly associated with obesity, lean NAFLD is also a health concern. Studies showed that in the NAFLD population, 19% of people were lean and 41% were non-obese [22]. A prevalence rate of 7% of normal-weight (lean) NAFLD patients in the USA, while a range between 25-30 % in rural areas of some Asian countries [19, 23] was shown.

From the world population with NAFL, 15-30 % progresses to NASH (among biopsied NAFL patients increase to 59 %), therefore 15-25 % develops fibrosis. From the ones that reach fibrosis stage, around 7 % advance to hepatocarcinoma stage [17]. From 2007 to 2017, cirrhosis-related disability-adjusted life years (DALYs) due to NAFLD/NASH increased by 23.4%, while the increment was 37.5% for liver cirrhosis and liver cancer-related DALYs due to NAFLD/NASH [24]. NASH has a global prevalence estimated between 3% to 5%, and recent projections estimate an increase of 56% in NASH incidence amongst 2016 and 2030 in developed countries [25]. Still, NASH is responsible for 18% of all HCC cases in the USA, corresponding to an 8-fold increase from 2002 to

2017 [26] (**Figure 1**). In Canada, NAFLD and alcohol-related liver disease will cause practically all new cirrhosis cases by 2040 [27]. More recently, a study on Swedish children and young adults (≤25 years) showed that the 20-year absolute risk of overall mortality was higher in NAFLD patients than the general population (7.7% vs 1.1%) [28].

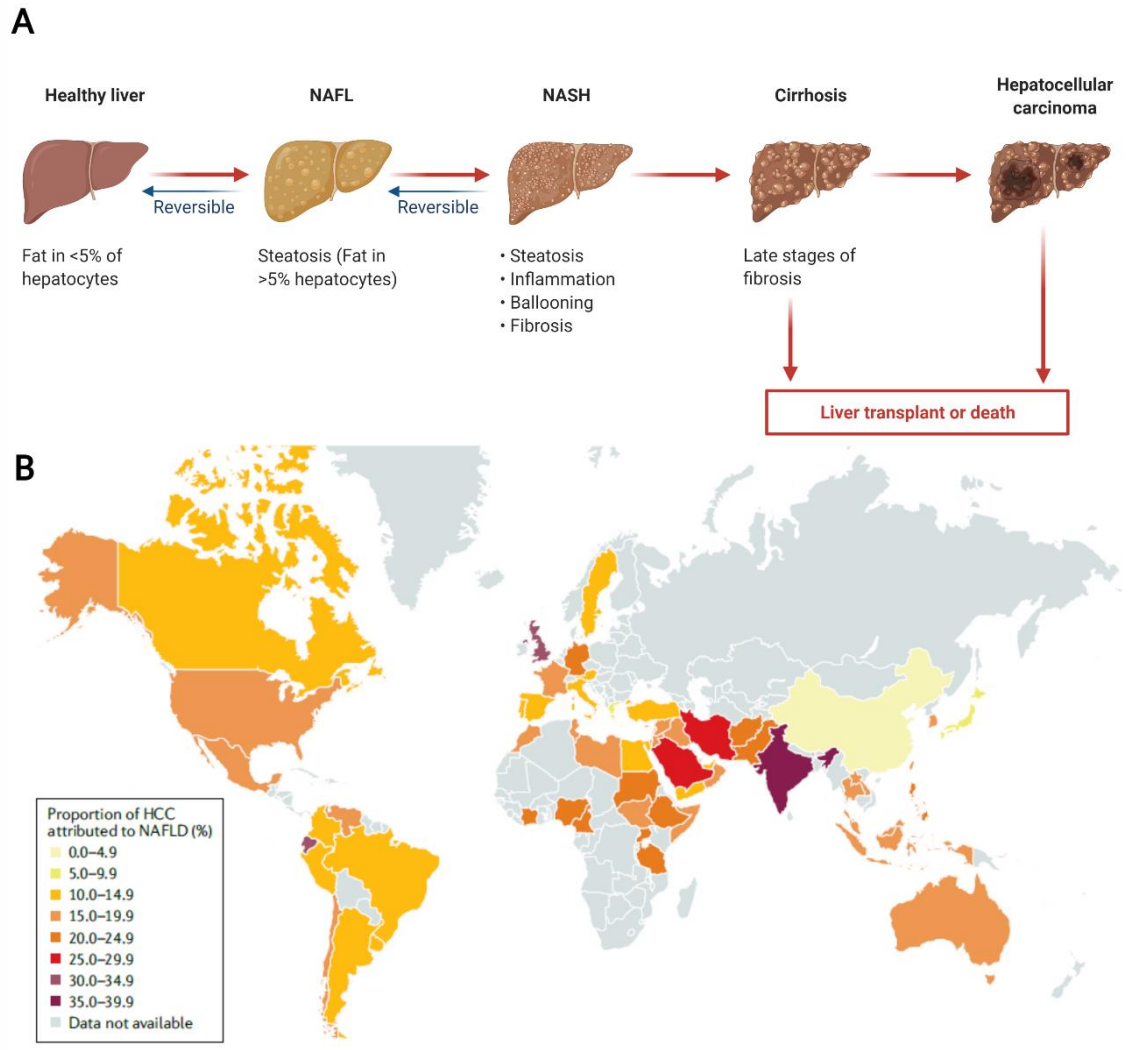

Figure 1. NAFLD spectrum and the estimated proportion of HCC attributed to NAFLD. (A) Different stages of nonalcoholic fatty liver disease (NAFLD), comprising non-alcohol fatty liver (NAFL), non-alcoholic steatohepatitis (NASH), cirrhosis, and hepatocellular carcinoma (HCC). **(B)** The proportion of HCC attributable to NAFLD is high in the UK, India, Germany, and the Middle East. Image 1B is available: https://www.nature.com/articles/s41575-020-00381-6?proof=t

NAFLD-related HCC rates will follow the obesity increase curve. For instance, 35% of the USA population in 2012 was obese and the percentage is expected to increase to 48.9% by 2030.

1.3. Risk factors

NAFLD is intrinsically related to the metabolic syndrome, including obesity, dyslipidemia, hypertension, and a higher incidence of developing type 2 diabetes *mellitus* (T2DM). A meta-analysis noticed that 51% of patients with NAFLD were obese, 23% had T2DM, 69% had hyperlipidemia, 39% had hypertension, and 42% had metabolic syndrome [29].

The prevalence of NAFLD is proportional to the rise in body mass index BMI [29]. The World Health Organization (WHO) defined overweight as a BMI higher or equal to 25 and obesity as a BMI higher or equal to 30. Although BMI has been used as general tool to access overweight and obesity, the population diversity (especially in Asia) required a more precise approach. Since the BMI does not account for visceral obesity, the measurement of waist circumference should also be part of assessing the risk and progression of NAFLD [30].

Dyslipidemia, which is characterized by exacerbated triglycerides (TG) and low-density lipoprotein cholesterol (LDL-C) levels and by diminished high-density lipoprotein cholesterol (HDL-C) concentrations, is also a risk factor for NAFLD. The overall hyperlipidemia/dyslipidemia prevalence estimates among NAFLD and NASH patients are 69 % and 72 %, respectively [17]

T2DM is another critical risk factor for NAFLD and NASH. The prevalence of NAFLD among diabetic patients is 56%, whereas the overall prevalence of NASH in people who have diabetes is around 37% [31]. Although T2DM incidence in children is scarce, the risk of T2DM increases with age, especially at puberty. Concernedly, T2DM accelerates NAFLD progression and can predict advanced fibrosis and mortality [31]

Hypertension is also a major (cardio-)metabolic risk for NAFLD, since 50% of hypertensive patients have NAFLD [31]. Moreover, the incidence of prevalent hypertension and high-normal systolic blood pressure (BP) in nonhypertensive individuals is higher in NAFLD patients than in the overall population [32, 33]. In fact, uncontrolled hypertension contributes as an increased factor of cardiovascular disease (CVD)-related mortality [34].

Although NAFLD is associated with unhealthy dietary habits such as excessive caloric intake, high fructose consumption, and a sedentary lifestyle [35], genetic

contributions to NAFLD development have been documented. The heritability component was suggested in NAFLD development [35]. In the last decade, the role of genetic variations in the pathophysiology of NAFLD has been a focus of research, specifically the finding of single nucleotide polymorphisms (SNPs), [36]. So far, at least five major variants in exclusive genes associated with NAFLD were described: *PNPLA3* (patatin-like phospholipase domain containing 3); *TM6SF2* (transmembrane 6 superfamily member 2); *GCKR* (glucokinase regulator); *MBOAT7* (Membrane Bound O-Acyltransferase Domain Containing 7) and *HSD17B13* (Hydroxysteroid 17-Beta Dehydrogenase 13). Expression patterns and function of genes associated with NAFLD risk are described in **Table 1**.

More recently, other rare variants of protein phosphatase 1 regulatory subunit 3B (*PPP1R3B*, rs4240624), immunity-related GTPase M (*IRGM*, rs10065172), Lipin 1 (*Lpin1*, rs13412852), superoxide dismutase 2 (*SOD2*, rs4880) and kruppel like factor 6 (*KFL6*, rs3750861) were also identified in NAFLD patients [37].

Table 1. Expression patterns and function of genes associated with NAFLD risk.

Gene	Function	Variant	Outcomes in NAFLD
PNPLA3	Lipid remodeling; Lipogenesis	rs738409	Decreased lipolysis, phospholipase and retinyl-plamitate lipase activity; [38] Increased hepatic fat content, elevated liver enzymes, hepatic fibrosis, and cirrhosis.[39]
GCKR	Glucose uptake; Lipogenesis	rs1260326	Inhibition of glucokinase; [40] Increased glycolytic flux and malonyl-CoA levels; [41] Increased hepatic fat storage and decreased β-oxidation.[42]
TM6SF2	VLDL secretion	rs58542926	Increased hepatic TG content and higher risk of advanced fibrosis in NAFLD;[43] Lower concentration of hepatic-derived TG-rich lipoproteins; [44] Impaired incorporation of polyunsaturated fatty acids into hepatic TGs, phospholipids, and cholesterol ester.[45]
HSD17B13	Lipid droplet remodeling; Retinol metabolism	rs72613567	Decreased risk of chronic liver damage in NAFLD patients;[46] Increased hepatic phospholipids and downregulation of inflammation-related genes.[47]
MBOAT7	Remodeling of PI	rs641738	Increased liver damage;[48] Decreased PI species with arachidonoyl side chains; [49] Increased PI species with monounsaturated fatty acids;[49] Elevated plasma levels of LPI. [48]

Abbreviations: LPI, lysophosphatidylinositol; TG, triglyceride; PI, phosphatidylinositol. VL

1.4. Clinical diagnosis

The diagnosis of NAFLD requires evidence of an excessive accumulation of TG in the hepatocytes, while excluding other factors of hepatic steatosis.

The gold standard for NAFLD diagnosis is liver biopsy, an invasive technique that provides information about hepatic steatosis, hepatocellular inflammation, and fibrosis [50]. Liver biopsy can grade (severity of the disease) and stage (degree of progression to cirrhosis) liver illness. NAFLD activity score (NAS), a well-established scoring system for the histological diagnosis of NAFLD, provides a composite score based on the degree of steatosis, lobular inflammation, hepatocyte ballooning, and fibrosis. Due to the complexity and invasiveness of liver biopsy, most patients with NAFLD are tentatively diagnosed and staged using noninvasive strategies (**Table 2**) [51].

The most common outcomes in NAFLD patients are high serum TG and low HDL levels. Moreover, a mild increase of ALT and AST (3-times higher than the upper limit of a healthy person) can result from NAFLD [52]. [53]. Besides that, the diagnostic utility of ALT activity is still poor in NAFLD, with a sensitivity of 45% [54]. In fact, 25% to 50% of NAFLD patients revealed normal transaminase levels. NAFLD is also associated with increased serum ferritin levels [55]. Additionally, inflammatory markers are being identified in NASH pathogenesis. Adiponectin, an anti-inflammatory cytokine, is decreased while cleaved cytokeratin-18 (CK-18) fragment (released during apoptosis) is significantly elevated in the serum of patients with biopsy-proven NASH [56, 57]. Because no single biomarker is sufficient to diagnose NASH, a combination of clinical features with serum markers are being used to estimate NASH. Within these methods, we can find NASHTest, NASH Clinical Research Network (CRN) model, National Institute for Health Care Excellence (NICE) model, NAFLD diagnostic panel, and oxNASH risk score [51, 58]. In patients in later stages of NAFLD, which show fibrosis already, it is quite important to stage the level of fibrosis for future prognosis and guiding management. There are several methods to estimate the fibrosis before the need for liver biopsy (**Table 2**).

Table 2. Biochemical markers as predictors of non-alcoholic steatohepatitis and advanced fibrosis

Test	Predictors
NAFLD fibrosis score	Age, blood glucose, BMI, platelet count, albumin, and AST/ALT ratio
BAAT	BMI, age, ALT and TGs
BARD	BMI, AST/ALT ratio and diabetes
ELF	Hyaluronic acid, TIMP-1, and PIIINP
Hepascore	Bilirubin, γ-GTP, α2-macroglobulin and hyaluronic acid levels
FIBROSpect	hyaluronic acid, TIMP-1 and α2-macroglobulin
Fibrometer	Prothrombin index, platelet count, AST, urea, α2-macroglobulin and hyaluronic acid
NashTest	Age, sex, height, weight, serum TGs, cholesterol, α2-macroglobulin, apolipoprotein A1, haptoglobin, γ-GTP, ALT, AST and total bilirubin

Abbreviations: *ALT, alanine aminotransferase; AST, aspartate transaminase; BMI, body mass index; PIIINP, procollagen III amino terminal peptide (PIIINP); TGs, triglycerides; TIMP-1, tissue inhibitor of metalloprotein 1; γ-GTP, gamma-glutamyl transpeptidase*.

Besides biochemical markers, ultrasound techniques should be used as the first-line diagnostic test to access NAFLD. The most common imaging tool is the conventional ultrasound (e.g., grayscale abdominal ultrasound evaluation of the liver), which present good sensitivity and specificity in detecting moderate to severe levels of steatosis [59]. Ultrasound has several advantages compared to other imaging modalities, including ease of use, portability, accessibility, real-time capability, and low cost. Nevertheless, simple grayscale ultrasound has reduced sensitivity in detecting mild hepatic steatosis [60]. To overcome these limitations, quantitative ultrasound-based (QUS) techniques have been used to improve the diagnosis and classification of hepatic steatosis in NAFLD, such as:

- **Controlled attenuation parameter (CAP)**, in which liver fat quantification is measured by the ultrasound attenuation rate using a vibration-controlled transient elastography (TE) device, commercially available as FibroScan [61].
- **Attenuation (AC) coefficient,** in which acoustic waves are attenuated differently by steatotic when compared with normal liver parenchyma. This

approach allows a robust discerning between grade ≥ 1, grade ≥ 2 and ≥ 3 of steatosis [62].

- **Backscatter coefficients (BSC),** in which backscattered signals from liver tissue are used to detect intra-hepatocyte fat. Repeatability and reproducibility studies of AC and BSC techniques showed similar results [63];
- **Computerized calculation of hepatorenal index (HRI),** in which the assessment of hepatic steatosis is calculated by drawing regions of interest in the liver parenchyma and right kidney at similar depths, and extrapolating ultrasound-beam parameters [60].
- **Ultrasound envelop statistic parametric imaging,** in which the passive parametrization of ultrasonic speckle patterns establishes statistical distributions/models that can be relate to the structural and acoustic properties of tissues (scatterer density and size) [64]

Other techniques such as magnetic resonance spectroscopy (MRS), magnetic resonance imaging (MRI) or computed tomography (CT) can be used for NAFLD diagnosis. However, the need of centers with MRS expertise and the high-cost demand limits its widespread in clinical use.

In summary, the pathogenesis of fatty liver NAFLD/NASH is multifactorial, altering various serum biomarkers in different stages of the disease, which challenge the premature NASH diagnosis. Noninvasive tests should be used to assess NASH and advanced fibrosis, using liver biopsy only in undetermined situations.

2. Chapter
Mitochondria in NAFLD

NAFLD is well-defined as excess fat in the liver where at least 5% of hepatocytes exhibit lipid droplets (LD) that surpass 5–10% of total liver weight in patients. FFAs can reach the liver from three distinct sources: lipolysis (the hydrolysis of FFA and glycerol from triglyceride) within adipose tissue; dietary sources, and *de novo* lipogenesis (DNL) [65]. In order hand, FFA can be metabolized either through β-oxidation, re-esterification to TGs and storage as LD, or wrapped and exported as very low-density lipoprotein (VLDL) (**Figure 2**).

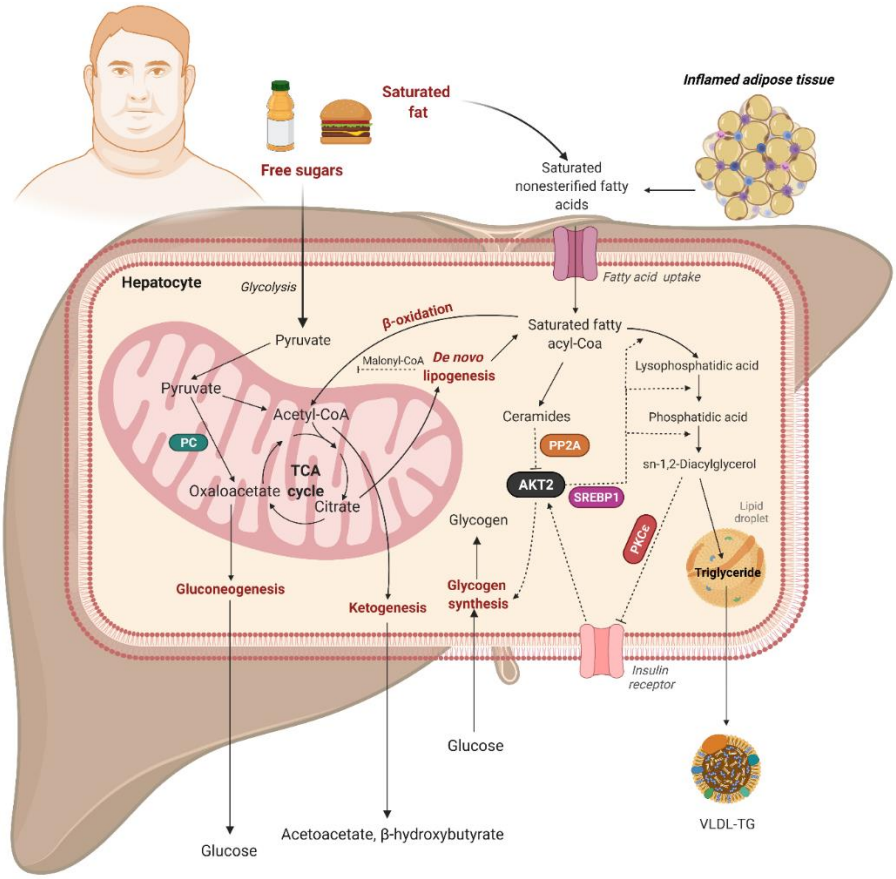

Figure 2. Metabolism of saturated fat and free sugars overload. Saturated fatty acyl-CoA can reach mitochondria for β-oxidation to generate acetyl-CoA in the liver, where it can further suffer ketogenesis or be oxidized to CO_2 in the TCA cycle. Otherwise, saturated fatty acyl-CoA can be metabolized into *sn*-1,2- diacylglycerols (sn-1,2- DAGs). *Sn*-1,2- DAGs promote PKCε translocation from cytosol to the plasma membrane, inhibiting insulin signaling at insulin receptor (INSR) [66]. This process reduces activation of

protein kinase AKT2 and following glycogen synthesis. In addition, *sn*-1,2- DAGs are precursors of TGs, which can be stored in hepatic LD or hydrolyzed and re-esterified in the endoplasmic reticulum (ER) as VLDL for secretion. Saturated fatty acyl-CoAs, specially palmitoyl-CoA, can likewise enter the *de novo* ceramide synthetic pathway. Ceramides can also stimulate this pathway via SREBP1and fatty acid uptake by PKCζ-mediated stimulation of the lipid transport protein CD36. Finally, ceramides can inhibit distal insulin signaling via PP2A-mediated inhibition of AKT2 [67]. Excessive intake of free sugars can stimulate DNL, which fully produces saturated fatty acids (SFA). AKT2, AKT Serine/Threonine Kinase 2; PC, pyruvate carboxylase; PKCε, protein kinase Cε; PP2A, protein phosphatase 2; SREBP1, sterol regulatory element-binding protein 1; TCA, tricarboxylic acid cycle. Created with BioRender.com.

Hepatic fat accumulation occurs in response to increased fat synthesis and delivery, decreased fat export, and/or diminished fat oxidation. In accordance, NAFLD patients exhibited 60% of liver TG content derived from FFA influx from adipose tissue, 26% from DNL, and 15% from diet, while DNL only contributes to <5% of healthy individuals hepatic TG formation [68].

Although the process of how fat accumulates in the liver is well-documented, the pathogenesis of advanced forms of NAFLD remains unclear. Between the hypotheses proposed so far, the one that collected more consensus is the “two-hit” hypothesis. According to this, NAFLD is a progressive disease in which increased free fatty acids (FFA) flux to the liver (“first hit”), combined with an imbalance in its oxidation or secretion, leading to hepato-steatosis [69]. Hepatic steatosis can progress to further stages due to “second hits” such as mitochondrial dysfunction, cytokines, adipokines, ER stress and bacterial endotoxins, for example, leaking from the gut. The theory suffered some alterations as new evidence showed that NAFLD may result from parallel “multi-hits” [70]. In this context, insulin resistance leads to enhanced lipogenesis and increased uptake of FFAs into the liver, which predispose liver to injury by “multiple parallel hits” (oxidative damage, activation of fibrogenic pathways, activation of hepatic stellate cells (HSC), altered expression of adipokines) leading to NASH and fibrosis.

2.1. Mitochondria physiology

Mitochondrial dysfunction is a crucial driver in NAFLD progression. The amount and degree of internal mitochondrial structure diverge from tissue to tissue, reliant on their metabolic states. Mitochondrial heterogeneity can occur even within the same

tissue. The liver is one of the organs richest in mitochondria, occupying 20–25% of the cytoplasm in liver cells (≈2000 mitochondria per cell) [71, 72]. Mitochondria are responsible for the cell's energy supply through adenosine triphosphate (ATP) production upon oxidative phosphorylation (OXPHOS). Importantly, this organelle is also crucial in calcium homeostasis, biogenesis of iron-sulfur clusters, heme and steroid synthesis, fatty acids catabolism, redox regulation of cellular signaling, and cell death pathways [73].

2.1.1. Mitochondrial morphology

Structurally, mitochondria are surrounded by two lipid bilayer membranes. The outer mitochondrial membrane (OMM) contains residues of cholesterol and is highly permeable to solutes and small metabolites (≈ 5kDa) by the existence of a non-selective channel, a voltage-dependent anion channel (VDAC) [74, 75]. The OMM separates the cytoplasm from the intermembrane space (IMS). IMS is a space where the proton gradient is accumulated, being also the site for some proteins involved in OXPHOS or in mitochondrial-dependent signaling. On the other hand, the inner mitochondrial membrane (IMM) is rich in cardiolipin and highly impermeable to the majority of the ions, containing only specific transporters (proton pumps or substrate-specific shuttles) [74, 75] to maintain metabolite transport as well as the proton gradient and optimal thermodynamic conditions for specific biochemical reactions [76]. More recently, intra-*cristae* space was also identified as a mitochondrial compartment [77]. The number of *cristae* in mitochondria has been associated with the cell's energy demand [78]. Functionally, the IMM separates IMS from an entirely different compartment, the mitochondrial matrix, where enzymes of the tricarboxylic acid cycle (TCA) (also called the citric acid cycle or Krebs cycle) are present (**Figure 3**).

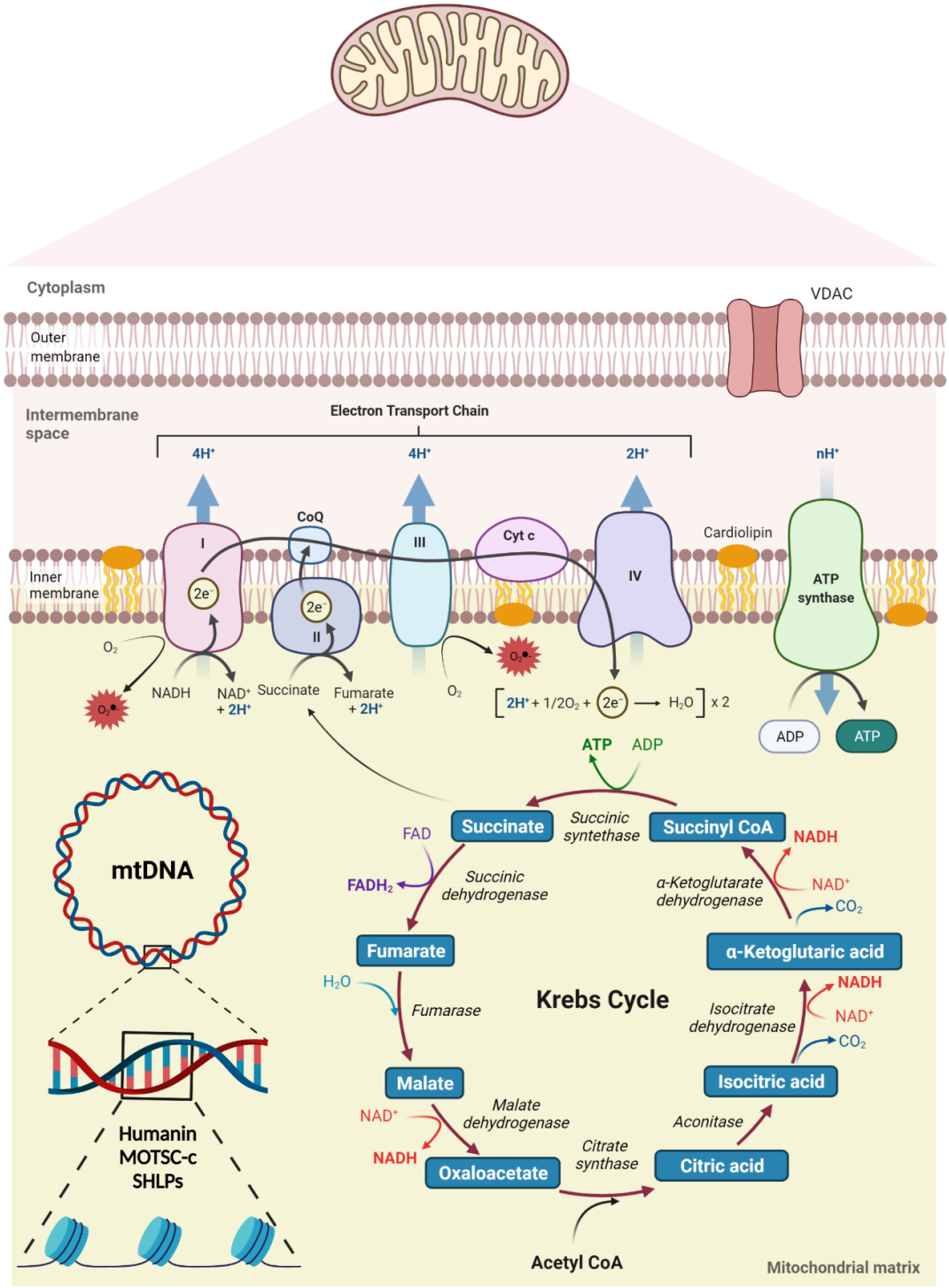

Figure 3. Mitochondrial morphology. Structurally, mitochondria are divided into four compartments: the mitochondrial outer membrane (OMM), the intermembrane space (IMS), the mitochondrial inner membrane (IMM), and the matrix. The respiratory chain is localized at the IMM, whereas mitochondrial DNA (mtDNA) is located in the matrix. The TCA cycle (Krebs cycle or citric acid cycle) takes place within the mitochondrial matrix. The respiratory chain, also known as the electron transport chain (ETC) is composed of approximately 100 proteins, 13 of which are encoded by the mtDNA (located in matrix). The oxidative phosphorylation system (OXPHOS) consists of five protein complexes; complex I (NADH

dehydrogenase) and complex II (succinate dehydrogenase) receive electrons (e^-) from intermediary metabolism, which are then transferred to coenzyme Q (Q) and subsequently delivered to complex III (cytochrome c reductase). The electron shuttling protein cytochrome c (cytc) transfers the electrons to complex IV (cytochrome c oxidase), which constitutes the final step in the ETC in which molecular oxygen is reduced to water. The electron transport is coupled to proton pumping across the IMM by complexes I, III, and IV. The resulting proton gradient drives ATP synthesis through complex V (ATP synthase). Reactive oxygen species (ROS), specifically superoxide ($O_2^{\bullet -}$), can be generated at complexes I and II. Created with BioRender.com.

Mitochondria have their genetic material (mtDNA), a double-stranded circular DNA about 16 kbp devoid of introns or histones, which is usually found in 2-10 copies per mitochondrion [79] with a ratio lower than 1:100 between mtDNA and total cellular deoxyribonucleic acid (DNA) content. Each hepatocyte has around 5000 individual copies of mtDNA [80]. Although the mitochondrial genome encodes for 13 polypeptides together with 22 transfer RNA (tRNA) and 2 ribosomal RNA (rRNA), most of the mitochondrial respiratory chain (MRC) different subunits are encoded by the nuclear genome (nDNA) and then translated in the cytoplasm and then imported to the IMS or the inner IMM through TIM/TOM machinery complex [81, 82]. More recently, short open reading frames (sORF) within the mtDNA's 16S and 12S rRNA regions were identified (**Figure 3**) [83]. Mitochondrial-derived peptides (MDPs) are small bioactive peptides encoded by sORF and further copied within the mitochondria. So far, humanin [84], MOTSC-c (mitochondrial open reading frame of the 12S rRNA-c) [85] and various SHLPs (small humanin-like peptides) have been found [86]. MDPs has been described as modulators of mitochondrial bioenergetics and metabolism, playing an important role in aging and age-associated disorders [87].

2.1.2. Mitochondrial ATP production

The TCA produce reduced molecules (NAD^+, NADH and succinate), which are crucial to sequential redox reactions and conformational changes in the MRC to produce energy [88]. At MRC, the electrons go through several multi-subunit proteins (Complexes I-IV) driven by a decrease in its redox potential, ultimately reaching oxygen as final acceptor [88](**Figure 3**). Complex I (EC: 1.6.5.3, NADH dehydrogenase, NADH

ubiquinone oxidoreductase) catalyzes the transfer of two electrons from NADH to ubiquinone (CoQ) along with proton translocation across the membrane. From each two-electron transferred, four protons moved from the matrix to the IMS. Moreover, complex II (EC: 1.3.5.1, succinate:ubiquinone oxidoreductase, succinate dehydrogenase) can be a second point of entry of electrons into MRC as it can connect directly to TCA [88]. Complex II has dual function, since it can oxidize succinate to fumarate as a component of the TCA cycle, while it transfers electrons from succinate to CoQ in the ETC. The potential energy of succinate oxidation nulls proton translocation. [89]. Subsequently, ubiquinone is reduced to ubisemiquinone and then to ubiquinol ($CoQH_2$), which transfers the electrons to complex III (EC: 1.10.2.2, ubiquinol:cytochrome-c oxidoreductase, cytochrome bc1 complex). Simultaneously, two protons are released to the IMS [88]. Finally, electrons flow to Complex IV (EC: 1.9.3.1, Cytochrome-c:oxygen oxidoreductase, cytochrome-c oxidase) via reduced cytochrome c (cytc), a process that involves a total of four electrons and four protons for the reduction of one molecule of oxygen to two of water [90]. The protons that were pumped from the matrix to the IMS create an electrochemical gradient (Δp), comprising an electric component (ΔΨm), which provides a negative charge inside mitochondria, and a pH component (ΔpH) in the matrix. Mitochondrial matrix has a pH of about 7.8, which is higher than the pH of the IMS of the mitochondria, which is around 7.0–7.4 [90, 91]. At a physiological stage, the proton gradient created by the ETC is used to produce ATP, as protons can re-flow through the ATP synthase (EC:3.6.3.14, ATP phosphohydrolase (H^+-transporting), F_OF_1-ATPase, Complex V) proton channel, phosphorylating ADP into ATP [90, 91].

Respiratory complexes of MRC can interact throughout a high organized supramolecular structure (supercomplexes), the “solid-state model" [92, 93]. Supercomplexes increase the catalytic activity of ETC individual complexes to transfer electrons due to the reduction of the diffusion distance between respiratory complexes [92], contributing to the assembly and stability of OXPHOS complexes monomers[94], and reducing electron leakage, which consequently prevents ROS generation into mitochondria [95]. Cardiolipin, a phospholipid mainly located in the IMM, is crucial in the assembly and stability of supercomplexes alterations, since modifications in

cardiolipin can disrupt supercomplexes stability and are associated with reduced OXPHOS efficiency [96].

2.1.3. Mitochondrial reactive oxygen species, antioxidant system defenses and oxidative stress

Cells maintain their homeostasis by regulating their redox status through modulation of oxidant and antioxidant species [97]. In (bio)chemistry, an oxidizing agent is a substance that can accept electrons, while antioxidants are molecules that can slow or stop the oxidation by scavenging free radicals, chelating prooxidative metals, quenching singlet oxygen and photosensitizers, and inactivating lipoxygenase [98]. By definition, a free radical is a specie that contains an unpaired electron in an atomic orbital [99].Notably, radicals have specific characteristics in biological systems, such as a high reactivity and a very short lifespan ($\leq 10^{-6}$ seconds). Under basal cell metabolism, reactive species (RS) are continuously formed, some with normal, and important, physiological functions such as regulation of cell proliferation and survival through the post-translational modifications of kinases and phosphatases [100].

Free radicals containing oxygen are highly reactive molecules that include numerous partially reduced oxygen species such as H_2O_2, hydroxyl radical ($^{\bullet}OH$) and superoxide anion radicals ($O_2^{\bullet -}$). Although several other redox systems throughout the cell showed to be capable of forming significant amounts of ROS [101]: endoplasmic reticulum (e.g., cytochrome P450 and b5 and diamine oxidase); peroxisomes (e.g., fatty acid oxidation enzymes, D-amino acid oxidase, L-2-hydroxyacid oxidase, and urate oxidase); cytosol (e.g., NO synthase, lipoxygenases and prostaglandin H synthase); plasma membrane (e.g., NADPH oxidase, lipoxygenase); extracellular matrix (e.g., xanthine oxidase), mitochondria are the main generators of cellular ROS in non-phagocytic human cells [102, 103]. Exacerbated mitochondrial ROS (mtROS) generation is particularly active in pathophysiology, playing key molecular functions and signal transduction pathways in inflammatory response, growth arrest and cell death [104, 105].

The MRC is most likely the major redox system in the cell and one important source of ROS under pathological conditions, as several redox carriers can potentially leak single electrons to molecular oxygen producing small amounts of mitochondrial ROS (mROS). Under physiological condition, 1-2 % of oxygen consumed is converted to $O_2^{\bullet-}$ during OXPHOS in mitochondria [102, 106, 107]. In fact, the one-electron reduction of O_2 to $O_2^{\bullet-}$ is thermodynamically favored *in vivo* [108]. While several redox couples in mitochondria have enough reduction potential to promote one-electron reduction of O_2, only some produce RS. The two major sites of $O_2^{\bullet-}$ production in mitochondria are complex I and complex III [108, 109].Mitochondria produce $O_2^{\bullet-}$ predominantly at complex I level in three distinct reduced components: FMN, FeS clusters, and CoQ binding sites [110]. Furthermore, Complex I has two different pathways for $O_2^{\bullet-}$ production, namely forward electron transference (FET) and reverse electron transference (RET). In FET, the NADH/NAD^+ ratio plays a crucial role by controlling the proportion of reduced FMN, as increased levels of reduced flavin can de-route electrons from their regular route to oxygen [111, 112].

On the other hand, studies in isolated mitochondria showed that a highly reduced CoQ pool, in conjugation with a maximal Δp and the absence of ATP synthesis results in $O_2^{\bullet-}$ production at complex I. This mechanism is responsible for most ROS production observed and is readily inhibited by rotenone and uncouplers [113]. Moreover, complex I is more sensitive to ΔpH component of Δp since an H^+/K^+ antiporter eliminates $O_2^{\bullet-}$ production [114].

At Complex III, $O_2^{\bullet-}$ production has the same magnitude as in FET, although considerably lower than in RET. In the presence of antimycin A, a complex III inhibitor, electrons are still routed to cytochrome b but the half-time of semi-CoQ at the QO site is enhanced, which increases the odds of electron slip to O_2 producing ROS at a higher rate. Although electron transfer can be hampered at high ΔΨm in complex III, by increasing the semiCoQ occurrence, complex III-induced ROS production is very low under normal conditions [110].

$O_2^{\bullet-}$ has a very short half-life, cannot cross the IMM, and upon formation is rapidly dismutated to hydrogen peroxide (H_2O_2) by two dismutases including Cu/Zn-superoxide dismutase (Cu/ZnSOD) in IMS (although this enzyme is mainly present in cytosol) and

manganese-dependent superoxide dismutase (MnSOD) in mitochondrial matrix (**Figure 4)** [72]. MnSOD activity is higher in the liver and kidney when compared to heart [115]. At low physiological levels (nanomolar range), H_2O_2 act as a second messenger due to its neutral and membrane-permeable capacity, diffusing freely from a site generation [104]. H_2O_2 selectively reacts with cysteine residues in redox-sensitive proteins, modifying activities or conformations of the proteins to regulate signal transduction [72, 116]. The state of low-level H_2O_2 maintenance and its associated physiological redox signaling is called "oxidative eustress" [117].

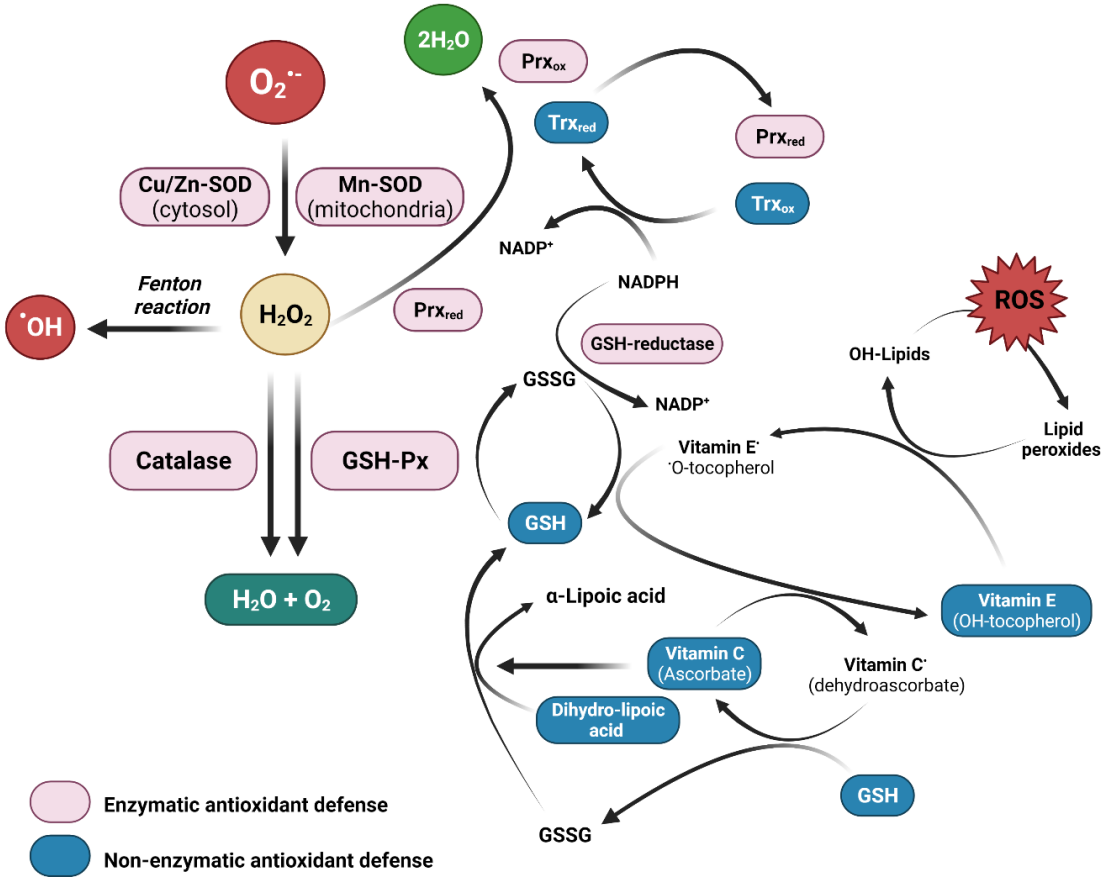

Figure 4. Endogenous antioxidant defenses. Oxidative stress (OxS) can be caused by endogenous and exogenous agents (see text for details). Production of $O_2^{\bullet-}$ by one-electron reduction of O_2 is mainly through leakage of electrons from the mitochondrial respiratory chain, particularly from ubisemiquinone ($QH^{\bullet-}$) or NADPH oxidases. Then, the dismutation of $O_2^{\bullet-}$ into H_2O_2 is guaranteed by superoxide dismutases (SOD). MnSOD is located exclusively in the mitochondrial matrix, whereas copper-zinc SOD (CuZnSOD) mainly performs this reaction in the cytosol or the intermembrane space. After H_2O_2 formation, it can be broken down into H_2O and O_2 by 15 enzymes, including catalase, the five peroxiredoxins (Prx) that use thioredoxin (Trx) or the eight glutathione peroxidases (GSH-Px or GPx).

Catalase is mainly localized in peroxisomes, although low amounts were reported in mitochondria. H_2O_2 does not readily oxidize most molecules but it can react rapidly with transition metals such as iron to produce hydroxyl radical ($^{\bullet}OH$). H_2O_2 elimination by Gpx is mediated by glutathione (GSH) with its consequent oxidative formation of glutathione disulfide (GSSH). GSH can regenerate vitamins C and E to their active form and act as a cofactor for GPx. Moreover, GSH is regenerated from GSSG, a process carried out by glutathione reductase (GSH-reductase or GR), which requires NADPH as a cofactor. Finally, H_2O_2 can be converted in H_2O, involving the formation of oxidized peroxiredoxin (Prx). Then, Prx is back to its reduced form by TRx oxidation, a task that requires NADPH and thioredoxin reductase (TRxR). Created with BioRender.com.

Subsequently, H_2O_2 can be converted to $^{\bullet}OH$ by Fenton reaction (**Figure 4**). Mitochondrial $O_2^{\bullet-}$ can also bind with protons to form uncharged $HOO^{\bullet}$ radicals and subsequently react with unsaturated fatty acid of mitochondrial membrane lipids to produce lipid radicals. Supraphysiological concentrations of H_2O_2 (> 100 nM) result in unspecific oxidation of proteins and altered response patterns, which reversible and irreversible damage biomolecules, causing growth arrest and cell death, with associated pathological states ('oxidative distress') [104].

In mitochondria, H_2O_2 can be degraded by the action of glutathione peroxidases (GPx), catalase, peroxiredoxins (Prxs) and thioredoxins (Trxs) (**Figure 4**). Catalase can convert two H_2O_2 molecules to H_2O and O_2, being mainly expressed in peroxisomes but also found in mitochondria. Moreover, its levels are higher in the liver followed by kidneys and heart [115]. Catalase also requires NADPH as a reducing equivalent to prevent oxidative inactivation of the enzyme [118]. Alternatively, H_2O_2 can be eliminated by Gpx through conversion of H_2O_2 to H_2O, which requires glutathione (GSH) (**Figure 4**) [115, 119]. GPx is found throughout the cell and its levels are high in the liver, kidney and heart [115]. Oxidized GSH (GSSG) is reduced to GSH by glutathione reductase (GR) activity, which is crucial since GSSG cannot be transported into cytosol [66]. Similarly, oxidized Prx can be reduced by direct reaction with thioredoxin (Trx) which in turns can be recycled by the action of Trx reductase (TrxR) in a nicotinamide adenine dinucleotide phosphate (NADPH)-dependent manner [115]. These H_2O_2 scavenging system ultimately relies on reduced NADPH, which is regenerated by three mitochondrial matrix-located enzymes: $NADP^+$-linked isocitrate dehydrogenase (IDH),

malate dehydrogenase (MDH) and nicotinamide nucleotide transhydrogenase (NNT) [120].

Besides the enzymatic approaches mentioned before, ROS can be eliminated by non-enzymatic approaches. Non-enzymatic strategies comprise membrane soluble α-tocopherol (vitamin E), ascorbic acid (vitamin C), retinol (vitamin A), favonoids and lipoid acid (**Figure 4**) [119]. α-tocopherol is particularly important in restraining lipid peroxidation progression due to its high octanol/water partition coefficient [108]. GSH is another non-enzymatic molecule, in which thiol group on cysteine residue can reduce disulfide bounds. GSH is the major water-soluble antioxidant, being synthesized in cytosol, where only ≈ 10% of the total amount is transported into mitochondria in liver cells [108, 121]. Interestingly, upon extracellular/plasma membrane insults, cytoplasmic GSH pool is consumed while the mitochondrial one remains intact [122], which show that mitochondrial GSH pool is the last one to be oxidized even in global stressful events.

mtROS production can occur even when mitochondria are working normally to produce ATP or using the ΔpH for other functions, such as thermogenesis [123]. However, the H_2O_2 efflux from mitochondria in this situation is insignificant compared with other mechanisms. Noteworthy, other sources of mitochondrial ROS^-, including α-ketoglutarate dehydrogenase, pyruvate dehydrogenase, glycerol phosphate dehydrogenase, and monoaminoxidase have been shown to be quantitatively sizable [124–126]. The generation of mROS seems to be affected by certain intrinsic properties of mitochondrial energetics. High ΔΨm conditions favor the production of mROS under specific conditions, whereas mitochondrial uncoupling agents can dissipate ΔΨm and consequently decrease in mROS formation [127, 128]

Excessive generation of ROS can occur due to a multiplicity of endogenous factor, comprising metabolism and inflammation or exogenous environmental factors, including pollution or radiation [100]. Mitochondrial antioxidant capacity is not infinite, and once consumed, ROS levels will increase progressively. Uncontrolled stimulation of basal ROS production or failure of antioxidant defenses to neutralize ROS results in a harmful state termed oxidative stress (OxS). Consequences of this state can range from

inactivation of different enzymes because of alteration in thiol status to more widespread damage as lipid peroxidation, or protein and nucleic acid oxidation [104].

Oxidative damage products of lipids include malondialdehyde (MDA), 4-hydroxy-2-nonenal (4-HNE), lipid peroxides, and 8-isoprostane. MDA and 4-HNE are extremely reactive aldehydic derivatives generated by the reaction with $O_2^{\bullet-}$ and H_2O_2 on the double bonds of polyunsaturated fatty acids (PUFAs) [129].

In the case of nucleic acids, oxidation can lead to the fragmentation of single or double strands or the modification of bases or sugars, which result in products such as 8-hydroxy-2'-deoxyguanosine (8-OH-dG) and 8-hydroxyguanine (8- OH-G) [130].

Proteins also can suffer oxidation, causing protein cross linkage, amino acid modification, and protein carbonyl formation [130]. Protein carbonylation is a main form of redox-dependent posttranslational modification (PTM). This process induce formation of stable protein-lipid Michael adducts, which is known as a mechanistic link between OxS and metabolic disorders [131]

Additionally, several mitochondrial proteins contain Fe–S clusters, which are highly reactive towards $O_2^{\bullet-}$. For instance, matrix aconitase is sensitive to ROS and can become inactivated upon oxidation [132]. Also, the assembly of Fe–S clusters is redox sensitive [133], in which oxidant insult will inevitably influence mitochondrial functions in metabolism, since respiration to subsequent oxidant generation.

Oxidants also have a tight bidirectional interplay with mitochondrial dynamics, markedly by fusion and fission events and *cristae* remodeling that regulate the morphology and the functionality of the mitochondrial network [134, 135].

2.1.4. Mitochondrial dynamics and quality control mechanisms

Mitochondrial morphology differs across cell types and tissues, changing in response to external insults and metabolic challenges [136]. Mitochondria have a strict relation morphology-function, which is influenced by ongoing events of fusion and fission of outer and inner membranes. While fission causes mitochondrial fragmentation, which is typically associated with metabolic dysfunction and disease, fusion results in a hyperfused network and tends to counteract metabolic insults, keep cellular integrity, and protect against autophagy [136].

Both mitochondrial fission and fusion processes require proteins from the dynamin family, the guanosine triphosphatases (GTPases) [137]. Fission is mediated by a cytosolic dynamin family member (DRP1). On the other hand, mitochondrial outer membranes fusion is guaranteed by membrane-anchored dynamin family members named MFN1 and MFN2, whereas fusion between mitochondrial inner membranes is mediated by a unique dynamin family member called OPA1.

In the liver, systemic glucose homeostasis relies on hepatic mitochondrial function. Sebastián *et al.* showed that MFN2 deletion in the liver results in mitochondrial fragmentation and ER stress, impairs insulin signaling and increases hepatic glucose production [138]. Livers with a knockout in DRP1 enlarged hepatic mitochondria and disrupted the spatial connection between mitochondria and ER by impairing mitochondrial fission [139].

As described so far, mitochondria can be damaged by several mechanisms (irregular mitochondrial morphology, insufficient ATP production, accumulation of mtDNA mutations, increased mtROS production), leading to the buildup of mitochondria that cannot develop proper functions. However, mitochondria by themselves can use quality-control proteases to eradicate impaired proteins [140] and act in response to unfolded protein stress through transcriptional induction of chaperone expression [141]. Cells have quality control mechanism, such as autophagy, that can eliminate inapt proteins or whole organelles.

Autophagy (or autophagocytosis) is the well-established and regulated self-degradation mechanism of the cell that removes unnecessary or dysfunctional components to compensate for nutrient depletion, low oxygen levels, decreased energy supply, stress, or other insults, contributing to cell homeostasis. Indeed, impaired autophagy has been associated with several human pathologies, including neurodegeneration, cancer and NAFLD [142–144].

Normally, autophagy follows a sequential mechanistic chain of events: initiation of the isolation membrane, elongation, closure of the isolation membrane, and autophagosome (double-membrane-bounded structures) formation, autophagosome–lysosome fusion, and lysosomal degradation (**Figure 5**). However, different forms of

autophagy have been identified: macroautophagy, microautophagy, chaperone-mediated autophagy (CMA), and crinophagy (**Figure 5**).

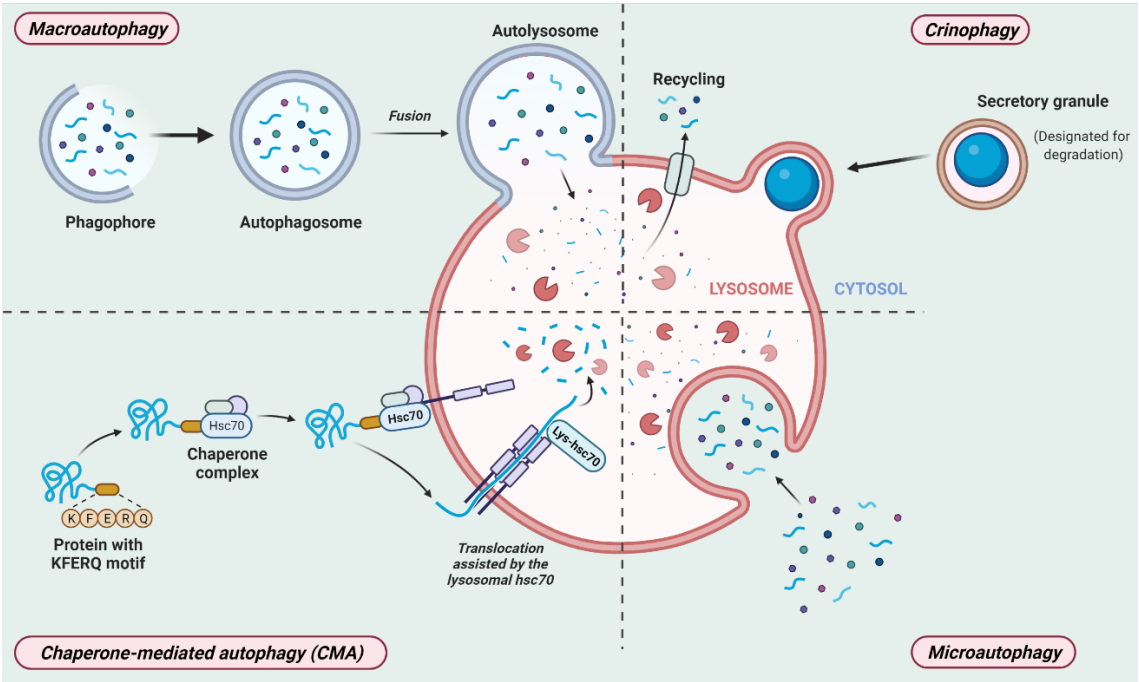

Figure 5. Mechanisms of autophagy. Macroautophagy delivers cytoplasmic cargo to the lysosome through the autophagosome that fuses with the lysosome to form an autolysosome, microautophagy take the cytosolic components direct by the lysosome itself via invagination of the lysosomal membrane. Both macro and microautophagy can engulf large structures by selective and non-selective mechanisms. In the case of chaperone-mediated autophagy (CMA), the proteins selected for degradation are translocated across the lysosomal membrane in a complex with chaperone, leading to their unfolding and degradation. Crinophagy is the least known and characterized autophagic process. In this process, secretory granules that are not released directly fuse with late endosomes or lysosomes, resulting in rapid digestion and reuse of their contents. Created with BioRender.com.

As referred before, autophagy is also required for maintaining a healthy mitochondrial network, ensuring the elimination of old and damaged mitochondria in a process called mitophagy (**Figure 6**) [145].

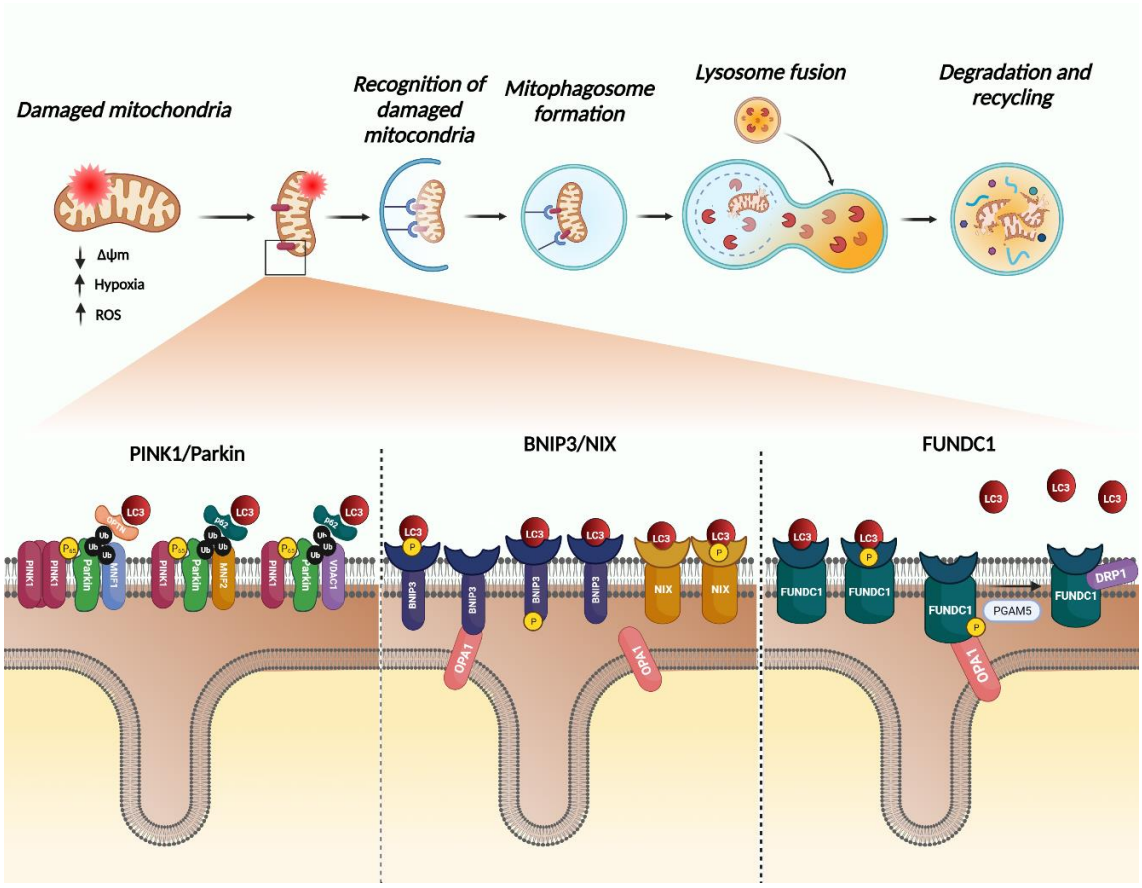

Figure 6. The main mechanisms of canonical mitophagy pathways upon autophagosome recognition of the different receptors in a damaged mitochondrion. First, PINK1/Parkin-mediated ubiquitination of mitochondrial proteins enables the autophagy cargo receptors p62 and optineurin (OPTN) to bridge the mitochondria/autophagosome interaction. Alternatively, BNIP3, NIX, and FUNDC1 can directly bind the LC3 molecules decorating the autophagosome, through a mechanism modulated by their phosphorylation status. Created with BioRender.com.

Mitophagy depends highly on the mitochondrial dynamics process and can be induced by several pathways. For instance, a dominant-negative mutant of DRP1 inhibits mitophagy and results in accumulated oxidized mitochondrial proteins, suggesting an importance role of fission in this process. During fission events, a sub-population of mitochondria with reduced $\Delta\Psi_m$ and diminished levels of OPA1 is generated, decreasing their ability to fuse and, subsequent, can be eliminated. Interestingly, overexpression of OPA1 decreases mitochondrial autophagy, suggesting that fission followed by selective fusion segregates dysfunctional mitochondria and allow their removal by autophagy [146].

Among the mechanisms by which mitochondria can be eliminated, the one involving PTEN-induce kinase 1 (PINK1) and Parkin is, so far, the best characterized (**Figure 6**) [147]. PINK1 is a mitochondrial serine/threonine-protein kinase that contains a mitochondrial target sequence, whose activity allows Parkin, an E3 ubiquitin ligase protein, to bind to depolarized mitochondria inducing mitophagy [148]. In healthy mitochondria, PINK1 is imported through the outer membrane via the TOM complex and partially through the inner mitochondrial membrane via the TIM complex. In the IMM, PINK1 (64 KDa) is cleaved by proteases, including mitochondrial-processing protease (MPP) and the inner membrane presenilin-associated rhomboid-like protease (PARL) in 60 kDa and 52 KDa forms, respectively. Then, PINK1 is proteolytically degraded within the mitochondria, which control the PINK1 levels in physiological conditions [149]. Dysfunctional mitochondria, in which the IMM turns out to be depolarized, PINK1 cannot be imported, therefore not cleaved by PARL, which increases PINK1 concentration in OMM. In this context, PINK1 serves as a sensor for mitochondrial damage. Then, PINK1 phosphorylates Parkin ubiquitin ligase at Ser65, which initiates Parkin recruitment at the mitochondria [150, 151]. Parkin phosphorylation at Ser65 is homologous to the local where ubiquitin is phosphorylated. Parkin suffers dimerization upon phosphorylation, which leads to an active state. Moreover, this mechanism allows for Parkin-mediated ubiquitination on other proteins [152]. Besides, the recruitment of Parkin occurs at the mitochondrial surface, increasing the probability of Parkin ubiquitylate proteins in the OMM [153], such as MFN1/MFN2 [150] (**Figure 6**). The ubiquitylation of mitochondrial surface proteins seems to serve as a mitophagy initiating factor. Parkin promotes ubiquitin chain linkages to recruit autophagy adaptors LC3/GABARAP (markers of autophagosomes), leading to mitophagy (**Figure 6**). However, the precise system and which proteins are necessary to initiate mitophagy is still unknown.

Although the PINK1-Parkin axis is the most mitophagy process studied so far, other pathways can induce mitophagy. Receptors in the OMM, such as NIX (BNIP3L), BNIP3 and FUNDC1, contain LC3-interacting region (LIR) consensus sequences that bind LC3/GABARAP, therefore degrading mitochondria by autophagy (**Figure 6**). Elimination of mitochondria during hypoxia is essential to reduce ROS production and maintain

oxygen homeostasis in mammalian cells [154]. BNIP3 is upregulated by hypoxia-inducible factor 1 α (HIF1α), being later phosphorylated at its serine residues near the LIR sequence, promoting LC3 binding. Activation of hypoxia-inducible factor induces expression of NIX and BNIP3, which at high levels disturb the interaction between BCL2 and Beclin-1. Consequently, free-Beclin-1 can nucleate pre-autophagosomal membranes and induce ATG5-dependent autophagy [155]. Also, under hypoxia conditions, FUNDC1 binds to LC3 through a conserved LIR motif that facilities mitochondria's engulfment by autophagosomes, inducing mitophagy (**Figure 6**) [156].

However, it is essential to empathize that additional activation of macroautophagy could be necessary to efficient clearance during mitophagy. Noteworthy, if events such as mitochondrial ROS generation or mitochondrial calcium (Ca^{2+}) are too extensive and overload the antioxidant network, besides the removal of damaged mitochondria by autophagy, a more drastic solution could be necessary, the triggering of cell death [157].

2.1.5. Calcium, mitochondrial permeability transition and cell death pathways

It is accepted that mitochondria accumulate and handle Ca^{2+}, participating in calcium homeostasis. Although mitochondrial Ca^{2+} affinity is low, the spatial organization of the mitochondrial network close to intracellular Ca^{2+} stores (e.g., ER) allows the mitochondrial calcium uniport (mCU) to sense Ca^{2+} concentrations much higher than those in cytosolic bulk.

The importance of mitochondrial Ca^{2+} accumulation is mainly the regulation of metabolism. Several enzymes present in the mitochondrial matrix are crucial, providing reducing equivalents (NADH and molecules that reduce $FADH_2$) for OXPHOS have allosteric Ca^{2+}-dependent activation sites and can be modulated by mitochondrial Ca^{2+} concentration. Mitochondria controls Ca^{2+} by three distinct and cooperative ways, all tightly coupled to its energetic shape: a) Ca^{2+} uptake from the extra-mitochondrial compartment ($\Delta\Psi$-dependent); b) Ca^{2+} buffering in the mitochondrial matrix (ΔpH-dependent) and; c) Ca^{2+} efflux to closer areas (Δp-dependent) [158, 159].

Although mitochondria have mechanisms to maintain mitochondrial calcium homeostasis, in situations in which $[Ca^{2+}]_e$ increases above a specific set-point (≈500 nM), the Ca^{2+}-dependent mCU is activated and Ca^{2+} is accumulated in the mitochondrial matrix.

Supra-physiological accumulation of free mitochondrial Ca^{2+} can result in mitochondrial permeability transition events, which are characterized by an abrupt increase in the permeability of the IMM. It occurs by the opening of non-selective pores, which permits the free passage of molecules smaller than 1.5 kDa [160]. Abnormal swelling of mitochondria induced by mitochondrial permeability transition pore (mtPTP) opening was observed upon high calcium overload [161]. Moreover, long-lasting episodes of mPTP opening occur when OxS accompanies mitochondrial Ca^{2+} accumulation, mitochondrial depolarization, augmented phosphate concentrations, and adenine nucleotide depletion [162–164]. In the continuous opening of mPTP, under several circumstances, the alterations in mitochondrial structural can lead to the expansion of IMM and consequent mechanical rupture of OMM (**Figure 7**). This process results in the release of several apoptotic initiators usually fenced in the IMS (e.g., cytc, the apoptosis-inducing factor (AIF) and the second mitochondria-derived activator of caspase/direct inhibitor of apoptosis (IAP)-binding protein with low isoelectric point (SMAC/DIABLO) protein) [165].

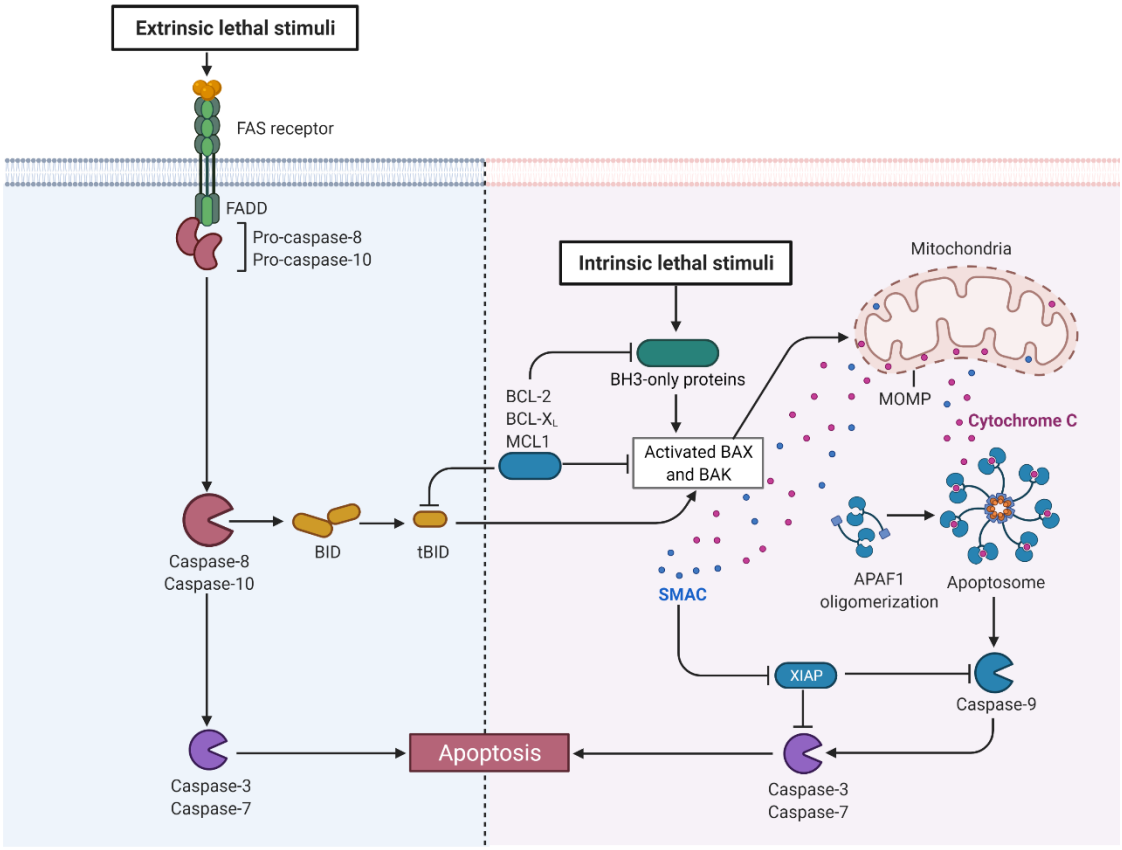

Figure 7. Extrinsic and intrinsic apoptotic pathways. Apoptosis can occur by the binding "death ligands" [e.g., Fas ligand (FasL) tumor necrosis factor alpha (TNF-α) and TNF-related apoptosis-inducing ligand (TRAIL)] to cell surface receptors (extrinsic pathway) or OMM permeabilization (intrinsic pathway). Both processes required caspase cascade activation. A core of B-cell lymphoma 2 (BCL-2) proteins that regulate mitochondrial membrane integrity can have a different role in apoptosis. For instance, BCL-2-associated protein, BAX, and BCL-2-killer 1 (BAK) have pro-apoptotic functions, while B-cell lymphoma-extra-large (BCL-XL), Bcl-2, and others are anti-apoptotic or pro-survival proteins [166]. In mitochondrial-dependent apoptosis, pro-apoptotic BCL-2 family proteins induce OMM permeabilization of additional pro-apoptotic molecules such as cytc, Omi/HtrA2 or SMAC/DIABLO. Upon translocation to cytosol, cytc binds to apoptotic protease activating factor 1 (Apaf-1), originating a multimeric complex that led to the activation of caspases cascades do or the AIF stimulation, which triggers caspase-independent cell death [166]. Other proteins from BCL-2 family proteins, the BH-3-only proteins (e.g., Bim, Bid, Puma and Noxa), are involved in regulating BAX/BAK activation. Caspases are a family of protease enzymes with specific cysteine protease activity. In intrinsic apoptotic pathway, the multimeric complex of cytc-Apaf1 activates caspase-9 and, therefore, the apoptosome complex. This process end up in caspase-3 and -7 activation [166]. In opposition, anti-apoptotic members can inhibit pro-apoptotic proteins or obstruct the BH-3-only activator proteins, preventing mitochondrial outer membrane permeabilization [167]. Created with BioRender.com.

Exacerbated mPTP opening is associated with several pathologies including myocardial ischemia-reperfusion injury, hepatic ischemia-reperfusion injury, traumatic brain injury, premature aging, Parkinson's disease and NAFLD [161, 168, 169].

Additionally, ROS-induced activation of c-jun N-terminal kinase (JNK) can also stimulate apoptotic signaling [170]. JNK is a member of the mitogen-activated protein kinase (MAPK) family, which plays an important role in mitochondrial dysfunction with consequent initiation of apoptosis [171]. In cancer cells, the activation of ROS/JNK elevated and sustained p53 activity, leading to apoptosis [172]. Apoptosis signal-regulating kinase 1 (ASK1) is also redox-sensitive, being upregulated by ROS/JNK axis. In fact, ASK1 activity is inhibited by interactions with redox proteins such as glutaredoxin 1 (Grx1) and Trx1. Upon OxS, Trx1 is dissociated from the ASK1-Trx1 complex, which recruit TNF receptor-associated factors to the complex [173]. Activated ASK1 can induce apoptosis either via mitochondrial signaling or via transcription of AP-1-dependent proapoptotic genes [174]. Finally, ROS can disrupt the mitochondrial ASK1/ ASK2/Trx2 complex, inducing cytochrome c release [175].

ROS can also be involved in other cell death pathways. Necrosis is a form of cell death which results in the unregulated digestion of cell components. On the other hand, regulated necrosis induced by TNF is known as necroptosis [176]. In this process, the phosphorylation of receptor-interacting serine/threonine protein kinase (RIPK) 1 and RIP3K is vital to necrosome assembly, an amyloid-like complex responsible for transmission initiation of the pro-necrotic signal, triggering ROS production [177]. RIPK3 deletion in liver cells reduces ROS levels in necrosis-induced cells, while RIPK3 overexpression exacerbates ROS production in HK-2 cells [178, 179]. Moreover, mtROS production mediated by RIPK1 activation can be regulated by the interaction between signal transducer and activator of transcription 3 (STAT3) and the mitochondrial electron transport chain complex I subunit GRIM-19 [180–182]. Interactions between RIPK3 and enzymes that catalyzes the conversion of glutamate and ammonia to glutamine in cytosol [glutamate-ammonia ligase (GLUL)] and glutamate to α-ketoglutarate [glutamate dehydrogenase 1 (GLUD1)] in mitochondria as well as a rate-limiting enzyme that catalyze glycogenolysis [glycogen phosphorylase (PYGL)], also increase mtROS production [183]. Likewise, NADPH oxidase NOX enzyme complexes can interact with

the TNF receptor, resulting in death-inducing ROS during necrosis [176]. Noteworthy, activated RIPK3 can recruit and phosphorylate mixed lineage kinase domain-like protein (MLKL), which oligomerizes and migrates to the cell membrane, creates pores that lead to cell death [184].

2.1.6. Mitochondrial β-oxidation

The β-oxidation of long-chain fatty acids (LCFA) is essential to obtain energy for the organism, vital for cardiac and skeletal muscle. Nevertheless, several other tissues, especially the liver, can utilize the products of β-oxidation for ketone body generation, which can be employed for energy provision in other tissues.

Fatty acid uptake into cells is guaranteed by specific proteins such as CD36 and plasma membrane fatty acid-binding protein ($FABP_{pm}$, also known as GOT2), while fatty acids (FA) are activated to acyl-coenzyme A (CoA) esters by acyl-CoA synthetases in the cytosol. Fatty acid oxidation (FAO) requires mitochondrial import of acyl-CoA, to which mitochondrial membranes are impermeable. A carnitine cycle formed by two acyltransferases, carnitine palmitoyltransferases 1 and 2 (CPT1 and CPT2), and carnitine acylcarnitine translocase (CACT), a member of the mitochondrial carrier family of proteins (SLC25A20), allows the acyl-CoA import to mitochondria (**Figure 8**).

CPT1, present in OMM catalyzes the acyl-CoA's transesterification to acylcarnitine, while CACT manages the transport of acylcarnitines across the IMM by releasing a free carnitine molecule in the cytosol. CPT2, a peripheral IMM protein, ends the cycle by reconverting the acylcarnitine into an acyl-CoA inside the mitochondria. Carnitine is mainly obtained by diet, although some tissues can synthesize it. Carnitine reaches the inside of the cell by the organic cation transporter OCTN2 (SLC22A5) (**Figure 8**) [185]. Then, acyl-CoAs are degraded via β-oxidation, a cyclic process consisting of four enzymatic steps inside mitochondria (**Figure 8).**

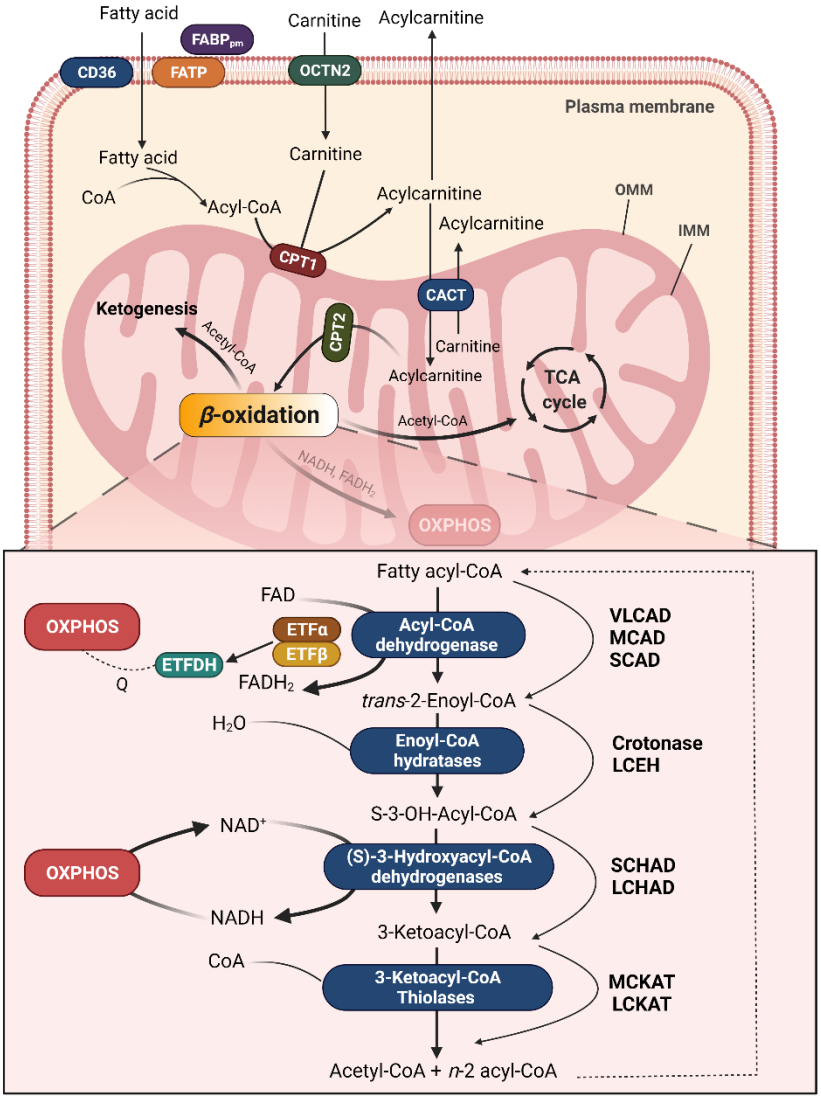

Figure 8. Mitochondrial fatty acid β-oxidation. In each cycle, acetyl-CoA is formed by the release of two carboxy-terminal carbon atoms in the acyl-CoA. The cycle is initiated by dehydrogenation of the acyl-CoA to *trans*-2-enoyl-CoA by an acyl-CoA dehydrogenase. This process is followed by a hydration catalyzed by an enoyl-CoA hydratase, which generate (S)-3-hydroxyacyl-CoA. Then, generated (S)-3-hydroxyacyl-CoA is dehydrogenated to 3-ketoacyl-CoA in a reaction performed by (S)-3-hydroxyacyl-CoA dehydrogenase. Finally, a thiolase cleaves the 3-ketoacyl-CoA into a 2-carbon chain–shortened acyl-CoA and an acetyl-CoA. The resulting acetyl-CoA is used to fuel the TCA cycle and ketogenesis and reduce flavin adenine dinucleotide (FAD) to $FADH_2$ and nicotinamide adenine dinucleotide to NADH [186]. The resulting $FADH_2$ is then oxidized by the electron transfer flavoprotein (a heterodimer of ETFα and ETFβ) and via ETF dehydrogenase (ETFDH) donate electrons to coenzyme Q, feeding the MRC. In the case of NADH, it is reoxidized via OXPHOS. The chain-shortened acyl-CoA reenters the fatty acid β-oxidation cycle. CACT, carnitine acylcarnitine translocase; CPT1/2, carnitine palmitoyltransferases 1 and 2; ETFDH, ETF dehydrogenase; $FABP_{pm}$, plasma membrane fatty acid-binding protein; FATP, fatty acid transport protein; LCEH, long-chain enoyl-CoA hydratase; LCHAD, long-chain (S)-3-hydroxyacyl- CoA dehydrogenase; LCKAT,

long-chain 3-ketoacyl-CoA thiolase; IMM, inner mitochondrial membrane MCAD, medium-chain acyl-CoA dehydrogenase; MCKAT, medium-chain 3-ketoacyl-CoA thiolase; OMM, outer mitochondrial membrane; SCAD, short-chain acyl-CoA dehydrogenase; SCHAD, short-chain (S)-3-hydroxyacyl-CoA dehydrogenase; VLCAD, very long-chain acyl-CoA dehydrogenase.

Both transcriptional and posttranscriptional mechanisms can regulate FAO. Peroxisome proliferator–activated receptor α (PPARα), PPARβ/δ, and PPARγ, a class of ligand-activated nuclear receptors, are activated by FA and has precise roles in physiology. In the liver, PPARα controls the expression of many genes involved in FAO and plays a crucial role in the adaptation of the liver to starvation by also empowering the induction of microsomal ω-oxidation, peroxisomal dicarboxylic acid metabolism, and ketogenesis [186, 187]. Additionally, PPARγ coactivator-1α (PGC-1α) is a crucial transcriptional coactivator in various metabolic processes such as thermogenesis in brown adipose tissue (BAT), mitochondrial biogenesis, FAO, and gluconeogenesis [186].

2.2. Mitochondria dysfunction in NAFLD

2.2.1. Mitochondrial adaptation (Hormesis) vs mitochondrial maladaptation to stress

Mitochondrial dysfunction is a crucial driven force in NAFLD progression. The relevant problem is how upregulation of mitochondrial activity precedes and amplifies the negative feedback loop of metabolic disruption and OxS, leading to inflammation and non-alcoholic steatohepatitis (NASH).

The term “hormesis” arises to define a “biphasic dose-response”, where a low dose of stress can stimulate an adaptive response in cells and organisms to preserve homeostasis, promoting health and even longevity, whereas higher doses become can be toxic, therefore leading to death. Hormesis has been accepted as the main mechanism for the health benefits of various external environmental factors. More recently, the “mitohormesis” concept was introduced as the hormetic response that promotes health and vitality upon sublethal mitochondrial stress [188]. Mitohormesis can involve other cellular mechanisms and requires precise coordination between the nucleus and mitochondria. ROS are one of the primary molecules involved in

mitochondria-nucleus communication [137], the crucial factor in mitohormesis regulation [189]. Low-intensity mtROS production initiates a hormetic response via latent feedback mechanism that boosts host-antioxidant defense pathways, including antioxidant enzymes as CAT and SOD, reducing OxS [190]. These hormetic responses carried out by mtROS were observed in caloric restriction (CR), intermittent fasting, exercise, and dietary phytonutrients [189].

Mitochondrial Ca^{2+}, which is described as having a role in mitonuclear communication, can activate mitochondrial biogenesis during exercise [191]. On the other hand, insistent mitochondrial Ca^{2+} uptake can trigger OXPHOS, boost ROS production and induce apoptosis. Lack of VDAC 1 phosphorylation, which controls the channel's permeability in response to Ca^{2+}, impacting the OMM permeability was observed in liver steatosis in humans [192].

ATP can also modulate hormetic responses. The ATP depletion observed in mitochondrial dysfunction leads to increased AMP/ATP ratio, which activates AMPK [193]. AMPK can then maintain mitochondrial homeostasis by regulating lipid and glucose metabolism to promote oxidation and inhibit anabolism, decreasing ATP utilization. Intermediaries of mitochondrial metabolism, such as NAD^+ or NADH, can also be used as signaling molecules. In fact, NAD^+ is an essential co-substrate in reactions involving sirtuins, poly (ADP-ribose) polymerases, and histone acetyltransferases [194]. Activation of SIRT1-PGC-1α pathway can modulate mitochondrial energy metabolism and biogenesis, promoting healthspan and lifespan [195]. Interestingly, SIRT1 overexpression attenuated high fat diet (HFD)-induced liver steatosis and inflammation by inhibiting CD36 expression and the NF-κB signaling pathway in mice models [196]. At the same time, $Sirt1^{LKO}$ mice exhibited hyperglycemia and IR due to increased hepatic gluconeogenesis, and are associated with increased intracellular ROS accumulation in multiple tissues, including the liver [197].

Proteotoxic signals are also involved in the hormetic processes. Defects in biogenesis, folding, trafficking, and degradation of proteins within the mitochondria leads to the accumulation of damaged or dysfunctional proteins in this organelle, which triggers the activation of a stress response to recover proteostasis. So far, mitochondrial unfolded protein response (UPR^{mt}) is the most documented mitochondrial stress

response [198]. Expression of UPR^{mt} target genes encodes for mitochondrial proteases and chaperones, mitochondrial transporters, and antioxidant enzymes, as well as cytosolic proteins involved in mitochondrial fission, glycolysis, and detoxification [199]. Receptors for mitokines such as growth differentiation factor 15 (GDF15) decreased the expression of pro-inflammatory cytokines and fibrotic mediators in livers of mice with CCl_4-induced liver fibrosis [200]. Moreover, the administration of nicotinamide riboside, a precursor of NAD^+ biosynthesis, protected against hepatic fat accumulation in high fat high sugar (HFHS)-fed mice by SIRT1 and SIRT3-mediated UPR^{mt}, triggering a mitohormetic pathway that increased hepatic β-oxidation and mitochondrial complex I activity [201].

During aging, mitochondrial function declines, contributing to deleterious processes such as inflammation and cell senescence. For example, a reduction in the target of rapamycin (TOR) signaling pathway resulted in fewer signs of cellular senescence and augmented autophagy. Activation of mTOR suppresses ULK1 activity and inhibits lipophagy, which regulates lipid metabolism in healthy cells by the autophagic degradation of lipid droplets [202]. Autophagy blockage has already been correlated with NAFLD progression. About 40–50% of human HCCs have upregulated mTOR activity [203].

Nuclear factor erythroid-derived 2-like 2 (Nrf2, NFE2L2), a redox-sensitive transcriptional factor that acts as a master regulator of the antioxidant response, also contributes to the hormetic induction of increased stress resistance [204]. Upon nuclear translocation, Nrf2 binds to the specific consensus *cis-element*, called the antioxidant response element (ARE), or to the electrophilic response element (EpRE) present in the promoter region of antioxidant genes. Nrf2 can also connect to other trans-acting factors, such as small Maf-F/G/K, the coactivators of ARE, which includes the cAMP response element binding protein (CBP) and p300, that can coordinately regulate the ARE-driven antioxidant gene transcription [205]. Nrf2 activation can improve the function of the ETC and prevent excessive ROS generation in mitochondria by increasing mitochondrial biogenesis and the endogenous antioxidant defense system [206]. Interestingly, in an initial disease stage, NAFLD patients showed increased serum levels

of antioxidant enzymes such as SOD, GPx, and GSH [207], indicating a possible adaptation in these patients (**Figure 9**). Moreover, the specific overexpression of hepatic Nrf2 in mice protects against OxS induced by prolonged methionine-and choline-deficient (MCD) exposure [208], while Nrf2 deletion result in progression from simple steatosis to NASH in HFD-fed mice [209].

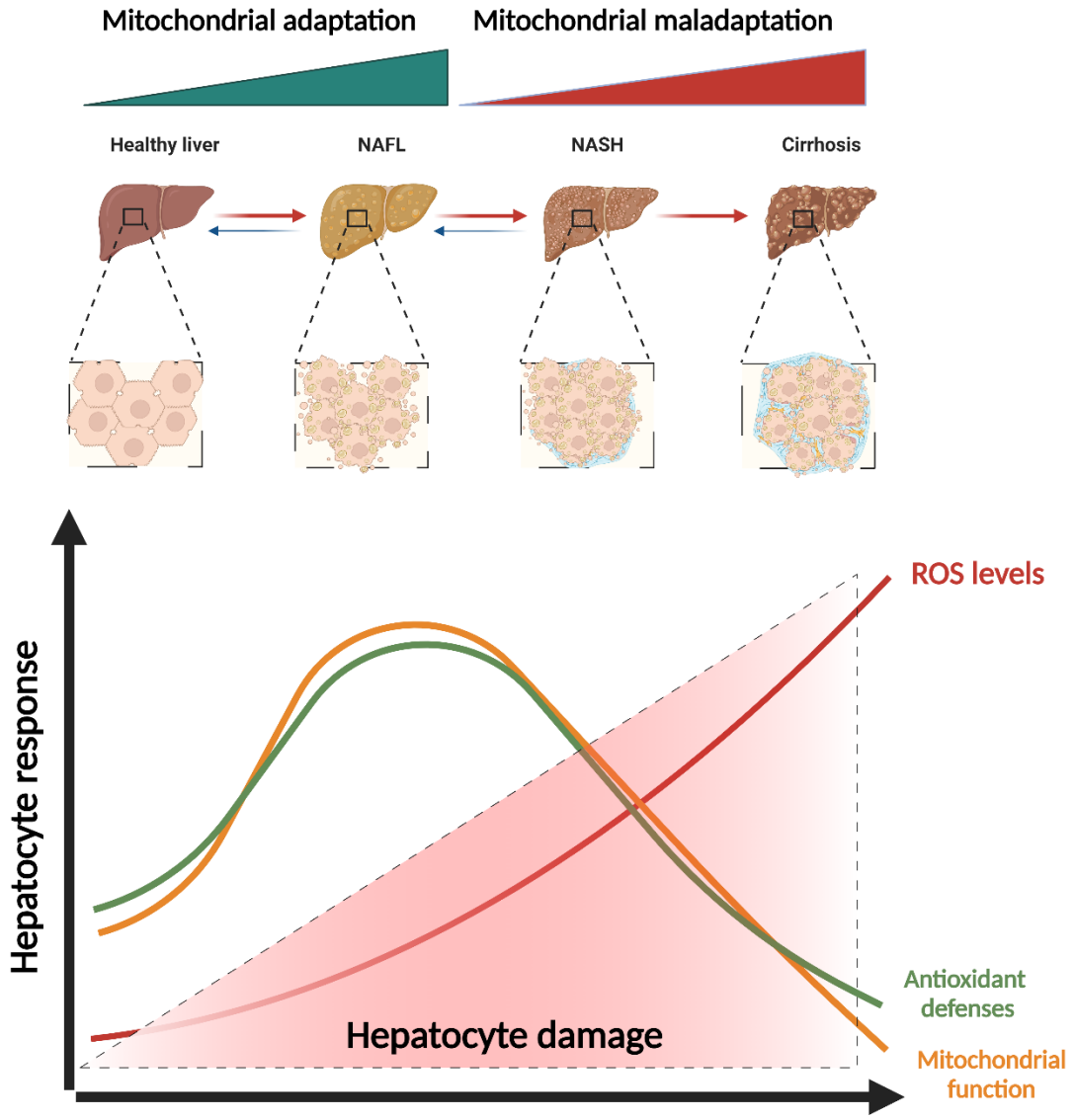

Figure 9. Mitochondrial adaptation and maladaptation in NAFLD progression. During NAFLD development, mitochondria increase their function in order to counteract lipotoxic insults. However, uncontrolled stimulation of basal ROS production or failure of antioxidant defenses to neutralize ROS results in exacerbated ROS levels that lead to oxidative stress and culminate in hepatocyte injury. ROS, reactive oxygen species. Created with BioRender.com.

Mitochondrial redox homeostasis is guaranteed by successfully removing physiological ROS through antioxidant mechanisms and by enabling metabolic adaptations that prevent substrate supply to the TCA cycle. However, the mechanisms through how cells maintain its ROS levels at a physiological state can be lost in NAFLD, resulting in amplified mtROS production and oxidative processes that damage mitochondria. This deleterious cycle continuously damages mitochondria as more FA reach mitochondria for oxidation and ROS are unchecked by the antioxidant defenses (**Figure 9**) [210].

2.2.2. Mitochondrial adaptations and dysfunctions in simples steatosis

In simples steatosis, the dysregulation of lipid and glucose metabolism occurs in the presence of high intake of high-caloric fat diets, which results in accumulation of TGs and FFAs in the liver, therefore modifying the mitochondrial proteome [211]. The two major metabolic fates of hepatic FFAs are mitochondrial β-oxidation and esterification to form TGs [212]. In response to fat overload, hepatocytes increase fatty acid oxidation (FAO) processes, followed by induction of the TCA cycle and enhancement of OXPHOS, avoid deleterious fat accumulation. AMPK induces catabolic pathways (e.g. fatty acid and glucose oxidation pathways) by inducing the activation of PGC-1α (**Figure 10**) [193]. When PGC-1α is activated, it powerfully coordinates gene expression that stimulates mitochondrial fatty oxidation. PGC-1α interacts with PPAR-α to induce the expression of several enzymes involved in fatty acid metabolism, including CPT-1 and acyl-CoA dehydrogenases [213]. The activity of PGC-1α can be also regulated by several post-transcriptional mechanisms such as reversible acetylation. For instance, hyperacetylation of LCAD, which catalyze the first step in oxidation of long-chain fatty acids after importation into the mitochondrial matrix, in Sirt3 knockout (KO) results in FAO disorders during fasting, as evidenced by the reduced ATP levels and intolerance to cold exposure [214]. The carnitine palmitoyltransferase system is an essential step in the β-oxidation of long chain fatty acids, as CPT-1 catalyzes the import of FFAs into the mitochondria. High carbohydrate consumption results in exacerbated acetyl-CoA levels, which increase malonyl-CoA levels, leading to inhibition of CPT-1 and reduced β-

oxidation [215, 216]. Clinically, CPT-1 activation improved NAFLD biomarkers in patients, as demonstrated by the decrease of serum levels of AST, ALT, bilirubin, and mtDNA [217].

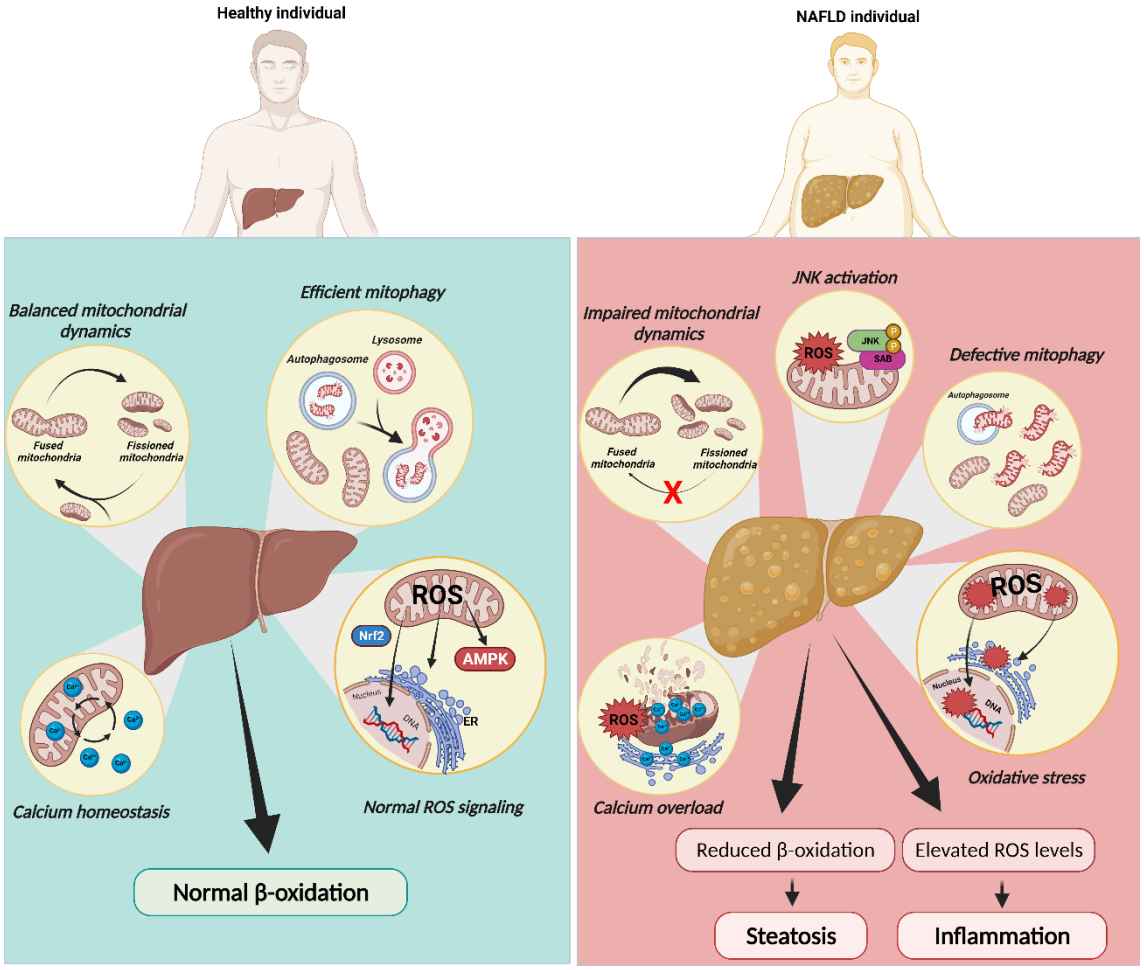

Figure 10. Mitochondrial dysfunction in NAFLD. Mitochondria rely on diverse mechanisms to preserve their function, including dynamics, redox signaling, mitophagy, and calcium homeostasis. In contrast to a healthy liver, mitochondria in NAFLD were reported to be fragmented, overloaded with calcium, with decreased oxidative capacity and increased ROS production, which causes JNK activation. JNK activation itself can induce these same defects in mitochondrial function, constituting a feed-forward cycle of mitochondrial dysfunction. Mitochondrial dysfunction in NAFLD was also explained by defective mitophagy. The decrease in fatty acid oxidation (FAO) caused by this compromise in mitochondrial function was believed to induce FA accumulation in hepatocytes while impairing insulin signaling. ER, endoplasmic reticulum; JNK, c-Jun NH2-terminal Kinase; SAB, SH3 homology associated BTK binding protein; ROS, reactive oxygen species. Created with BioRender.com

Alterations in mitochondrial composition mediated by higher FAO and mitochondrial function could reflect the adaptation to a chronic rise in gluconeogenesis

and intracellular lipid deposition induced by NAFLD, leading to the accumulation of mitochondrial ATP and TCA cycle intermediates.

Studies in human and mice with fatty liver demonstrated that mitochondrial pyruvate oxidation and TCA cycle flux are elevated in the fasted stage. However, ketogenesis does not follow the same tendency [218]. Because FAO is a major source of ketone bodies, the absence of ketosis conflicts with the elevated FAO reported in obese humans with IR [219]. Nevertheless, Flecther and colleagues explained this contradiction by showing that FAO-derived acetyl-CoA, normally used for ketogenesis, is diverted to the TCA cycle in simple steatosis. This result suggests that NAFLD is not a consequence of acetyl-CoA production *per se*, but how acetyl-CoA is later metabolized in the liver [220].

Mitochondria's ability to maintain high TCA fluxes alongside with high FAO rates could be the key pathogenic mechanism in NAFLD. Impaired ketosis can drive elevated TCA flux in NAFLD, which increases acetyl-CoA available. Accordingly, deletion of the mitochondrial pyruvate carrier 1 (MPC1), which decreases TCA fluxes, led to diminished hepatic glucose production and inflammation in HFD-mice [221, 222]. Notwithstanding, the hepatic steatosis reversion was not achieved in liver-specific MPC1 or MPC2 KO HFD feeding mice [221, 223]. MPC deletion is likely to decrease *de novo* FA synthesis but not dietary FA esterification, suggesting that steatosis occurs by increasing dietary FA esterification into intrahepatic TG in HFD fed MPC KO mice [224]. In contrast to what observed in HFD-fed mice, up to 38 % of hepatic TG accumulated in obese-NAFLD patients driven from DNL [225]. Higher levels mitochondrial acetyl-CoA fuels citrate and malonyl-CoA synthesis, stimulating the DNL. In fact, pharmacological inhibition of the enzymes responsible for malonyl-CoA synthesis, acetyl-CoA carboxylases (ACC1 and ACC2), reversed hepatic TG accumulation in humans (**Chapter 3)**.

Dyslipidemia has also a strong connection with NAFLD occurrence. The increase in plasma lipids is due to upregulation in hepatic TG synthesis directed towards VLDL assembly and excretion. Moreover, elevated VLDL assembly results from transcriptional upregulation of the rate-limiting enzyme in hepatic TG synthesis, glycerol phosphate acyltransferase 1 (GPAT1). This phenomenon occurs as consequence of increased

SREBP-1c activity [226]. Furthermore, elevated circulating levels of TG and VLDL upon acetyl-CoA carboxylase (ACC) inhibition strongly suggest the presence of a pool of FA that leak from fat oxidizing mitochondria and are entirely destined to VLDL synthesis.

2.2.3. The vicious cycle between mitochondrial OxS and mitochondrial dysfunction

Continuous supply at respiratory complexes promotes the production of $O_2^{\bullet-}$ [227]. While the mitochondrial ETC are the preferential site of ROS production, other mitochondrial enzymes such as GPDH and OGDH can participate in mitochondrial redox power and contribute to a decline in mitochondrial homeostasis [227], which induces a stress signaling response and mitochondrial dysfunction (**Figure 9-10**). Noteworthy, liver mitochondria present a very different pattern of ROS production compared with other tissues as FAO-originated ROS can be a vital player in OxS during hepatic FFA overload. Mitochondrial flavoproteins such as long and very-long-chain acyl-CoA dehydrogenases (LCAD and VLCAD, respectively) are both significant H_2O_2-generators in mitochondrial FAO in the liver, where LCAD showed to have a stronger capacity to generate H_2O_2 [228]. Indeed, these proteins were upregulated in HFD-fed-mice [229].

Liver tissues from patients with NASH exhibited high mitochondrial levels of ROS and mtDNA damage [230]. In accordance, hepatic tissues from obese (ob/ob) mice presented augmented formation of mROS, paralleled by higher OxS and lipid peroxidation and reduced levels of mitochondrial ETC apparatuses and diminished ATP levels [231–233]. Lipid peroxidation products (e.g., MDA and 4-HNE) are associated with various histological features of NASH [234, 235]. Patients with NAFLD presented plasmatic biomarkers of lipid peroxidation, and their concentrations are positively correlated with disease severity [236]

Steatotic livers from ob/ob mice also showed exacerbated levels of TNF-α and FFAs [232, 237, 238], together with decreased ETC coupling as observed by a higher degree of proton leak and subsequent decrease in ATP synthesis [239]. Due to the high demand for FA, patients with NAFLD have elevated mitochondria FAO and TCA cycle turnover, which result in consistent high source of reducing equivalents to the ETC. Noteworthy, livers of NAFLD animal models and patients showed increased TCA cycle

function [218, 240] but impaired respiratory coupling [241, 242], which explain a high ROS production rate.

Mitochondria dysfunction-associated ROS showed to act at AMPK and JNK level (**Figure 10**) [243, 244]. The activation of pathways involving these MAPKs plays a critical role in developing liver diseases and injuries, such as steatosis, NASH, fibrosis and hepatocarcinoma [70]. Primary hepatocytes exposed to high levels of FAs activate JNK to phosphorylate the mitochondrial protein SH3 homology associated with BTK binding protein (SAB), resulting in increased mtROS production and diminished production O_2 consumption [245]. In accordance, hepatocytes with JNK1/2 deletion exhibited enlarged mitochondria and elevated mitochondrial FAO, protecting obese mice from hepatic steatosis [246]

Alteration in cardiolipin (CL) content contributes to mitochondria dysfunction by decreasing ETC complex activity and promoting the mPTP opening [247]. This process seems to involve ALCAT1, a lyso-CL acyltransferase, upregulated by OxS and diet-induced obesity (DIO). Located at the mitochondria-associated membrane, ALCAT1 catalyzes remodeling of CL that leads to mitochondrial dysfunction, ROS production, and insulin resistance [247]. Furthermore, cytochrome c can be released from cardiolipin into the cytosol, initiating a caspase-mediated apoptotic pathway and subsequent cell death [247]. Apart from IMM, elevated ROS production has also been reported to be associated with OMM permeabilization, altered $\Delta\Psi m$ and loss of mitochondrial integrity in NAFLD [241].

In addition, the augmented hepatic ceramide synthesis in response to HFD feeding resulted in decreased mitochondrial respiration, inducing NASH in mice. Sphingolipid ceramide 16:0 directly decreases mitochondrial FAO in hepatocytes from steatotic mice, accompanied by reduced hepatic insulin signaling and, therefore, hyperglycemia [248]. In human NASH, it was also observed that exacerbated hepatic ceramide content is linked to diminished mitochondrial oxidative capacity [249].

The mtDNA molecules are very vulnerable to deleterious oxidative damage, an effect that is exacerbated by the lack of histones and diminished capacity for DNA repair when compared to the nuclear DNA [250]. In NAFLD, both mtDNA depletion and

augmented levels of 8-OHdG, an oxidized form deoxyguanosine, were reported [251]. OxS can compromise the transcription of nuclear-encoded mitochondrial genes by damaging nuclear DNA, leading to mitochondrial dysfunction. For instance, critical regulators of mitochondrial metabolism and biogenesis such as TFAM, Nrf2, and PGC-1α showed reduced expression levels in NAFLD [227].

Although increased mitochondrial FAO characterizes NAFLD, it was recently shown that reduced mitochondrial FAO capacity is also associated with steatosis and disease progression [211, 252]. Moreover, upregulation of PPARα and ACOX genes and higher levels of peroxisomal-related proteins in livers of HFD fed-mice [253, 254] and in NAFLD patients [255, 256] were reported. Increased peroxisomal FAO rate protect A/J mouse against diet-induced fatty liver [257]. Peroxisomes have an essential role in hepatic FAO, specifically when mitochondrial oxidative capacity is overloaded, as observed in high-fat diet-induced steatosis [257].

Mitochondrial and peroxisomal-oxidative pathways have been linked to aggravation of ROS production [258, 259]. OxS contributes to pathogenesis, mainly by inflammation-associated processes. It can be the triggering factor of some diseases, which is the case of NAFLD, where it prompts a progressive and irreversible escalation of oxidative damage caused by RS that markedly influences critical aspects of human biology, contributing to impaired physiological functions [260], with a particular impact on mitochondrial physiology, which might contribute to disease progression

Cellular mechanisms to battle OxS exacerbation in NAFLD relies on antioxidants defenses. Interestingly, concentrations/activities of these antioxidants are decreased in most patients with NAFLD/NASH [261–263] as well as many mouse models (mainly NASH) [124, 241, 264], although they are increased or unaltered in few cases [124].

Importantly, patients diagnosed with NASH showed a negative correlation between cholesterol content and mitochondrial GSH levels [265], probably resulting from impairment in the mitochondrial GSH transport system. Regarding SOD2, the data is inconsistent, as several authors showed both increase and decrease of SOD2 levels in NAFLD/NASH [266, 267]. This fact can be understood facing an early mitochondrial adaptation to OxS, that cannot persist in time (**Figure 9**). Interestingly, nutritional and genetic NASH models exhibited an increased expression of SOD2, paralleled by a

significant impairment in the activity, which may reflect sensitivity to OxS in later NAFLD stages [268].

Hepatocyte-specific deletion of GPx1 resulted in diminished hepatic lymphocytic infiltration, inflammation and liver fibrosis in mice fed with diet-induced NASH phenotype [269]. As a result of GPx1 ablation, H_2O_2 signaling led to inactivating protein-tyrosine phosphatase 1B (PTP1B). In fact, hyperactivation of PTP1B promotes IR and steatosis by dephosphorylating the insulin receptor and increasing SREBP-1c activity [270, 271]. The deletion of heme oxygenase 1 (HMOX1) in hepatocytes also increased H_2O_2-mediated PTP1B inactivation, protecting mice from NAFLD and hyperglycemia [272]. Although the beneficial effects induced by H_2O_2 actions in HMOX1 deletion came from mitochondria, the exact mechanism through how it occurs remains uncertain. Biliverdin is a product of heme degradation by HMOX1 and it is quickly converted into bilirubin. Remarkably, bilirubin decreased respiration and ATP production in isolated mitochondria [273], as well ability to reduce $O_2^{\bullet-}$ and H_2O_2 levels [274]. Though bilirubin is present in mitochondria [275], its mitochondrial role in NAFLD development remains unclear.

2.2.4. Impaired mitophagy in NAFLD progression

As mitochondrial dysfunction is undeniably a driving force in NAFLD progression, removing damaged mitochondria through mitophagy is an essential protective mechanism to counteract disease severity. Several *in vitro* studies mimicking NAFLD condition and mice subjected to HFD exhibited impaired mitophagy, culminating in increased fat accumulation, elevated OxS and inflammation [276–279] (**Figure 10**). HFD-fed mice showed exacerbated expression levels of ALCAT1 and defective mitophagy, a connection that requires more studies. Genetic deletion of Parkin in NAFLD mice models led to different outcomes. Hepatocyte-specific deletion of Parkin exacerbates fatty liver disease and IR [280], while protective effects in HFD-fed mice were also observed. The positive effects promoted by Parkin shutdown are due to ubiquitin-mediated stabilization of the lipid transporter, CD36 [281, 282].

Another protein involved in mitophagy, BNIP3, also acts as an important regulator in hepatic lipid metabolism. BNIP3 knockout in mice led to augmented lipid synthesis, mainly by reducing AMPK activity and increasing the expression of lipogenic genes. Besides, decreased β-oxidation was reported in BNIP3 knockout mouse livers [283]. SIRT3, mainly expressed in mitochondria, promotes the expression of BNIP3 and BNIP3-mediated mitophagy through activating the extracellular-signal-regulated kinase-cAMP-response element-binding (ERK-CREB) protein signaling pathway. In fact, primary hepatocytes overexpressing SIRT3 were protected against PA-induced apoptosis [276].

Although the impact of autophagic dysregulation in NAFL progression to NASH is inconclusive, several mechanisms of autophagy impairment have been described. For instance, decreased autophagy-related (ATG) 7 expression levels reduced autophagy flux in NAFLD [225] and anomalous activation of proteases, such as calpain-2, which can diminish autophagy proteins levels, namely ATG3, ATG5, Beclin-1 and ATG7 [284]. The accumulation of LC3-II and p62 was also detected in NASH patients, and its increase correlated positively with disease severity [285, 286]. Knockout of macrophage stimulating 1 (MST1), a novel cell survival regulator, stimulated the PINK1/Parkin-mediated mitophagy and counteracted the HFD-induced liver injury [287].

In NASH, decreased lysosomal acidification and expression of proteases activated at the low pH found in lysosomes (cathepsins) compromise the lysosomal proteolytic capacity and impair autophagic substrate elimination [288, 289]. Additionally, the alteration on lipid profile and content of both autophagosomes and lysosome during lipid accumulation decrease fusion between autophagosomes with lysosomes, leading to autophagic flux blockage [290]. SFA such as palmitic acid (PA) upregulate Rubicon, a beclin1-interacting negative regulator for autophagosome-lysosome fusion, suppressing the late state of autophagy fusion with lysosomes [291].

Recently, the inhibition of hepatic ATP2A2/SERCA2, an ER influx calcium pump in response to saturated FA deposition, leads to a lasting increase in cytosolic Ca^{2+} levels, which causes a defect in the autophagy process [292]. Exacerbated levels of well-known inactivators of autophagy, such as S-adenosylmethionine (SAMe) and methionine, through HFD-feeding mice showed to activate protein phosphatase 2A (PP2A) in a methylation process, which later blocked the autophagic flux [293].

As described above, mitochondria undergo morphological and functional changes in response to metabolic challenges, suggesting the importance of mitochondrial dynamics and mitophagy in metabolic adaptation (**Figure 10**). Decreased MFN2 activity induced by JNK activation during inflammation triggers mitophagy defects, as MFN2 supports the formation of autophagosomes [294]. Moreover, OPA1 ablation in the liver recovered mitochondrial homeostasis and reduced the accumulation of mitophagy intermediates, which could alleviate MCD diet-induced liver damage [295].

2.2.5. Mitochondria involvement in NASH and Non-alcoholic Fibrosis (NAF) development: the crosstalk between mitochondria, ER and innate immune response

Liver biopsies from NASH patients revealed mitochondrial ultrastructural abnormalities [296]. The sequential events of increased FFAs, DNL and accumulation of TGs induce adaptations of mitochondrial oxidative metabolism in NAFLD. Hepatic TCA cycle increases in response to incomplete β-oxidation, impairment of ketogenesis, and decreased mitochondrial respiratory chain and ATP synthesis [297]. However, even a dynamic organelle as mitochondria cannot infinitely protect cells against lipotoxicity in a chronically elevated influx of FFAs. Indeed, choline-deficient diet-fed mice exhibited higher levels of hepatic mitochondrial biogenesis and mitochondrial mass in the early stage of NAFLD, compared with livers from control mice (**Figure 9**) [298].

During NAFLD progression, mitochondrial dysfunction was described due to changes in the ETC complexes and ΔΨm, subsequently decreasing ATP synthesis. In this context, the capacity of mitochondria to metabolize the excess of FFAs vanish in later stages of NAFLD. To date, studies that assessed liver mitochondrial respiration in NASH patients have reported a severe reduction in mitochondrial O_2 consumption and ETC complex activity [299, 300]. In HFD-induced rodent models of NASH, the data is more inconsistent although the activity of complexes I and II progressively decayed over time in MCD-fed mice [301].

A consistent reduction in hepatic ATP content has described in patients and rodent models with NASH [302, 303]. While impaired ATP synthesis in early stages of NAFLD

could be the result of increased hepatic expression of uncoupling protein-2 (UCP2) [304], in NASH it occurs mainly by the suppression of ETC complexes activities [259].

The imbalance between mitochondrial FAO and ETC lead to ROS overproduction by increasing electron leakage from the ETC. Exacerbated mtROS production has been linked to NASH [305]. Moreover, OxS and lipid peroxidation are involved in the inflammatory response by activating NF-κB and producing of pro-inflammatory cytokines (TNF-α, IL-1β, Il-6 and IL-8), which culminate in apoptosis and necrosis of hepatocytes [306, 307].

Episodes of mPTP opening appear to be critical in hepatocyte cell death [231]. The pathogenesis of NAFLD has an ER stress component, as the accumulation of unfolded protein response (UPR) leads to ER stress, impairing a vital organelle in protective stress response in hepatic lipid metabolism [308]. The ER contains cytochrome P450 enzymes responsible for drug metabolism and acting primarily in lipid synthesis and cellular membrane biogenesis [308]. In fact, liver cells from obese mice showed decreased protein synthesis and increased lipid synthesis in ER, contributing to hepatic steatosis in obesity [309]. Downstream transcription factors of ER stress such as transcription factor 6 (ATF6), X-box–binding protein 1 (XBP1 s) and C/EBP homologous protein (CHOP) exhibited higher expression levels in livers from patients with NAFLD and NASH when compared to healthy individuals [310]. Essential mediators in proteins misfolding, ER chaperons (e.g., GRP78 and GRP94) were decreased in liver tissue from NAFLD and NASH patients [298, 310]. The UPR is also associated with DNL activation, which can boost lipid accumulation [298]. Prolonged ER stress or chronic activation of the UPR also stimulates hepatocyte damage (**Figure 11**) and inflammation via the CHOP-dependent signaling pathway, which activates NF-κB expression as recently demonstrated [311].

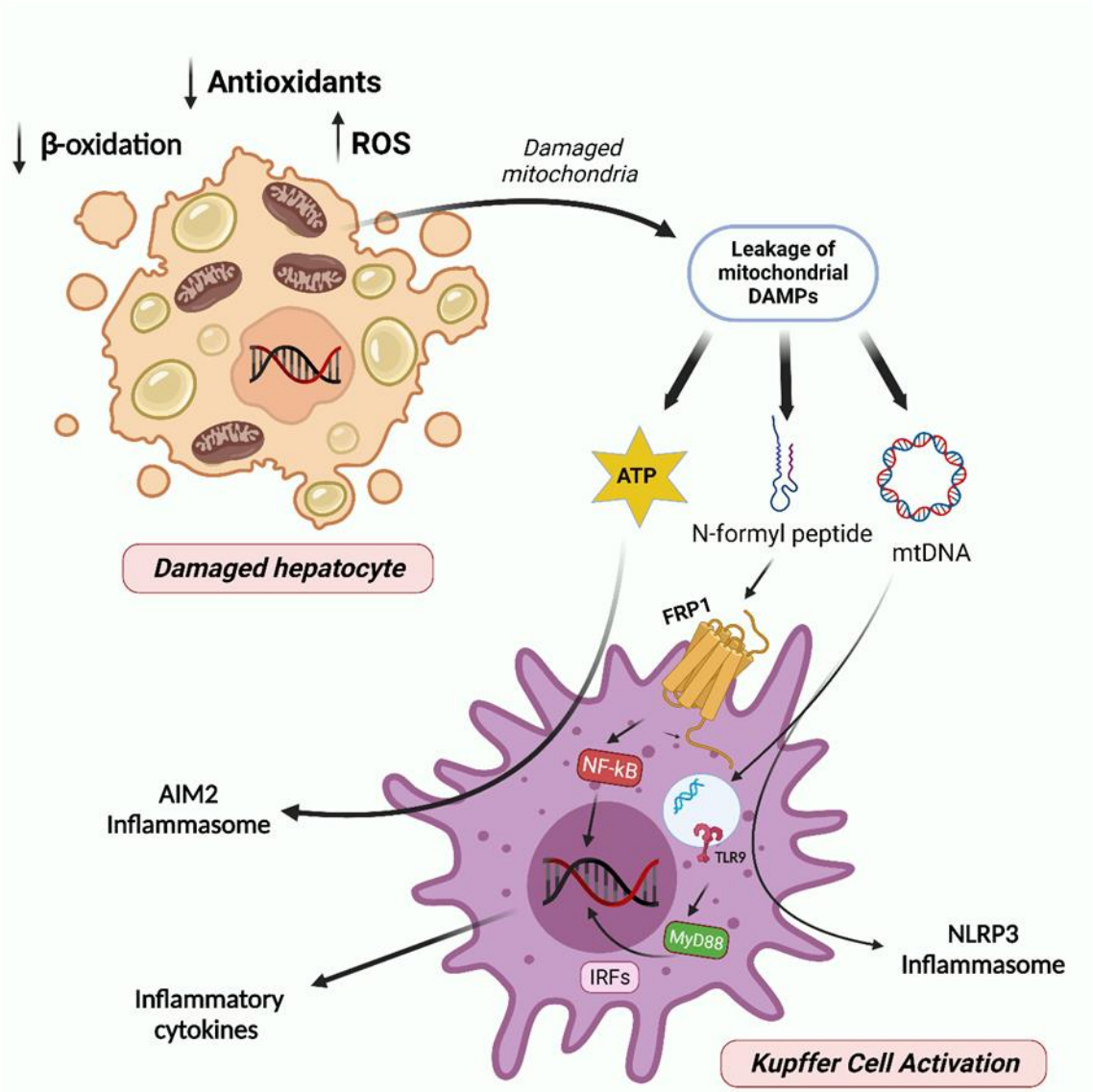

Figure 11. Mitochondria involvement in NAFL progression to steatohepatitis and fibrosis. The augmented accumulation of damaged/dysfunctional mitochondria within hepatocytes results in cell necrosis and induces the leakage of mitochondrial DAMPs, such as mtDNA, N-formyl peptides, and ATP. Further, these signals active toll-like receptor 9 (TLR9) and formyl peptide receptor 1 (FPR1), which activates the IRFs and NF-kB, thereby producing inflammatory cytokines. mtDNA and ATP also activate the inflammasomes NLRP3 and AIM2, respectively. Multiple inflammatory cytokines and the activation of inflammasomes provide a chronic inflammatory milieu, which contributes to steatohepatitis and fibrosis. Created with BioRender.com

Additionally, proteins involved in necrotic pathway such as RIPK3 and MLKL expression were augmented in the liver of a MCD mouse model of NASH [312]. RIPK1, RIPK3 and MLKL were also elevated in the serum of human NAFLD [313]. Recently, an association between TNF-α-induced RIPK3 expression, stimulation of necroptosis and

OxS has observed in primary murine hepatocytes [314]. mtROS formation showed to be RIPK3-dependent, promoting necroptosis pathway. Accordingly, RIPK3 deletion restored MRC complex activity while reducing OxS in mice fed with a choline-deficient L-amino acid-defined (CDAA) diet.

Hepatocyte necrosis leads to mitochondria-derived danger-associated molecular patterns (DAMPs) (**Figure 11**). Mitochondrial DAMPs activate NOD-like receptor family pyrin domain containing 3 (NLRP3) inflammasome and other innate immune systems through pattern recognition receptors such as toll-like receptors (TLRs) (**Figure 11**) [298, 315, 316].

In NASH, mtDNA released by injured hepatocytes in HFD-fed mice can interact with the TLR9 on Kupffer cells and hepatic stellate cells (**Figure 11**), stimulating the innate immunity as well as fibrogenic responses [317]. The combination of events comprising ROS-associated lipid peroxidation, mitochondrial DAMPs and activation of caspases promote chronic liver injury via intrusion of inflammatory cells [306, 317].

In summary, multiple pathways can be involved in regulating hepatocytes' mitochondrial physiology to maintain hepatic mitochondrial mass, integrity, and function. Alterations in mitochondria-related signaling pathways are determinant in hepatocyte fate and progression of NAFLD/NASH.

3. Chapter
Therapeutic strategies in NAFLD

NAFLD treatment is a challenge due to its complex etiology, difficult diagnosis, wide spectrum of NAFLD stages, and other comorbidities. Therefore, an individually personalized approach is recommended to improve outcomes of both NAFL and NASH patients. Individuals diagnosed with NAFL (fatty liver with no signs of inflammation) can revert this phenotype by adopting healthier lifestyle routines, including changing the diet and increasing physical activity. Nevertheless, in more advanced NAFLD stages, the administration of drugs to reduce IR and hyperlipidemia is highly suggested [318] (**Table 3**). However, so far there is no drug approved for direct therapy of NAFL or NASH.

Table 3. Clinical practice guidelines recommended by joined EASL–EASD–EASO associations

Stage		Current therapy
NAFL	Simple steatosis Steatosis and mild inflammation	Lifestyle modifications Energy restriction Macronutrient composition Exclusion of fructose intake Strict daily limit for alcohol consumption Physical activity Bariatric surgery
NASH	Early - none or slight fibrosis (F0-F1)	
	Advanced – significant and bridging fibrosis	As above, plus pharmacotherapy Pioglitazone Vitamin E Statins
Cirrhosis	Late-stage fibrosis (F4)	Liver transplantation
HCC	Liver tumor	Resection Liver transplantation Radiotherapy Chemotherapy (e.g., sorafenib)

3.1. Current and future therapies for NAFLD/NASH treatment

3.1.1. Dietary changes and lifestyle modifications

Several studies demonstrated a strong association between NAFLD and an unhealthy lifestyle. Modifications at this level are a mandatory starting point for all patients (**Table 3**). Dietary changes and lifestyle modifications are now the first-line therapy for patients with NASH. Patients who lost ≥ 10% of their weight resolved 90% of NASH cases while 45% showed fibrosis regression [319]. Moreover, numerous diets are seen as tools to counteract NAFLD incidence and progression [320]. Calorie-restricted diets seem to collect some scientific agreement as a determinant of nutritional interventions in NASH [321]. Recently, the Mediterranean diet (MD) was recommended for NAFLD patients by the EASL–EASD–EASO Clinical Practice Guidelines [322], due to its easy follow characteristics and beneficial metabolic effects on ameliorating steatosis and cardiovascular events obtained by its nutritional components [320]. Nevertheless, other dietary patterns such as the ketogenic diet and "dietary approach to stop hypertension" (DASH) diet can be useful in NAFLD patients [320].

Combination of diet and exercise represents a backbone for weight loss. In this context, physical activity is another lifestyle modification that contributes decisively for NAFLD improvement. Studies showed that exercise significantly decreases steatosis and prevents NAFL progression to NASH [323, 324]. Furthermore, both aerobic and resistance exercise programs (similar frequency, duration, and period of exercise) exhibited positive results in hepatic steatosis reduction of NAFLD patients. A randomized study in lean NAFLD patients with a BMI lower than 25, involving regular exercise, resulted in the first signs of NAFLD remission after 1 year. Notably, remission of NAFLD was achieved in 67% of non-obese patients after lifestyle intervention and even a weight reduction of 3–5% had positive outcomes [325].

These lifestyle modifications proved to have positive effects on weight reduction and metabolic control. Notwithstanding, pharmacotherapy in combination with lifestyle modifications is recommended for progressive NASH (≥ F2 stage) patients as described in the following topics.

3.1.2. Recommended drugs in NAFLD/NASH

Despite intensive studies, there is not a single, and specific FDA-drug approved for NASH. However, patients with early-stage NASH that possess a high risk of developing fibrosis should be enrolled for treatment with prescribed drugs. In fact, are some medicines that are already used worldwide:

3.1.2.1. Pioglitazone

Pioglitazone, an insulin sensitizer that acts as PPAR-γ agonist, showed positive effects against steatosis and necroinflammation in diabetic NASH patients [326, 327]. Pioglitazone efficacy was evaluated in a phase 4 clinical trial, where it showed a decrease of NAS by more than 2 points without worsening of fibrosis, in both prediabetic and diabetic NASH patients. Recently, the long-term safety and efficacy of Pioglitazone was confirmed in a 3-year randomized controlled trial (RCT) in NASH patients with prediabetes/T2DM [328]. Pioglitazone can be used as pharmacotherapy in NASH according to the clinical guidelines published by the joint EASL–EASD–EASO Associations [329] (**Table 3**). Nevertheless, extensive use of pioglitazone comprises several secondary effects such as increased risks at prostate or pancreas cancer, body weight gain, fluid retention, bone fracture in women and increased cardiovascular events.

3.1.2.2. Vitamin E

OxS is involved with NASH progression as described previously. In this context, vitamin E, an important free radical scavenger with anti-inflammatory and anti-apoptotic activity, has been suggested for NASH treatment. Patients diagnosed with NASH exhibited lower levels of vitamin E when compared with healthy individuals [330]. Moreover, a 1-year vitamin E supplementation in NASH patients reduced serum transaminase activities as well as transformed growth factor-β1 (TGFB1, associated with liver fibrosis development) [331]. Vitamin E alone or in combination with pioglitazone significantly reduced steatosis, lobular inflammation and NAS score, in nondiabetic patients with non-alcoholic steatohepatitis (PIVENS), without improving fibrosis or portal inflammation [332]. A meta-analysis confirmed that vitamin E therapy improves

serum biochemical parameters and improved hepatic histology in NAFLD/NASH, especially in adult NASH patients, vitamin E also improves hepatic fibrosis, hepatic inflammation and ballooning. [333]. In Japan, NASH patients subjected to a long-term vitamin E treatment (more than 2 years) showed some improvement in hepatic fibrosis, especially in those where serum transaminase activities and IR could be restored [334]. Vitamin E is another drug proposed by the EASL–EASD–EASO for NASH [329] (**Table 3**), although it is recommended only for biopsy-proven NASH patients without diabetes. Besides the beneficial effects observed, high-dose or long-treatment with vitamin E can increase all-cause mortality, prostatic cancer and hemorrhagic stroke [335].

3.1.2.3. Statins

Since NAFLD/NASH patients exhibit atherogenic dyslipidemia and increased cardiovascular risk, statins can be used in NASH patients (**Table 3**). Simvastatin improved NASH-related fibrosis by decreasing iNOS, increasing eNOS, and inhibiting HSC activation in rats [336]. Simvastatin also decreased inflammation and fibrosis by inhibiting Ras/ERK and RhoA/Rho kinase signaling pathways [337]. Moreover, several statins prevented NASH and increased mitochondrial and peroxisomal FAO via induction of PPAR-α in MCD-fed mice [338]. Statin therapy showed to be safe in patients with NASH [339]. Rosuvastatin monotherapy ameliorated biopsy-proven NASH and resolved metabolic syndrome within 12 months in patients. Despite the beneficial effects observed in several animal studies, there is a need for larger high-quality human clinical trials to establish clinical care.

3.1.3. Drugs candidates for NAFLD/NASH

Pharmacotherapy available and lifestyle modifications are not sufficient to reduce liver fibrosis and inflammation in many patients. Current complications with the resolution of the histological lesions, together with the dangerous increase in NASH prevalence in some populations, indicate a vital need for the development of new pharmacotherapies to manage this disease. Treatments under study for NAFLD and NASH include the following classes (detailed in **Table 4**):

- **PPAR agonists**, which activate PPARs and play a role in treatment of symptoms of the metabolic syndrome, mainly for lowering triglycerides and blood sugar;
- **Glucagon and glucagon-like peptide-1 (GLP-1) agonists**, to mimic hormones that regulate appetite and affect glucose and lipid metabolism;
- **Fatty acid synthase inhibitors**, to reduce fat liver production and inflammation;
- **Acetyl-CoA carboxylase (ACC) inhibitors**, to block an enzyme involved in lipogenesis;
- **Farnesoid X receptor (FXR) agonists**, which activate FXR by regulating bile acid synthesis and lowering triglycerides and blood sugar;
- **Thyroid hormone receptor agonists**, which activate hormones that play a role in fat metabolism
- **Fibroblast growth factor analogues**, which mimic a hormone that regulates bile acid metabolism and fat storage in the liver;
- **Apoptosis signal-regulating kinase 1 (ASK1) inhibitors**, to block an enzyme that promotes inflammation and fibrosis;
- **Anti-fibrotics agents,** which block recruitment, migration and infiltration of monocytes and macrophages and the activation and proliferation of HSC;
- **General antioxidants**, to counteract oxidative stress and prevent inflammation.

Table 4. Drugs candidates for NAFLD/NASH treatment.

Drug candidate	Mechanism of action	Sponsor	Outcome measures	Last or active ID trial
Elafibranor	PPAR-α/δ agonist	Genfit	Achieving resolution of NASH without worsening of fibrosis at 52 weeks; [340] Composite long-term outcome composed of all-cause mortality cirrhosis and liver-related clinical outcomes.[340]	NCT02704403 (Phase III)
Lanifibranor	Pan-PPAR agonist	Inventiva Pharma	Improvement in steatosis activity fibrosis score without worsening of fibrosis at 24 weeks. [341]	NCT03008070 (Phase II)
Saroglitazar	PPAR-α/γ agonist	Zydus Cadila	Improvement in ALT, LFC, insulin resistance, and atherogenic dyslipidemia at 16 weeks.[342]	NCT03061721 (Phase II)
Pemafibrate	PPAR-α modulator	Kowa Pharmaceutical	Improvement in liver function parameters and fibrosis marker at 24 weeks.[343]	NCT04998981 (Phase III)
Liraglitude	GLP-1 agonist	Novo Nordisk	Body weight reduction and amelioration of NAS score, stage of fibrosis and serum liver injury biomarker levels at 24 weeks;[344, 345] Remission of steatohepatitis without worsening of fibrosis.[278, 345]	NCT01237119 (Phase II)
Semaglutide	GLP-1 agonist	Novo Nordisk	Resolution of NASH with no worsening of fibrosis, where at least one fibrosis stage was counteracted at 72 weeks.[346]	NCT02970942 (Phase II)
Aramchol	SCD inhibitor	Galmed Pharmaceuticals	Reduced fat content in patients with NAFLD at 12 weeks.[347]	NCT04104321 (Phase III)
Firsocostat	ACC inhibitor	Gilead Sciences	Decrease in hepatic steatosis, selected markers of fibrosis, and liver biochemistry;[348, 349] Improvement in NASH activity when combinate with cilofexor for 48 weeks. [350]	NCT03449446 (Phase III)
Obeticholic acid	FXR agonist	Intercept Pharmaceuticals	Improving of necro-inflammation without worsening o fibrosis at 72 weeks;[351] Reduction in hepatic fibrosis and diminished steatosis, lobular inflammation and hepatocyte ballooning.[351]	NCT02548351 (Phase III)
Resmetirom	THR-β agonist	Madrigal Pharmaceuticals	Decrease in the amount of liver fat by approximately 40%, with few adverse reactions; [352] Improvement in liver fat, atherogenic lipids, and liver enzymes at 36 weeks.[353]	NCT04951219 (Phase III)

Selonsertib	ASK1 inhibitor	Gilead Sciences	Improvement in fibrosis without worsening of NASH-CRN at 48 weeks;[354] No antifibrotic effect in patients with NASH patients with stage 3 or cirrhosis.[354]	NCT03053050 (Phase III)
Tipelukast	Anti-inflammatory	MediciNova	TGs reduction in NASH/NAFLD patients with hypertriglyceridemia at 24 weeks.	NCT02681055 (Phase II)
Emricasan	Pan-caspase inhibitor	Histogen	Mean change in hepatic venous pressure gradient at 24 weeks;[355] No improvement in liver histology. [356]	NCT04806750 (Phase II)
Cenicriviroc	Blockade of CCR2 and CCR5	Tobira Therapeutics	Improvement in fibrosis without worsening steatohepatitis at 1 year;[357] Decrease in N-terminal type 3 collagen propeptide levels, biomarkers of systemic inflammation (CRP, IL-6, IL-1β and soluble CD14), and enhanced liver fibrosis scores.[357]	NCT03028740 (Phase III)
Belapectin	Galectin-3 inhibitor	Galectin Therapeutics	Improvement in liver histology, accompanied by a substantial reduction in NASH activity and collagen deposition in animal models; [358] No improvement in fibrosis or portal hypertension in patients with NASH, cirrhosis, and portal hypertension.[359]	NCT02462967 (Phase II)
Pegbelfermin	recombinant FGF-21	Bristol-Myers Squibb	Improvement in liver stiffness, adiponectin, ALT, and AST at 16 weeks;[360] Reduction in liver fat and improved N-terminal type III collagen propeptide. [360]	NCT03486899 (Phase II)
Silibinin	Antioxidant	Rottapharm Madaus	Reduction in mean AST to platelet ratio index, fibrosis-4 score and NAFLD fibrosis score at 48 weeks. [361] Ameliorate fibrosis based on histology (reductions of 1 point or more) and liver stiffness measurements. [361]	NCT02006498 (Phase II)
Berberine	Antioxidant	Xintria Pharmaceutical Corporation	Improvement in liver fat, body weight, HOMA-IR; [362] Reduction in body weight and improvement in lipid profile.[362]	NCT03198572 (Phase IV)

***Abbreviations**: ACC, Acetyl-CoA carboxylase; ALT, Alanine transaminase; ASK1, apoptosis signal-regulating kinase 1; AST, aspartate transaminase; CCR, CC chemokine receptor; FXR, farnesoid X receptor; FGF, fibroblast growth factor; GLP, glucagon-like peptide, LFC, liver function compensatory value; NAFLD, non-alcoholic fatty liver disease; NAS, NAFLD activity score, NASH, non-alcoholic steatohepatitis; PPAR, peroxisome proliferator-activated receptors, SCD, stearoyl-CoA desaturase; PiS, pilot study*

4. Chapter
Antioxidant therapy

OxS can act as a primary cause of pathology or as a secondary contributor to disease progression, such as the case of NAFLD. As mentioned in **section 2.1.3**, organisms hold important defense mechanisms to repair cells' injury, to protect against oxidative damage. Upon exposure to oxidants and other electrophiles, these defenses can be increased and boost the cell's detoxifying capacity, leading to the repair of oxidative injury. Interestingly, some exogenous agents can upregulate those same defenses, constituting the principal strategies underlying antioxidant therapy.

4.1. Antioxidant therapeutic strategies in NAFLD

The potential effects of using antioxidant as therapeutic approach relies mainly on antioxidant defenses induction and how it prevents disease progression. Several antioxidant therapeutic strategies have been studied in the last years, with some of them reaching human clinical trials. The strategies investigated comprised mainly SOD and SOD–catalase mimics; GSH synthesis stimulators (using precursors); iron-chelating agents; inducers of antioxidant enzymes expression (mainly by Nrf2 activation); NOXs inhibitors and dietary antioxidants supplements.

4.1.1. SOD and SOD–catalase mimics

SOD mimics were mainly metalloporphyrins, porphyrins, or porphyrin-related mimics [363]. Inside cells, the contribution of SOD mimics to the cytosolic antioxidant defense is relatively poor when compared with endogenous antioxidants defenses: however, their antioxidant effect seems to be higher in extracellular spaces. Moreover, some SOD mimics (manganese (Mn) porphyrins, Mn cyclic polyamines and M40403) can act as pro-oxidants in the mitochondrial matrix, thereby modulating redox-sensitive signaling pathways and cellular transcription [364]. In this context, some beneficial effects of SOD mimics can be consequent of distinct mechanisms other than mimicking

SOD. Manganese (III) meso-tetrakis (N-ethylpyridinium-2-yl) porphyrin (MnP), a SOD mimic, improved hepatic steatosis and biomarkers of liver dysfunction with redox modulation in HFD-fed mice [365]. Mn(iii)- comprising salen complexes can eliminate $O_2^{\bullet-}$ and H_2O_2, being the emerging class of SOD mimics. In fact, EUK-8 and EUK-134 reduced serum aminotransferases, glutathione transferase and alkaline phosphatase, cholesterol, and LDL contents, accompanied by an improvement in NASH pathological features in the liver of MCD-fed rats. Nevertheless, no human clinical trial for salens have been initiated

4.1.2. Glutathione peroxidase (GPx) mimics

Ebselen is the best characterized GPx mimics, as it showed large selectivity to H_2O_2 and hydroperoxides. Ebselen may also induce phase II detoxification enzymes, which reduce oxidative damage and inflammation in non-human studies [366]. Ebselen significantly caused the resolution of carbon tetrachloride (CCl_4)-induced hepatic fibrosis in rats [367]. Nevertheless, ebselen effects in the context of NAFLD were never reported.

4.1.3. Stimulators of GSH synthesis

N-acetylcysteine (NAC) is a widely used antioxidant in literature [368]. In cells, NAC is deacetylated in cysteine, which culminates in GSH reloading [369]. NAC treatment rescued the liver steatosis and apoptosis induced by HF diet in C57BL/6 mice [370]. Moreover, NAC significantly decreased the serum ALT levels in patients with NAFLD [371]. Although NAC is involved in many preclinical and clinical trials, its beneficial effects in NAFLD is not consensual [366].

4.1.4. Iron-chelating agents

Iron and copper, when released from proteins, can participate in $^{\bullet}OH$ production. Hepatic iron overload, which occurs in some NASH patients, facilitates the conversion of H_2O_2 to $^{\bullet}OH$ via the Fenton reaction [372]. Ferroptosis, a widely recognized process of cell death caused by the accumulation of iron-dependent lipid peroxides, has been connected to the pathogenesis of diverse liver diseases such as HCC, fibrosis, NASH, hepatic I/R injury, and liver failure. The use of inhibitory chelators would be an excellent

strategy to avoid ROS propagation. In fact, treatment with ferroptosis inhibitors in NASH-induce mice models (e.g., trolox or deferoxamine) reduced cell death, as well as infiltration of inflammatory cytokines, indicating that the ferroptosis pathway was activated in the liver of MCD-fed mice [373]. GPx4 downregulation is a known trigger of ferroptosis [374]. In accordance, livers of mice feeding with MCD diet showed a decrease in GPx4 expression and an increase in 12/15-lipoxygenase (ALOX15), and AIF, demonstrating that ferroptosis plays a significant role in NASH-related lipid peroxidation and its link to cell death. In the same study, deferoxamine or sodium selenite (a GPX4 activator) significantly reduced NASH severity in the MCD-fed mice [375].

4.1.5. Nrf2 activators

Impaired Nrf2 signaling is involved in many oxidative stress-related diseases, including NAFLD [376]. Accordingly, Nrf2 activators are being sought as potential agents to induce antioxidant capacity and ameliorate pathologies conditions. Small molecules such as polyphenols can induce antioxidant enzyme expression in Nrf2-mediated signaling [377].

Nrf2 activators can act by different mechanisms [366]. Under basal conditions, cells continuously synthesized transcription factor Nrf2 but its transport to the nucleus is relatively low. This Nrf2 degradation maintains this regulation through association with Kelch-like ECH-associated protein 1 (KEAP1), which enables its degradation by the 26S proteasome.

Nevertheless, as described previously, there is much evidence that boosting Nrf2 synthesis can represent a therapeutic antioxidant approach. Upon exposure to electrophiles, KEAP1 is inactivated when its sensor cysteines form adducts with electrophiles or when they are oxidized to disulfide. In this process, KEAP1 lose ability to contribute to Nrf2 degradation, highlighting the use of non-toxic electrophiles to alkylate KEAP1 as important therapeutic approach.

Additionally, glycogen synthase kinase 3β (GSK3β) can phosphorylates Nrf2 and, in combination with β-transducin repeat-containing protein (βTrCP), result in Nrf2 degradation by the proteasome, a process that can inhibited by oxidative inactivation of

GSK3β [378]. Upon oxidation, the interaction between Nrf2 and βTrCP is disrupted by inhibition of GSK3β and the phosphorylation of Nrf2 at the Deh6 domain [378], suggesting that inhibiting GSK3β can be also a potential therapeutic approach to modulate Nrf2 signaling.

KEAP1 degradation as a consequent of oxidative insults can also occurs through p62-mediated sequestration of KEAP1 and autophagy [379]. This process is initiated by the phosphorylation of p62 via TANK-binding kinase 1 (TBK1) and mTORC1 targeting, indicating p62 as another potential therapeutic target.

Other interactions between Nrf2 and proteins such as p21 [380] and BRCA1 [365] [381] as well as Nrf2 phosphorylation by protein kinase C (PKC) also stimulate Nrf2 activity [382]. On the other hand, BTB Domain and CNC Homolog 1 (BACH1) downregulate Nrf2 activity by competing to form heterodimers with small Maf (sMaf) or Jun proteins and binding to the electrophile response element (EpRE) in the nucleus [383]. Therefore, compounds that inhibit BACH1 could increase the expression of some Nrf2-regulated genes.

Several extracts of fruits and vegetables showed the ability to activate Nfr2 signaling. Numerous clinical trials using turmeric extract, broccoli or broccoli sprout supplement were performed in pathologies [366]. In general, induction of antioxidant capacity was achieved in clinical trials. Noteworthy, coumarins and polyphenols existent in vegetables and fruits act mainly by their oxidation to electrophilic quinones and, therefore, by forming adducts with KEAP1 cysteines [377]. Several dietary molecules such as curcumin, sulforaphane, and resveratrol have been established as Nrf2 activators, and some of them are in clinical trials for disease treatment [366, 384]. Moreover, several chemical Nrf2 activators are being tested in the NAFLD context (**Table 5**).

Table 5. Chemical inducers of the Nrf2 signaling pathway in NAFLD.

Compound/extract	Model	Downstream effects of Nfr2 activation
Acerola polysaccharides	C57BL/6 mice	HMOX1 and NQO1 ↑ SREBP1c↓ [385]
Apigenin	C57BL/6 mice; Hepa1-6 cells	SOD, CAT, GPx ↑ [386]

CPT	Wister rats	HMOX1, NQO1, SOD and GSH/GSSG ↑ MDA ↓[387]
Curcumin	C57BL/6 mice	SREBP1c and FAS ↓ [388]
	Sprague-Dawley rats	GSH, HMOX1 and SOD ↑ MDA ↓[388]
Gastrodin	C57BL/6 mice; HL-7702 cells	HMOX1 and SOD ↑ MDA and ROS ↓ [389]
Green tea extract	C57BL/6 mice; HC-04 cells	NQO1 mRNA ↑ [390]
Lemon balm extract	C57BL/6 mice	SOD2 and pAKT ↑ [391]
Osteocalcin	C57BL/6 mice	SOD, CAT and GPx ↑ [392]
Resveratrol	C57BL/6 mice	SREBP1c and FAS ↓ [393]
Scutellarin	C57BL/6 mice; HepG2 cells	HMOX1 and NQO1 ↑ [394]
Silybin	C57BL/6 mice	CYP2E1, 4-HNE ↓ SOD, GCLM, GCLC, NQO1 and HMOX1↑ [395]
Swertiamarin	Adult male kunming mice	SOD, CAT, GPx ↑ [396]

Abbreviations: ↓ decrease; ↑ increase; AKT, protein kinase B; CAT, catalase; CYP2E1, cytochrome P450 family 2 subfamily E member 1; CPT, Triterpenic acids-enriched fraction from *Cyclocarya paliurus*; FAS, fatty acid synthetase; GPx, glutathione peroxidase; GSH, glutathione; GSSG, glutathione disulphide; HMOX1, heme oxygenase 1; MDA, malondialdehyde; NOQ1, NAD(P)H quinone oxidoreductase; SOD, superoxide dismutase; SREBP1c, sterol regulatory element-binding protein 1; 4-HNE, 4-Hydroxynone

4.1.6. NADPH oxidase inhibition

As previously described, NOXs can be a source of ROS, and its exacerbated activation can result in tissue damage. In activated phagocytes such as Kupffer cells, the NOX family is a crucial source of ROS [397]. Several isoforms of NOX have been identified in the liver (NOX1, NOX2, and NOX4). Although the impact of NOX2 in the NASH pathology has been mutable in different animal models [398, 399], the involvement of NOX4 and NOX1 oxidase in NASH development was demonstrated in mouse models [400, 401]. Immunohistochemical analysis showed that NOX4 protein levels were markedly augmented in the liver of patients with NASH [397]. In this context, NOXs

inhibition could be an essential tool to target OxS and treat NAFLD. Apocynin, an inhibitor of NADPH-oxidase, reduced inflammatory factors in the blood and liver, ameliorating IR in HFD-fed mice [402]. Moreover, treatment with setanaxib, a dual NOX1/4 inhibitor, suppressed inflammation and fibrosis in CCl_4-induced hepatic fibrosis [403] and fast-food diet−fed mice [401]. So far, setanaxib was not used in clinical trials in the context of NAFLD, although a phase II/III study is currently recruiting patients with elevated liver stiffness (NCT05014672).

4.1.7. Dietary polyphenols

Dietary polyphenols are bioactive molecules that have antioxidant properties as they can act directly as ROS-scavengers or indirectly as up-regulators of endogenous antioxidant defenses [404].

Polyphenols contain at least one aromatic ring in their structure that is/are connected to diverse chemical groups, including phenolic, hydroxyl or carbon groups. The chemical variability of polyphenols rises with minimal substitutions in hydroxyl and methoxy moieties, in the interaction by hydrogen bonds (among them or with proteins), or by the capacity to polymerize, originating thousands of derivatives [405]. Polyphenols can be particularly active in chelating transition metals such as iron and copper ions, avoiding their participation in radical-generating reactions [406]. Some polyphenols exhibited beneficial effects by activating adaptative stress response signaling pathways in cancer, cardiovascular and neurodegenerative [407–409]. In accordance, a polyphenol-enriched diet showed to reduce the risk of chronic diseases appearance [205].

Regarding liver diseases, polyphenols were demonstrated to control *de novo* lipogenesis, inhibiting lipogenic proteins (e.g., ACC, SREBP-1, FAS and LXRα) and increasing lipolytic proteins (e.g., AMPK, PPAR-α and CPT-1) [410]. For instance, resveratrol increased complex I activity, which resulted in augmented mitochondrial NAD^+/NADH ratio and SIRT3-dependent stimulation of Krebs cycle and FAO in HepG2 cells [411]. Epigallocatechin gallate (EGCG), an ester of epigallocatechin and gallic acid, showed ability to increase mitochondrial respiratory proteins levels and mtDNA content as well as to decrease lipid accumulation and stimulate autophagy in several *in vitro*

models (HepG2, Huh7 and mouse primary hepatocytes cells) and HF/HFHS-fed-mice [412, 413].Cyanidin-3-O-β-glucoside (an anthocyanin) protected primary mouse hepatocytes against high glucose-induced apoptosis by modulating mitochondrial dysfunction [414]. Silibinin, the major active constituent of silymarin, enlarged mitochondria and upregulate β-oxidation and ATP production in FaO liver cells [415].

Notwithstanding, antioxidant therapy resulted in controversial data. Failures in human clinical trials were registered [416, 417] due to several reasons:

- **Some antioxidants can work either as antioxidants or pro-oxidants**. Phenolic systems can be involved in glycation reactions, altering their redox state *in vivo* systems, which explain the lack of successful results in antioxidant therapeutic approaches [404];
- **ROS are major redox signaling molecules, indispensable for maintaining homeostasis and generating an adaptative response to OxS-induced death**. Antioxidants act by more than a direct ROS-scavenging activity, compensating the decrease in endogenous defenses by upregulating antioxidants enzymes expression. However, using exogenous antioxidants (from diet or pharmacologically intervention) is quite complex and does not consistently achieve the desired purpose [418];
- **Low specificity**. Exogenous antioxidants are widely spread in the body, while oxidative injury may be restricted to particular cell types and organelles, such as mitochondria. As a result, the antioxidant concentration in the particular locals of oxidative damage can be insufficient to prevent oxidative damage in pathological conditions [418];
- **Low bioavailability of these molecules in biological systems**. Exogenous dietary antioxidant bioavailability depends on endogenous factors such as food matrix, molecular weight, physicochemical properties, and the amount consumed or endogenous factors like the activity of the digestive enzymes, gut microflora-associated biotransformations, the gastrointestinal epithelium, and the liver biliary/urinary excretion. Many dietary antioxidants present low bioavailability, poor solubility/ stability towards gastric and colonic pH or weak absorption across the intestinal wall [419]. Glucuronidation of phenolic antioxidants in the intestine and liver combined with detoxification reactions of cytochrome P450 (CYP) enzymes can also contribute to poor

bioavailability at the target site [420]. In fact, many polyphenols failed in preclinical/clinical trials, mainly due to stability and bioavailability drawbacks [421, 422].

4.2. Hydroxycinnamic acids as a therapeutic approach

Hydroxycinnamic acids (HCAs) are one of the main classes of phenolic compounds found in nature. Ferulic acid, caffeic acid, *p*-coumaric acid, chlorgenic acid, sinapic acid, curcumin, and rosmarinic acid are part of phenolic acid family.

HCAs have been reported mostly as dietary antioxidants as they act as radical scavengers due to their hydrogen atom donating ability and particular stabilization of the resulting phenoxyl radical [423]. Its –CH=CH-COOH side chain seems to guarantee a more remarkable H-donating ability and subsequent radical stabilization by resonance [424] . Moreover, catecholic and gallolyl phenolic acids type systems provide them metal chelating properties [425].

During the last decades, several studies showed that HCAs derivatives display beneficial effects on metabolic syndrome-related hallmarks, including decreasing inflammation and the ability to decrease fat deposition and lower plasma lipid profile in both *in vitro* and *in vivo*. Caffeic acid derivatives inhibited the iNOS expression and prevented NO production from RAW macrophage cells [426]. In metabolic syndrome-associated diseases such as diabetes, caffeic acid attenuated hepatic glucose output in C57BL/KsJ-*db/db* mice [427] and streptozotocin (STZ)-induced diabetic rats [428]. In addition, caffeic acid administration also improved glucose intolerance in HFD-fed mice [429]. In TNF-α-induced insulin-resistant mouse liver FL83B cells, caffeic acid stimulated insulin receptor tyrosyl phosphorylation and increased the expression of insulin signal associated proteins such as insulin receptor, phosphatidylinositol-3 kinase (PI3K), glycogen synthase, and glucose transporter 2 (GLUT2), which improved IR and the import of glucose [430]. Moreover, caffeic acid reduced inflammatory cytokine and downregulated the inflammatory pathway JNK, NF-κB, and cyclooxygenase-2 (COX-2) expression [431]. Finally, caffeic acid activated AMPK phosphorylation, which led to glucose uptake and GLUT4 content in L6-GLUT4*myc* cells [432].

Despite the beneficial effects observed during *in vitro* and *in vivo* studies, HCAs bioavailability and pharmacokinetics in human trials are still unresolved. For instance, a

cell permeability study in Caco-2 intestinal cells using HCAs indicated their low cell permeability [433]. In this context, the development of drug delivery systems, such as liposomes, phospholipid complexes or smart antioxidant carriers may counteract the bioavailability issues and boost the potential therapeutic application of HCA.

5. Chapter
Mitochondrial pharmacology

The recognition of the mitochondrion as the gatekeeper of cell life and death and the impairment of the diverse mitochondrial functions observed in various pathological states, such as cancer, metabolic disorders, and age-related diseases, encouraged active drug discovery.

In drug discovery programs aiming the specific targeting of mitochondria, two complementary approaches have been followed: 1) bottom-up, focusing on individual rare heritable disorders caused by gene mutations and; 2) top-down, addressing a defined disorder in which mitochondrial dysfunction may be part of more complex pathophysiology [434–436]. Moreover, because mitochondria impairment may contribute to diverse pathologies, a single therapeutic approach might be applicable in multiple disorders. To handle mitochondrial dysfunction, a drug must selectively accumulate within mitochondria and link to one/multiple mitochondrial targets or modulate a process outside of mitochondria that ultimately can modify a mitochondrial dysfunction. So far, the drug discovery projects were aimed to find drugs able to restore mitochondrial function throughout the regulation of mitochondrial ROS production [437].

5.1. Lipophilic cations as smart carriers

The use of lipophilic cations, such as triphenylphosphonium (TPP^+), as smart carriers to target mitochondria is a recognized and robust strategy as TPP^+ derivatives can be rapidly and extensively taken up by mitochondria [438]. Triphenylphosphonium cation (TPP) consists of a positively charged phosphorus atom surrounded by three hydrophobic phenyl groups that contribute to an extended hydrophobic surface and charge stabilization. Triphenylphosphonium cations can pass easily through lipid bilayers and IMM due to their extensive hydrophobic surface area and the large out ionic radius, which can effectively lower the activation energy needed for membrane passage (**Figure 12**) [438].

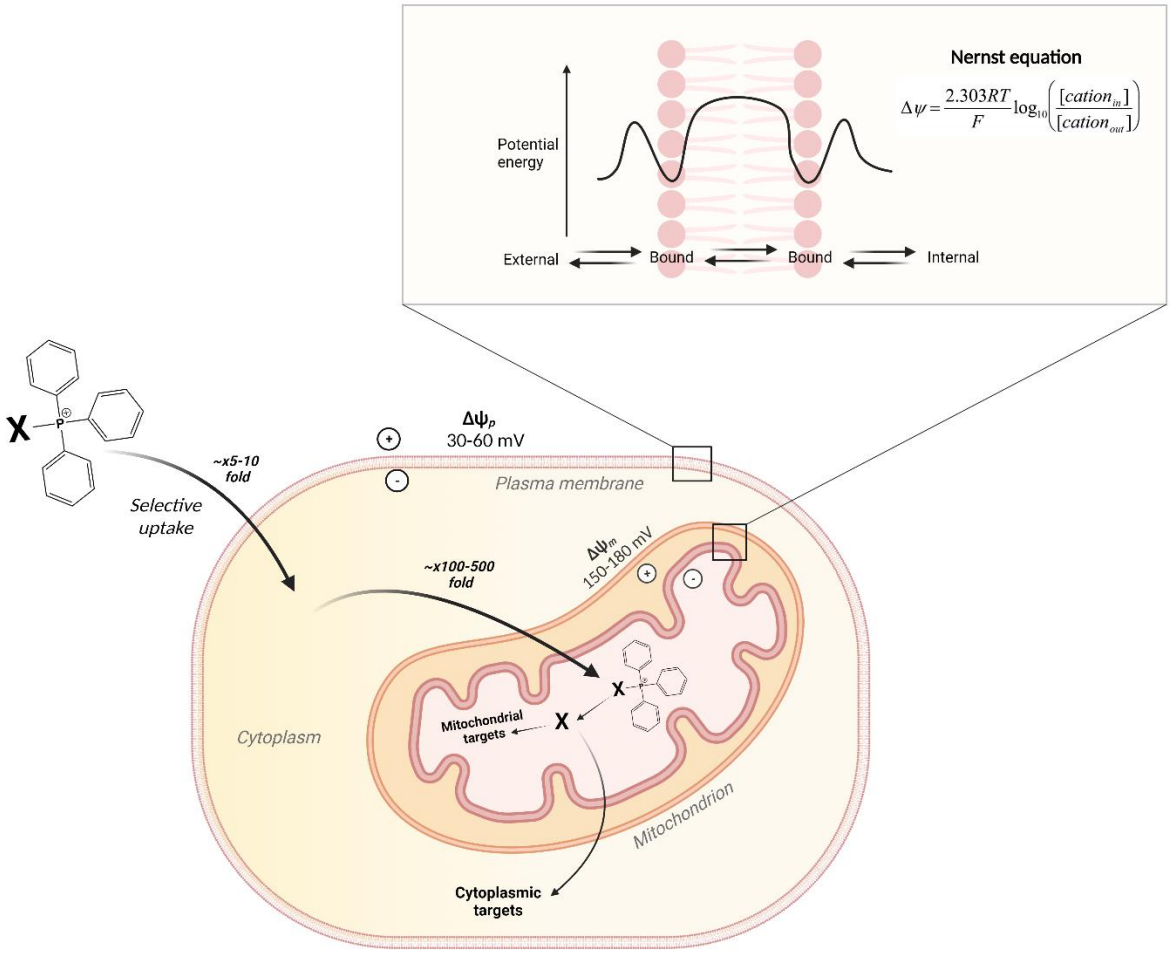

Figure 12. Strategy to pharmacologically intervene in mitochondrial dysfunction. Uptake by mitochondria of a triphenylphosphonium cation conjugated to X, showing passage through the inner membrane and adsorption to the phospholipid bilayer. The energy profile for the movement of a triphenylphosphonium cation through a phospholipid bilayer, showing adsorption to potential energy wells close to the carbonyls of the phospholipid fatty acids. Created with BioRender.com

The uptake of TPP into mitochondria depends on the membrane potential and can be estimated by Nernst equation: an increase of 10-fold for every ≈ 60 mV of ΔΨ can lead to 100–500-fold accumulation within mitochondrial matrix (**Figure 12**) [439]. Once inside mitochondria, TPP^+ conjugated agents are in general located on the mitochondrial matrix upon surpassing the phospholipid bilayer, maintaining the linker and bioactive molecule positioned within the IMM [440].

5.2. Mitochondriotropic agents in liver disease / NAFLD

Generally, the mitochondrial-targeting strategy encloses the expenditure of carrier systems, such as TPP, suitable to couple to a diversity of bioactive agents that are poorly taken up by mitochondria (e.g. due to the lack of hydrophobicity), allowing their targeting to mitochondria [441, 442]. Within mitochondria, mitochondriotropic agents can elicit beneficial effects in conditions related to OxS and mitochondrial dysfunction by diverse mechanisms, namely by scavenging reactive radicals modulating mitochondrial redox signaling processes [438]. Several mitochondria-targeted antioxidants obtained by conjugation to the TPP lipophilic cation have been developed, reinforcing the assumption that targeting mitochondria is an effective avenue to find a new therapeutic solution for several disease, including NAFLD [443, 444].

MitoQ is the most studied mitochondria-targeted antioxidant. It consists of a TPP^+ unit covalently attached to the endogenous antioxidant ubiquinone (co-enzyme Q, CoQ) through a 10-carbon aliphatic linker. MitoQ exerts antioxidant protection in several animal models with pathologies associated with increased OxS, including NAFLD and neurodegenerative diseases, ischemia-reperfusion, hypertension, sepsis, and kidney damage in type I diabetes [445]. MitoQ also decreased the ethanol-dependent micro and macro hepatic steatosis in Sprague-Dawley rats consuming ethanol using the Lieber-DeCarli diet [446] and increased liver mitochondrial cardiolipin content in obesogenic diet-fed rats [447]. MitoQ decreased features of the metabolic syndrome in $ATM^{+/-}/ApoE^{-/-}$ mice [448]. Facing the promising data, MitoQ was evaluated in a clinical trial for Parkinson's patients. However, improvement of neurodegenerative symptoms by MitoQ was not observed [449]. In a phase 2 clinical trial, MitoQ significantly decreased plasma ALT and AST in patients with chronic HCV infection [450]. In addition, a phase 2 clinical trial for MitoQ in NAFLD was approved but the study was terminated due to poor participant recruitment (NCT01167088).

MitoTEMPOL was developed by conjugating TEMPOL (a stable piperidine nitroxide radical) to TPP^+ using a five-carbon aliphatic linker [451]. MitoTEMPOL can detoxify ferrous iron by oxidizing it to ferric form and act like a SOD mimetic system to convert $O_2^{\bullet -}$ into water. MitoTEMPOL showed beneficial effects in several *in vitro* settings of

mitochondrial OxS, for instance, in protecting pancreatic β-cells against OxS [452] and in a model of ischemia-reperfusion, inhibiting the ATP depletion-recovery mediated by mPTP opening and cell death [453]. Using an animal model of diabetes, MitoTEMPOL prevented mitochondrial and cytosolic ROS production [454]. MitoTEMPOL ameliorated hepatic steatosis and suppressed the mRNA and protein expressions of myeloid-derived suppressor cells (MDSC)-associated proinflammatory mediators in livers of HFD-mice [455]. Nevertheless, no human clinical trial for MitoTEMPOL has been initiated.

Several other mitochondriotropic agents have been synthesized in the past years, such as MitoVit-E, Mitoresveratrol, MitoCurcumin and SkQ1 [456]. Although showing several beneficial effects on counteracting OxS complications, no data in the context of NAFLD are available.

Despite the expected attractiveness, the success of this strategy has been hampered by several challenges and limitations such as clinical trials design and implementation, the lack of animal models, and the poor druggability and drug-likeness of the drug candidates [457]. Consequently, to date, neither of the approaches have resulted in a drug approved by Food and Drug Administration (FDA) for mitochondrial therapy.

5.2.1. The mitochondria-targeted phenolic acid antioxidant derivative Anti-$OxCIN_4$

$AntiOxCIN_4$, a mitochondriotropic antioxidant based on the dietary antioxidant caffeic acid, was developed by Prof. Borges group by linking the antioxidant moiety to lipophilic TPP cation through a 6-carbon aliphatic chain (**Figure 13**) [458].

$AntiOxCIN_4$ did not interfere with mitochondrial morphology and polarization and showed remarkable antioxidant and iron-chelation properties, preventing Fe^{2+}/H_2O_2-induced damage in isolated liver mitochondria and hepatic cells. $AntiOxCIN_4$ was shown to maintain intracellular GSH homeostasis by increasing its supply (**Figure 13**) [458].

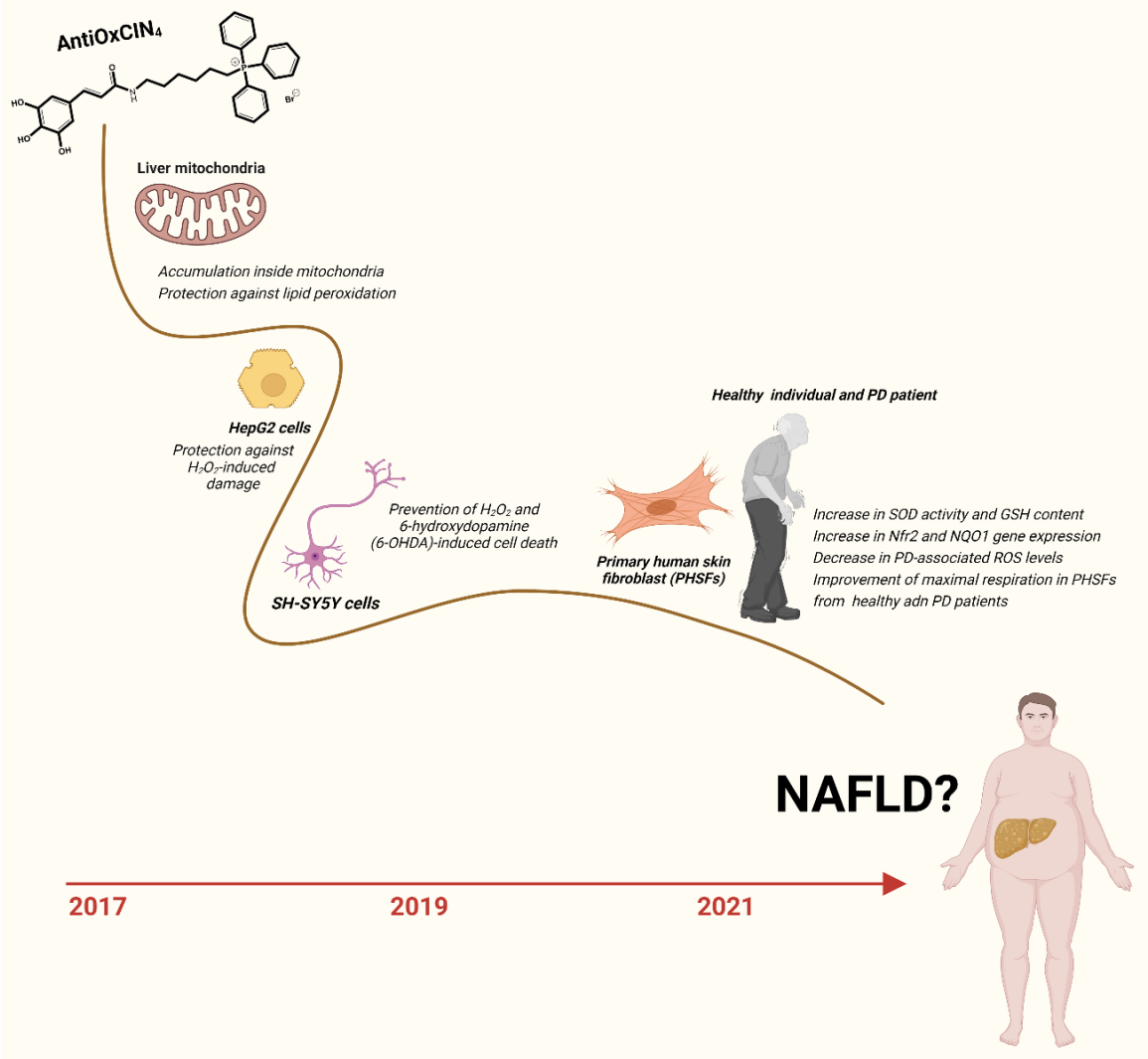

Figure 13. Mitochondria-targeted phenolic acid antioxidant derivative AntiOxCIN$_4$ road. AntiOxCIN$_4$ was first described in 2017 and since then, diverse beneficial effects against OxS in *in vitro* models were shown. PD, Parkinson Disease.

Moreover, studies in human neuroblastoma (SH-SY5Y) cells revealed that non-toxic concentrations of AntiOxCIN$_4$ prevented H_2O_2 and 6-hydroxydopamine (6-OHDA)-induced cell death (**Figure 13**). Although designed as classic antioxidants, the cytoprotection conferred by AntiOxCIN$_4$ was paralleled by moderately increased ROS levels, suggesting that AntiOxCIN$_4$ can also act as pro-oxidant [459]. In fact, recent studies showed that AntiOxCIN$_4$ sustainably cause a mild increase in ROS levels, thereby activating endogenous ROS-protective pathways, such as the Nrf2/KEAP1 pathway, efficiently preventing skin fibroblasts against subsequent OxS [460] and improving

several cellular and mitochondrial metabolic parameters in skin fibroblasts from sporadic Parkinson's disease patients (**Figure 13**) [461].

Thus, AntiOxCIN$_4$ target-specific affinity (delivery to mitochondria) and the ability to regulate several cellular processes (mitochondrial redox status and quality control mechanisms) confer cellular protection against oxidative insults, emerging as a potential drug candidate in metabolic-related disorders.

6. Chapter
Studying NAFLD mitochondrial physiology and toxicology

Liver toxicity is a major concern in risk assessment as the liver is constantly subjected to xenobiotic compounds and their metabolites. The chronic or prolonged exposure to toxic substances or overload of dietary nutrients makes the liver susceptible to chemical-induced liver diseases and metabolic syndrome-associated pathologies.

6.1. *in vitro*: HepG2 as a screening model

In the pharmaceutical industry, early detection of drug-induced hepatotoxicity is vital as it is a determinant in drug selection during the later stages of drug development. Moreover, the toxicology research field recommends using alternative *in vitro* models to implement the 3R (reduce, refine, and replace) strategy. In this context, a constant surge for advanced, robust, cost, and time-efficient *in vitro* models for the safety assessment is mandatory, even to counterbalance the possible inaccurate prediction of animal models due to inter-species variability.

The HepG2 cell line is one of the most used human liver-based *in vitro* models. This human hepatoma-derived cell line is epithelial in morphology and was established from liver tissue of a 15-year-old caucasian male with a well-differentiated hepatocellular carcinoma. Cultured HepG2 cells grow mainly in islands, reaching a monolayer form. Its use has been determinant in various fields, such as the study of hepatocyte function and specific protein expression [462]. HepG2 cells are an excellent model to investigate mitochondrial toxicity, due to their high content of organelles and mtDNA [462]. Importantly, HepG2 cells have equal or slight lower capacity for induction of cytochrome P450 (CYP) when comparable to human hepatocytes. In fact, HepG2 cells were highly responsive to CYP inducers, such as 3-methylcholanthrene for CYPh1A2 or phenobarbital for CYP2B6 and CYP3A4 [463], suggesting that HepG2 cells is cell-based model in screening for CYP inducers in drug discovery.

Noteworthy, HepG2 cells can grow in different cell culture conditions, such as galactose medium (in which glucose was absent), blocking ATP generation via glycolysis and forcing the cells to rely upon OXPHOS for the production of ATP [464]. Indeed, many pharmaceutical companies adopted this model in mitochondrial toxicity screening using HepG2 cells.

HepG2 cells has been widely used to study NAFLD *in vitro*. For instance, bisphenol A-treated HepG2 cells exhibited a dose-dependent increase in lipid accumulation and genes involved in *de novo* lipogenesis, such as sterol regulatory element-binding transcription factor 1 (SREBF1) [465]. Most patients treated with valproate, an antiepileptic drug, have been diagnosed with hepatic steatosis [466]. The expression of CD36, an essential fatty acid transport system, and diacylglycerol acyltransferase 2 (DGAT2) were significantly upregulated in HepG2 after treatment with valproate, leading to augmented lipid accumulation [466]. Moreover, HepG2 cells incubated with a mixture of different proportions of saturated (palmitate) and unsaturated (oleate) showed a dose-dependent increase in lipid accumulation, paralleled by elevated production of TNF-α, a proinflammatory cytokine that plays a key role in the pathogenesis and NAFLD disease progression [467, 468]. In addition, after treating HepG2 cells with increasing concentrations of several steatotic-inducing compounds, toxicity parameters such as lipid accumulation, OxS, ΔΨm and cell viability were investigated using fluorescent probes. These techniques allowed the creation of a high-content imaging technology to evaluate drug-induced steatosis [469].

In conclusion, HepG2 is a low-cost *in vitro* model with important hepatic properties, being a feasible option for high-scale screening of mitochondrial-targeted molecules. Additionally, it can be a suitable starting point to access NAFLD development and possible chemical therapies.

6.2. *in vivo*: Western Diet (WD)-fed mouse models

Rodent models have unmeasurable value in biomedical research. Preclinical research with rodents aims to discover mechanisms and/or therapies that can be translated to humans. NAFLD has a strong association with metabolic syndrome, which is exponentially growing due to the Western diet (WD). So far, mice model diets can be

divided into two main categories: the MCD and the WD. Exacerbated hepatic steatosis that can progress to fibrosis was observed in both diets, however these developments occur over different mechanisms.

The WD contains high amounts of saturated fat, trans-fat, and sucrose (table sugar) [470]. Human diets based on these components can induce obesity, metabolic syndrome, NAFL, and NASH in some cases [471]. HFD results in augmented FFA levels in the liver, contributing to hepatic IR and decreased FAO, promoting *de novo* lipogenesis in hepatocytes. These altered mechanisms culminate in weight gain and hepatic steatosis [472]. Indeed, overload in saturated fat intake is associated with hepatocyte ER stress and hepatic steatosis [473].

WD can also contain high levels of cholesterol and cholate, which are known to induce atherogenesis, apoptosis, and inflammation. In fact, consumption of diets presenting high cholesterol and HFD concentrations promoted hepatic inflammation [474]. WD composition is quite heterogeneous and typically results in various hepatic changes in WD-fed mice, depending on the content of the diet. However, WD mimetic better what is observed in human NAFLD pathogenesis as human diets also vary substantially. The WD terminology comprises several types of diets, ranging from cafeteria diet to obesogenic diet to HFD. Several WD mouse models are used in NAFLD research, varying from composition, mouse strain or study duration (**Table 6**).

The mentioned studies using WD models utilize either the C57BL/6 mouse strain or the C57BL/6-derivated substrains (**Table 6**). Mice with a C57BL/6 background are more susceptible to liver injury than other mouse strains [475–477].

Although hepatic steatosis was obtained in diverse WD models, in this thesis, the WD model described by Inês Simões *et al* will be used as a dietary mouse model.

Table 6. Some western diet (WD) mouse models of non-alcoholic fatty Liver disease (NAFLD) and non-alcoholic steatohepatitis (NASH).

Dietary Model	Composition	Strain	Treatment Length	Main outcomes
HFD	21% fat from coconut oil + 19.5% fat from casein + 1.25% cholesterol	C57BL/6J	7 weeks	Fibrosis, steatosis [479]
HFD	60% kcal from fat	C57BL/6J	16 weeks	Steatosis, increased liver weight and TGs [481]
HFD	40% of energy from fat with 30% of fat from lard, 30% from butterfat, and 30% from Crisco and liquid fructose and sucrose (42 g/L total at a ratio of 55% fructose to 45% sucrose)	C57BL/6NHsd	12 weeks	Glucose intolerance, insulin resistance, adipose tissue dysfunction, increased levels of intrahepatic triglycerides, plasma ALT, liver weight, hepatic fibrosis, and inflammation [482]
HFD + HFHS	44.6% kcal from fat (61% saturated fatty acids) + 40.6% kcal from carbohydrates (sucrose 340 g/kg)	C57BL/6J	Up to 18 weeks	Macrovesicular steatosis, fibrosis, Inflammation [483]
HFD + HFCS	44.6% kcal from fat (61% saturated fatty acids) + 40.6% kcal from carbohydrates (sucrose 340 g/kg)	C57BL/6J	Up to 16 weeks	Steatosis [484–486]
HFD + HFCS	45% kcal from fat (saturated fat) + 0.2% cholesterol + fructose and glucose (55% and 45%, respectively, w/w)	C57BL/6J	16 weeks	Steatosis and fibrosis coupled with NASH [399]
WD	51% kcal from from fat + 26% from carbohydrates + 23% from protein. 30% fat [14% SFAs, 12% monounsaturated fatty acids (MUFAs) and 1% polyunsaturated fatty acids (PUFAs)], 284 mg/kg cholesterol and liquid sucrose (30 g/L)	C57BL/6J	16 weeks	Steatosis, increased liver weight and TGs[487]
WD	45% kcal fat (20% partially hydrogenated vegetable oil) + HFCS + 0.2% cholesterol	C57BL/6J	16 weeks	Steatosis, increased TGs, increased liver weight, fibrosis [471]
WD	21% kcal fat + 0.2% cholesterol	C57BL/6J	10–12 weeks	Steatosis, increased liver weight and TGs [488]

Abbreviations: HFD, high-fat diet [also consistent with Western-like diet (WD)]; HFCS, high-fructose corn syrup; TGs, triglycerides.

PART II

Hypothesis and Aims

The incidence and prevalence of NAFLD are dangerously rising worldwide. The patient's heterogeneity, which makes the diagnosis challenging to monitor, together with the absence of approved pharmacologic strategies other than dietary lifestyle intervention, spurred the finding of new drug developments. Although mechanisms underlying disease pathophysiology are not fully clarified, mitochondrial dysfunction and oxidative stress are potential key players.

Antioxidants can be used as a therapeutic approach to boost intrinsic antioxidant defenses and tackle OxS, therefore, implicated in disease phenotype improvement.

Polyphenols of plant origin (nutritional supplements) have recently received increased attention due to their pleiotropic effects. Among them, phenolic acids such as HCAs have remarkable antioxidants, although suffering from bioavailability constraints. On the other hand, their chemistry plasticity makes them suitable scaffolds for the rational design and development of new antioxidants. AntiOxCIN$_4$, a mitochondria-targeted phenolic acid derivative, was developed, and its antioxidant properties were validated in several *in vitro* models.

This work hypothesizes that the hydroxycinnamic-derived mitochondriotropic antioxidant AntiOxCIN$_4$ can improve NAFLD-associated phenotype in FFA-treated HepG2 cells and Western diet-fed mice.

In this context, the main objectives of this thesis were**:**

1) Investigate the effects of AntiOxCIN$_4$ in the modulation of antioxidant defenses of human hepatoma HepG2 cells, to validate the use of that molecule to treat NAFLD or other hepatic conditions. This work intended initially to clarify the fundamental molecular mechanisms of AntiOxCIN$_4$-induced cellular adaptative response, focusing on activating the Nrf2/KEAP1 pathway in HepG2 cells (**Chapter 7**)
2) Characterize human HepG2 cells as an *in vitro* model for steatosis by testing a) how different lipotoxicity protocols induce a time-dependent mitochondrial disruption, b) whether mitochondrial dysfunction is cause or consequence of oxidative stress burst and induction of cell death in the context of lipotoxicity and (c) whether fructose worsens the cellular lipotoxicity profile under the different treatment

protocols. The aim is to validate this *in vitro* NAFLD model in terms of mitochondrial dysfunction and oxidative stress to test further new innovative strategies targeted to mitochondria to improve the NASH/NAFLD phenotype (**Chapter 8**)

3) Evaluate the beneficial effects of AntiOxCIN$_4$ in an *in vitro* HepG2-based NAFLD model, by measuring lipid profile and mitochondrial damage-associated parameters. (**Chapter 9**)
4) Test for the first time the *in vivo* potential therapeutic effect of AntiOxCIN$_4$ in a NAFLD context, by using a Western diet (WD)-induced simple steatosis mouse model. (**Chapter 9**).

PART III

Experimental Procedure and Results

7. Chapter

Mitochondriotropic antioxidant based on caffeic acid AntiOxCIN$_4$ activates Nrf2-dependent antioxidant defenses and quality control mechanisms to antagonize oxidative stress-induced cell damage

Data in this chapter was published in:

Ricardo Amorim, Fernando Cagide, Ludgero C Tavares, Rui F Simões, Pedro Soares, Sofia Benfeito, Inês Baldeiras, John G Jones, Fernanda Borges, Paulo J Oliveira, José Teixeira. Mitochondriotropic antioxidant based on caffeic acid AntiOxCIN$_4$ activates Nrf2-dependent antioxidant defenses and quality control mechanisms to antagonize oxidative stress-induced cell damage. *Free Radic Biol Med.* 2022 Feb 1;179:119-132. doi: 10.1016/j.freeradbiomed.2021.12.304.

7.1. Introduction

Mitochondria are vital organelles involved in cellular survival, differentiation, and death induction [489]. In the presence of mild mitochondrial stress, cellular responses, such as alterations on redox and mitochondrial homeostasis, are required to increase cellular quality control mechanisms and upregulate mitochondrial function, which subsequently leads to an increase in cellular resistance and survival to further insults [490–492]. Although mild transient increase of mitochondrial ROS (mtROS) production may play a role in initiating mitochondria-to-nucleus ("retrograde") signaling [493] or alter cell metabolism [494], exacerbated mtROS levels were described to be involved in the pathogenesis of many diseases. In this context, targeting mtROS has been looked at as a potential pharmacological solution for several disorders [495–497]. Nevertheless, the discovery of mitochondrial drug candidates is a unique challenge as it requires a target-specific affinity (drug delivery to mitochondria) and, at the same time, a narrow drug safety window, as the candidates must not present mitochondrial toxicity.

In the last decades, dietary polyphenols such as hydroxycinnamic acids (HCAs) have been shown to have health beneficial effects [498–500]. HCAs are secondary plant

metabolites with significant antioxidant capacity, acting through different mechanisms, ranging from direct ROS scavenging and/or transition metal chelating to the activation of cellular or organelle antioxidant networks [501]. However, HCAs suffer from poor body distribution and low accumulation in intracellular sites, such as mitochondria, due to high hydrophilic characteristics and inherent difficulties to cross biological membranes [502, 503]. HCAs pharmacokinetic drawbacks were overcome by the conjugation of the antioxidant core of caffeic acid with an alkyl linker and a triphenylphosphonium cation (TPP^+). A lead optimization process, guided by structure-activity relationships, led to the development of a mitochondriotropic antioxidant ($AntiOxCIN_4$) with remarkable antioxidant properties (**Figure 14A**) either in human hepatoma-derived (HepG2) (100 µM; 48 h) and differentiated human neuroblastoma (SH-SH5Y) (10 µM; 24 h) cells [458, 459]. We recently demonstrated that $AntiOxCIN_4$ sustainably increased ROS levels, thereby activating endogenous ROS-protective pathways that protected primary human skin fibroblasts (PHSF) against subsequent OxS (12.5 µM; 72 h) [460] and it can improve several cellular and mitochondrial metabolic parameters in PHSF from sporadic Parkinson's disease patients (25 µM; 48 h) [461].

Besides being a polyphenolic antioxidant, $AntiOxCIN_4$ contains in its structure a Michael acceptor moiety suggesting that the mechanism of action may involve activation of nuclear factor erythroid 2-related factor 2 (Nrf2; a.k.a. Nuclear factor erythroid-derived 2-like 2; NFE2L2), the master regulator of the oxidative stress response [501]. This work aims to better understand the molecular mechanisms underlying the $AntiOxCIN_4$-induced coordinated cellular adaptative response involving Nrf2 and its impact on mitochondrial dynamics, including biogenesis, cellular antioxidant defenses, and quality control mechanisms regulation, through autophagy in human hepatoma-derived (HepG2) cells. HepG2 cells are a sensitive, cost-effective, and fast first-tier cell model to study mitochondrial toxicity in hepatic cells and a biosensor used in pre-clinical studies [504]. In fact, HepG2 cells have been widely used to model metabolic-related hepatic disorders, including NASH/NAFLD and type II diabetes in vitro. Consequently, HepG2 cells are an excellent model to investigate the effects of mitochondria-targeted molecules, such as $AntiOxCIN_4$, in the context of the hepatic tissue [462].

Our data demonstrated that AntiOxCIN$_4$ increases cell stress resistance by activating the Nrf2-p62-KEAP1 axis. Nrf2 activation led to up-regulation of local pools of antioxidant defense, trigger macroautophagy and/or mitophagy and mitochondrial biogenesis, cellular mechanisms that contributed to HepG2 cells increased capability to counteract oxidative stress-related conditions

7.2. Materials and methods

7.2.1. Chemicals and reagents

Cell culture medium, media components, chemicals and reagents were purchased from Sigma-Aldrich (St. Louis, MO, USA) unless otherwise specified.

7.2.2. Synthesis of AntiOxCIN$_4$

The synthesis, analysis, and spectroscopic elucidation of the mitochondriotropic antioxidant AntiOxCIN$_4$ were previously described [458].

7.2.3. Cell culture and AntiOxCIN$_4$ treatment

Human hepatocellular carcinoma HepG2 cells (Catalogue 85011430, ECACC, UK) were cultured in a low-glucose medium composed by Dulbecco's modified Eagle's medium (DMEM; Catalogue D5030, Sigma-Aldrich, USA) supplemented with 5 mM glucose, sodium bicarbonate (3.7 g/L), HEPES (1.19 g/L), L-glutamine (0.876 g/L), sodium pyruvate (0.11 g/L), 10% fetal bovine serum (FBS), 1% penicillin-streptomycin 100x solution. Alternatively, HepG2 cells were cultured in OXPHOS medium (OXPHOS$_m$) composed by Dulbecco's Modified Eagle's Medium (Catalogue D5030, Sigma-Aldrich, USA) without glucose and supplemented with sodium bicarbonate (1.8 g/L), sodium pyruvate (0.11 g/mL), galactose (1.8 g/L), L-glutamine (0.876 g/L), 10% fetal bovine serum (FBS) and 1% penicillin-streptomycin 100x solution in a humidified atmosphere (5 % CO_2, 37 ºC). HepG2 cells were seeded (4.5 x 10^4 cells/cm^2) and grown for 24 h, reaching 60–70 % confluence before treatment. Cells were then treated in the presence of the mitochondriotropic antioxidant AntiOxCIN$_4$, 100 µM or dimethyl sulfoxide (DMSO), 0,1 %.

7.2.4. Palmitic acid/BSA conjugation

Palmitic acid (PA)/Bovine Serum Albumin (BSA, Catalogue A6003, Sigma-Aldrich, USA) solution was prepared by mixing free-fatty acid BSA (0.1 g/mL) with 10 mM palmitic acid in the proportion of 1:1 during 1 h at 37 ºC. The free-fatty acid BSA (0.1 g/mL) was diluted in the same proportion with 150 mM NaCl and used as a control [415].

7.2.5. Nile red Staining

The steatotic protection of the mitochondria-targeted antioxidant was evaluated in the presence of PA. Cells were seeded in 96-well plate and incubated with AntiOxCIN$_4$ (100 µM) 48 h. Then, PA/BSA (500 µM) was added to the culture medium of HepG2 cells for more 6 h. After incubation, the neutral lipid accumulation was assessed through the Nile Red assay [505]. Briefly, cell culture medium was removed and 100 µL of the Nile red solution was added to each well for 1 h/1.5 h in the dark conditions at 37 ºC. Nile Red is freshly diluted 1:200 in medium without FBS from the stock solution (stock: 0.5 mg/mL dissolved in acetone). Nile Red was then removed, and cells were washed twice with PBS 1X. The fat content per well (in 100 µL PBS 1X) was measured fluorimetrically with 520 nm excitation and 620 nm emission wavelengths in a Biotek Cytation 3 reader (Biotek Instruments, Winooski, VT, USA). Results were normalized for cell mass content at the end of assay, using the SRB method [506].

7.2.6. Cell mass measurements

Cells were seeded in 96-well plates and then subjected to the different treatments. After incubation time, the sulforhodamine B (SRB) assay was used for cell mass determination based on the measurement of cellular protein content [506]. Briefly, the cell culture medium was removed and wells rinsed with PBS (1X). Cells were fixed by adding 1% acetic acid in 100% methanol for at least 2 h at -20 ºC. Later, the fixation solution was discarded and the plates were dried in an oven at 37 ºC. One hundred and fifty microliters of 0.05% SRB in 1% acetic acid solution was added and incubated at 37 °C for 1 h. The wells were then washed with 1% acetic acid in water and dried. Then, 100 µl of Tris (pH 10) was added and the plates were stirred for 15 min and optical density

was measured at 540 nm in Biotek Cytation 3 reader (Biotek Instruments, Winooski, VT, USA).

7.2.7. Metabolic cell viability determination using resazurin assay

Cells were seeded in 96-well plate and then subjected to the different treatments. After incubation time, the metabolic cell viability was assessed through the resazurin reduction assay [507]. Briefly, the culture medium was removed and cells were incubated for 1 h with 80 µl of culture medium supplemented with 10 µg/ml resazurin. The amount of resazurin reduced to resorufin, indicative of metabolic activity, was measured fluorimetrically with 570 nm excitation and 600 nm emission wavelengths in Biotek Cytation 3 reader (Biotek Instruments, Winooski, VT, USA).

7.2.8. Mitochondrial superoxide anion detection

Cells were seeded in 96-well plate (flat bottom clear, black polystyrene plate) and then subjected to the different treatments. After incubation time, mitochondrial superoxide anion was assessed through MitoSOX Red (M36008, ThermoFisher Scientific) assay. Briefly, cells were loaded with the MitoSOX Red as indicator of mitochondrial superoxide by incubating them with 5 µM of the MitoSOX Red in assay buffer (NaCl 120 mM, KCl 3.5 mM, $NaHCO_3$ 5 mM, $NaSO_4$ 1.2 mM, KH_2PO_4 0.4 mM, HEPES 20 mM supplemented with $CaCl_2$ 1.3 mM, $MgCl_2$ 1.2 mM and sodium pyruvate 10 mM, pH 7.4) and the changes fluorescence assessed every 2 min for 90 min in a Biotek Cytation 3 spectrophotometer at 510/580 nm (Biotek Instruments, Winooski, VT, USA).

7.2.9. Caspase-like colorimetric activity assay

Cells were seeded in 100 mm cell culture dishes and then subjected to the different treatments. Then, total cellular extracts were collected by trypsinization and centrifuged twice at 1000X*g*, 4 °C during 5 min. Floating cells were also collected. The pellet was resuspended in collecting buffer (20 mM HEPES/NaOH pH 7.5, 250 mM Sucrose, 10 mM KCl, 2 mM $MgCl_2$, 1 mM EDTA) supplemented with 2 mM DTT, 100 µM phenylmethylsulfonyl fluoride (PMSF) and a protease inhibitor cocktail, containing 1 µg/ml of leupeptin, antipain, chymostatin and pepstatin A. Protein contents were

determined by the Bradford assay [508]. To measure caspase 3- and 9-like activity, aliquots of cell extracts containing 25 µg (for caspase 3) and 50 µg (for caspase 9) of protein were incubated in a reaction buffer containing 25 mM HEPES (pH 7.4), 10% sucrose, 10 mM DTT, 0.1% CHAPS and 100 µM caspase substrate (Ac-DEVDpNA for caspase 3 or Ac-LEHDpNA for caspase 9 (Calbiochem, Billerica, MA) for 2 h at 37 ºC. Caspase-like activities were determined by following the detection of the chromophore p-nitroanilide after cleavage from the labeled substrate Ac-DEVD-p-nitroanilide or Ac-LEHD-pnitroanilide. The method was calibrated with known concentrations of p-nitroanilide (pNA) (Calbiochem). After incubation with caspase 3 and 9 substrates, absorbance was measured in a Cytation 3 reader (BioTek Instruments Inc., USA) at 405 nm.

7.2.10. Measurement of malondialdehyde (MDA) levels

Cells were seeded in 100 mm cell culture dishes and then subjected to the different treatments. Oxidative damage of lipids was evaluated by the formation of a thiobarbituric acid (TBA) adduct of malondialdehyde (MDA) and then separated by HPLC. Cell lysates were boiled during 60 min with TBA and phosphoric acid, then were deproteinized with methanol/NaOH 1 M (10:1) and centrifuged. The supernatant (20 µl) was injected into a Spherisorb ODS2 5 µm (250 × 4.6 mm) column. Elution was performed with 60% (v/v) potassium phosphate buffer 50 mM, pH 6.8, and 40% (v/v) methanol at a flow rate of 1 ml/min. The TBA-MDA adducts were detected at 532 nm and quantified by extrapolating the area of the peaks from a calibration curve of 1,1,3,3-tetraetoxipropane (TEP) standard solutions.

7.2.11. Cellular oxygen consumption measurements

Cells were seeded in 96-well plate in the same conditions described above at a density of 10000 cells/100µL/well. After incubation time, oxygen consumption was measured at 37 ºC using a Seahorse XFe96 Extracellular Flux Analyzer (Agilent Scientific Instruments, California, USA). In addition, an XFe96 sensor cartridge for each cell plate was placed in a 96-well calibration plate containing 200 µL/well calibration buffer and left to hydrate overnight at 37 ºC. The cell culture medium from the plates was replaced

the following day with 175 µL/well of pre-warmed low-buffered serum-free minimal DMEM (D5030, Sigma-Aldrich, USA) medium, the pH adjusted to 7.4 and incubated at 37 ºC for 1 h to allow the temperature and pH of the medium to reach equilibrium before the first-rate measurement. Oligomycin, FCCP, rotenone and antimycin A were prepared in DMSO.

For oxygen consumption rate (OCR) measurements in acute treatment, 100 µM AntiOxCIN$_4$, injected into reagent delivery port A. 2 µM oligomycin, injected into reagent delivery port B. 0.3 µM FCPP injected into port C, which followed the injection of oligomycin was diluted in low-buffered serum-free DMEM medium. One µM rotenone and 1µM antimycin A injected into reagent delivery port D was diluted in low-buffered serum-free DMEM medium and the pH adjusted to 7.4 with 1 M NaOH.

For oxygen consumption rate (OCR) measurements in 48 h treatment, 2 µM oligomycin, injected into reagent delivery port A. 0.3 µM FCPP injected into port B, which followed the injection of oligomycin was diluted in low-buffered serum-free DMEM medium. One µM rotenone and 1 µM antimycin A injected into reagent delivery port C was diluted in low-buffered serum-free DMEM medium and the pH adjusted to 7.4 with 1 M NaOH. 25 µL of compounds was then pre-loaded into the ports of each well in the XFe96 sensor cartridge. The sensor cartridge and the calibration plate were loaded into the XFe96 Extracellular Flux Analyzer for calibration. When the calibration was complete, the calibration plate was replaced with the study plate. Three baseline rate measurements of OCR of the HepG2 cells were made using a 3 min mix, 5 min measure cycle. The compounds were then pneumatically injected by the XFe 96 Analyzer into each well, mixed and OCR measurements made using a 3 min mix, 5 min measure cycle. Results were analyzed by using the Software Version Wave Desktop 2.6.1.

7.2.12. Gene expression measurements

Transcript analysis was assessed by performing quantitative polymerase chain reaction (qPCR). Cells were seeded in 100 mm cell culture dishes and later subjected to the respective treatments. After the 48 h incubation period, total cellular extracts were obtained by firstly washing the cells with PBS 1x and immediately thereafter through gentle scraping of the bottom of the plates onto a milliliter of PBS 1x. In order to collect

the highest number of cells possible, two microtube centrifugation steps were performed at 12000X*g* for 10 min at 4 ºC. Total cellular RNA contents were extracted utilizing the Qiagen RNeasy kit (Qiagen, Hilden, Germany) according to the manufacturer's instructions. RNA was readily quantified, and its purity assessed utilizing Thermo Scientific® NanoDrop 2000™ spectrophotometer (Thermo Fisher Scientific, Waltham, Massachusetts, USA). Upon quantification, the RNA conversion into complementary DNA (cDNA) was performed utilizing the iScript™ cDNA Synthesis Kit, by utilizing Bio-Rad® CFX96™ Real-Time PCR system (Bio-Rad Laboratories, Hercules, California, USA). RT-PCR was performed using the SsoFast Eva Green Supermix, in a CFX96 real time-PCR system (Bio-Rad, Hercules, CA, USA), with the primers defined **Table 7**, at 500 nM. Amplification of 25 ng was performed with an initial cycle of 30 s at 95 ºC, followed by 40 cycles of 5 s at 95 ºC plus 5 s at 60 ºC. At the end of each cycle, Eva Green fluorescence was recorded to enable determination of Cq. After amplification, melting temperature of the PCR products was determined by performing melting curves. One of the negative controls included one sample being subjected to a similar conversion in the absence of the reverse transcriptase enzyme (no reverse transcriptase – NRT). Additionally, for each primer, a second negative control was performed, one in which the DNA sample was replaced by water (No template control – NTC). Each reaction was performed in triplicate with efficiency between 90 and 110 %. Each sample was run in triplicate. Total gene expression was calculated utilizing the Bio-Rad® CFX96 Manager Software (version 3.1) (Bio-Rad Laboratories, Hercules, California, USA). All primers were designed using the web-based Primer–Basic Local Alignment Search Tool (Primer-BLAST) after obtaining nucleotide accession numbers from the database. Both services are public and supported by the National Center for Biotechnology Information (NCBI). Primers were diluted in RNase-free water to the concentration of 100 µM upon arrival and stored at -20ºC.

7.2.13. Mitochondrial DNA copy number measurements

Mitochondrial DNA (mtDNA) copy number was measured using quantitative polymerase chain reaction (qPCR). HepG2 cells were seeded in 60 mm cell culture dishes and subjected to the different treatments. Cells were then harvested at the time-points indicated by aspirating media and washing plates with ice cold PBS. For measurement

of mtDNA copy number, RNase-treated total DNA was isolated using the Qiagen DNeasy kit (Catalogue 69104, Qiagen, Germany) according to the manufacturer's recommended protocol. DNA abundance and purity were assessed in a NanoDrop 2000 spectrophotometer (ThermoScientific, Waltham, MA, USA). DNA was used as template for qPCR based on amplification of cytochrome B (CytB) (encoded on the mitochondrial genome; variable number in each cell) and beta-2-microglobulin (b2m) (encoded on the nuclear genome; fixed number in each cell) using a Roche Light Cycler and Roche FastStart DNA Master SYBR Green protocols. Human primers for *MT-CYB* were: forward 5'- CCACCCCATCCAACATCTCC-3', reverse 5'-GCGTCTGGTGAGTAGTGCAT-3' (Pair rating: 66,1; Product length: 112); primers for *B2M* were: forward 5'-GAATTCCAAATTCTGCTTGCTTGC-3', reverse 5'- CCTCTAAGTTGCCAGCCCTC-3' (Pair rating: 71,2; Product length: 199). Each reaction was performed in triplicate with efficiency between 90 and 110 %. Amplification of 25 ng total DNA was performed with an initial cycle of 2 min at 95 ºC, followed by 40 cycles of 5 seconds at 95 ºC plus 20 seconds at 63 ºC and 20 seconds at 72 ºC. At the end of each cycle, Eva Green fluorescence was recorded to enable determination of Cq. Each qPCR experiment contained parallel reactions in which standards with serial dilutions of purified amplicon were used as template; reactions with no template served as negative control. The specificity of each reaction for a single product was verified by melting analysis. The cycle number of linear amplifications for each sample was compared with the five-point standard curve to determine the number of template copies present at the start of each reaction. To estimate the mtDNA copy number relative to nuclear genomes, the number of copies of cytochrome B template was divided by the number of copies of beta-2 microglobulin template. The reactions were performed on a CFX™96 Real-Time system (Bio-Rad, CA, USA). The normalized expression was calculated by the comparative quantification algorithm ΔΔCt (CFX Manager™ 3.1 software, 18 Bio-Rad).

7.2.14. Western blotting analysis

Cells were seeded in 100 mm cell culture dishes and then subjected to the different treatments. To obtain total cellular extracts, all cells were harvested and washed once with PBS 1X. In order to collect total cells, two centrifugation steps were

performed for 10 min at 1000X*g* (4 °C). Cellular pellet was resuspended in RIPA buffer (50mM Tris pH 8.0, 150 mM NaCl, 5mM EDTA, 15mM $MgCl_2$ and 1% TritonX-100) supplemented with 0.5 mM phenylmethylsulfonyl fluoride (PMSF), 20 mM sodium fluoride (NaF), 10 mM nicotinamide (NAM), 5 mM sodium butyrate, 0,5 % sodium deoxycholate (DOC) and Protease Inhibitor Cocktail (PIC, 2 µL/mL). Protein contents were determined by the BCA method [509] using BSA as a standard. After denaturation at 95 °C for 5 min in Laemmli buffer (161-0737, Bio-Rad), an equivalent amount of proteins (20–40 µg) was separated by electrophoresis on SDS–polyacrylamide gels (SDS–PAGE) and electrophoretically transferred to a polyvinylidene difluoride (PVDF) membrane. After blocking with 5 % milk or BSA in TBST (50 mM Tris–HCl, pH 8; 154 mM NaCl and 0.1 % tween 20) for 2 h at room temperature, membranes were incubated overnight at 4 °C with the antibodies directed against the denatured form OXPHOS complexes cocktail (1:1000, ab110411, Abcam), Membrane Integrity cocktail (1:1000, ab110414, Abcam), PGC-1α (1:750, ST1202, Sigma-Aldrich), PINK1 (1:1000; ab65232, Abcam), SQSTM1/p62 (1:1000, sc28359, Santa Cruz Biotechnology), LC3B (1:1000, cs3868, Cell Signaling), MNF1 (1:500, sc50330, Santa Cruz Biotechnology), Fis1 (1:500, sc376447, Santa Cruz Biotechnology), β-actin (1:5000, MAB1501, Sigma-Aldrich), Beclin-1 (1:1000, cs3495, Cell Signaling), KEAP1 (1:1000, cs8047, Cell Signaling), Nrf2 (1:1000, sc365949, Santa Cruz Biotechnology), Atg5 (1:1000, cs12994, Cell Signaling), Lamin B1 (1:2500, ab65986, Abcam), GAPDH (1:5000, sc59540, Santa Cruz Biotechnology). Once incubation was completed, membranes were washed with TBST and incubated at room temperature with anti-rabbit (1:5000, 1677074S, Cell Signaling) or anti-mouse (1:5000, 1677076S, Cell Signaling) HRP-conjugated secondary antibodies. β-actin and GAPDH (cytosolic markers), and Lamin B1 (nuclear marker) were used as housekeeping proteins as no treatment-related changes in the protein levels were observed. Clarity Western ECL Substrate (1705061, Bio-Rad Laboratories) was used for chemiluminescence detection. The densities of each band were calculated with TotalLab TL120 Software (version 2009).

7.2.15. Nuclear fraction extraction

Cells were seeded in 100 mm cell culture dishes and then subjected to the different treatments for 1, 6, 24 and 48 h. Then, cells were washed twice with ice-cold PBS, lysed with cytosolic extraction buffer (50 mM Tris-HCl pH 8.0, 2 mM EDTA, 0.5 % Nonited P-40, 20 % glycerol, 0.5 mM PMSF and PIC) for 5 min on ice, and then micro-centrifugated at 720X*g* for 5 min. Supernatants were used as cytosolic extracts and the pellet was lysed in nuclear extraction buffer (20 mM HEPES pH 7.6, 420 mM NaCl, 2 mM EDTA, 1 % Triton X-100, 20 % glycerol, 25 mM B-glycerophosphate, and 0.5 mM PMSF) for 30 min on ice and was then micro-centrifuged at 16000X*g* for 15 min. Protein contents were determined by the Bradford method [508]. Cytosolic and nuclear extracts were used for Western blot analysis as described above.

7.2.16. Measurement of superoxide dismutase (SOD) activity

HepG2 cells were seeded at a concentration of 4.5 $x10^3/cm^2$ in 100 mm tissue-culture dishes, with a final volume of 10 ml. Total SOD activity was measured by using a SOD activity assay kit (SOD activity Enzo Life Sciences, USA) following the manufacturer's instructions. After 48 h, cells were harvested, washed with ice-cold 1x PBS and lysed as described in kit protocol. Protein concentration was determined using the BCA method [509]. Cell lysates of each sample or standards (25 µL) were incubated with 150 µL reaction mixture containing WST - 1 and Xanthine oxidase and then xanthine solution was added. Formazan formation was measured for 10 min at 37 ºC, and the absorbance was monitored at 450 nm in a Biotek Cytation 3 spectrophotometer (BioTek Instruments Inc., USA). SOD standard curve was also generated following the manufacturer's instructions.

7.2.17. Measurement of catalase (CAT) activity

HepG2 cells were seeded in 100 mm cell culture dishes and then subjected to different treatments. To obtain total cellular extracts, all cells were harvested and washed once with PBS 1X. For total cells collection, a centrifugation at 300X*g* (4 ºC) for 5 min was performed. Subsequently, cell pellets were resuspended in 50 mM phosphate

buffer, pH = 7.8 (PB, 50 mM of KH_2PO_4, 50 mM of K_2HPO_4). The protein amount was measured by BCA method [509], using BSA as standard. 20 µL of all samples (2 mg/mL) were added to 180 µL of PB. A 240 nm initial basal absorbance was determined for background correction and protein loading assessment. After that, 100 µL of H_2O_2 solution 90 mM was added immediately before starting the kinetic reading [510]. Catalase activity was followed by the variation of H_2O_2 absorbance at 240 nm during 2.5 min, with a readout each 15 s using a Cytation3 multi-mode microplate reader (BioTek Instruments, Inc.,Winooski,VT,USA).

7.2.18. Measurement of glutathione peroxidase (GPx) activity

Cells were seeded in a 100 mm cell culture dish, subjected to the different treatments and then harvested at the times indicated by aspirating media and washing plates with ice-cold PBS, which was then aspirated and plates sealed with Parafilm and stored at -80 ºC. Protein contents were determined by the BCA method using BSA as a standard. Glutathione peroxidase activity was evaluated by spectrophotometry using tert-butylperoxide as a substrate, monitoring the formation of oxidized glutathione, through the quantification of the oxidation of NADPH to $NADP^+$ at 340 nm [510]. Results are expressed in international units of enzyme per microgram of protein (U/µg prot).

7.2.19. Measurement of glutathione disulfide reductase (GR) activity

Cells were seeded in 100 mm cell culture dish, subjected to the different treatments and then harvested at the times indicated by aspirating media and washing plates with ice-cold PBS, which was then aspirated and plates sealed with Parafilm and stored at -80 ºC. Protein contents were determined by the BCA method using BSA as a standard. Glutathione reductase activity was determined using GSSG as a substrate and monitoring its reduction to GSH through quantification of NADPH oxidation at 340 nm in a thermostatized spectrophotometer UVIKON 933 UV/Visible, at 37 °C. GR activity was expressed in international units of enzyme per microgram of protein (U/µg prot).

7.2.20. NAD^+/NADH measurements

Cells were seeded in 100 µL of culture medium, in a white opaque-bottom, 96-well plate and then subjected to the different treatments. After incubation time, intracellular NAD^+ and NADH levels were measured by using the NAD/NADH-Glo™ assay (G9071, Promega) following the manufacturer's instructions. Briefly, the cell culture medium was removed and replaced with 50 µL of PBS (1x). Then, 50 µL of 1% dodecyltrimethylammonium bromide (DTAB) was added. Each 100 µL solution containing well was separated into two 50 µL containing wells, one for NAD^+ and one for NADH. For the NAD^+ quantification, 25 µL of HCl (0.4 M) was added and then cells were incubated at 60 ^oC for 15 min and then kept at room temperature for 10 min to cool down. 25 µL of Trizma base was added to the NAD^+ wells. For NADH quantification 50 µL of the HCl/Trizma solution was added. Finally, the NAD/NADH detection reagent was added to each well in a 1:1 proportion. Subsequently, the luminescence signal was obtained in a BioTek Cytation 3 reader (BioTek Instruments Inc., USA)

7.2.21. Mitochondrial Transmembrane Electric Potential Measurements

Vital confocal fluorescent microscopy was used to visualize alterations in mitochondrial electric potential polarization and network distribution in HepG2 cells. Cells were seeded in pre-coated (collagen I, 0.15 mg/mL) µ-Slide 8 well ibiTreat Ibidi (2 x $10^4/cm^2$) with a final volume of 300 µL per well, and then subjected to the different treatments. Cells were incubated with fluorescent dyes tetramethylrhodamine (TMRM) (100 nM, Catalogue T668, ThermoFisher Scientific) and Hoechst 33342 (1 µg/mL, Catalogue H1399, ThermoFisher Scientific) for mitochondrial network and nuclei, respectively, 30 min before the end of the treatment time in fresh cell culture medium with no FBS at 37 °C and 5 % CO_2 in the dark conditions. Images were acquired using a Laser Scanning Confocal Microscope (LSM 710, Zeiss, USA) equipped with a α-Plan-Apochromat 63x/1.4 Oil DIC M27 objective (Zeiss) and analyzed with ImageJ Fiji program (Scion Corporation, USA). Mitochondrial network was quantified by using a *Mitochondria Morphology* Macro [511].

7.2.22. Mitochondrial and lysosomal co-localization

Cells were seeded in pre-coated (collagen I 0.15 mg/mL) µ-Slide 8 well ibiTreat Ibidi (2 x 10^4/cm^2) with a final volume of 300 µL per well, and then subjected to the different treatments. Cells were incubated with MitoTracker™ Green FM (200 nM, Catalogue M7514, ThermoFisher Scientific), Lysotracker Red (75nM, Catalogue L7528) and Hoechst 33342 (1 µg/mL, Catalogue H1399, ThermoFisher Scientific) for mitochondrial network, lysosomes and nuclei, respectively, 30 min before the end of the treatment time in fresh cell culture medium with no FBS at 37 °C and 5 % CO_2 in the dark conditions. Images were acquired using a Laser Scanning Confocal Microscope (LSM 710, Zeiss, USA) equipped with a α-Plan-Apochromat 63x/1.4 Oil DIC M27 objective (Zeiss) and analyzed with ImageJ Fiji program (Scion Corporation, USA). Co-localization was quantified using *JACoP v2.0 Macro* [512].

7.2.23. $NADP^+$/NADPH measurements

Cells were seeded in 100 µL of culture medium, in a white opaque-bottom, 96-well plate and then subjected to the different treatments. After incubation time, intracellular $NADP^+$ and NADPH levels were measured by using the NADP/NADPH-Glo™ assay (Catalogue G9081, Promega) following the manufacturer's instructions and as described in the NAD/NADH measurements section.

7.2.24. Measurement of glutathione (GSH) and glutathione disulfide (GSSG) levels

Cells were seeded in a 100 mm cell culture dish, subjected to the different treatments and then harvested at the times indicated by aspirating media and washing plates with ice-cold PBS, which was then aspirated and plates sealed with parafilm and stored at -80 ºC. Protein contents were determined by the BCA method using BSA as a standard. GSH and GSSG levels were determined with fluorescence detection after reaction of the supernatant containing H_3PO_4/NaH_2PO_4–EDTA or H_3PO_4/NaOH, respectively, of the deproteinized homogenate solution with ophthalaldehyde (OPT), pH 8.0 [513]. In brief, cell homogenate resuspended in 1.5 ml phosphate buffer (100 mM

NaH_2PO_4, 5 mM EDTA, pH 8.0) and 500 µl H_3PO_4 4.5% were rapidly centrifuged at 50,000 rpm (Beckman, TL-100 Ultracentrifuge) for 30 min. For GSH determination, 100 µl of supernatant was added to 1.8 ml phosphate buffer and 100 µl OPT. After thorough mixing and incubation at room temperature for 15 min, the solution was transferred to a quartz cuvette and the fluorescence was measured at 420 nm and 350 nm emission and excitation wavelengths, respectively. For GSSG determination, 250 µl of the supernatant was added to 100 µl of N-ethylmaleimide and incubated at room temperature for 30 min. After the incubation, 140 µl of the mixture was added to a 1.76 ml NaOH (100 mM) buffer and 100 µl OPT. After mixing and incubation at room temperature for 15 min, the solution was transferred to a quartz cuvette and the fluorescence was measured at 420 nm and 350 nm emission and excitation wavelengths, respectively. The GSH and GSSG levels were determined from comparisons with a linear GSH or GSSG standard curve, respectively.

7.2.25. Measurement of α-tocopherol (vitamin E) content

Cells were seeded in 100 mm cell culture dish, subjected to the different treatments and then harvested at the times indicated by aspirating media and washing plates with ice cold PBS, which was then removed and plates sealed with Parafilm and stored at -80 ºC. Protein contents were determined by using BSA as a standard. Extraction and separation of reduced α-tocopherol (vitamin E) from cells were performed by following a previously described method [514]. Briefly, 1.5 ml sodium dodecyl sulfate (10 mM) was added to 0.5 mg of total cellular extract, followed by the addition of 2 ml ethanol. Then 2 ml hexane and 50 µl of 3 M KCl were added, and the mixture was vortexed for about 3 min. The extract was centrifuged at 500X*g* (Sorvall RT6000 Refrigerated Centrifuge) and 1 ml of the upper phase, containing n-hexane (n-hexane layer), was recovered and evaporated to dryness under a stream of N_2 and kept at − 80 °C. The extract was dissolved in n-hexane, and the α-tocopherol content was analyzed by reverse-phase HPLC. A Spherisorb S10w column (4.6 × 200 nm) was eluted with n-hexane modified with 0.9% methanol, at a flow rate of 1.5 ml/min. Detection was performed by a UV detector at 287 nm. The content of cellular vitamin E was calculated as pmol/µg protein.

7.2.26. Extracellular acidification measurements

Cells were seeded in a 96-well plate in the same conditions described above at a density of 10,000 cells/100µL/well. After incubation time, extracellular acidification rate (ECAR) was measured at 37 ºC using a Seahorse XFe96 Extracellular Flux Analyzer (Agilent Scientific Instruments, California, USA). In addition, an XFe96 sensor cartridge for each cell plate was placed in a 96-well calibration plate containing 200 µL/well calibration buffer and left to hydrate overnight at 37 ºC. The cell culture medium from the plates was replaced the following day with 175 µL/well of pre-warmed low-buffered serum-free minimal DMEM (D5030, Sigma-Aldrich, USA) medium, the pH adjusted to 7.4 and incubated at 37 ºC for 1 h to allow the temperature and pH of the medium to reach equilibrium before the first-rate measurement. Oligomycin was prepared in DMSO and 2-DG was prepared in pre-warmed low-buffered serum-free minimal DMEM (D5030, Sigma-Aldrich, USA) medium. For extracellular acidification rate (ECAR), 25 mM glucose injected extracellular acidification rate (ECAR), 25 mM glucose injected into reagent delivery port A was diluted in low-buffered serum-free DMEM medium and the pH adjusted to 7.35 with 1 M NaOH. Two µM oligomycin injected into port B, which followed the injection of glucose was diluted in low-buffered serum-free DMEM medium. One hundred mM 2-DG injected into reagent delivery port C was diluted in low-buffered serum-free DMEM medium and the pH adjusted to 7.35 with 1 M NaOH. 25 µL of compounds was then pre-loaded into the ports of each well in the XFe96 sensor cartridge. The sensor cartridge and the calibration plate were loaded into the XFe96 Extracellular Flux Analyzer for calibration. When the calibration was complete, the calibration plate was replaced with the study plate. Three baseline rate measurements of ECAR of the HepG2 cells were made using a 3 min mix, 5 min measure cycle. The compounds were then pneumatically injected by the XFe 96 Analyzer into each well, mixed and ECAR measurements made using a 3 min mix, 5 min measure cycle. Results were analyzed by using the Software Version Wave Desktop 2.6.1.

7.2.27. Nuclear magnetic resonance (NMR) analysis

^{1}H NMR spectra provide information about several metabolites detectable (present in extracellular medium) in one single spectrum. For NMR experiments, cells were seeded in a 100 mm cell culture dish and then subjected to the different treatments. During the antioxidant incubation time, 200 µL media aliquots were collected at 0, 8, 24, 36 and 48 h and kept at -80ºC until analysis. At the end of the antioxidant incubation period, cells were washed with PBS and collected by solvent scraping as described by Dettmer *et al*. [515], where direct 80% methanol and 20% H_2O ($MeOH/H_2O$) scraping yielded the most efficient and reproducible extraction. This extract was transferred onto 2 mL microtubes, which were centrifuged at 5725X*g* for 5 min at 4 ^{o}C. The resulting pellet contained mostly protein and lipids in contrast to the supernatant, which contained the aqueous phase. This aqueous phase was promptly transferred onto a different set of microtubes and evaporated in a freeze dryer. The pellet was resuspended in chloroform and centrifuged at 5725X*g* for 5 min at 4 ^{o}C in order to extract the organic phase. The resulting supernatant was once again transferred to another set of microtubes.

Aqueous extracts were resuspended in 160 µL of $^{2}H_2O$ and supplemented with 40 µL of deuterated PBS 0.25 M, 5 mM TMS, pD=7.4 and loaded on 3 mm NMR tubes. For media aliquots, 160 µL was simply mixed with 40 µL of the same deuterated PBS for providing lock and an internal standard. ^{1}H spectra were acquired on a 14.1 T Varian VNMR 600 MHz (Varian Inc., Palo Alto, CA, USA) spectrometer equipped with a 3 mm inverse configuration probe. Spectra were acquired at 25 ºC, 20 Hz spin rate, with a presat pulse sequence (d1=4s, satdly=3s, at=3s), ss=2, sw=6000 Hz, np=32000, nt=32. Every spectrum was processed using ADC lab's 12.0 ^{1}D NMR processor software (Advanced Chemistry Development, Inc., Toronto, Ontario, Canada) applying a line broadening of 0.2 Hz, zero-filling to 64k, phasing and baseline correction.

7.2.28. Adenine nucleotide measurement (ATP/ADP/AMP)

ATP, ADP and AMP levels were measured by HPLC. Cells were seeded in 100 mm cell culture dishes and then subjected to the different treatments. For the nucleotides

extraction, cells were rinsed with PBS, followed by the addition of 500 µl ice-cold 0.6 M $HClO_4$ to each dish. The dishes were scraped and the lysates were centrifuged for 10 min at 14000X*g*. The supernatant, containing adenine nucleotides, was neutralized and analyzed by reverse-phase HPLC for quantification of the adenine nucleotides. The chromatographic apparatus was a Beckman-System Gold (Beckman Coulter, Fullerton, CA), consisting of a 126 Binary Pump Model and a 166 Variable UV detector, computer-controlled. Detection was performed by an ultraviolet detector at 254 nm and the column was a Lichrospher 100RP-18 (5 µm) from Merck (Dramstadt, Germany). Samples were eluted with 100 mM phosphate buffer (KH_2PO_4), pH 6.5, and 1 % methanol with a flow rate of 1.1 ml/min. Pellet protein concentration was determined after the addition of 1 M NaOH, by using the BCA method, with BSA as a standard [509]. Energy charge was calculated as ([ATP] + 0.5 [ADP])/([ATP] + [ADP] + [AMP]).

7.2.29. Statistics

Data were analyzed in GraphPad Prism 8.0.2 software (GraphPad Software, Inc.). Data was normalized by the control condition (CTL = 100 %) with results expressed as means ± SEM. Student's t-test for comparing two means and one-way ANOVA with Dunnet multiple comparison post-test was used to compare more than two groups with one independent variable used in data analysis. Significance was accepted with *P<0.05, **P<0.01, ***P<0.0005, ****P<0.0001.

Table 7. Informative table on primers utilized for transcript amplification.

Gene	Accession number	mRNA Sequence Name	Forward Primer	Reverse Primer
ATP5MC1	NM_001002027	Homo sapiens ATP synthase, H^+ transporting, mitochondrial F_O complex, subunit C1 (subunit 9), transcript variant 2, mRNA	GGCTAAAGCTGGGA-GACTGAAA	GTGGGAAGTTGCTGTAGGAAGG
COX4I1	NM_001861	Homo sapiens cytochrome C oxidase subunit 4 isoform 1, mitochondrial, mRNA.	GAGAAAGTCGAGTTGTATCGCA	GCTTCTGCCACATGATAACGA
FIS1	NM_016068	Homo sapiens fission, mitochondrial 1, mRNA.	AGCGGGATTACGTCTTCTACC	CATGCCCACGAGTCCATCTTT
GABPA	NM_002040	Homo sapiens GA binding protein transcription factor, alpha subunit, transcript variant 1, mRNA.	GGAACAGAACAGGAAACAATG	CTCATAGTTCATCGTAGGCTTA
HPRT1	NM_000194	Homo sapiens hypoxanthine phosphoribosyltransferase 1, mRNA.	CCCTGGCGTCGTGATTAGTG	CGAGCAAGACGTTCAGTCCT
HMOX1	NM_002133	Homo sapiens heme oxygenase 1, mRNA	CTGCTGACCCATGACACCAA	GGGCAGAATCTTGCACTTTGT
MFN1	NM_033540	Homo sapiens mitofusin 1, mRNA.	AGTTGGAGCGGAGACTTAGCA	TTCTACCAGATCATCTTCAGTGGC
MNF2	NM_014874	Homo sapiens mitofusin 2, transcript variant 1, mRNA	AGCTACACTGGCTCCAACTG	AACCGGCTTTATTCCTGAGCA
MT-ND5	NC_012920 (12337-14148)	Homo sapiens mitochondrially encoded NADH:Ubiquinone Oxidoreductase Core Subunit 5, mRNA	AGTTACAATCGGCATCAACCAA	CCCGGAGCACATAAATAGTATGG
NFR1	NM_005011	Homo sapiens nuclear respiratory factor 1, transcript variant 1, mRNA.	TTGAGTCTAATCCATCTATCCG	TACTTACGCACCACATTCTC
NQO1	NM_000903	Homo sapiens NAD(P)H quinone dehydrogenase 1, transcript variant 1, mRNA.	CTGGAGTCGGACCTCTATGC	GGGTCCTTCAGTTTACCTGTGAT

OPA1	NM_015560	Homo sapiens mitochondrial dynamin like GTPase (autosomal dominant), transcript variant 1, mRNA.	GCTCTAAACCATTGTAAC-CTTTGT	TTCTCTAATCGCCTAACTTCAGT
PPARGC1A	NM_013261	Homo sapiens peroxisome proliferator-activated receptor gamma coactivator 1-Alpha, mRNA.	GCGAAGAGTATTTGTCAACAG	TTGGTTTGGCTTGTAAGTGT
SDHA	NM_004168	Homo sapiens succinate dehydrogenase complex, subunit A, flavoprotein (Fp), transcript variant 1, mRNA.	CGGGTCCATCCATCGCATAAG	TATATGCCTGTAGGGTG-GAACTGAA
TBP	NM_003194	Homo sapiens TATA box binding protein, transcript variant 1, mRNA.	CGAATATAATCCCAA-GCGGTTTGC	AGCTGGAAAACCCAACTTCTGT
TFAM	NM_003201	Homo sapiens mitochondrial transcription factor 1, transcript variant 1	GTTTCTCCGAAGCATGTG	GGTAAATACACAAAACTGAAGG
UQCRC2	NM_003366	Homo sapiens ubiquinol-cytochrome c reductase core protein II, mRNA	TTCAGCAATTTAGGAACCACCC	GGTCACACTTAATTTGCCACCAA
YWHAZ	NM_003406	Homo sapiens tyrosine 3-monooxygenase/tryptophan 5-monooxygenase activation protein, transcript variant 1, mRNA	TGTAGGAGCCCGTAGGTCATC	GTGAAGCATTGGGGATCAAGA

7.3. Results

7.3.1. AntiOxCIN$_4$ transiently impacted mitochondrial oxygen consumption either in the presence or absence of glucose

The mitochondria-targeted antioxidant AntiOxCIN$_4$ was previously shown to accumulate within the mitochondrial matrix, presenting substantial cytoprotective effect without affecting the viability of human hepatoma-derived (HepG2) cells (100 μM; 48 h) [458]. This work evaluated its time-dependent effects on mitochondrial oxygen consumption rate (OCR) of HepG2 cells by using the Seahorse XF-96 Extracellular Flux Analyzer (**Figure 14B**). To assess the effects of an acute treatment, AntiOxCIN$_4$ (100 μM) was injected into port A of the Seahorse XF-96 Extracellular Flux Analyzer. Additionally, HepG2 cells were previously incubated for 48 h with AntiOxCIN$_4$ (100 μM) before the assay (longer treatment protocol). AntiOxCIN$_4$ (100 μM) acute treatment reduced the basal (41.1 %), maximal (59.1 %) and non-mitochondrial (70.1 %) OCR, while no statistically significant changes were observed on the proton leak-related (152.6 %) and ATP production-linked (103.4%) OCR when compared with untreated cells (**Figure 14C-G**). Interestingly, long-term treatment with AntiOxCIN$_4$ (100 μM, 48 h), when compared with the acute treatment, resulted in equal or higher control values. In fact, an increase in basal (119.49%), maximal (37.6%), ATP-linked (65.5 %), and non-mitochondrial (53.4 %) was measured after 48h treatment. Moreover, AntiOxCIN$_4$ (100 μM) longer-term treatment significantly increasing basal (160.6 %), maximal (96.7 %) ATP-linked (169.0 %), and non-mitochondrial (123.5 %) OCR, while no changes were observed on the proton leak-related (144.2 %) OCR when compared with untreated cells (**Figure 14C-G**). To better understand how AntiOxCIN$_4$ influences the OCR, we evaluated the AntiOxCIN$_4$ time-dependent effects on the OCR of human HepG2 cells in culture media lacking glucose (OXPHOS$_m$) (**Figure 15**). The glucose-free and galactose / glutamine / pyruvate-containing culture medium forces cells to use oxidative phosphorylation (OXPHOS) as the primary source for energy synthesis [464].

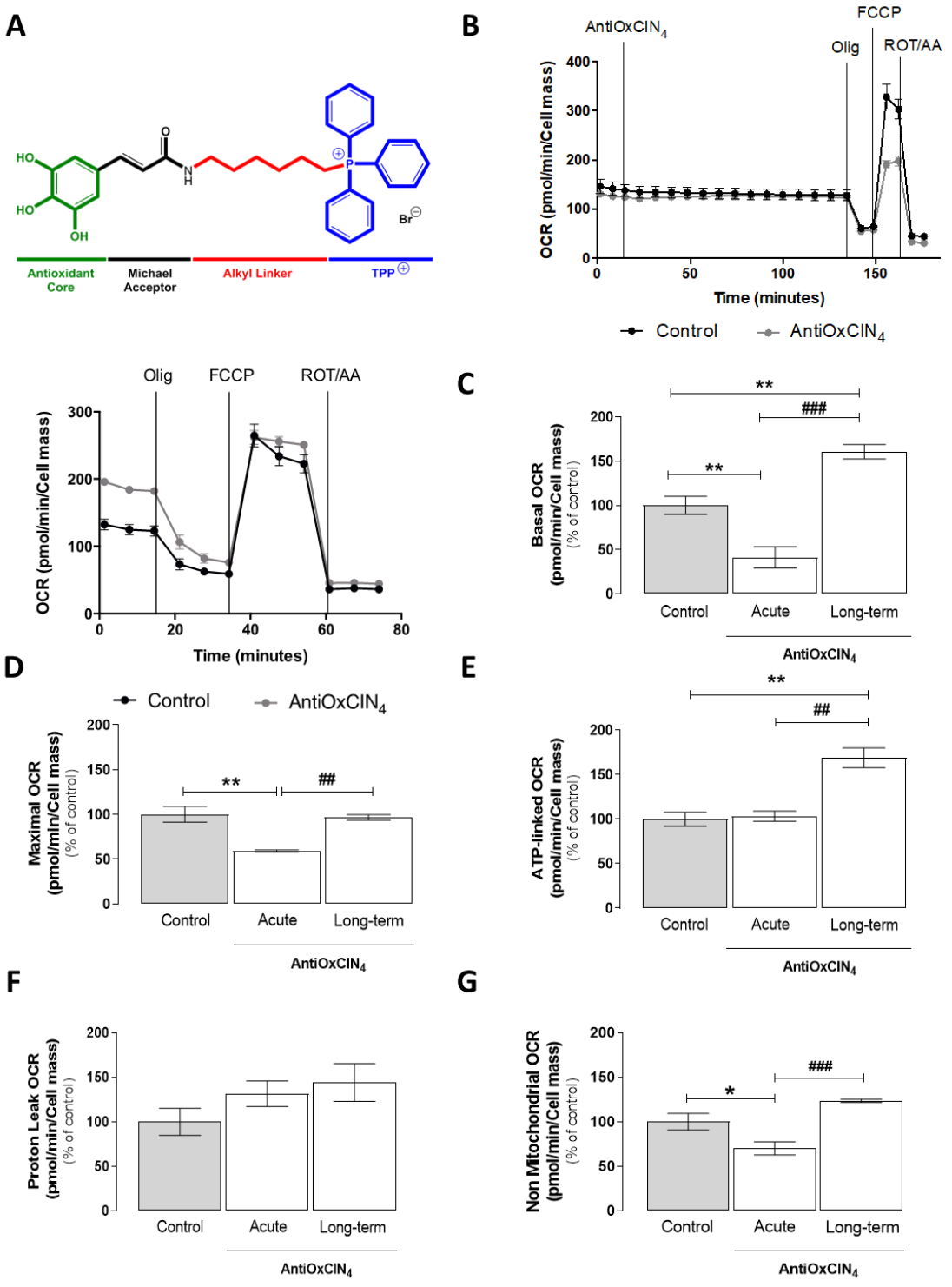

Figure 14. Transient impact of AntiOxCIN$_4$ on mitochondrial oxygen consumption of HepG2 cells. (**A**) Chemical structure of the hydroxycinnamic acid mitochondria-targeted antioxidant AntiOxCIN$_4$. (**B**) Representative image of oxygen consumption rate (OCR) measurement in HepG2 cells treated with vehicle (CT) or AntiOxCIN$_4$ (100 µM) acutely or for 48 h. Several respiratory parameters were evaluated: (**C**) cellular basal OCR; (**D**) maximal OCR; (**E**) ATP production-linked OCR; (**F**) proton leak-linked OCR; and (**G**) non-mitochondrial OCR. Data are mean ± SEM of four independent experiments, and the results are

expressed as pmol O_2/min/cell mass and normalized to the control condition (CTL = 100 %). The data obtained with AntiOxCIN$_4$ was compared to CTL using a two-way ANOVA with Tukey multiple comparison post-test. Significant differences between the indicated conditions are marked by *(p<0.05), **(p<0.01). Significant differences between acute and long-term incubations with AntiOxCIN$_4$ are marked by $^{\#\#}$(p<0.01), $^{\#\#\#}$(p<0.0005). Olig, Oligomycin A; FCCP, carbonyl cyanide-4-(trifluoromethoxy)phenylhydrazone; ROT, rotenone; AA, Antimycin A

In the OXPHOS$_m$, AntiOxCIN$_4$ effects on the cellular OCR were similar to those observed in low-glucose medium. AntiOxCIN$_4$ (100 µM) acute treatment reduced the cellular OCR, an effect that was not observed for AntiOxCIN$_4$ long-term treatment (48 h) (**Figure S15A-E**). Together, the data suggests that AntiOxCIN$_4$ induced a time-dependent remodeling of mitochondrial bioenergetics by modulating mitochondrial respiration.

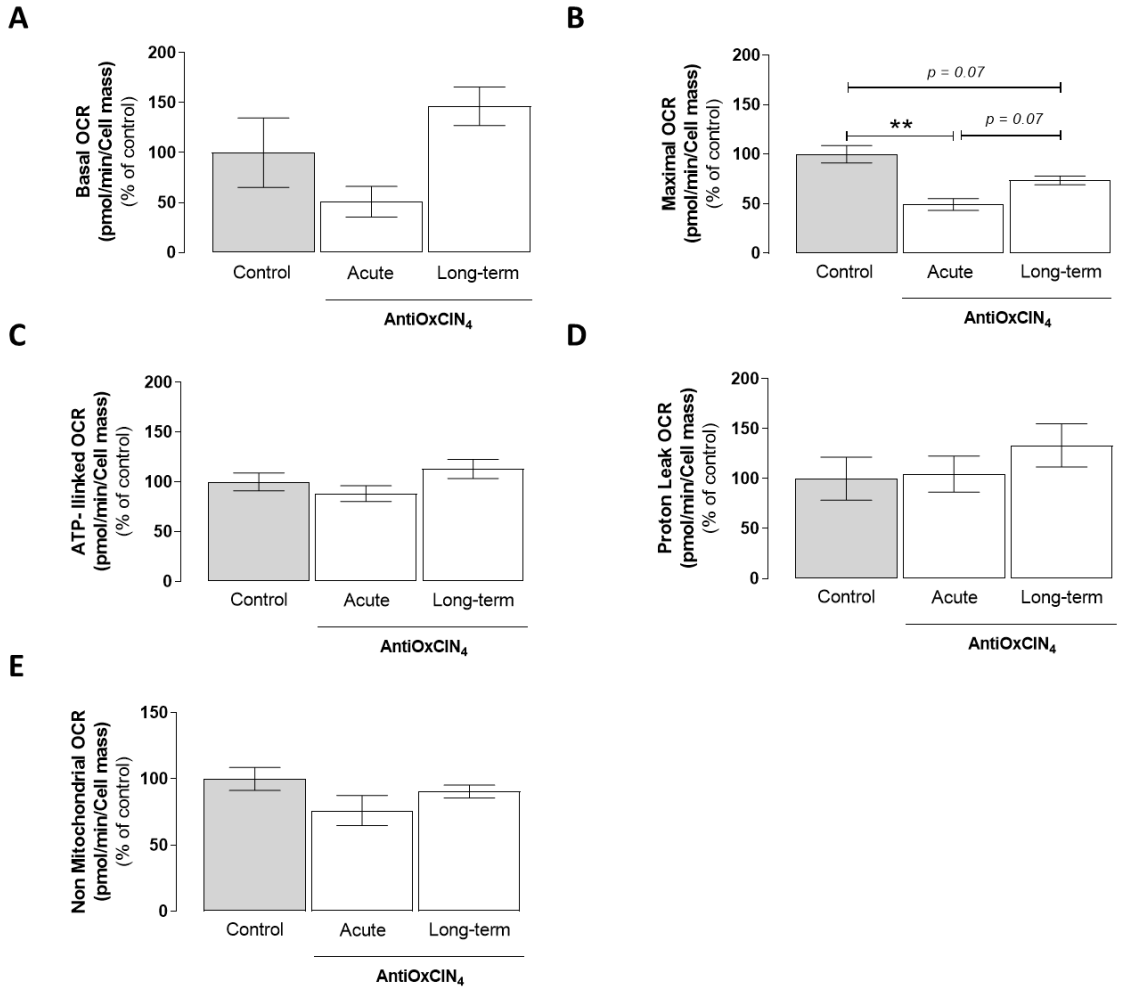

Figure 15. Transient impact of AntiOxCIN$_4$ on mitochondrial oxygen consumption of HepG2 cells in the absence of glucose (OXPHOS$_m$). (**A**) Basal oxygen consumption rate (OCR); (**B**) maximal OCR; (**C**) ATP production-linked OCR; (**D**) proton leak-linked OCR; and (**E**) non-mitochondrial OCR measurement in

HepG2 cells treated with vehicle (CTL) or AntiOxCIN$_4$ (100 µM) acutely or for 48 h in a glucose-free and galactose / glutamine / pyruvate containing culture medium (OXPHOS medium). Data are the mean ± SEM of four independent experiments, and the results are expressed as pmol O_2/min/cell mass and normalized to the control condition (CTL = 100 %) on time 0 h. The data obtained with AntiOxCIN$_4$ was compared to CTL using a one-way ANOVA with Dunnet multiple comparison post-test. Significant differences between the indicated conditions are marked by **($p<0.01$).

7.3.2. AntiOxCIN$_4$ stimulated mitochondrial function and increased extracellular acidification

Glycolysis products and Krebs cycle-derived CO_2 are the major contributors to extracellular acidification [516]. Thus, the impact on extracellular acidification of cells treated with AntiOxCIN$_4$ (100 µM; 48 h) was measured by evaluating lactate levels and appearance rate in the extracellular medium by ^{1}NMR (**Figure 16A**). Data showed that AntiOxCIN$_4$ treatment did not alter lactate levels (**Figure 16B**). Similarly, the lactate production rate (CTL; 0.0946 ± 0.006 mM/µg protein) remained unchanged by AntiOxCIN$_4$ treatment (100 µM; 48 h) (AntiOxCIN$_4$; 0.0959 ± 0.005 mM/µg protein) (**Figure 16C**). To confirm the impact of long-term treatment of AntiOxCIN4 (100 µM; 48 h) on the extracellular acidification rate (ECAR) of HepG2 cells, the Seahorse XF-96 Extracellular Flux Analyzer was used (**Figure 16D**). AntiOxCIN$_4$ significantly increased the glycolysis-associated ECAR (120.4 %) and non-glycolytic ECAR (116.3 %) (**Figure 16E-F**). Taken together, these results suggest that the increase in extracellular acidification may be due to an improved mitochondrial function as no changes in lactate production were observed.

7.3.3. AntiOxCIN$_4$ did not alter AMP/ATP ATP/ADP ratios nor the cellular energy charge

To further clarify the energy state of treating HepG2 cells with AntiOxCIN$_4$ (100 µM; 48 h), we measured the intracellular AMP, ADP and ATP levels, and energy charge by using HPLC techniques. AMP/ATP (**Figure 16G**) and ATP/ADP (**Figure 16H**) ratios, as well as the cellular energy charge (**Figure 16I**) remained unchanged after AntiOxCIN$_4$ (100 µM; 48 h) treatment. Overall, these results suggest that AntiOxCIN$_4$ did not affect the cellular adenine nucleotide content.

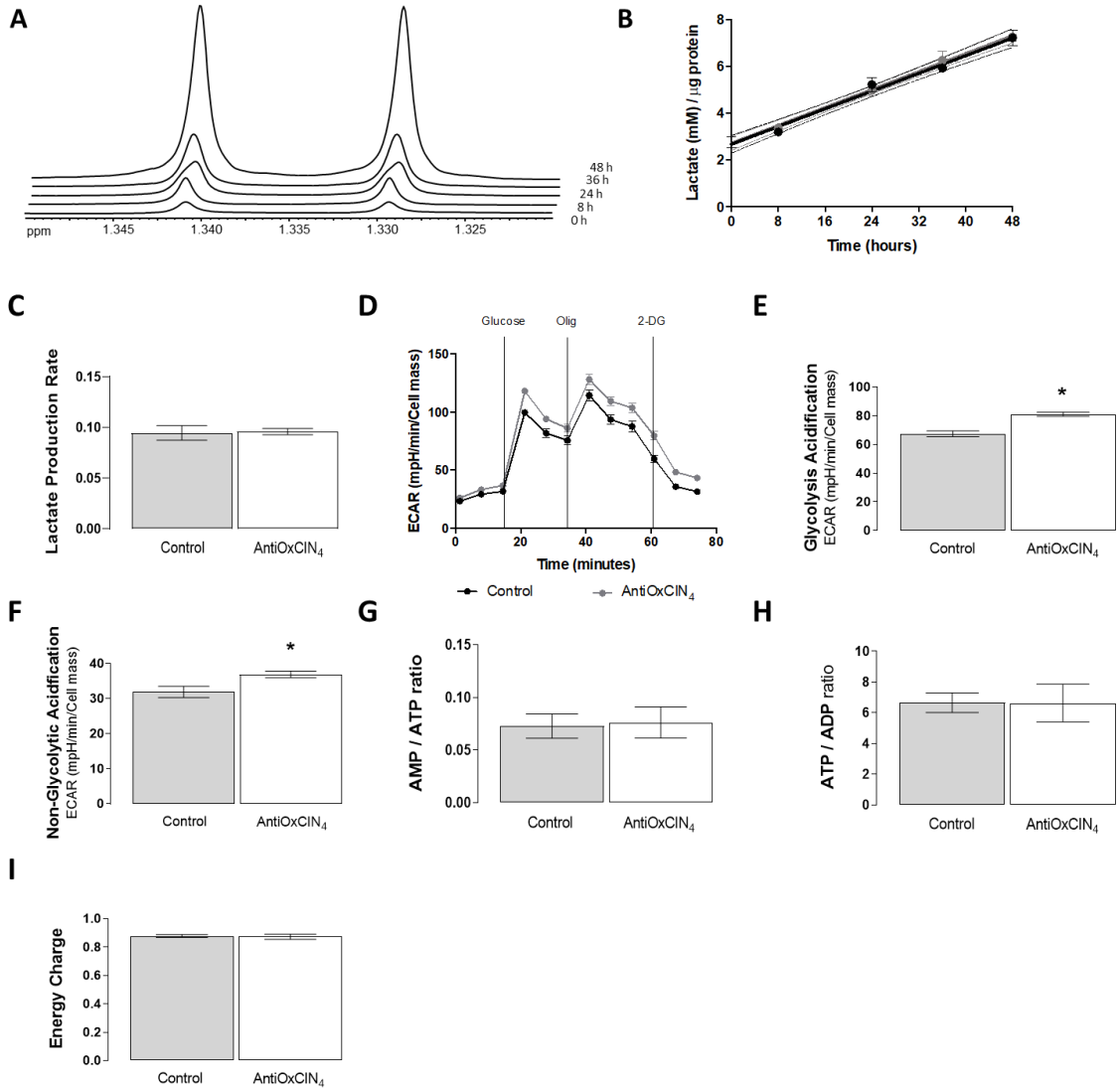

Figure 16. Effects of AntiOxCIN$_4$ on lactate levels, extracellular acidification, and energy status of HepG2 cells. (**A**) Evaluation of extracellular ^{1}H NMR lactate signals over time in HepG2 cells treated with AntiOxCIN$_4$ (100 µM). (**B**) Lactate levels in cells treated with AntiOxCIN$_4$ (100 µM) for various periods. Data are mean ± SEM of six independent experiments, and the results expressed as mM of lactate. (**C**) Lactate production rate of HepG2 cells treated with vehicle (CTL) or AntiOxCIN$_4$ (100 µM). The rate value was calculated by fitting the data with a linear regression equation for CTL (R^2=0.93) and AntiOxCIN$_4$ (R^2=0.96). (**D**) Typical representation of extracellular acidification rate (ECAR) measurement in HepG2 cells treated with vehicle (CTL) or AntiOxCIN$_4$ (100 µM) for 48 h. Several ECAR parameters were evaluated: (**E**) glycolysis; and (**F**) non-glycolytic acidification. Data are mean ± SEM of four independent experiments, and the results expressed as mpH/min/cell mass for ECAR. (**G**) [AMP]/[ATP], (H) [ATP]/[ADP] ratios and (**I**) Energy charge ([ATP] + 0.5 [ADP])/([ATP] + [ADP] + [AMP]) in HepG2 cells treated with AntiOxCIN$_4$ (100 µM) for 48 h. The data obtained with AntiOxCIN$_4$ was compared to CTL using the Student's t-test to compare two mean values. Significant differences between the indicated conditions are marked by

*(p<0.05).

7.3.4. AntiOxCIN$_4$ transiently increased mitochondrial reactive oxygen species (mtROS) levels

As alterations to normal mitochondrial metabolism and homeostasis are frequently associated with increased ROS production [493], we next quantified mitochondrial superoxide anion levels using a fluorescent reporter molecule (MitoSOX). Antimycin A (AA), an inhibitor of mitochondrial complex III, and the antioxidant N-Acetyl Cysteine (NAC) were used as positive and negative controls, respectively. As expected, AA (5 µM; 1 h) induced an increase in the oxidation rate of MitoSOX, which was significantly prevented in the presence of NAC (10 mM; 3 h) (**Figure 17**).

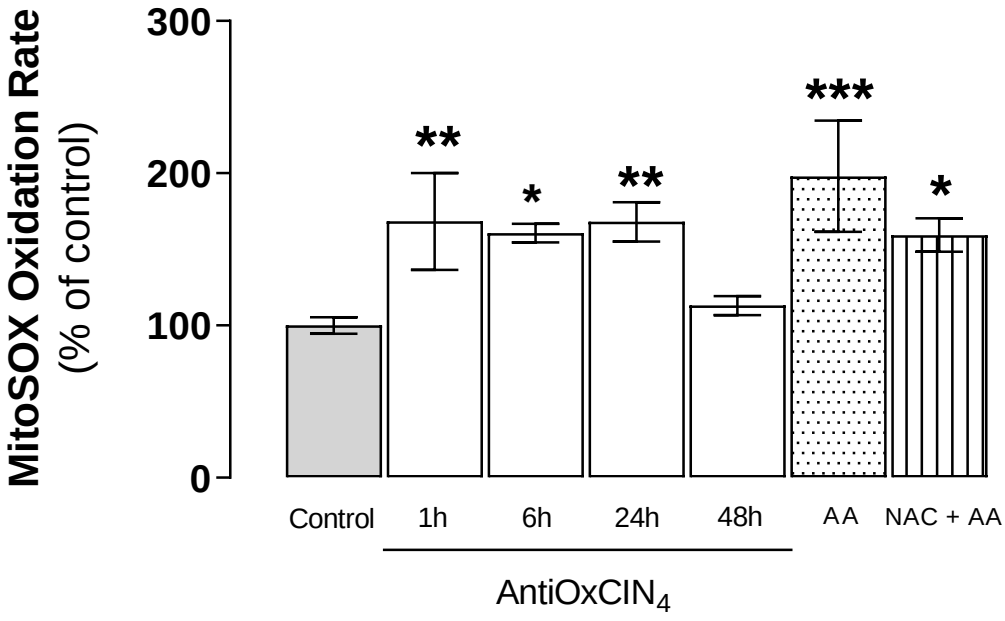

Figure 17. Transient impact of AntiOxCIN$_4$ on mitochondrial superoxide anion levels. Time-dependent variations on fluorescence signal of MitoSOX-oxidation products in HepG2 cells treated with vehicle (CTL) or AntiOxCIN$_4$ (100 µM). Data are mean ± SEM of 3-4 independent experiments, and the results normalized on the control condition (CTL = 100 %). The data obtained with AntiOxCIN$_4$ was compared to CTL using the Student's t-test to compare two mean values. Significant differences between the indicated conditions are marked by *(p<0.05), **(p<0.01), ***(p<0.0005).

Interestingly, AntiOxCIN$_4$ induced a rapid (~180 %) transient increase in the MitoSOX oxidation rate, which was maintained until the 24 h time-point, and returned

to control levels at the 48 h time-point (**Figure 17**). Despite the data, no increase in malondialdehyde (MDA) levels, a marker of lipid peroxidation, was observed (**Figure 18A**).

7.3.5. AntiOxCIN$_4$ did not induce pro-apoptotic cell hallmarks

As the ROS produced by mitochondria can trigger cell death due to mitochondrial disruption [517], we next whether AntiOxCIN$_4$-induced increase in superoxide anion (mtROS) was accompanied by decreased cell mass, metabolic activity and increased caspase-like activity. Despite the mild increase in superoxide anion levels, AntiOxCIN$_4$ did not alter cell metabolic activity or cell mass (**Figure 18B**) or caspase 3- and 9-like activity (**Figure 18C**) of HepG2 cells. The data suggest that AntiOxCIN$_4$ transient induction in superoxide anion levels was not detrimental and triggered cells' adaptive response.

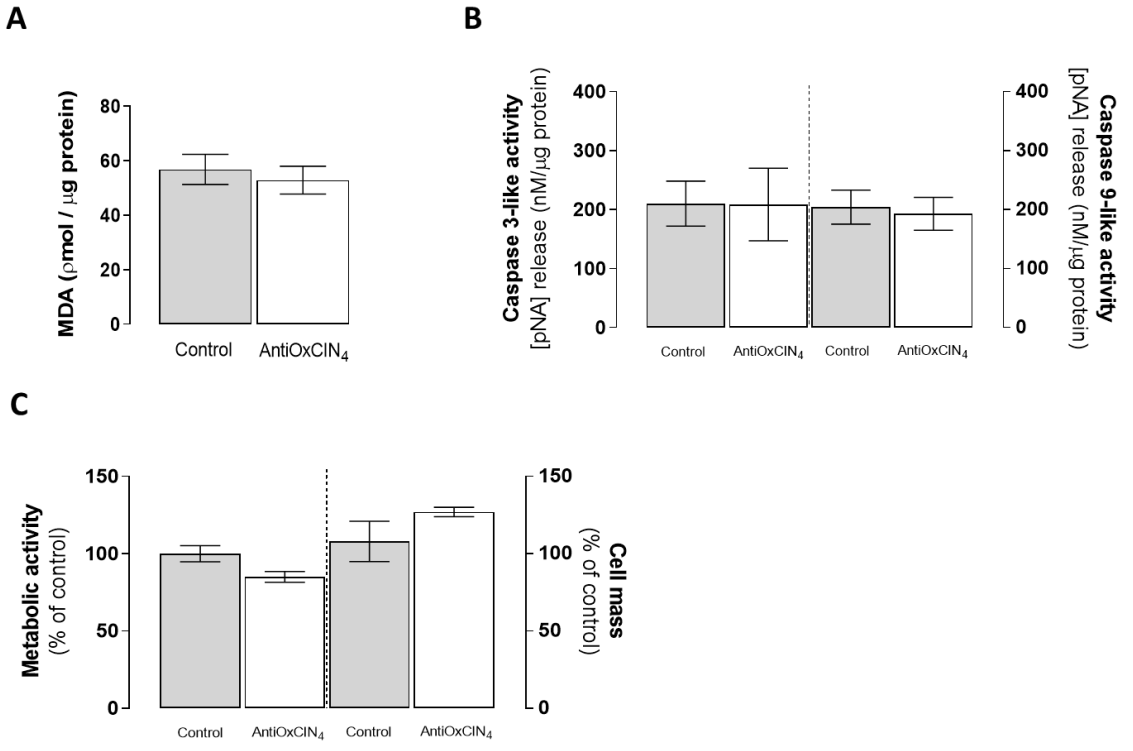

Figure 18. Effects of AntiOxCIN$_4$ on cell metabolic activity and mass, malondialdehyde (MDA) levels and caspase-like activity of HepG2 cells. (**A**) Malondialdehyde (MDA) levels in HepG2 cells treated with vehicle (CTL) or AntiOxCIN$_4$ (100 μM) for 48h. Data are the mean ± SEM of four independent experiments, and the results are expressed as pmol of MDA/μg protein. (**B**) Caspase 3- and 9-like activity in HepG2 cells

treated with vehicle (CTL) or AntiOxCIN$_4$ (100 μM) for 48h. Data are the mean ± SEM of four independent experiments, and the results are expressed as the concentration of pNA released per μg protein. (**C**) Cellular metabolic activity and mass of HepG2 cells treated with vehicle (CTL) or AntiOxCIN$_4$ (100 μM) for 48h. Data are the mean ± SEM of four independent experiments, and the results normalized on the control condition (CTL = 100 %). The data obtained with AntiOxCIN$_4$ was compared to CTL using the Student's t-test for comparison of two mean values.

7.3.6. AntiOxCIN$_4$ induced a ROS-dependent Nrf2 activation

Under regulated amounts, ROS can also display a physiological role as mediators in signal transduction pathways. Given the transient effects of AntiOxCIN$_4$ on mtROS (superoxide anion) levels, we determined whether AntiOxCIN$_4$ (100 μM) treatment altered Nrf2 protein levels in both nuclear and cytosolic cellular fractions.

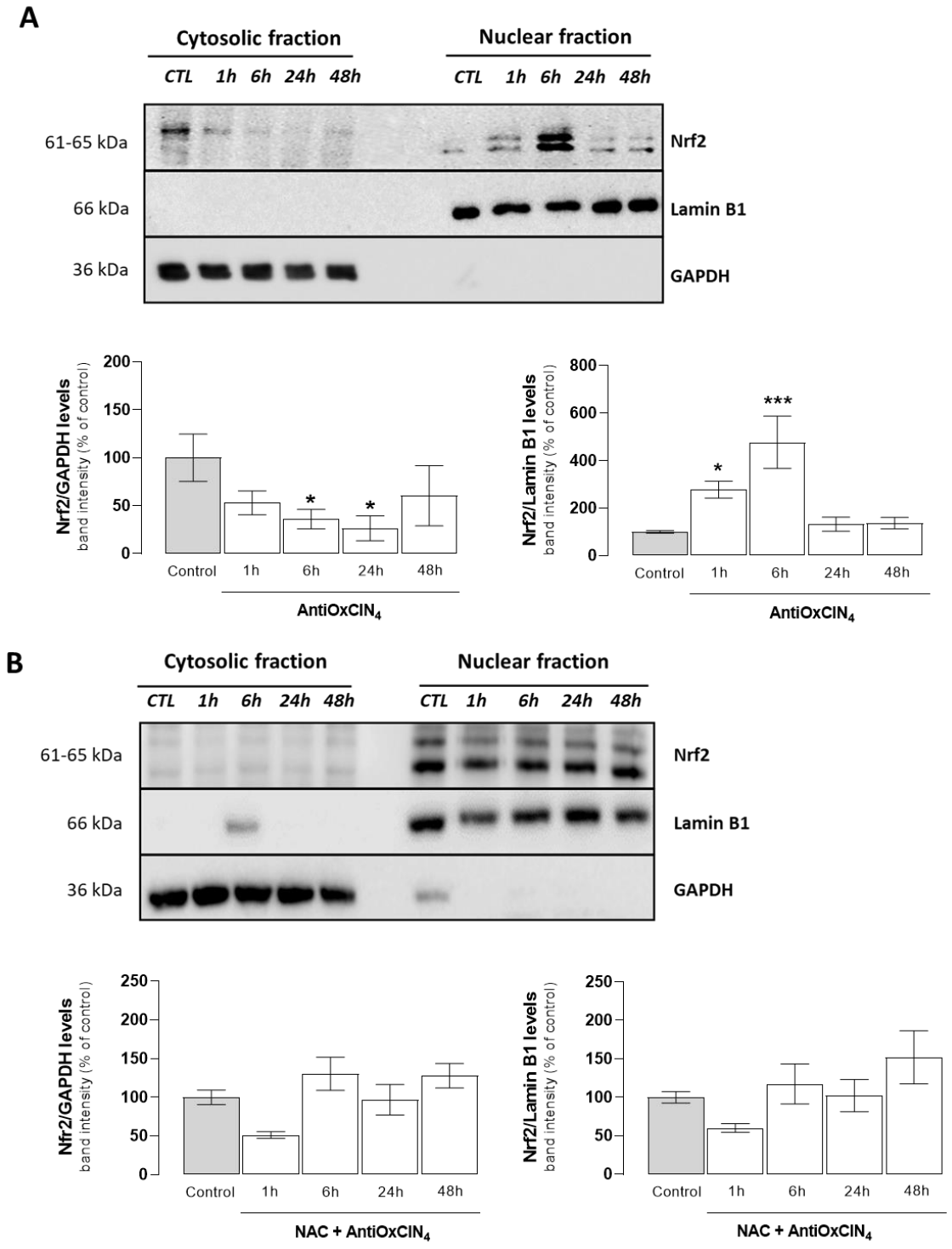

Figure 19. Effects of AntiOxCIN$_4$ on Nrf2 activation. (**A**) Typical Western blot result depicting the time-dependent content of Nrf2, GAPDH (cytosolic marker), and Lamin B1 (nuclear marker) proteins in nuclear and cytosolic compartments of cells treated with vehicle (CTL) or AntiOxCIN$_4$ (100 μM). These blots were inverted and contrast-optimized for visualization purposes. Quantification of the bands was performed using the original blots. Quantification of Nrf2 protein levels in three independent experiments was normalized to Lamin B1 and GAPDH, for nuclear and cytosolic quantification, respectively. (**B**) Typical

Western blot result depicting the time-dependent content of Nrf2, GAPDH (cytosolic marker), and Lamin B1 (nuclear marker) protein level in nuclear and cytosolic compartments. HepG2 cells were pre-incubation with NAC (10 mM, 3 h) and then challenged with AntiOxCIN$_4$ (100 µM, 48 h). These blots were inverted and contrast-optimized for visualization purposes. Quantification of the bands was performed using the original blots. Quantification of Nrf2 protein levels in three independent experiments was normalized to Lamin B1 and GAPDH, for nuclear and cytosolic quantification, respectively. The data obtained with AntiOxCIN$_4$ was compared to CTL using the Student's t-test to compare two mean values. Significant differences between the indicated conditions are marked by *($p<0.05$), ***($p<0.0005$).

Western Blot analysis revealed a time-dependent increase in Nrf2 protein content in nuclear fractions, which peaked at 6 h (477.0 %) and returned to normal after 48 h (136.7 %) (**Figure 19A**). These variations in nuclear Nrf2 protein content occurred with decreased protein levels in the cytosolic fractions (**Figure 19A**). Subsequently, we used the antioxidant NAC to investigate the role of AntiOxCIN$_4$-induced increase in superoxide anion in Nrf2 activation. Cells were pre-treated with NAC (10 mM; 3 h) before AntiOxCIN$_4$ treatment. Interestingly, co-incubation with NAC blurred the time-dependent variation of Nrf2 protein content in both nuclear and cytosolic fractions (**Figure 19B**). Together, these results suggest that activation of Nrf2 during AntiOxCIN$_4$ treatment depends on mROS (superoxide anion) transient increase, possibly by triggering an adaptive antioxidant response in HepG2 cells.

7.3.7. AntiOxCIN$_4$ activated the KEAP1-Nrf2-p62/SQSTM1 pathway during selective autophagy

KEAP1/Nrf2 signaling plays a vital role in protecting cells from oxidative stress [518]. Moreover, the p62/SQSTM1 (sequestosome 1) protein, which behaves as a cargo receptor for autophagic degradation of ubiquitinated targets, is overexpressed by various stressors and can act in a positive feedback loop within the KEAP1/Nrf2/p62 axis [379]. To determine whether Nrf2 activation by AntiOxCIN$_4$ alters autophagy fluxes, we measured protein levels of KEAP1, p62/SQSTM1, LC3BII, LC3BI, Beclin-1, and ATG5 by Western Blot.

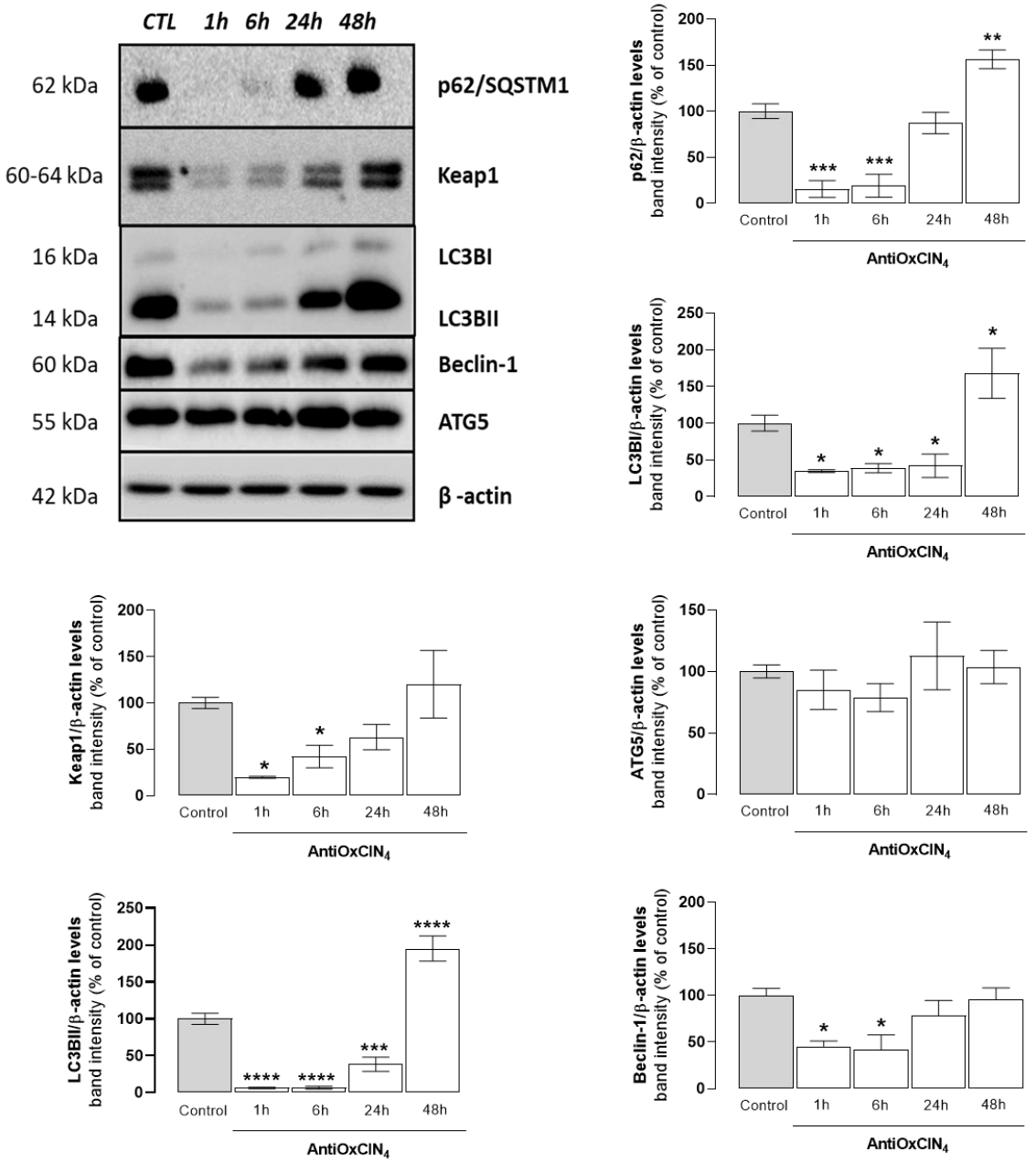

Figure 20. Effects of AntiOxCIN$_4$ on ROS-induced autophagy via a KEAP1/Nrf2/p62 positive feedback loop. Typical Western blot result of whole-cell homogenates depicting the time-dependent variations in the p62, KEAP1, LC3B-I, LC3B-II, Beclin-1, ATG5 and β-actin (cytosolic marker) protein levels in cells treated with vehicle (CTL) or AntiOxCIN$_4$ (100 µM). This blot was inverted and contrast-optimized for visualization purposes. Quantification of the bands was performed using the original blots. Quantification of protein levels in three independent experiments was normalized to β-actin levels and control conditions (CTL = 100 %). The data obtained with AntiOxCIN$_4$ was compared to CTL using a one-way ANOVA with Dunnet multiple comparison post-test, while Student's t-test was used to compare two mean values. Significant differences between the indicated conditions are marked by *(p<0.05), **(p<0.01), ***(p<0.0005), ****(p<0.0001).

The results showed a time-dependent variation in p62, KEAP1, LC3BI and LC3BII, and Beclin-1 protein content. These protein levels reached the lowest value after 6 h (15.4 %; 19.9 %; 38.7 %; 3.9 % and 41.8 %, respectively) and returned to normal or higher than control cells after 48 h (**Figure 20**). Interestingly, LC3BI (280.3 %), LC3BII (317.0 %), and p62/SQSTM1 (156.3 %) protein levels were significantly increased after 48 h of AntiOxCIN$_4$ treatment when compared with untreated cells (**Figure 20**). The data suggested that AntiOxCIN$_4$ induces selective autophagy upon Nrf2 activation that could lead to later macroautophagy.

The impact of AntiOxCIN$_4$ on autophagic flux was also measured by evaluating LC3BII protein levels in the presence or absence of an autophagy inhibitor (chloroquine; 100 µM, 6 h) or activator (rapamycin; 100 nM, 5 h). Both chloroquine and rapamycin significantly increased LC3BII protein level (500% and 200%, respectively). By itself, AntiOxCIN$_4$ also significantly increased the LC3BII protein level (250 %), an effect that was significantly more pronounced in the presence of chloroquine (± 600 %) but not in the presence of rapamycin (± 250 %) (**Figure 21**). AntiOxCIN$_4$ presented a similar outline as rapamycin when considering LC3BII protein level.

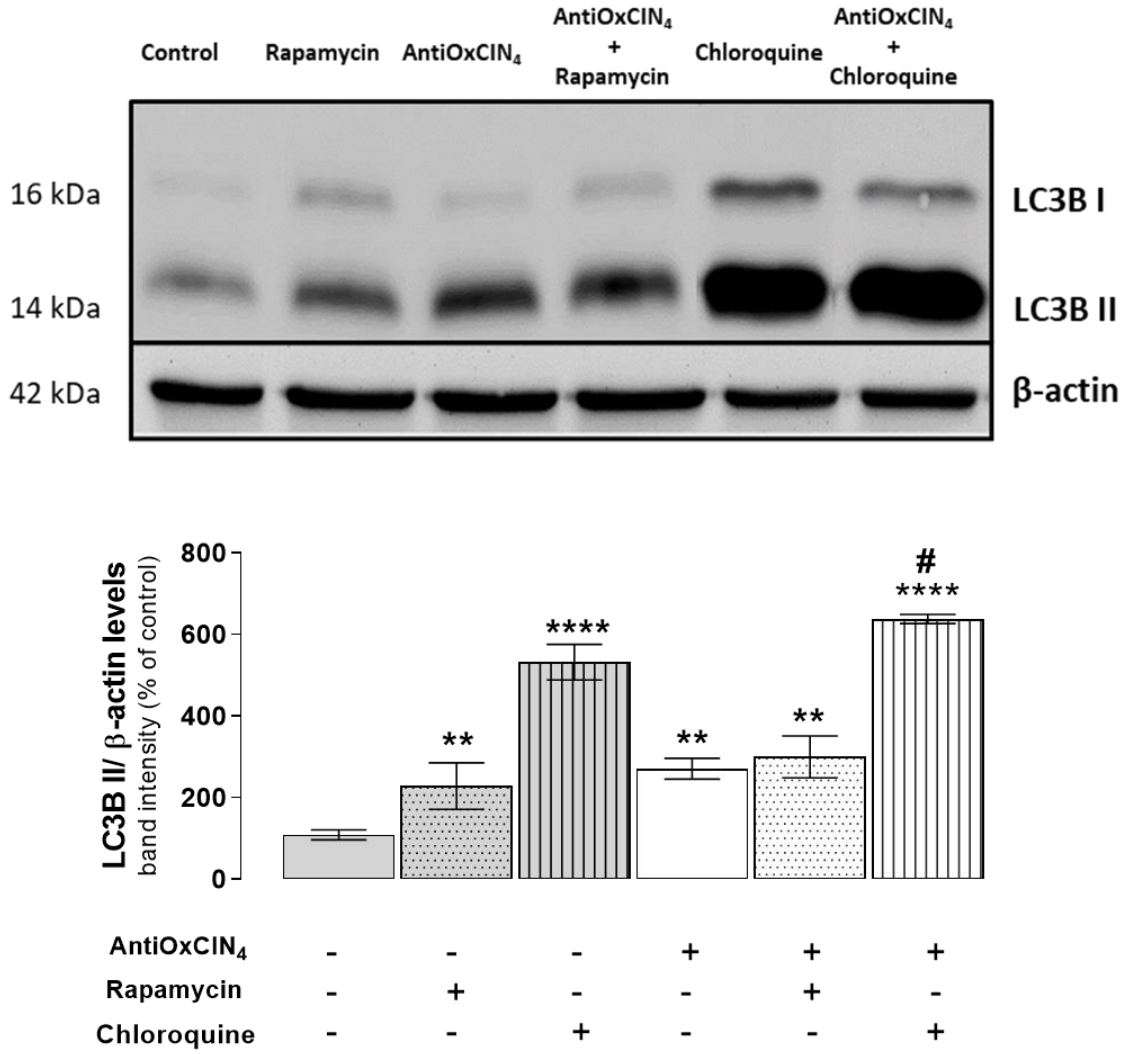

Figure 21. Effects of AntiOxCIN4 on autophagic flux. Typical Western blot result of whole-cell homogenates depicting the protein level of LC3-I, LC3B-II and β-actin (cytosolic marker) in cells treated with vehicle (CTL) or AntiOxCIN4 (100 µM) for 48 h in the presence or absence of rapamycin (100 nM; 5 h) or chloroquine (100 µM; 6 h). This blot was inverted and contrast-optimized for visualization purposes. Quantification of the bands was performed using the original blots. Quantification of protein levels in 3-6 independent experiments was normalized to β- actin levels and control conditions (CTL = 100 %). The data obtained with AntiOxCIN4 was compared to CTL using a one-way ANOVA with Dunnet multiple comparison post-test, while Student's t-test was used to compare two mean values. Significant differences between the indicated conditions are marked by **($p<0.01$), ****($p<0.0001$). Significant differences between AntiOxCIN4 and AntiOxCIN4 + chloroquine are marked by $^{\#}$($p<0.05$).

7.3.8. AntiOxCIN$_4$ increased lysosomal particles, mitochondrial network area, and mitochondrial co-localization within cells

Mitochondrial autophagy (mitophagy) is essential for maintaining mitochondrial quality by eliminating dysfunctional mitochondria [147]. Although no single parameter is sufficient to demonstrate mitophagy unequivocally, we investigated the co-localization of Lysotracker red-labeled acidic bodies with Mitotracker Green-labeled mitochondria. This approach may be useful to indicate the initial steps of mitophagy that can occur in the presence of AntiOxCIN$_4$ (100 µM; 48 h) (**Figure 22A**). Bafilomycin A1 (100 nM, 12 h), a known inhibitor of the latter stages of autophagy, and trichostatin A (2 µM, 12 h), a pan-histone deacetylase inhibitor that can stimulate mitophagy, were used as controls. AntiOxCIN$_4$ treatment increased the percentage of co-localization (145.9 %) of mitochondrial particles with lysosomal bodies, quantified using the Menders's coefficient. The percentage of multiple large lysosomes co-localized with the mitochondrial network significantly increased in the presence of trichostatin A (226.8 %). In the presence of bafilomycin A1, no Lysotracker red-labeled acidic bodies were observed, as expected (**Figure 22B**). As expected, bafilomycin A1 significantly decreased the number of lysosome particles (**Figure 22C**). Interestingly, AntiOxCIN$_4$ significantly increased the number of lysosome particles (154.1%), similarly to the effects observed after trichostatin A treatment (273.5 %). Moreover, AntiOxCIN$_4$ also improved the area of the mitochondrial network (126.7 %) compared to control cells (**Figure 22D**). We next investigated whether AntiOxCIN$_4$ (100 µM; 48 h) would affect mitophagy markers by semi-quantifying the protein levels of the mitophagy-related protein PINK1. Western Blot analysis revealed that AntiOxCIN$_4$ increased PINK1 protein levels at 48 h by about 165.0 % (**Figure 22E**) compared to untreated cells. Overall, the data suggest that auto(mito)phagy may be involved in the AntiOxCIN$_4$-induced cellular adaptive response.

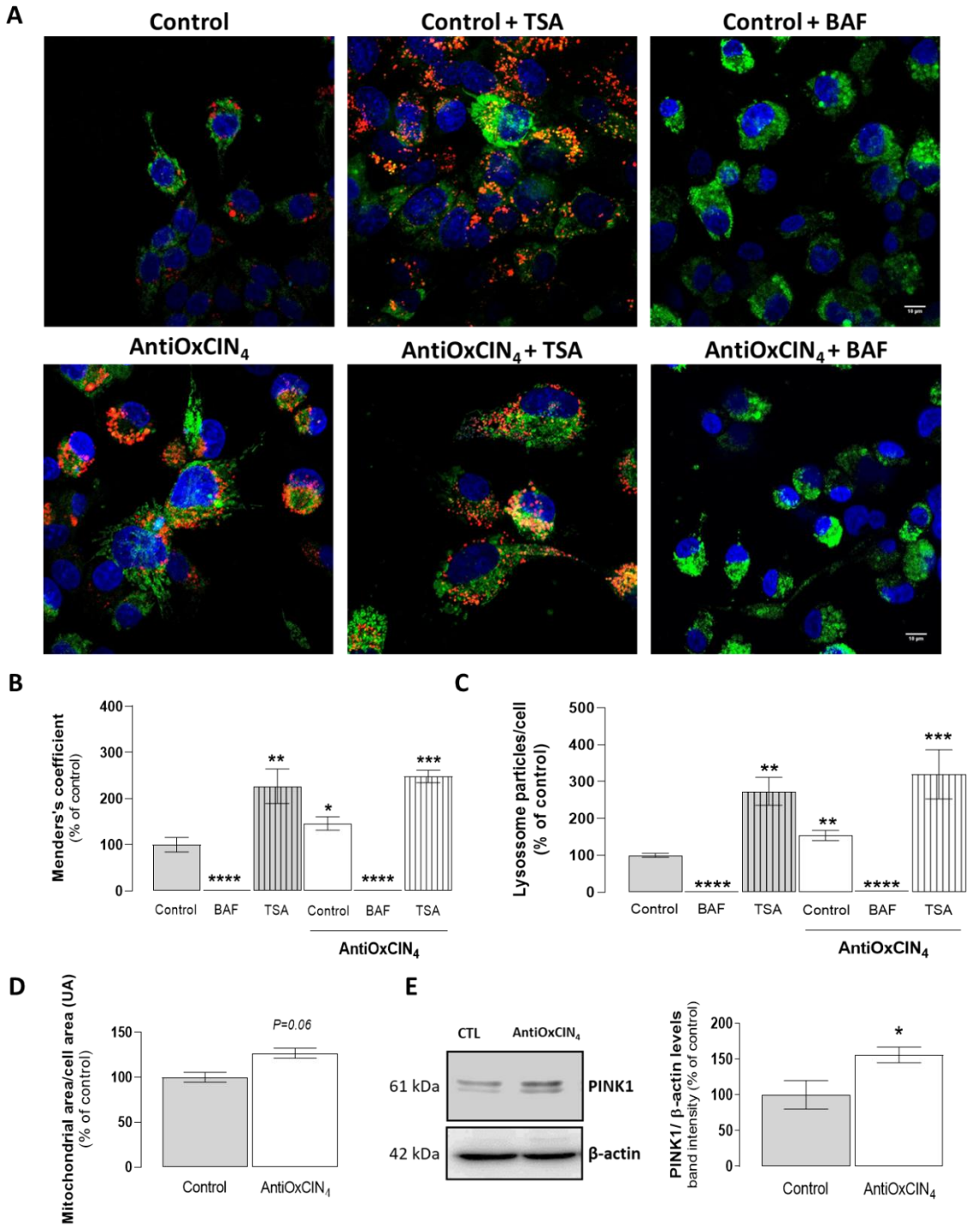

Figure 22. Effects of AntiOxCIN$_4$ on autophagy and mitophagy markers. (**A**) Typical background-corrected image of HepG2 cells stained with the fluorescent cation MitoTracker green, Lysotracker red, and Hoechst 33342 in cells treated with vehicle (CTL) or AntiOxCIN$_4$ (100 µM) for 48 h in the presence or absence of bafilomycin A1 (50 nM; 12 h) and trichostatin A (2 µM; 12 h). The MitoTracker Green, Lysotracker red, and Hoechst 33342 fluorescence intensities were color-coded to green, red and blue, respectively. (**B**) Co-localization of the mitochondrial network (labeled with MitoTracker green) and lysosomes (labeled with Lysotracker red) calculated from the images in cells treated with vehicle (CTL) or AntiOxCIN$_4$ (100 µM) for

48 h in the presence or absence of bafilomycin A1 (50 nM; 12 h) and trichostatin A (2 μM; 12 h). The Menders's coefficient (M2) was calculated by using *JACoP v2.0 Macro*. (**C**) Lysosome particles in HepG2 cells treated with vehicle (CTL) or AntiOxCIN$_4$ (100 μM) for 48 h in the presence or absence of bafilomycin A1 (50 nM; 12 h) and trichostatin A (2 μM; 12 h). The lysosome particles were calculated by using *MRI_Lipid_Droplets_Tool* Macro. (**D**) Mitochondrial network area (labeled with MitoTracker green) in HepG2 cells treated with vehicle (CTL) or AntiOxCIN$_4$ (100 μM) for 48 h. The mitochondrial network area was calculated by using Mitochondria Morphology Macro. Data are mean ± SEM of 4-6 independent experiments, and the results normalized on the control condition (CTL = 100 %). (**E**) Typical Western blot result of whole-cell homogenates depicting the protein level of PINK1 and β-actin (cytosolic marker) in cells treated with vehicle (CTL) or AntiOxCIN$_4$ (100 μM) for 48 h. This blot was inverted and contrast-optimized for visualization purposes. Quantification of the bands was performed using the original blots. Quantification of protein levels in 6 independent experiments was normalized to β-actin levels and to the control condition (CTL = 100 %). The data obtained with AntiOxCIN$_4$ was compared to CTL using a one-way ANOVA with Dunnet multiple comparison post-test, while Student's t-test was used to compare two mean values. Significant differences between the indicated conditions are marked by *($p<0.05$), **($p<0.01$), ***($p<0.0005$), ****($p<0.0001$). BAF, Bafilomycin A1; TSA, Trichostatine A.

7.3.9. AntiOxCIN$_4$ did not affect mRNA or protein levels relevant for mitochondrial fusion and fission

To further enhance our understanding of the cellular effects of AntiOxCIN$_4$ (100 μM; 48 h) on the mitochondrial dynamics hallmarks, the mRNA transcripts and protein levels of both fusion and fission key players were evaluated. Mitochondrial fusion is enabled by mitofusins 1 and 2 (MFN1 and MFN2) and optic atrophy 1 (OPA1), which mediate mitochondria outer membrane (OMM) and mitochondria inner membrane (IMM) fusion, respectively [147]. Moreover, human FIS1 promotes fission by acting as a negative regulator of the pro-fusion machinery [147]. AntiOxCIN$_4$ (100 μM; 48 h) did not alter mRNA levels either for *FIS1* or *MFN1*, *MFN2*, and *OPA1*, compared to untreated cells (**Figure 23A**). Similarly, the levels of FIS1 and MFN1 proteins remained unchanged (**Figure 23B**). The results suggest that in a longer-term treatment of AntiOxCIN$_4$ the levels of transcripts and/or proteins involved in mitochondrial dynamics were similar to those found in untreated cells.

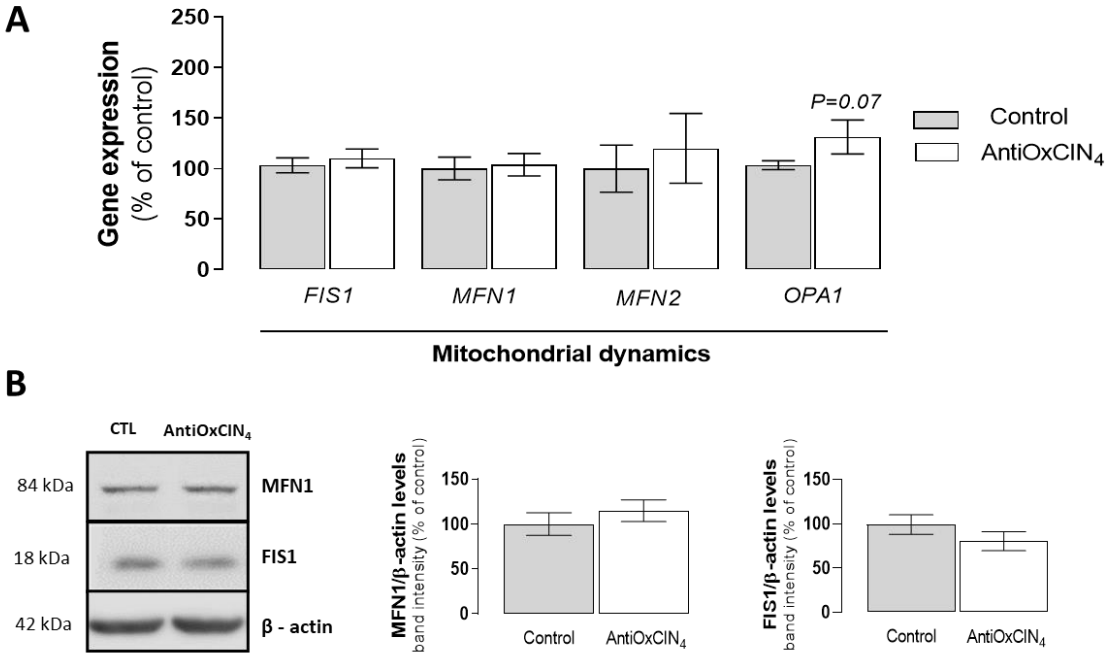

Figure 23. Effects of AntiOxCIN$_4$ on mitochondrial dynamics in HepG2 cells. (**A**) mRNA transcript levels of *FIS1*, *MFN1*, *MFN2*, and *OPA* genes in cells treated with vehicle (CTL) or AntiOxCIN$_4$ (100 μM) for 48 h. Data are the mean ± SEM of four independent experiments, and the results were normalized to *TBP*, *HPRT1* mRNA transcript levels and to the CTL condition (CTL = 100%). (**B**) Typical Western blot result of whole-cell homogenates depicting the protein level of MNF1, FIS1, and β-actin (cytosolic marker) in cells treated with vehicle (CTL) or AntiOxCIN$_4$ (100 μM) for 48 h. This blot was inverted and contrast-optimized for visualization purposes. Quantification of the bands was performed using the original blots. Quantification of protein levels in four independent experiments was normalized to β-actin levels and control conditions (CTL = 100%). The data obtained with AntiOxCIN$_4$ was compared to CTL using the Student's t-test for comparison of two mean values.

7.3.10. AntiOxCIN$_4$ increased mRNA transcript of mitochondrial biogenesis-associated hallmarks

Mitochondrial biogenesis is essential to maintain mitochondrial homeostasis, integrity, and regeneration of the mitochondrial network [519]. To understand the effects of AntiOxCIN$_4$ (100 μM; 48 h) on mitochondrial biogenesis hallmarks, key mRNA transcripts levels of key players were evaluated. AntiOxCIN$_4$ significantly increased the mRNA levels for *PPARGC1A* (204.4 %), *NRF1* (205.9%), and *GAPBA* (235.2 %) transcripts, when compared to untreated cells (**Figure 24A**). AntiOxCIN$_4$ also showed a slight increase of mRNA levels for *TFAM* (143.4 %) (**Figure 24A**) although the differences were

not statistically significant. The data suggest that the transcription of mitochondrial biogenesis-related proteins is activated upon AntiOxCIN$_4$ treatment.

7.3.11. AntiOxCIN$_4$ increased mitochondrial DNA (mtDNA) copy number

Mitochondrial biogenesis involves, among other processes, the replication of mtDNA molecules [520]. Our data indicate that AntiOxCIN$_4$ (100 μM; 48 h) significantly increased mtDNA copy number (130.3 %) when compared to untreated cells (**Figure 24B**). The data support the hypothesis that AntiOxCIN$_4$ may induce mitochondrial biogenesis.

7.3.12. AntiOxCIN$_4$ increased mitochondrial content in OXPHOS-related proteins

As OXPHOS function undergoes by dual genetic control of both the nuclear and mitochondrial genomes, we next evaluated whether the increased mitochondrial biogenesis-related signaling and mtDNA copy number were associated with an improved expression of different mitochondrial proteins involved in OXPHOS. To further understand the effects of AntiOxCIN$_4$ (100 μM; 48 h) on the mitochondrial OXPHOS system, mRNA transcripts and protein levels of OXPHOS complexes were evaluated. Measurement of mRNA levels for mitochondrial OXPHOS complexes transcripts showed a significant increase in complex V *ATP5G1* subunit (141.9 %) and mitochondrially encoded complex I *MT-ND5* subunit (126.1 %), while complex II *SDHA* (92.8 %), complex III *UQCRC2* (130.5 %), and complex IV *COX4i* (105.1 %) subunits remained unchanged (**Figure 24C**).

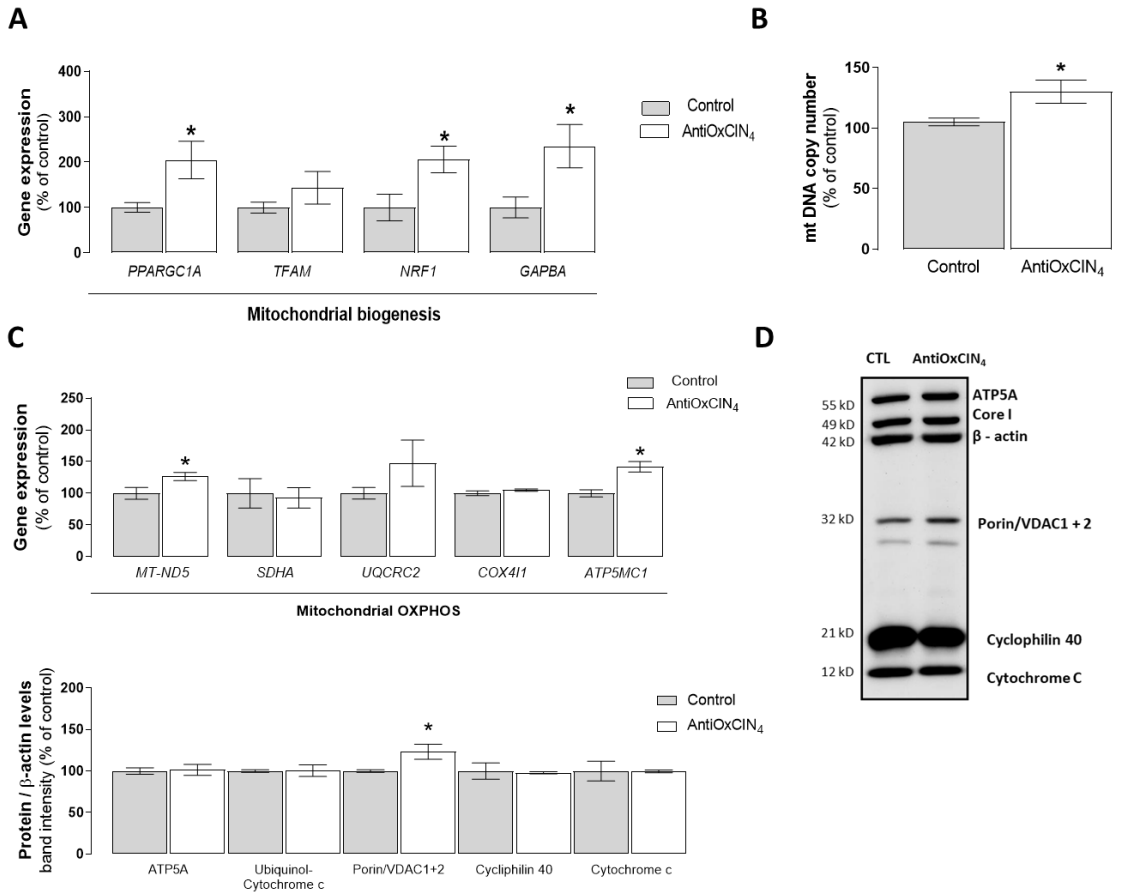

Figure 24. **Effects of AntiOxCIN$_4$ on mitochondrial biogenesis in HepG2 cells**. (**A**) mRNA transcript levels of *PPARGC1A, TFAM, NRF1*, and *GAPBA* genes in cells treated with vehicle (CTL) or AntiOxCIN$_4$ (100 µM) for 48 h. Data are the mean ± SEM of four independent experiments, and the results were normalized to TBP, HPRT1 mRNA transcript levels and the control condition (CTL = 100 %). (**B**) mtDNA copy number of HepG2 cellstreated with vehicle (CTL) or AntiOxCIN$_4$ (100 µM) for 48 h. mtDNA copy number was based on the amplification of cytochrome B (encoded on the mitochondrial genome) and β-2-microglobulin (encoded on the nuclear genome) ratio. Data are mean ± SEM of four independent experiments, and the results were normalized to the CTL condition (CTL = 100 %). (**C**) mRNA transcript levels of ND5 complex I, SDHA complex II, UQCRC2 complex III, COX4I1 complex IV, and ATP5MC1 complex V genes in cells treated with vehicle (CTL) or AntiOxCIN$_4$ (100 µM) for 48 h. Data are the mean ± SEM of four independent experiments, and the results were normalized to TBP, HPRT1 mRNA transcript levels and on the CTL condition (CTL = 100 %). (**D**) Typical Western blot result of whole-cell homogenates depicting the protein level of mitochondrial integrity associated proteins (ATP5A complex V, Ubiquinol cytochrome C reductase, Porin/VDAC 1+2, Cyclophilin 40 and Cytochrome C) and β-actin (cytosolic marker) in cells treated with vehicle (CTL) or AntiOxCIN$_4$ (100 µM) for 48 h. This blot was inverted and contrast-optimized for visualization purposes. Quantification of the bands was performed using the original blots. Quantification of protein levels in four independent experiments was normalized to β- actin levels and to the control condition (CTL = 100 %) The data obtained with AntiOxCIN$_4$ was compared to CTL using the Student's t-

test to compare two mean values and the one-way ANOVA with Dunnet multiple comparison post-test to compare more than two groups with one independent variable. Significant differences between the indicated conditions are marked by *($p<0.05$).

Noteworthy, western blot analysis revealed that AntiOxCIN$_4$ (100 μM; 48 h) significantly increased voltage-dependent anion channel (VDAC) protein content (123.2%), a non-specific solute carrier in the outer mitochondrial membrane when compared to untreated cells (**Figure 24D**). The data suggest that AntiOxCIN$_4$ up-regulates mRNA transcripts and protein levels of mitochondrial structures in HepG2 cells.

7.3.13. AntiOxCIN$_4$ induced mitochondrial membrane potential hyperpolarization

Mitochondrial stress induction and/or alterations in mitochondrial homeostasis directly impact mitochondrial membrane potential (ΔΨm) and morphology [521]. To determine whether AntiOxCIN$_4$ induced alterations on ΔΨm, HepG2 cells pre-incubated with AntiOxCIN$_4$ (100 μM; 48 h) were loaded with fluorescent cation TMRM in the presence or absence of oligomycin (ATP-synthase inhibitor; 2 μM, 30 min) or FCCP (OXPHOS uncoupler; 10 μM, 30 min) (**Figure 25A**). Oligomycin treatment resulted in a significant increase in TMRM fluorescence (207.1 %), while FCCP significantly decreased it (4.15 %), as expected (**Figure 25B**). AntiOxCIN$_4$ by itself also slightly increased TMRM fluorescence (140.9 %) but did not potentiate or aggravate oligomycin (218.7 %) or FCCP (2.05 %) effects (**Figure 25B**). These results demonstrate that under non-lethal conditions: (**i**) AntiOxCIN$_4$ significantly increased ΔΨm; (**ii**) AntiOxCIN$_4$ did not induce proton leak; and (**iii**) AntiOxCIN$_4$ did not show protonophoretic effects in HepG2 cells.

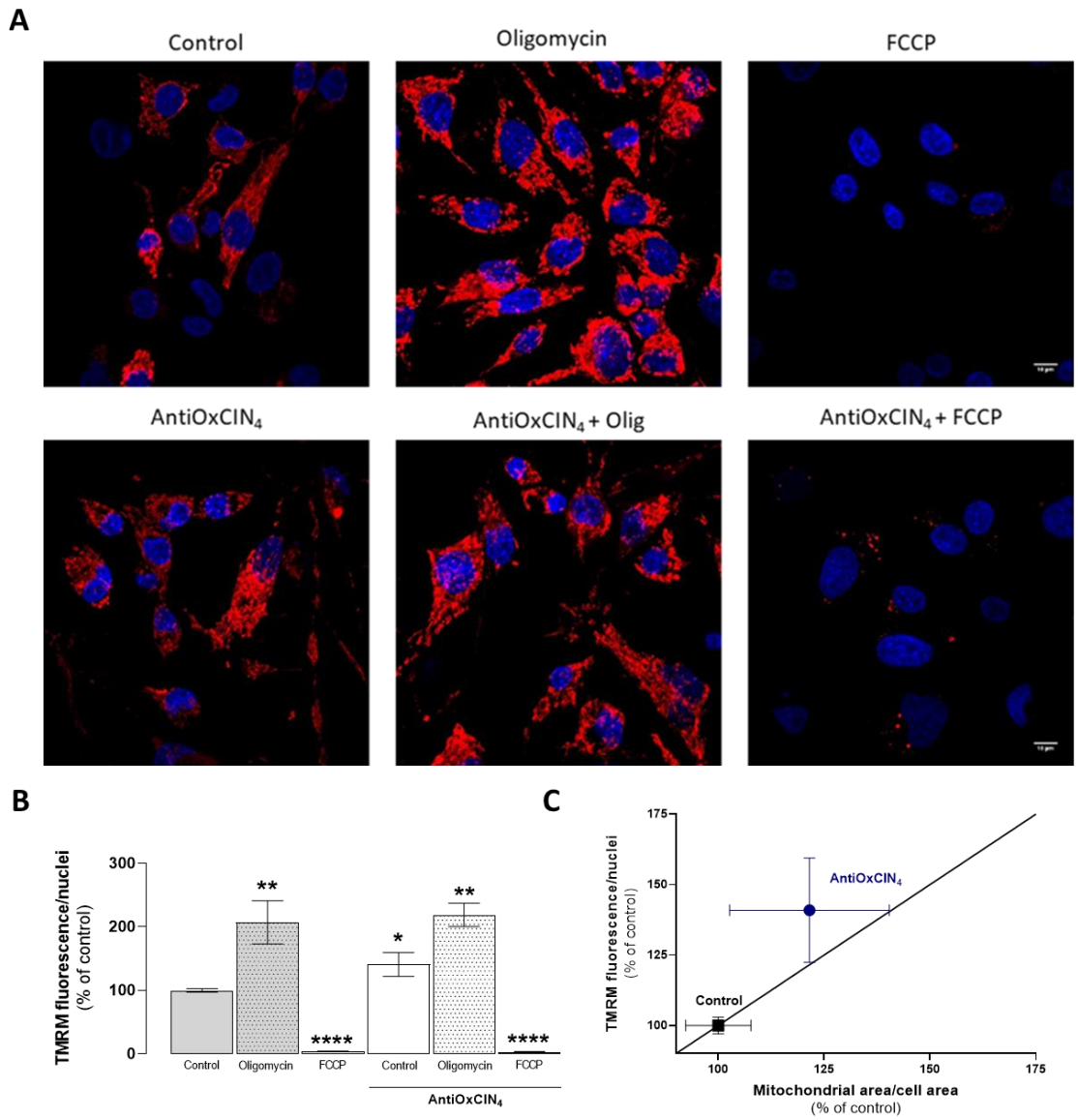

Figure 25. Effects of AntiOxCIN$_4$ on mitochondrial membrane potential in HepG2 cells. (**A**) Typical background-corrected image of HepG2 cells stained with the fluorescent cation TMRM and Hoechst 33342 in cells treated with vehicle (CTL) or AntiOxCIN$_4$ (100 µM) for 48 h in the presence or absence of oligomycin (2 µM; 30 min) and FCCP (10 µM; 30 min). The TMRM and Hoechst fluorescence intensity was color-coded to red and blue, respectively. (**B**) Average mitochondrial TMRM fluorescence intensity calculated from the images. Data are mean ± SEM of three independent experiments, and the results were normalized to the CTL condition (CTL = 100 %). (**C**) Average mitochondrial network area was plotted against the average TMRM fluorescence signal (data points taken from Figure **22D** and **25B**, respectively). An increase in both mitochondrial area and polarization was observed. The data obtained with AntiOxCIN$_4$ was compared to CTL using the Student's t-test to compare two mean values and the one-way ANOVA with Dunnet multiple comparison post-test to compare more than two groups with one independent variable. Significant

differences between the indicated conditions are marked by *(p<0.05), **(p<0.01), ****(p<0.0001). FCCP, carbonyl cyanide-4-(trifluoromethoxy)phenylhydrazone.

Moreover, we next plotted the average data of mitochondrial network area (data taken from **Figure 22D)** against the average TMRM fluorescence signal (data taken from **Figure 25B**). After performing a linear regression analysis of the average data, we observe that the data points for the AntiOxCIN$_4$ fell out of the straight line. This means that AntiOxCIN$_4$ treatment induced a non-proportional increase in both mitochondrial area and polarization (**Figure.** 2**5C**), suggesting that the mitochondriotropic antioxidant increased the number of mitochondria per cell and thereby mitochondrial mass and induced a hyperpolarization (higher ΔΨm) of the mitochondrial network in HepG2 cells.

7.3.14. AntiOxCIN$_4$ transiently increased the master regulator of mitochondrial biogenesis PGC-1α

The peroxisome proliferator-activated receptor-γ coactivator (PGC)-1α is the main regulator of mitochondrial biogenesis. Therefore, we determined whether AntiOxCIN$_4$ treatment altered the PGC-1α protein levels in both nuclear and cytosolic cellular fractions. Western blot analysis revealed that AntiOxCIN$_4$ (100 μM; 48 h), in a time-dependent manner, significantly increased the level of PGC-1α in the nuclear compartment, which reached its maximum after 6 h (7480.0 %) **(Figure 26)**. At the 48 h treatment point, AntiOxCIN$_4$ decreased PGC-1α protein levels relative to the 6h time-point, but still to a value higher than the control condition **(Figure 26).** No alterations were observed in PGC-1α protein levels in the cytoplasmic compartment **(Figure 26)**. The data reinforce the hypothesis that mitochondrial biogenesis is activated upon AntiOxCIN$_4$ treatment and that PGC-1α plays a central role in forming new mitochondria in AntiOxCIN$_4$-treated cells.

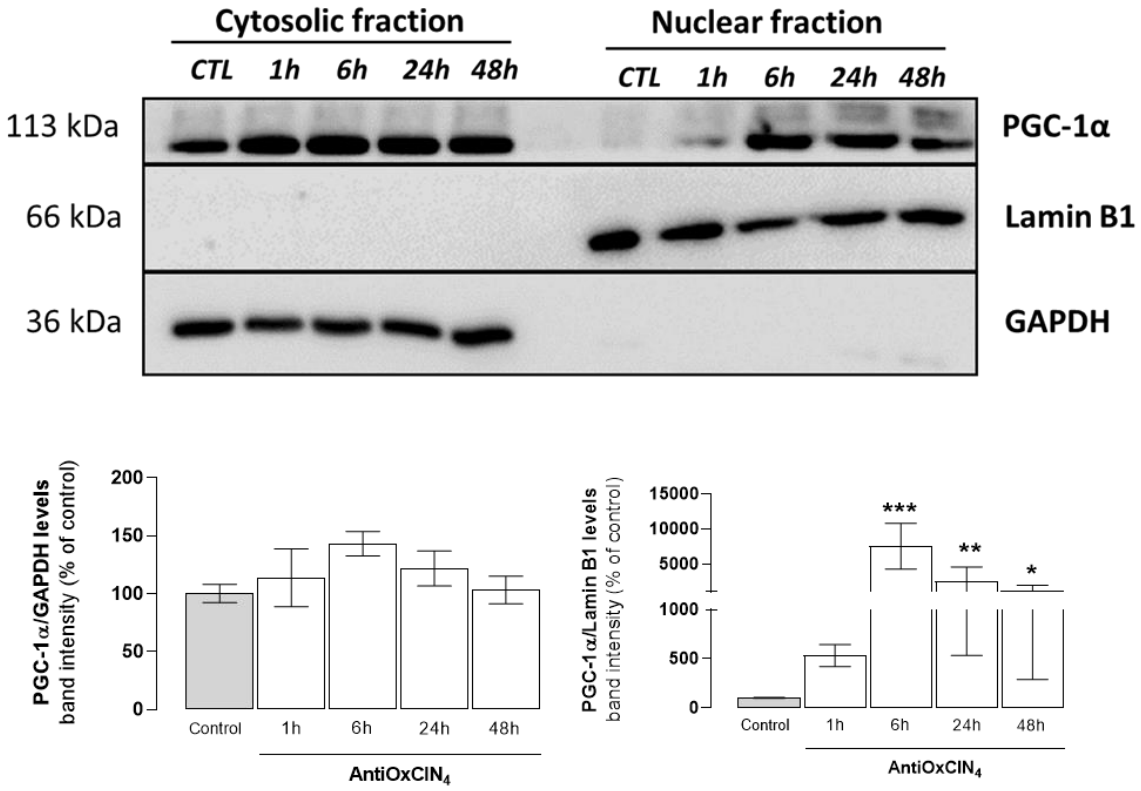

Figure 26. Effects of AntiOxCIN$_4$ on PGC-1α in HepG2 cells. Typical Western blot result depicting the time-dependent content of nuclear and cytoplasmic PGC-1α protein levels and, also, GAPDH (cytosolic marker) and Lamin B1 (nuclear marker) proteins in nuclear and cytosolic compartments in cells treated with vehicle (CTL) or AntiOxCIN$_4$ (100 μM) for 1, 6, 24 and 48 h. This blot was inverted and contrast-optimized for visualization purposes. Quantification of the bands was performed using the original blots. Quantification of protein levels in three independent experiments was normalized to β- actin levels and to the control condition (CTL = 100 %). The data obtained with AntiOxCIN$_4$ was compared to CTL using the Student's t-test to compare two mean values and the one-way ANOVA with Dunnet multiple comparison post-test to compare more than two groups with one independent variable. Significant differences between the indicated conditions are marked by *($p<0.05$), **($p<0.01$), ***($p<0.0005$).

7.3.15. AntiOxCIN$_4$ increased expression of Nrf2-regulated antioxidant genes *NQO1*, *HMOX1*

The redox regulation and coordination of Nrf2 in response to oxidative stress involve the induction of the expression of genes encoding antioxidant proteins [518]. So, we next investigated the cellular effects of AntiOxCIN$_4$ treatment (100 μM, 48 h) on mRNA transcripts levels linked to antioxidant genes associated with Nrf2 activation (e.g., HMOX1 and NQO1). AntiOxCIN$_4$ significantly increased *NQO1* (238.4 %) transcripts levels

compared to untreated cells (**Figure 27A**). AntiOxCIN$_4$ also increased the mRNA levels for *HMOX1* (159.5 %) (**Figure 27A**), although the differences were not statistically significant due to data dispersion. These results suggest that AntiOxCIN$_4$ may up-regulate the cellular antioxidant defenses by stimulating Nrf2-associated antioxidant genes.

7.3.16. AntiOxCIN$_4$ increased superoxide dismutase (SOD) and glutathione reductase (GR) activity

Superoxide dismutase (SOD), catalase (CAT), glutathione peroxidase (GPx) and glutathione reductase (GR) are the main enzymes in the first line of antioxidant defense against the formation or elimination of ROS within the cell [522]. Next, we measured the AntiOxCIN$_4$ (100 µM; 48 h) effects on the activity of antioxidant defense system. AntiOxCIN$_4$ significantly increased SOD (132.9 %) and GR (237.1 %) activity when compared to control cells, while no changes were observed in CAT and GPx enzymatic activity (**Figure 27B**).

7.3.17. AntiOxCIN$_4$ increased cellular glutathione and NAD(P)H content

Scavenging antioxidants, such as glutathione (GSH) or Vitamin E, are recognized as the group of endogenous antioxidants that can remove active radicals, therefore inhibiting chain initiation and breaking chain propagation reactions [523]. We next determined whether AntiOxCIN$_4$ induced alterations on cellular redox state, namely on GSH, nicotinamide adenine dinucleotide (NAD), and nicotinamide adenine dinucleotide phosphate (NADP) systems and vitamin (α-tocopherol) content. Interestingly, AntiOxCIN$_4$ (100 µM; 48 h) significantly increased the intracellular GSH/GSSG (117.8 %) (**Figure 27C**) and NADH/NAD$^+$ (129.3 %) ratios (**Figure 27D**). On the other hand, the NADPH/NADP$^+$ ratio was significantly reduced by AntiOxCIN$_4$ (83.7 %) (**Figure 27E**). AntiOxCIN$_4$ also increased vitamin E content in HepG2 cells (130.5 %), although the differences were not statistically significant (**Figure 27F**). These results support the hypothesis that non-lethal concentrations of AntiOxCIN$_4$ up-regulate both enzymatic and non-enzymatic endogenous antioxidant defense systems

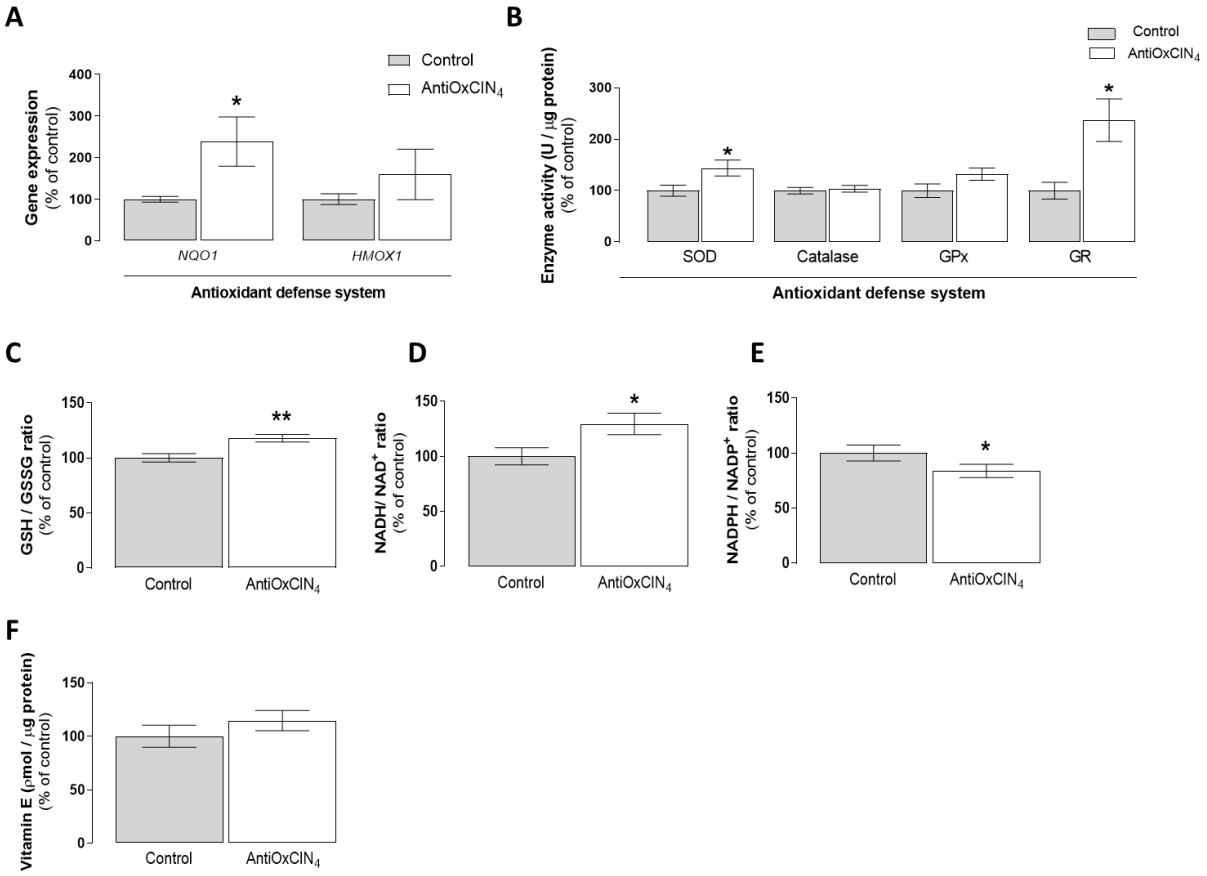

Figure 27. Effects of AntiOxCIN$_4$ on Nrf2-associated antioxidant genes and antioxidant (enzymatic and non-enzymatic) defense system during the cellular antioxidant response. (**A**) mRNA transcript levels of *NQO1*, *HMOX1* genes in cells treated with vehicle (CTL) or AntiOxCIN$_4$ (100 μM) for 48 h. Data are the mean ± SEM of four independent experiments, and the results were normalized to *TBP*, *HPRT1* mRNA transcript levels and to the CT condition (CTL = 100%). (**B**) Activity of enzymatic antioxidant defenses, including Superoxide Dismutase (SOD), Catalase, Glutathione Peroxidase (GPx), and Glutathione Reductase (GR) in cells treated with vehicle (CT) or AntiOxCIN$_4$ (100 μM) for 48 h. (**C**) GSH/GSSG ratio of HepG2 cells treated with vehicle (CT) or AntiOxCIN$_4$ (100 μM) for 48 h. (**D**) NADH/NAD$^+$ ratio of HepG2 cells treated with vehicle (CTL) or AntiOxCIN$_4$ (100 μM) for 48 h. (**E**) NADPH/NADP$^+$ ratio of HepG2 cells treated with vehicle (CTL) or AntiOxCIN$_4$ (100 μM) for 48 h. (**F**) α-tocopherol (vitamin E) levels in cells treated with vehicle (CTL) or AntiOxCIN4 (100 μM) for 48 h. Data are the mean ± SEM of four independent experiments, and the results normalized to the control condition (CTL = 100 %). The data obtained with AntiOxCIN$_4$ was compared to CTL using the Student's t-test for comparison of two mean values. Significant

differences between the indicated conditions are marked by *(p<0.05), **(p<0.01).

7.3.18. AntiOxCIN$_4$ decreases oxidative stress-induced and palmitic acid (PA)-induced cell damage

Oxidative stress-inducers, such as menadione, generate ROS through redox cycling, and high concentrations trigger cell death [524]. Moreover, exacerbated ROS production seems to be a determinant mediator in hepatocytotoxicity in fatty acid overload (e.g., palmitic acid) [525]. To test the hypothesis that AntiOxCIN$_4$-induced adaptative antioxidant response can protect cells against oxidative stress-induced damage, cells were exposed to insults of oxidative stress-induced and lipid overload-induced cell damage. Menadione (50 µM, 4 h), acting as a pro-oxidant via activation of NADPH oxidase, reduced the metabolic activity of HepG2 cells by about 50%, which was significantly prevented by AntiOxCIN$_4$ (100 µM, 48 h) (**Figure 28A**). Cells were also incubated with palmitic acid (PA; 500 µM, 6 h) to evaluate the potential of AntiOxCIN$_4$ (100 µM, 48 h) to prevent lipid-induced cell damage. PA treatment significantly increased lipid droplets (202.7 %) (**Figure 28C**), concomitant with a slight increase in metabolic activity (123.2 %) (**Figure 28B**), when compared with vehicle (BSA)-treated cells. Remarkably, AntiOxCIN$_4$ significantly prevented PA-induced lipid accumulation (159.6 %) (**Figure 28C**), while restoring the metabolic activity to vehicle (BSA) levels (**Figure 28B**). These results confirm that AntiOxCIN$_4$ pre-treatment protects cells from damage of oxidative stress insults.

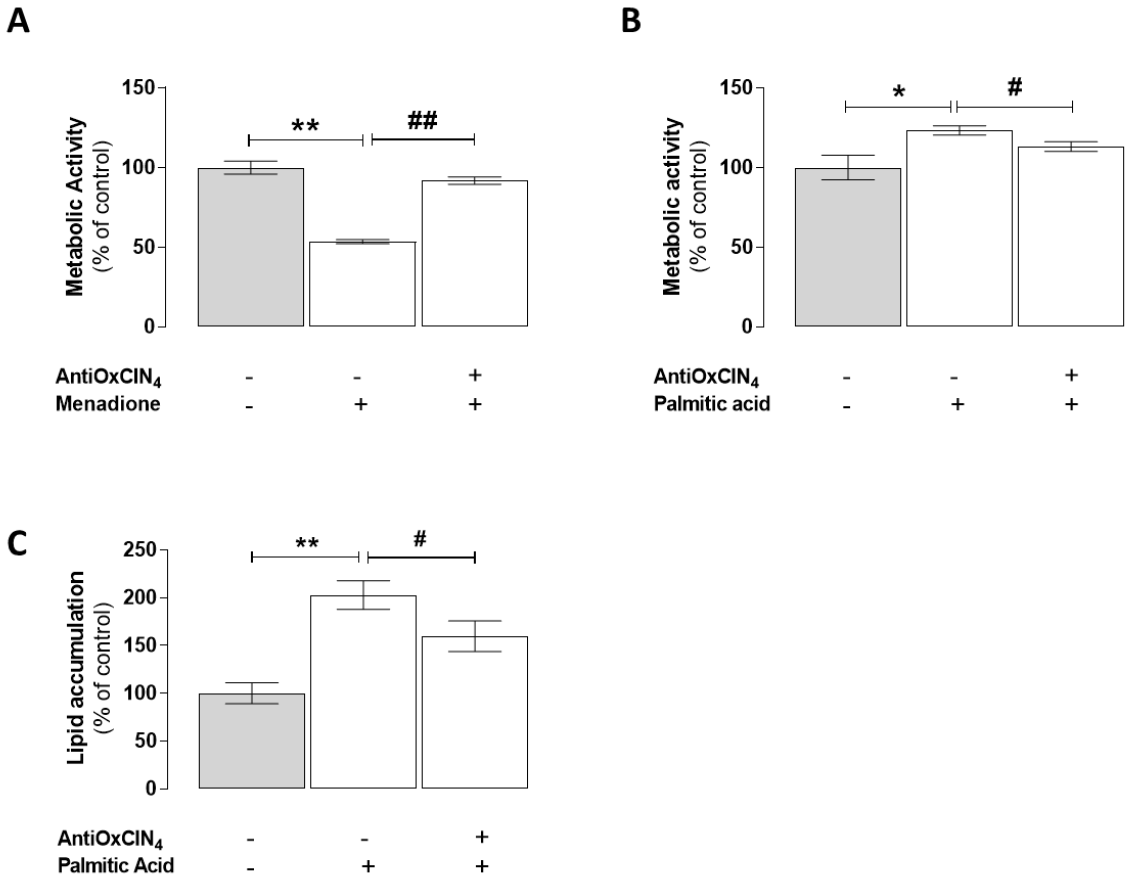

Figure 28. Effects of AntiOxCIN$_4$ on oxidative stress- and lipid overload-induced cell damage in HepG2 cells. (**A**) Effect of menadione (50 µM; 3h) on cell metabolic activity in the absence/presence of AntiOxCIN$_4$ (100 µM; 48 h). (**B**) Effect of palmitic acid (500 µM; 6 h) on metabolic activity in the absence/presence of AntiOxCIN$_4$ (100 µM; 48 h). (**C**) Effect of palmitic acid (500 µM; 6 h) on lipid accumulation in the absence/presence of AntiOxCIN$_4$ (100 µM; 48 h) Data are mean ± SEM of four independent experiments, and the results normalized on the control condition (CTL = 100 %). The data obtained with AntiOxCIN$_4$ was compared to CTL using a one-way ANOVA with Dunnet multiple comparison post-test, while Student's t-test was used to compare two mean values. Significant differences between the indicated conditions are marked by *($p<0.05$), **($p<0.01$). Significant differences between AntiOxCIN$_4$ and AntiOxCIN$_4$ + MEN/PA are marked by $^{\#\#}$($p<0.01$), $^{\#\#\#}$($p<0.0005$). PA, palmitic acid; MEN, menadione

7.4. Discussion

Polyphenolic antioxidants are one of the most important bioactive molecules obtained through diet. By conjugating the natural dietary caffeic acid with triphenylphosphonium cation (TPP^+), followed by structural optimization, we developed the mitochondriotropic antioxidant AntiOxCIN$_4$ (**Figure 14A**) [458, 459]. The

mitochondria-targeted antioxidant based on caffeic acid (AntiOxCIN$_4$) was shown remarkable antioxidant and iron chelation properties and rapidly accumulate within mitochondrial matrix of hepatic [458] and cardiac [497] mitochondria, protecting them from oxidative stress-induced mitochondrial lipid peroxidation and permeability transition pore opening [458]. In a cellular context, AntiOxCIN$_4$ (100 µM; 48 h) did not disturb mitochondrial morphology and polarization of HepG2 cells, preventing iron and hydrogen peroxide-induced cell damage probably due to its role in maintaining intracellular GSH homeostasis [458]. Moreover, analyses in human neuroblastoma (SH-SY5Y) cells revealed that non-toxic concentrations of AntiOxCIN$_4$ (100 µM; 48 h) prevented cell death induced by hydrogen peroxide (H_2O_2) or 6-hydroxydopamine (6-OHDA). Although designed as antioxidants, cell death protection conferred by AntiOxCIN$_4$ was paralleled by moderately increased ROS levels, suggesting that AntiOxCIN$_4$ can also act as prooxidant [459]. More recently, we also demonstrated that AntiOxCIN$_4$ (12.5 µM; 72 h) sustainably increased ROS levels, thereby activating endogenous ROS-protective pathways, such as the Nrf2/KEAP1 pathway, efficiently preventing PHSF cells against subsequent oxidative stress [460] and improving several cellular and mitochondrial metabolic parameters in PHSF from sporadic Parkinson disease patients (25 µM; 72 h) [461].

In this context, this study aimed to understand if the beneficial effects of AntiOxCIN$_4$ can be replicated in human hepatocytes, aiming to use this molecule in the context of NAFLD or other hepatic conditions. Moreover, this work was aimed to clarify the cellular mechanisms of action underlying the AntiOxCIN$_4$-induced coordinated cellular adaptative response, focusing on the activation of the Nrf2/KEAP1 pathway.

The present study showed that AntiOxCIN$_4$ sustainably increase mtROS levels, mainly superoxide anion levels, in HepG2 cells after an acute decrease in cellular OCR. Using a glucose-free and galactose / glutamine / pyruvate-containing culture medium (OXPHOS medium), we confirmed that AntiOxCIN$_4$ decreased mitochondrial oxygen consumption. Although mild increase of mitochondrial ROS (mtROS) production may play a role in initiating cell signaling pathways necessary for maintaining cell homeostasis [526, 527], exacerbated mtROS levels can promote mitochondrial membrane permeability (MMP), leading to mitochondrial dysfunction and ultimately cell death [517] being involved in the pathogenesis of many diseases. In this study, AntiOxCIN$_4$ did not affect cell

metabolic activity, mass, MDA levels, or pro-apoptotic caspase activity. Notably, an increased cellular oxygen consumption, paralleled by an increased extracellular acidification was observed in the longer treatment with AntiOxCIN$_4$ (100 µM, 48 h). Although extracellular acidification is frequently used to indirectly follow the glycolytic rate, mitochondrial-derived CO_2 from Krebs cycle, substantially contributes to extracellular acidification [516]. Altogether, the data strongly suggested an improvement of the mitochondrial function in AntiOxCIN$_4$ treated cells. Besides, AntiOxCIN$_4$ did not affect the pool of adenine nucleotides, suggesting a minimal, if any, impact on bioenergetic processes.

AntiOxCIN$_4$ accumulates within the mitochondrial matrix driven by the ΔΨm as it is positively charged at physiological pH. AntiOxCIN$_4$ acts as an effective chain-breaking antioxidant, probably by a proton-coupled electron-transfer process like other phenolic antioxidants. AntiOxCIN$_4$ radical scavenging activity is related to the *in situ* formation of a highly stabilized phenoxyl radical. The radical is stabilized by resonance, extended by conjugation with the α, β-unsaturated carbonyl system, and by the presence of intramolecular hydrogen bonds, coming from the participation of the pyrogallol moiety in the process [458, 528]. On the other hand, AntiOxCIN$_4$ contains a Michael acceptor substructure, the α, β-unsaturated carbonyl moiety, which can react with sulfhydryl groups of the cysteine residues of KEAP1, favoring Nrf2 nuclear translocation and Nrf2-ARE activation [529]. AntiOxCIN$_4$ balanced chemical properties are intrinsically related to the observed induced mild mitochondrial stress modulated by the Nrf2 activation and mediating beneficial cellular outcomes. The master regulator of the cellular antioxidant response to oxidative stress, Nrf2, is located in the cytosol, where it binds the specific inhibitor kelch-like ECH-associated protein1 (KEAP1). Upon stress conditions, a modification of KEAP1 in cysteine residues can occur, a process that can promote the disruption of Nrf2 from KEAP1 and its translocation to the nucleus to induce Nrf2-target gene expression [530]. We observed that AntiOxCIN$_4$ treatment induced a time-dependent increase in Nrf2 protein content in nuclear fractions, paralleled by a proportional decrease in cytosolic fractions. More interestingly, the time-dependent Nrf2 protein content variation in both nuclear and cytosolic fractions was prevented by NAC. NAC is a precursor of L-cysteine that contribute to glutathione biosynthesis and can also act directly as a scavenger of oxygen free radicals [531]. This data reinforce the hypothesis that

AntiOxCIN$_4$-induced mild increase in mtROS is responsible for the cell's adaptation due to the activation of the Nrf2/KEAP1 pathway. Although the Michael acceptor moiety of AntiOxCIN$_4$ can promote the oxidation of the KEAP1 protein, the presence of pyrogallol moiety can also contribute to Nrf2/KEAP1 activation via the production of intracellular H_2O_2 [532].

Nrf2 controls the expression of more than 200 genes that contain antioxidant response elements (AREs) in their regulatory regions [533]. The AntiOxCIN$_4$-induced Nrf2 activation in response to mild mitochondrial stress involved stimulating antioxidant-encoding genes *NQO1* and *HMOX1*. Functionally, HMOX1 is involved in heme catabolism and cellular iron homeostasis being its activation linked to antioxidant, anti-inflammatory, anti-apoptotic, and proangiogenic effects. NQO1 is involved in the detoxification of redox-cycling quinones, semiquinones and other type of electrophilles [534].

Nrf2 downstream effects directly impact ROS homeostasis, for instance, through the activation of local pools of antioxidant defenses involved in protective signaling pathways [517]. Nrf2 regulates, among others: (i) Glutamate cysteine ligase (GCL) and Glutathione synthase (GS) to modulate GSH de novo synthesis, (ii) cysteine influx to maintain intracellular GSH levels, (iii) GSH-based thiol redox state by regulating glutathione reductase (GR), and (iv) SOD expression/activity. In this context, we observed in our work that the cellular GSH/GSSG ratio and SOD and GR activity were increased in AntiOxCIN$_4$-treated cells. Moreover, we observed an increase in NADH/NAD$^+$ ratio, while the NADPH/NADP$^+$ ratio was decreased.

Altogether, the data suggest that the presence of both nucleophilic and electrophilic moieties in AntiOxCIN$_4$ resulted in synergistic activation of Nrf2 and phase II enzymes and positively contributed for the redox homeostasis [532]. In fact, the Michael acceptor moiety of AntiOxCIN$_4$ can promote the oxidation of the KEAP1 protein. Notwithstanding, the contribute of pyragallol moiety in Nrf2/KEAP1 activation via the mild increase in superoxide anion levels and subsequent production of intracellular H_2O_2 due to increased SOD activity cannot be excluded (Sirota, Gibson and Kohen, 2015). [532]. Moreover, upregulation of the overall cellular endogenous antioxidant defense system protect cells against subsequent stress-inducing events more efficiently. In fact, we

observed that AntiOxCIN$_4$ long-term treatment protected HepG2 cells against the detrimental effects of menadione (MEN) and/or palmitic acid (PA).

AntiOxCIN$_4$ cells led to initial acute mild mitochondrial dysfunction in HepG2 cells. Drug-induced mild alterations in mitochondrial morphology and/or function triggers mitochondria to participate in stress-induced adaptive pathways. The tight regulation between mitochondrial biogenesis and autophagy (mitophagy) is essential to regulate mitochondrial content and metabolism, and crucial to determine cell fate in response to cellular metabolic state, stress, and other intracellular or environmental signals [535]. KEAP1/Nrf2 signaling can regulate p62 in a positive feedback loop within the KEAP/Nrf2/p62 axis. Consequently, p62/SQSTM1, a multifunctional stress-inducible protein and a marker of autophagic degradation involved in cell signaling, oxidative stress, and autophagy, can contribute to the capacity of cells to defend themselves against oxidative stress. AntiOxCIN$_4$ led to an early p62-KEAP1 degradation after Nrf2 translocation to the nucleus, which was corroborated by autophagy markers (LC3BI/II, Beclin-1). Previous studies observed that p62 can be stimulated by Nrf2, acting on KEAP1-p62 degradation by autophagy. Our data indicated that long-term incubation of AntiOxCIN$_4$ did not maintain persistent Nrf2 activation or blockage of autophagic flux, as observed by the increase of LC3BII levels in the presence of chloroquine, an inhibitor of autophagosomes-lysosomes fusion. Rapamycin can bind to mTORC1 and allosterically inhibit its kinase activity, increasing autophagy, as previously demonstrated in several contexts [536–538]. In the present work, we used rapamycin as positive control for autophagy induction. Rapamycin increased LC3II protein level, suggesting autophagosome formation, as described in the literature [539]. AntiOxCIN$_4$ presented a similar profile to rapamycin on LC3BII protein level, which, combined with additional experimental evidence presented in our work, such as p62 degradation upon Nfr2 activation [540], suggest that AntiOxCIN$_4$ activate autophagy. Interestingly, no additive effect was observed when AntiOxCIN$_4$ and rapamycin were co-incubated, suggesting that the former may induce autophagy via rapamycin-sensitive pathways.

Dysfunctional mitochondria are targeted and engulfed by double-membrane vesicles known as autophagosomes and are transferred for degradation in lysosomes. Cells induce mitophagy to regulate the size and quality of their mitochondrial network in

response to energy demands [535]. Here, we observed that AntiOxCIN$_4$ increased the co-localization between mitochondrial and lysosomal particles which may suggest initial steps of mitophagy. Moreover, the protein levels of mitophagy-related processes PINK1 was also increased. Notwithstanding, mitochondrial fusion and fission dynamics hallmarks were not altered, suggesting that mitochondrial dynamics phenomena were already restored after AntiOxCIN$_4$ long-term treatment.

To restore mitochondrial homeostasis, mitochondrial biogenesis can also occur. Mitochondrial biogenesis involves, among others, mtDNA transcription, recruitment of newly synthesized proteins and lipids, import and assembly of mitochondrial and nuclear products in the expanding mitochondrial network [535]. We observed that AntiOxCIN$_4$ treatment induced a time-dependent translocation in PGC-1α protein to the nuclear compartment, while no changes were observed in the cytosolic fractions. Moreover, we observed that AntiOxCIN$_4$ treated HepG2 cells exhibited increased mtDNA copy number, paralleled by an increased mRNA levels of *NRF1* and *GAPBA*, and OXPHOS complexes. The peroxisome proliferator-activated receptor-γ coactivator (PGC)-1α is the main regulator of mitochondrial biogenesis. Several Nrf2 activators, such as berberine [541], quercetin [542], or physical exercise [543] also exhibited regulatory circles involving PGC-1α. Alongside PGC-1α, Nrf2 translocation to the nuclear compartment is also involved in mitochondrial biogenesis, as Nrf2 binds to the NRF1 promoter ARE (Antioxidant Response Element), which activates TFAM (Mitochondrial transcription factor A), leading to mtDNA replication.

Nrf2 affects mitochondrial membrane potential (ΔΨm) and mitochondrial respiration as it may regulate components of the mitochondrial electron transport chain [544]. In fact, basal ΔΨm is higher when Nrf2 is genetically constitutively up-regulated [545]. In our work, we also observed that AntiOxCIN$_4$-treated cells presented a higher TMRM fluorescence, suggesting a higher mitochondrial polarization. Moreover, plotting the average data of mitochondrial network area against the average TMRM fluorescence signal, we observed that AntiOxCIN$_4$ induces a non-proportional increase in both mitochondrial area and polarization. The data strongly suggests that AntiOxCIN$_4$ increased the mitochondrial mass and induced a hyperpolarization (higher ΔΨm) of the mitochondrial network in HepG2-treated cells. Moreover, the increased VDAC (mitochondrial porin)

protein content in HepG2-treated cells, normally used as a mitochondrial mass marker, reinforces the idea of an up-regulated mitochondrial biogenesis phenomena. Together, the data pointed out that AntiOxCIN$_4$ increases mtDNA copy number per cell and thereby mitochondrial mass due to mitochondrial biogenesis phenomena mediated by PGC-1α.

7.5. Conclusions

In conclusion, our work describes for the first time the Nrf2-dependent antioxidant mechanism of action behind the beneficial effects of mitochondriotropic antioxidant AntiOxCIN$_4$ (**Figure 29**). AntiOxCIN$_4$ induced an Nrf2-dependent cellular adaptative response mediated and triggered by a sustainable increase in mtROS that protected HepG2 cells against the detrimental effects of menadione (MEN) and/or palmitic acid (PA). Activation of Nrf2 resulting from a mild increase in mtROS leads to activation of different cell signaling pathways after AntiOxCIN$_4$ treatment. The activated cellular pathways may result in clearing damaging mitochondria through autophagy (via the KEAP/Nrf2/p62 axis) and/or mitophagy (involving PINK1). Mitochondrial homeostasis may be restored by increasing biogenesis (mediated by PGC-1α). The activation of Nrf2 combined with expression of downstream Nrf2-dependent stress response genes (NQO1 and HMOX1) would contribute to upregulate critical antioxidant systems (increased SOD and GR activity and GSH/GSSG ratio), that in turn, protect cells against oxidative and electrophilic stress, preventing cell death (**Figure 29**).

Unraveling the AntiOxCIN$_4$ mechanism of action in human hepatoma-derived (HepG2) cells opens a new avenue to extend its potential application in the context of liver disease, such as NASH/NAFLD. A redox imbalance promoted by exacerbated ROS production that leads to impairments in mitochondrial function and a compromised activation and execution of cellular quality control processes seems to be a determinant mediator in lipid-induced hepatotoxicity and inflammatory-related processes, thereby contributing decisively to NAFLD progression. Although the cellular mechanisms behind NAFLD pathogenesis are still a focus of controversy, the multi-factorial nature of the disease demands more broad and versatile therapeutic approaches. Thus, from the

described AntiOxCIN$_4$ mechanism of action, this molecule can be a valuable drug candidate in the context of metabolic-related hepatic disorders, such as NASH/NAFLD.

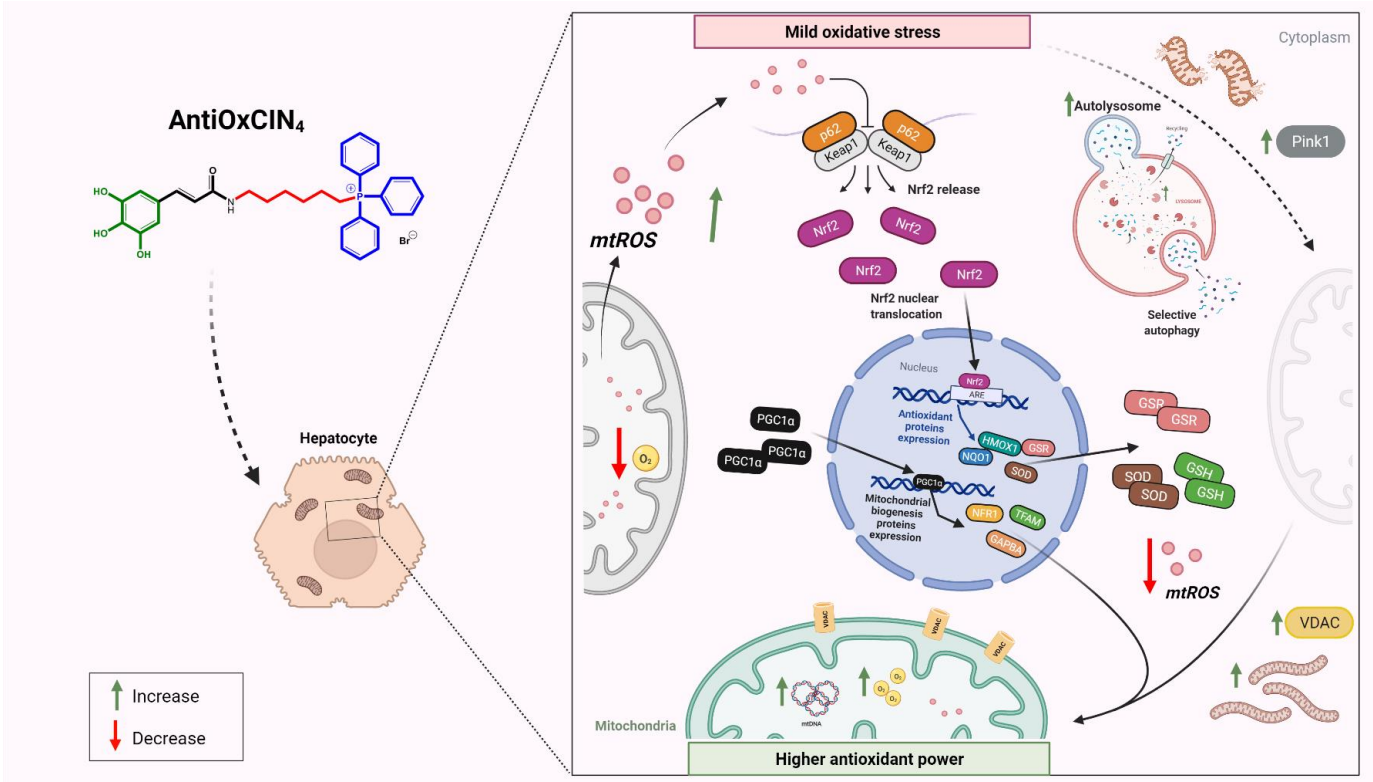

Figure 29 Proposed mode-of-action of mitochondriotropic phenolic acid antioxidant AntiOxCIN$_4$ in HepG2. Mitochondriotropic antioxidant AntiOxCIN$_4$ acutely decreased OCR, which was paralleled by time-dependent increase in mtROS levels. Moreover, AntiOxCIN$_4$ induced a ROS-dependent Nrf2 activation mediated by Nrf2-KEAP1-p62 axis and an efficient removal of potentially damaged mitochondria by triggering cellular quality control mechanisms, such as autophagy and/or mitophagy. Nrf2 activation also up-regulates the cellular antioxidant defense system of HepG2 cells and increases mitochondria biogenesis phenomena, contributing to a more resistant mitochondrial population. mtROS, mitochondrial reactive oxygen species; SOD, superoxide dismutase; GSH, reduced glutathione; GSR, glutathione reductase; KEAP1, kelch-like ECH-associated protein 1; NQO1, NAD(P)H dehydrogenase (quinone) 1; Nrf2, nuclear factor erythroid 2-related factor 2; HMOX1, heme oxygenase 1; NFR1, nuclear respiratory factor 1; PGC-1α, peroxisome proliferator activator α; VDAC, voltage dependent anion channel; PINK1, PTEN induced kinase.

8. Chapter

Exploratory Data Analysis of Cell and Mitochondrial High-Fat, High-Sugar Toxicity on Human HepG2 Cells

Data in this chapter was published in:

Ricardo Amorim; Inês C.M. Simões; Caroline Veloso; Adriana Carvalho; Rui F. Simões; Francisco B. Pereira; Theresa Thiel; Andrea Normann; Catarina Morais; Amália S. Jurado;, Mariusz R. Wieckowski; José Teixeira; Paulo J. Oliveira. Exploratory Data Analysis of Cell and Mitochondrial High-Fat, High-Sugar Toxicity on Human HepG2 Cells (2021). *Nutrients* 13, no. 5: 1723. https://doi.org/10.3390/nu13051723.

8.1. Introduction

NAFLD is a worldwide public health concern. The most recent data indicated that 25% of world population has some form of NAFLD, with the highest prevalence in the Middle East and South America [546]. NAFLD can progress from simple steatosis to NASH, a pathological stage characterized by inflammation and hepatocellular ballooning. Further progression of this condition can result in a fibrotic phenotype (cirrhosis) and, ultimately, in HCC.

NAFLD is well-defined as the augmented accumulation of hepatic TGs (more than 5%) in the absence of excessive alcohol consumption [547] or other liver disease etiology. Over-consumption of high fat-high sugar diets demands a great metabolic effort from the organism, leading to unregulated energy homeostasis processes [547]. Mitochondria are responsible, among other functions, for the oxidation of short and median chain fatty acids through β-oxidation. The deleterious sequence of cellular events includes fatty acid and/or carbohydrates overload followed by an ROS production, mitochondrial damage, and ER stress, resulting in activation of either pro-survival or pro-apoptotic pathways.

Several *in vitro* models are used to investigate NAFLD mechanisms based on fatty-acid overload. Those different models significantly differ in nature, amount, and fatty

acids (FA) overload incubation time, making the data difficult to compare. Although lipotoxicity resulting from incubating *in vitro* models with high concentrations of lipids and lipid derivatives exposure has been reported in several *in vitro* studies [548, 549], different cellular outcomes were attained depending on lipid composition and/or level of unsaturation, which suggests different cellular responses depending on FA composition and incubation time. For example, palmitic acid (PA; 16:0)-treated H4IIE liver cells displayed increased ER stress, caspase-3 activity and liver injury [483, 550]. The cellular pathways underlying this process involve activation of c-jun NH2-terminal kinase (JNK) and Bcl-2 Homology 3 (BH3)-only protein-induced mitochondrial and lysosomal dysfunction [551–555]. *In vitro* studies involving monosaturated fatty acids (MUFA) treatment in hepatocytes, such as oleic acid (OA, 18:1), reported a more severe hepatic steatosis when compared with PA exposure [549]. Still, oleic acid treatment showed protective effects against PA-induced toxicity [549, 556]. An increase in peroxisome proliferator-activated receptor (PPAR) β/δ expression dependent on the activation of free fatty acid receptor 1 (FFAR1) and a calcium-dependent mechanism was observed in human hepatocytes treated with oleic acid [557]. Moreover, polyunsaturated fatty acids (PUFA) also showed beneficial outcomes in several NAFLD models [558, 559]. Long-chain ω-3 PUFAs, especially icosapentaenoic acid (EPA) and docosahexaenoic acid (DHA), presented potent anti-inflammatory activity and anti-fibrosis effect by down-regulated the protein level of YAP/TAZ and, consequently, inhibition of hepatic stellate cells (HCS) activation and proliferation [560].More recently, studies with bioactive branched fatty acid esters of hydroxyl fatty acids (FAHFAs) showed protective effects against FA-induced mitochondrial dysfunction and intracellular lipid accumulation in HepG2 cells and primary hepatocytes (PMH) [561].

Another newer paradigm on NAFLD metabolic syndrome strongly suggested that carbohydrates-rich diets also play a vast, if not determinant, role in NAFLD development [562, 563]. The excess of carbohydrates (e.g. fructose) derived from these diets can be converted into FFA and TG in the liver, also resulting in an increased accumulation of hepatotoxic lipids such as lysophosphatidylcholine (LPC), ceramides, free cholesterol, and bile acids (BA) [564–568]. Fructose-rich diets are recognized to cause steatosis,

dyslipidemia, insulin resistance, and liver fibrosis in both animal and human studies [569, 570].

FA and/or sugars overload within cells lead to a significant increase in lipid accumulation in the cytoplasm, which can be toxic if high concentration levels are reached [571]. The multiplicity of models and lipid (and sugar)- induced toxicity makes an accurate analysis of the role of mitochondrial dysfunction in the progression of cellular damage *in vitro* difficult to characterize. In this context, the objectives of this work were to investigate in human HepG2 cells a) how mitochondrial disruption develops under different lipotoxicity protocols, b) whether mitochondrial dysfunction precedes oxidative stress and induction of cell death or is instead a consequence of those two events and c) whether fructose (F) worsens the cellular lipotoxicity profile under the different protocols. For these objectives, we characterized and compared the time-dependent cellular effects of different FA overload strategies in the presence or absence of carbohydrates (fructose), with particular focus on measuring mitochondrial structure, integrity, and bioenergetics, to attain a feasible and reproducible *in vitro* model for study mitochondrial impairment during progressive cellular lipotoxicity. A suite of computational data analysis tools was applied to several cellular and mitochondrial markers, aiming at identifying differences in the effects of the PA and FFA treatments. Unsupervised learning methods were applied to identify clear separations between groups of samples, corresponding to different cell treatments. The partition was performed with a minimal subset of experimental endpoints. This computational approach is thus an innovative tool for clustering biological effects of supra-physiological lipid levels.

8.2. Material and Methods

8.2.1. Chemicals

Dulbecco's modified Eagle's medium (DMEM, D5030), penicillin, streptomycin, fetal bovine serum (FBS) and Trypsin were purchased from Gibco-Invitrogen (Grand Island, NY, USA). Dithiothreitol (DTT), phenylmethanesulfonyl fluoride (PMSF), protease inhibitor cocktail (leupeptin, antipain, chymostatin, and pepstatin A), sulforhodamine B (SRB), palmitic acid (C16:0), stearic acid (C18:0), oleic acid (C18:1), linoleic acid (C18:2),

arachidonic acid (C20:4), D(-)-Fructose, Nile Red, Hoechst 33342, tetramethylrhodamine methyl ester (TMRM), and 5-(and-6)-chloromethyl-2',7'-dichlorodihydrofluorescein diacetate, acetyl ester (CM-H_2DCFDA) were purchased from Invitrogen (Eugene, OR, USA).

8.2.2. Fatty acid conjugation

Palmitic acid (PA)/Bovine Serum Albumin (BSA, A6003, Sigma-Aldrich, USA) solution was prepared by mixing free-fatty acid BSA (0.2 g/mL) with 10 mM palmitic acid in the proportion of 1:1 during 1 h at 37 ºC. The Free-fatty acid BSA (0.2 g/mL) was diluted in the same proportion with 150 mM NaCl and used as a control. The fatty acid mixtures (FFA) were prepared as saponified 10 mM stock solutions and complexed (1:1) with Free-fatty acid BSA (10 minutes at 50 °C), cooled to room temperature. The Free-fatty acid BSA (0.2 g/mL) was diluted in the same proportion with 25 mM KOH and used as a control. The same ratios of FA dilutions were used for free fatty acid BSA control. The amounts of the different FA in the mixture were: 39 % C16:0 (P0500, Sigma-Aldrich, USA); 5 % C18:0 (85679, Sigma-Aldrich, USA); 50 % C18:1 (O1008, Sigma-Aldrich, USA); 4 % C18:2 (L1376, Sigma-Aldrich, USA); 2 % C20:4 (A3611, Sigma-Aldrich, USA) [572, 573].

8.2.3. Cell culture and FA treatments

Human hepatocellular carcinoma HepG2 cells (85011430, ECACC, UK) were cultured in low-glucose medium composed by Dulbecco's modified Eagle's medium (DMEM; Catalogue Nº: D5030, Sigma-Aldrich, USA) supplemented with 5 mM glucose, sodium bicarbonate (3.7 g/L), HEPES (1.19 g/L), L-glutamine (0.876 g/L), sodium pyruvate (0.11 g/L), 10 % fetal bovine serum (FBS), 1 % penicillin-streptomycin 100x solution in a humidified atmosphere (5 % CO_2, 37 ºC). HepG2 cells were seeded (6 x 10^4 cells/cm^2) and grown for 24 h during which they reached 60–70 % confluence before treatment. Next, cells were incubated in the presence of vehicle (BSA 0,01 g/mL) and different mixtures of FA (PA, 0.5 mM or FFA, 0.25 mM) in the presence or absence of fructose (F, 10 mM) for 1, 6 and 24 h period.

8.2.4. Animals and dietary regimen

Four-week-old male C57BL/6J mice were purchased from SAS (Saint-Germain-Nuelles, France). The mice were fed a standard chow (CHOW) *ad libitum* starting at the age of seven weeks. The standard chow diet derives 9% of its energy from fat, 58% from carbohydrates and 33% from protein and comprises 3% fat and 5% sucrose. The CHOW (V1534) diet was purchased from Ssniff (Soest, Germany). All mice were housed in laboratory cages at 21-23 °C with 50-60% humidity (10-15 exchanges per h) with tap water and diet provided *ad libitum* for sixteen weeks. For tissue collection, the mice were anesthetized with isoflurane and further sacrificed by cervical dislocation.

8.2.5. Nile red Staining

Cells were seeded in 96-well plates and then subjected to the different treatments. After incubation, the neutral lipid accumulation was assessed through the Nile Red assay [505]. Briefly, cell culture medium was discarded and 100 µL of the Nile red solution was added to each well for 1 h/1.5 h in the dark conditions at 37 ºC. Nile Red is freshly diluted 1:200 in medium without FBS from the stock solution (stock: 0.5 mg/mL dissolved in acetone). Nile Red was then removed, and cells were washed twice with PBS 1X. The fat content per well (in 100 µL PBS 1X) was measured fluorimetrically with 520 nm excitation and 620 nm emission in a Biotek Cytation 3 reader (Biotek Instruments, Winooski, VT, USA). Results were normalized for cell mass content at the end of assay, using the SRB method [506].

8.2.6. Phospholipid analysis

HepG2 cells were seeded in 100 mm cell culture dish and submitted to the different treatments. After incubation time, cells were harvested and washed with cold PBS 1X. In order to obtain total cellular extracts, cells were harvested, washed with cold PBS 1X and then two centrifugation steps were performed for 5 minutes at 1000X*g* (4 °C). To obtain mitoplast fractions, digitonin (4 mg/mL) was added and kept on ice for 10 minutes. The resuspension was further diluted with PBS 1X and centrifuged during 10 minutes, 4 °C, 10000X*g*. The process was repeated two more times with a 5 minutes

centrifugation at 4 ºC, 10000X*g*. Mitoplasts were stored at -80 ºC until further processing. Mitochondrial lipids were extracted accordingly to Bligh and Dyer method [574]. Lipids quantification was performed according the phosphorous assay described by Rouser *et al*. [575]. The method was calibrated with a standard curve with known concentrations of KH_2PO_4. Pre-washed Whatmann LK5 thin-layer plates with chloroform/ methanol (1:1) where sprayed with 1.8 % of boric acid solution, air-dried and then activated for 15 minutes at 100 ºC. 40 µg of phospholipid samples were loaded in the concentration zone of the plates. After, plates were placed in chromatography tanks with a mixture of chloroform/ ethanol/ water/ trimethylamine (30/35/7/35, v/v) for 2 h. Phospholipids bands were then visualized by soaking the plate in 10 % (m/v) cupric sulfate/ 8% (v/v) phosphoric acid solution and just after, plates were heated in an oven at 140 ºC for 20 minutes. Different phospholipids classes were photographed with Biospectrum—Multispectral imaging system (UVP; LLC Upland, CA; Cambridge, UK). The densities of each band were calculated with TotalLab TL120 1D v2009.

8.2.7. Intracellular ROS levels

Cells were seeded in 96-well plate and then subjected to the different treatments. After incubation time, intracellular ROS levels were assessed using the oxidative stress-sensitive report molecule CM-H_2DCFDA (5-(and-6)-chloromethyl-2',7'-dichlorodihydrofluorescein diacetate, acetyl ester) (Life Technologies, Invitrogen). Briefly, cells were loaded with 5 µM of CM-H_2DCFDA in assay buffer (NaCl 120 mM, KCl 3.5 mM, $NaHCO_3$ 5 mM, $NaSO_4$ 1.2 mM, KH_2PO_4 0.4 mM, HEPES 20 mM supplemented with $CaCl_2$ 1.3 mM, $MgCl_2$ 1.2 mM and sodium pyruvate 10 mM, pH 7.4) at 37 °C and 5 % CO_2 in the dark for 15 minutes. Then, cells were washed twice with PBS 1X, and fluorescence signals were measured with 520 nm excitation and 620 nm emission wavelengths using a microplate reader (Cytation 3; BioTek US, Winooski, VT, USA). Results were normalized for cell mass content at the end of the assay, using the SRB method.

8.2.8. Mitochondrial morphology imaging

Vital confocal fluorescent microscopy was performed to visualize alterations in mitochondrial electric potential polarization and network distribution in HepG2 cells. Cells were seeded in pre-coated (collagen I 0.15 mg,mL) µ-Slide 8 well ibiTreat Ibidi (2 x 10^4/cm^2) with a final volume of 300 µL per well, and then subjected to the different treatments. Cells were incubated with fluorescent dyes tetramethylrhodamine (TMRM) (100 nM) and Hoechst 33342 (1 µg/mL) for mitochondrial network and nuclei, respectively, 30 minutes before the end of the treatment time in fresh cell culture medium at 37 °C and 5 % CO_2 in the dark conditions. Images were acquired using a Laser Scanning Confocal Microscope (LSM 710, Zeiss, USA) equipped with a α-Plan-Apochromat 63x/1.4 Oil DIC M27 objective (Zeiss) and analyzed with ImageJ Fiji program (Scion Corporation, USA). Index of interconnectivity was quantified by using a *Mitochondria Morphology* Macro [511].

8.2.9. Mitochondrial DNA copy number measurements

Mitochondrial DNA copy number was measured using quantitative polymerase chain reaction (qPCR). HepG2 cells were seeded in 60 mm cell culture dish and subjected to the different treatments. Cells were then harvested at the time-points indicated by aspirating media and washing plates with ice cold PBS. For measurement of mitochondrial DNA copy number, RNase-treated total DNA was isolated using the Qiagen DNeasy kit (Catalogue Nº: 69104, Qiagen, Germany) according to the manufacturer's recommendations. DNA amount and purity were evaluated in a NanoDrop 2000 spectrophotometer (ThermoScientific, Waltham, MA, USA). qPCR was performed based on the amplification of *cytochrome B (MT-CYTB)* (encoded on the mitochondrial genome; variable quantity in each cell) and *beta-2-microglobulin (B2M)* (encoded on the nuclear genome; fixed quantity in each cell) using a Roche Light Cycler and Roche FastStart DNA Master SYBR Green protocols. Human primers for *MT-CYTB* were: forward 5'-CCACCCCATCCAACATCTCC-3', reverse 5'-GCGTCTGGTGAGTAGTGCAT-3' (Pair rating: 66,1; Product length: 112); primers for *B2M* were: forward 5'-GAATTCCAAATTCTGCTTGCTTGC-3', reverse 5'- CCTCTAAGTTGCCAGCCCTC-3' (Pair rating: 71,2; Product length:

199). Each reaction was performed in triplicate with an efficiency between 90 and 110 %. For amplification purposes, total DNA (25 ng) went on an initial cycle of 2 minutes at 95 ºC, followed by 40 cycles of 5 seconds at 95 ºC plus 20 seconds at 63 ºC and 20 seconds at 72 ºC. At the end of each cycle, Eva Green fluorescence was recorded to enable determination of Cq. Several dilutions of control sample and DNA-free water were used as standards and negative control, respectively. The specificity of each reaction for a single product was verified by melting analysis. The cycle number of linear amplifications for each sample was compared with the five-point standard curve to determine the number of template copies present at the start of each reaction. Mitochondrial copy number was estimated by the number of copies of *cytochrome B* template divided by the number of copies of *beta-2 microglobulin* template. The reactions were performed on a CFX™96 Real-Time system (Bio-Rad, CA, USA). The normalized expression was calculated by the comparative quantification algorithm ΔΔCt (CFX Manager™ 3.1 software, 18 Bio-Rad).

8.2.10. Western blotting analysis

Cells were seeded in 100 mm cell culture dish and then subjected to the different treatments. In order to obtain total cellular extracts, cells were harvested, washed with cold PBS 1X, and then two centrifugation steps were performed for 5 minutes at 1000X*g* (4 °C). Cellular pellet was resuspended in cell RIPA buffer (50 mM Tris pH 8**,** 150 mM NaCl**,** 5 mM EDTA**,** 15 mM, $MgCl_2$ and 1 % Triton X-100) supplemented with 0.5 mM phenylmethylsulfonyl fluoride (PMSF), protease inhibitor cocktail (PIC) (Sigma P8340), 20 mM sodium fluoride (NaF), 5 mM sodium butyrate, 10 mM NAM, DOC 10% and keep on ice for 30 minutes. After that, the resuspension was mixed and centrifuged at 20000x *g* during 10 minutes. Soluble protein contents were determined by the BCA method using BSA as a standard. Laemmli buffer (from Bio-Rad) was added to the samples. An equal amount of proteins (20–50 µg) was separated by electrophoresis on 12 % SDS–polyacrylamide gels (SDS–PAGE) and electrophoretically transferred to a polyvinylidene difluoride (PVDF) membrane. After blocking with 5 % milk in TBST (50 mM Tris–HCl, pH 8; 154 mM NaCl and 0.1 % tween 20) for 2 h at room temperature, membranes were incubated overnight at 4 °C with the antibodies directed against the denatured form of

OXPHOS complexes cocktail (1:1000; ab110411, Abcam), Ketohexokinase (1:500, sc-377411, Santa Cruz Biotechnology) and β-actin (1:5000; MAB1501, Chemicon international). Membranes were further incubated with goat anti-mouse IgG (1:5000, CS7076, Cell Signaling Technology, USA) and goat anti-rabbit IgG (1:5000, CS7074, Cell Signaling Technology, USA) secondary antibodies for 1 h at room temperature. Membranes were then incubated with the ECL detection system (Bio-Rad 1705061) and imaged with the Biospectrum—Multispectral imaging system (UVP; LLC Upland, CA; Cambridge, UK). The densities of each band were calculated with TotalLab TL120 Software (version 2009).

8.2.11. BN-PAGE *in-Gel* Activity of Complex I

HepG2 cells were seeded in 100 mm cell (6 x 10^4/cm^2) culture dish and submitted to the different treatments. After 6 and 24 h, cells were harvested and washed with cold PBS 1X. Cell pellets were ressuspended in cold PBS 1X. To obtain mitoplast fractions, digitonin (4 mg/mL) was added and kept on ice for 10 min. The resuspension was further diluted with PBS 1X and centrifuge during 10min, 4°C, 10000X*g*. Two washings with PBS1x for 5 min (4ºC, 10000X*g*) were performed. When not used on the day, pellets were storage at -80ºC. OXPHOS complexes isolation was attained by adding ACBT buffer (1.5 M epsilon-aminocaproic acid, 75mM Bis-Tris, pH 7.0), 20% Lauryl maltoside and kept on ice during 10 min. Afterward, samples were centrifuged for 30 min (4ºC, 10000X*g*) and the supernatant collected. Protein content was assayed by BCA method using BSA as standard. Pre-cast gels with a gradient concentration of 3-12% were loaded with 10 µg of protein-containing BN-sample buffer 1:10 (750 mM Aminocaproic acid, 50mM Bis-Tris, 0.5mM EDTA, 5 % Serva Blue G, pH 7.0) [576]. Gel ran with a constant voltage at 75 V for 30min. Next, cathode blue buffer was replaced a cathode light buffer. The voltage was increased up to 150 V until the samples reached the bottom of the gel. After electrophoresis, gels were further processed for in-gel activity assays. **Complex I**: 3 mM Tris–HCl, pH 7.4, 80 µg/ml NADH, and 0.2 mg/ml Nitro tetrazolium blue (NTB)**.** For Complex I activity, gels were incubated for 20 min at 37°C. Complex activity was scanned or photographed with Biospectrum - Multispectral imaging system (UVP; LLC Upland,

CA; Cambridge, UK). The densities of each band were calculated with Image Studio Lite 5.2 Software (LI-COR Biosciences, U.S.A).

8.2.12. Cellular oxygen consumption rate measurements

Cells were seeded in 96-well plate (pre-coated with collagen I 0.15 mg/mL) under the same conditions described above at a density of 10000 cells/100µL/well. After incubation time, oxygen consumption was measured at 37 ºC using a Seahorse XFe96 Extracellular Flux Analyzer (Agilent Scientific Instruments, USA). In addition, an XFe96 sensor cartridge for each cell plate was placed in a 96-well calibration plate containing 200 µL/well calibration buffer and left to hydrate overnight at 37 ºC. The cell culture medium from the plates was replaced the following day with 175 µL/well of pre-warmed low-buffered serum-free minimal DMEM medium (D5030, Sigma-Aldrich, USA), the pH adjusted to 7.4 and incubated at 37 ºC for 1 h to allow the temperature and pH of the medium to reach equilibrium before the first-rate measurement. Oligomycin, carbonyl cyanide-4-(trifluoromethoxy)phenylhydrazone (FCCP), rotenone and antimycin A were prepared in DMSO.

For oxygen consumption rate (OCR) measurements, 2 µM oligomycin, injected into reagent delivery port A, 0.33 µM FCCP injected into port B, 1 µM rotenone and 1µM antimycin A injected into reagent delivery port C were diluted in low-buffered serum-free DMEM medium and the pH adjusted to 7.4 with 1 M NaOH. 25 µL of compounds was then pre-loaded into the ports of each well in the XFe96 sensor cartridge. The sensor cartridge and the calibration plate were loaded into the XFe96 Extracellular Flux Analyzer for calibration. When the calibration was complete, the calibration plate was replaced with the study plate. Three baseline rate measurements of OCR and extracellular acidification rate (ECAR) of the HepG2 cells were made using a 3 minutes mix, 5 minutes measuring cycles. The compounds were then pneumatically injected by the XFe96 Analyzer into each well, mixed and OCR measurements made using a 3 minutes mix, 5 minutes measuring cycles. Results were analyzed by using the Software Version Wave Desktop 2.6.

8.2.13. Measurement of caspase 8 and 9-like activities

Cells were seeded in 100 mm cell culture dish and then exposed to the different treatments. To obtain total cellular extracts, cells were harvested, washed with cold PBS 1X and then two centrifugation steps were performed for 5 minutes at 1000X*g* (4 °C). Floating cells were also collected and combined with adherent cells. Cellular pellets were resuspended in cell lysis buffer supplemented with 100 µM PMSF, 2 mM DTT. The resuspension was homogenized by 30 passages through a 27-gauge needle, followed by 3 cycles of freeze / thaw in liquid nitrogen and kept at –80 ºC until used. Protein content was determined by the Bradford method [506], using BSA as standard. To measure caspase 9-like activity, aliquots of cell extracts containing 100 µg of total protein were incubated in a reaction buffer containing 10 % sucrose, 10 mM dithiothreitol (DTT), 0.1% 3[(3-cholamidopropyl) dimethylammonio]-propanesulfonic acid, 25 mM HEPES (pH 7.4) and 100 µM caspase substrate (Ac-LEHD-pNA) for 2 h at 37ºC. Caspase-like activity was determined by following the appearance of the chromophore pNA after cleavage from the labeled substrate Ac-LEHD-pNA (405 nm). The method was calibrated with known concentrations of pNA. To measure caspase 8-like activity, 80 µg of total protein dissolved in reaction buffer containing 10% sucrose, 10 mM dithiothreitol (DTT), 0.1% 3[(3-cholamidopropyl)dimethylammonio]-propanesulfonic acid, 25 mM HEPES (pH 7.4) was added directly into a 96 well black polysterene microplate (CLS3603, Sigma-Aldrich, USA). To initiate the reaction, 5 µL of 1 mM substrate for caspase-8 (Ac-LETD-AFC, final concentration 50 µM) was added and the reaction mixture was incubated by 2 h at 37 ºC. Caspase-like activity was measured fluorimetrically with 400 nm excitation and 505 nm emission in a Biotek Cytation 3 reader (Biotek Instruments, Winooski, VT, USA). The method was calibrated with a standard curve of AFC (7-amino-4-trifluoromethyl coumarin).

8.2.14. Measurement of caspase 3/7-like activity

Caspase-Glo 3/7 (Promega, WI, USA) is a homogenous chemiluminescent kit available and widely used to measure apoptosis. Compound-treated plates were prepared as described above and after incubation time, caspase-3/7 activity was

measured by using Caspase-Glo 3/7 following manufacturer's instructions. Briefly, 100 µL per well Caspase-Glo 3/7 reagent was added to the cells and plates were agitated for 2 h in the dark at room temperature before luminescence was measured using a microplate reader (Cytation 3; BioTek US, Winooski, VT, USA).

8.2.15. Cell metabolic activity

Cells were seeded in 96-well plate and then subjected to the different treatments. After incubation time, the cell metabolic activity was assessed through the resazurin reduction assay [507]. Briefly, the culture medium was discarded and cells were incubated for 1 h with 80 µL of culture medium supplemented with 10 µg/mL resazurin. The appearance of resorufin, indicative of metabolic activity, was measured fluorimetrically with 570 nm excitation and 600 nm emission in a Biotek Cytation 3 reader (Biotek Instruments, Winooski, VT, USA).

8.2.16. Cell mass

Cells were seeded in 96-well plate and then subjected to the different treatments. After incubation time, the sulforhodamine B (SRB) assay was performed for cell mass determination based on the measurement of cellular protein content [506]. Briefly, the cell culture medium was discarded, and wells rinsed with PBS 1X. Cells were fixed by adding 1 % acetic acid in 100 % methanol for at least 2 h at -20 ºC. The fixation solution was then discarded, and the plates were dried at 37 ºC. 150 µL of 0.05 % SRB in 1 % acetic acid solution was added and incubated at 37 °C for 1 h. The wells were then washed with 1 % acetic acid in water and dried. Then, 100 µl of Tris (pH 10) was added and the plates were stirred for 15 minutes and optical density was measured at 540 nm in Biotek Cytation 3 reader (Biotek Instruments, Winooski, VT, USA).

8.2.17. Intracellular ATP levels

Cells were seeded in 100 µL of culture medium, in a white opaque-bottom, 96-well plate, and then subjected to the different treatments. After incubation time, intracellular ATP levels were measured using CellTiter-Glo Luminescent Cell Viability Assay (Promega, WI, USA). Briefly, 50 µL of culture medium was removed from the wells

and 50 µL of medium containing CellTiter-Glo Reagent (CellTiter-Glo Buffer + CellTiter-Glo Substrate) was added to the cells. Contents were mixed for 2 minutes on an orbital shaker to induce cell lysis and, after 10 minutes of incubation at 22 °C, the luminescence signal was monitored in a Cytation 3 reader (BioTek Instruments Inc., USA). An ATP standard curve was also generated following manufacturer's instructions.

8.2.18. Computational data analysis

Data analysis comprised the computation of correlation matrices to summarize correlations between every pair of variables, the estimation of individual feature importance regarding how useful they are to identify the different groups of the study and the definition of clusters to group similar samples. The correlation was computed using the Pearson coefficient, whose values belong to the interval [-1, +1]: +1 signals a total positive linear correlation, 0 identifies no linear correlation, and -1 refers to a total negative linear correlation. The individual feature importance for determining the target was estimated by calculating the mutual information gain measure, *i.e.*, by applying a nonparametric method that approximates the decrease of entropy [577]. Non-hierarchical clustering was performed with the K-means algorithm [578], after standardization of the data. The computational analysis of the data was performed using Python 3, version 3.7.3. We relied on the Pandas [579], NumPy [580], and SciPy [581] packages to load, store and transform the data. Correlations were calculated with Pandas, whereas mutual information gain and clustering were performed with scikit-learn [582]. All data analysis figures were created with Matplotlib and Seaborn modules.

8.2.19. Statistics

Data were analyzed in GraphPad Prism 8.02 software (GraphPad Software, Inc.). Unless stated otherwise, data from multiple experiments is presented as the mean ± standard error of the mean (SEM) and statistical significance was assessed using a 2-way ANOVA with Tukey multiple comparison post-test to compare more than two groups with two independent variables (treatment and time). A 2-way ANOVA with Sidak multiple comparison post-test allowed the comparation between different time

incubations in the same group. Significance was accepted with *P < 0.05, **P < 0.01, ***P < 0.0005, ****P < 0.0001 for comparisons between treatment vs CTL and $^{\#}$P < 0.05, $^{\#\#}$P < 0.01, $^{\#\#\#}$P < 0.0005, $^{\#\#\#\#}$P < 0.0001 for comparisons during time in the same group (24 and 6 h vs 1 h). Significance for additional fructose effect as accepted with $^{\$}$P < 0.05, $^{\$\$}$P < 0.01, $^{\$\$\$}$P < 0.0005.

8.3. Results

8.3.1. Supra-physiological concentrations of FA increase the accumulation of lipid droplets

Human hepatocarcinoma cells (HepG2) were incubated for a period of 1, 6, and 24 h with palmitic acid (PA; 0.5 mM) or with a mix of free fatty acid (FFA; 0.25 mM) [573] in the absence and presence of F (10 mM). The cytotoxic effects of each treatment were evaluated through changes in intracellular lipid content using Nile Red staining. PA and FFA treatments significantly increased intracellular neutral lipid content in a time-dependent manner (**Figure 30A**). Fructose by itself neither increased intracellular lipid content nor aggravated the effects of PA or FFA (**Figure 30A**). In agreement with results from neutral lipid droplets accumulation, the intracellular lipid content increased in the order: CTL ≈ F <<< FFA ≈ FFA+F ≈ PA ≈ PA + F. Taken together, these results demonstrate that the increase in intracellular lipid content is mainly due to the FA added, as the presence of sugar has a residual role on the different degrees of hepatic steatosis.

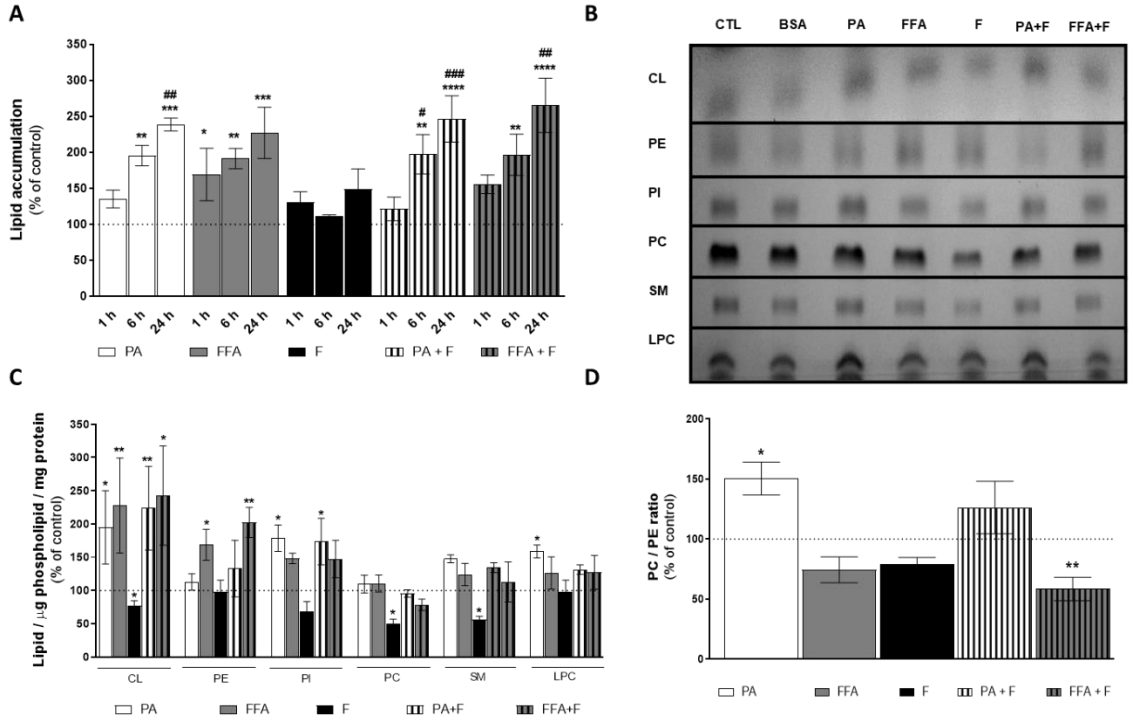

Figure 30. Effect of supra-physiological concentrations of FA on the accumulation of lipid and mitochondrial phospholipids content. (**A**) Lipid droplet content in HepG2 cells treated with palmitic acid (PA, 0.5 mM) or a mix of free fatty acids (FFA, 0.25 mM) in the presence or absence of fructose (F, 10 mM) for 1, 6, and 24 h. (**B**) A typical chromatogram showing the mitochondrial phospholipids profile (CL, cardiolipin; PE, phosphatidylethanolamine; PI, phosphatidylinositol; PC, phosphatidylcholine; SM, sphingomyelin; LPC, lysophosphatidylcholine) of HepG2 cells treated with PA or FFA in the presence or absence of F for 24 h. This image was inverted and contrast-optimized for visualization purposes. Quantification of the bands was performed using the original images. (**C**) Quantification of phospholipid content (CL, PE, PI, PC, SM, and LPC) in multiple experiments. (**D**) PC/PE ratios obtained in all conditions. Data are the mean _ SEM of four independent experiments, and the results normalized on the control condition (CTL = 100%, marked by a dotted line). Significance was accepted with * $p < 0.05$, ** $p < 0.01$, *** $p < 0.0005$, **** $p < 0.0001$ for comparations between treatment vs. CTL (BSA 0.01 g/mL) and $^{\#}$ $p < 0.05$, $^{\#\#}$ $p < 0.01$, $^{\#\#\#}$ $p < 0.0005$ for comparations during time in the same group (24 and 6 h vs. 1 h).

8.3.2. Fructose treatment increased HepG2 fructokinase protein levels

Fructose overload can lead to a large, rapid increase in the hexose- and triose-phosphate pools, potentially increasing substrate delivery for central carbon metabolic pathways increasing the risk for the development and progression of NAFLD [583, 584]. In this context, we measured the protein amount of the first enzyme responsible for fructolysis after 24h incubation with PA, FFA, F, PA + F and FFA+F. F treatments increased

hepatic fructokinase (Ketohexokinase; KHK) protein level, mainly in F and FFA + F groups (**Figure 31A-B**). Control liver homogenates from 16-week-old C57BL/6J mice was used as control, showing that KHK is noticeably more expressed in mouse liver than in HepG2 cell extracts, as expected (**Figure 31A-B**). These results suggest that the initial conversion of F to Fructose-1-P is likely to occur in HepG2 cells, although lipid accumulation resulting from F treatment was not observed under these experimental conditions.

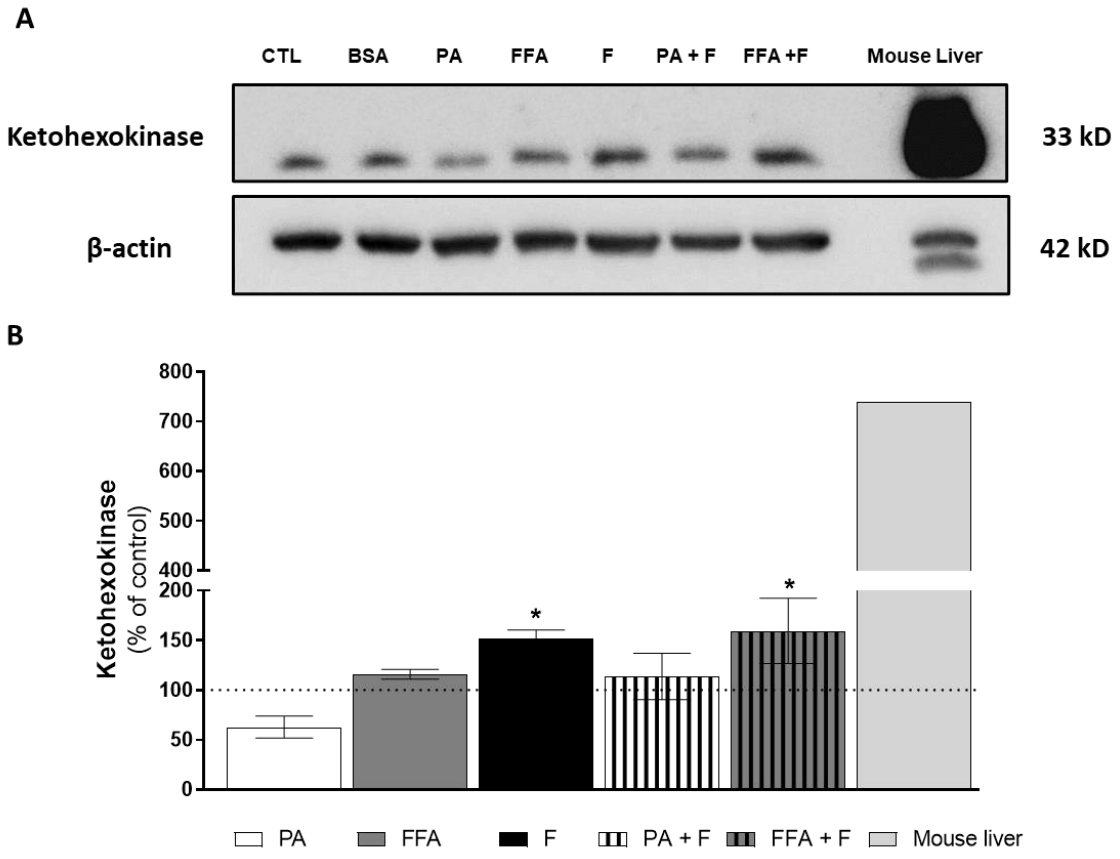

Figure 31. Effect of supra-physiological concentration of fructose on hepatic fructokinase protein level. (**A**) Typical Western blot result of whole cell homogenates showing the protein level of Ketohexokinase (KHK) in cells treated with palmitic acid (PA, 0.5 mM) or a mix of free fatty acids (FFA, 0.25 mM) in the presence or absence of F (F, 10 mM) for 24 h. Mouse liver homogenate (30 µg) was used as positive control, as KHK is highly expressed in liver. This blot was inverted and contrast-optimized for visualization purposes. Quantification of the bands was performed using the original blots. (**B**) Quantification of KHK protein levels under the different treatment conditions normalized to β-actin levels and for the control group (100% marked by a dotted line). Data are the mean ± SEM of four independent experiments, and

the results normalized on the control condition (CTL = 100 %, marked by a dotted line). Significance was accepted with *P < 0.05 for comparisons between treatment vs CTL or 0.1 % BSA.

8.3.3. Supra-physiological concentrations of FA altered mitochondrial phospholipid content

Given the higher amount of neutral lipids accumulation in cells under different treatments, we next investigated whether PA and FFA, alone or in combination with F for 24h could alter phospholipid composition of HepG2 mitochondrial-enriched fractions (**Figure 30B**). The analysis of phospholipid classes upon separation by thin-layer chromatography (TLC) showed no alterations in phosphatidylcholine (PC) content under the different PA- and FFA-treatment regimens. However, there was an increased content of PE for FFA alone or in combination with F (**Figure 30C**). Among the most abundant phospholipids in mitochondria, cardiolipin showed an increased content for all PA- or FFA-treatments (**Figure 30C**). Moreover, PA and PA + F treatment resulted in a significant increase in phosphatidylinositol (PI) content, and treatment with PA alone also resulted in a significant increase in LPC (**Figure 30C**). Interestingly, treatment with F, by itself, significantly decreased CL, PC, and SM (**Figure 30C**). On the other hand, PA-treatment significantly increased the PC/PE ratio, and FFA+F treatment decreased this parameter (**Figure 30D**). Overall, our results demonstrate that PA treatment caused broader changes in the content of mitochondrial membranes phospholipids.

8.3.4. Supra-physiological concentrations of FA time-dependently increase CM-H_2DCFDA oxidation

We next studied the effect of the different treatment groups in cellular oxidative stress by following CM-H_2DCFDA dye. PA- and FFA, alone or in combination with F, induced a significant time-dependent increase in intracellular ROS levels (**Figure 32**). Fructose by itself showed increased oxidative stress in comparison with control cells for all analyzed time points, although no time-dependent effects were observed (**Figure 32**). Interestingly, PA- but not FFA-induced dye oxidation was further increased by F (**Figure 32**). Taken together, these results demonstrate that an increase in intracellular oxidative

stress paralleled the increase in intracellular neutral lipid content and some phospholipids classes.

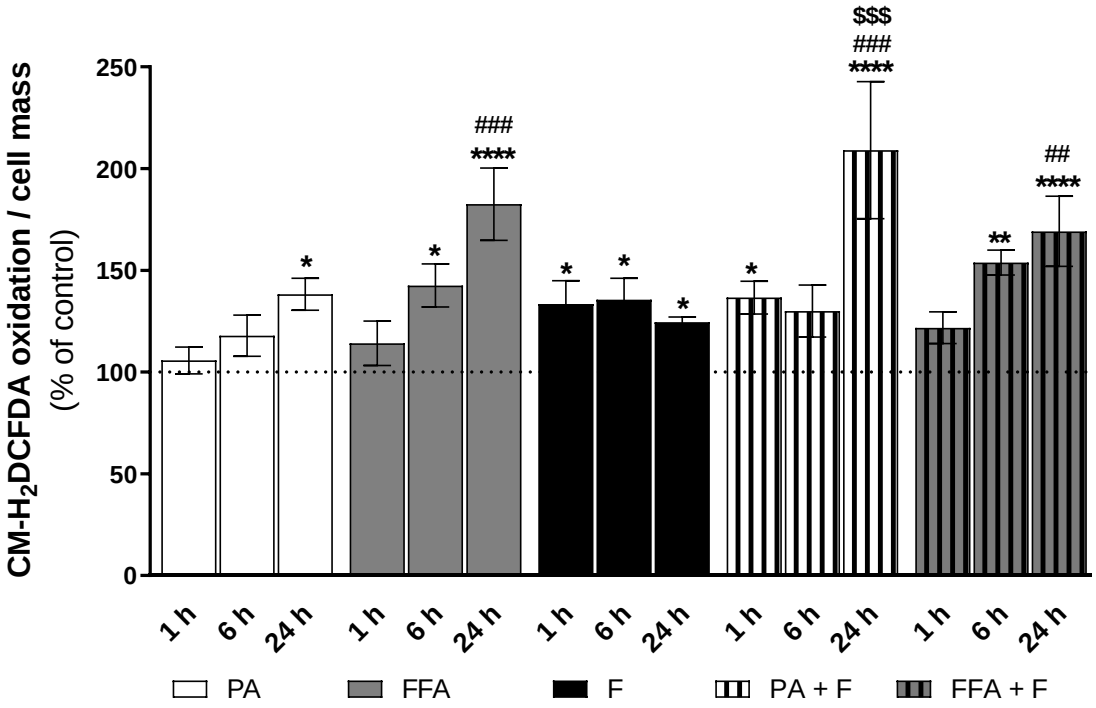

Figure 32. Time-dependent effect of supra-physiological concentrations of FA on the levels of CM-H_2DCFDA-oxidizing ROS. Average cellular CM-H_2DCFDA oxidation signal in cells treated with palmitic acid (PA, 0.5 mM) or a mix of free fatty acids (FFA, 0.25 mM) in the presence or absence of fructose (F, 10 mM) for 1, 6 and 24 h. Data are the mean _ SEM of four independent experiments, and the results normalized on the control condition (CTL = 100%, marked by a dotted line). Significance was accepted with * $p < 0.05$, ** $p < 0.01$, **** $p < 0.0001$ for comparisons between treatment vs. CTL (BSA 0.01 g/mL) and $^{\#\#}$ $p < 0.01$, $^{\#\#\#}$ $p < 0.0005$ for comparisons during time in the same group (24 and 6 h vs. 1 h). Significance for additional fructose effect as accepted with $^{\$\$\$}$ $p < 0.0005$.

8.3.5. Supra-physiological concentrations of FA altered mitochondrial membrane potential (ΔΨm) and induced changes in mitochondrial morphology

In order to determine whether PA or FFA treatments alone or in combination with F affected mitochondrial morphology and ΔΨm, HepG2 cells were labeled with the fluorescent dyes Hoechst (nuclear) and TMRM (polarized mitochondria) and visualized by confocal fluorescence microscopy. PA or PA + F treatments induced time-dependent alterations in mitochondria structure, including conversion into small round-shaped

structures, likely the result of mitochondria fragmentation (**Figure 33A**). Accordingly, a 60% decrease in ΔΨm was observed for these treatment regimens at 24h (**Figure 33B**). These alterations were paralleled by the observation of warped nuclei in PA- or PA + F-treated cells in contrast with more circular-like structures observed in control cells (**Figure 33A**). FFA alone or in combination with F also showed time-dependent mitochondrial fragmentation events, as proven by the decrease in the index of interconnectivity (**Figure 33C**), with no morphological differences in nuclei shape when compared with control (**Figure 33A**). A decrease in ΔΨm was observed under those conditions, but the difference only reached statistical significance for FFA treatment (**Figure 33B**). Fructose alone did not affect either cell morphology or ΔΨm (**Figure 33A-B**). Taken together the data suggests that FA decreased ΔΨm, which could result in or result from alterations in mitochondrial structure and integrity.

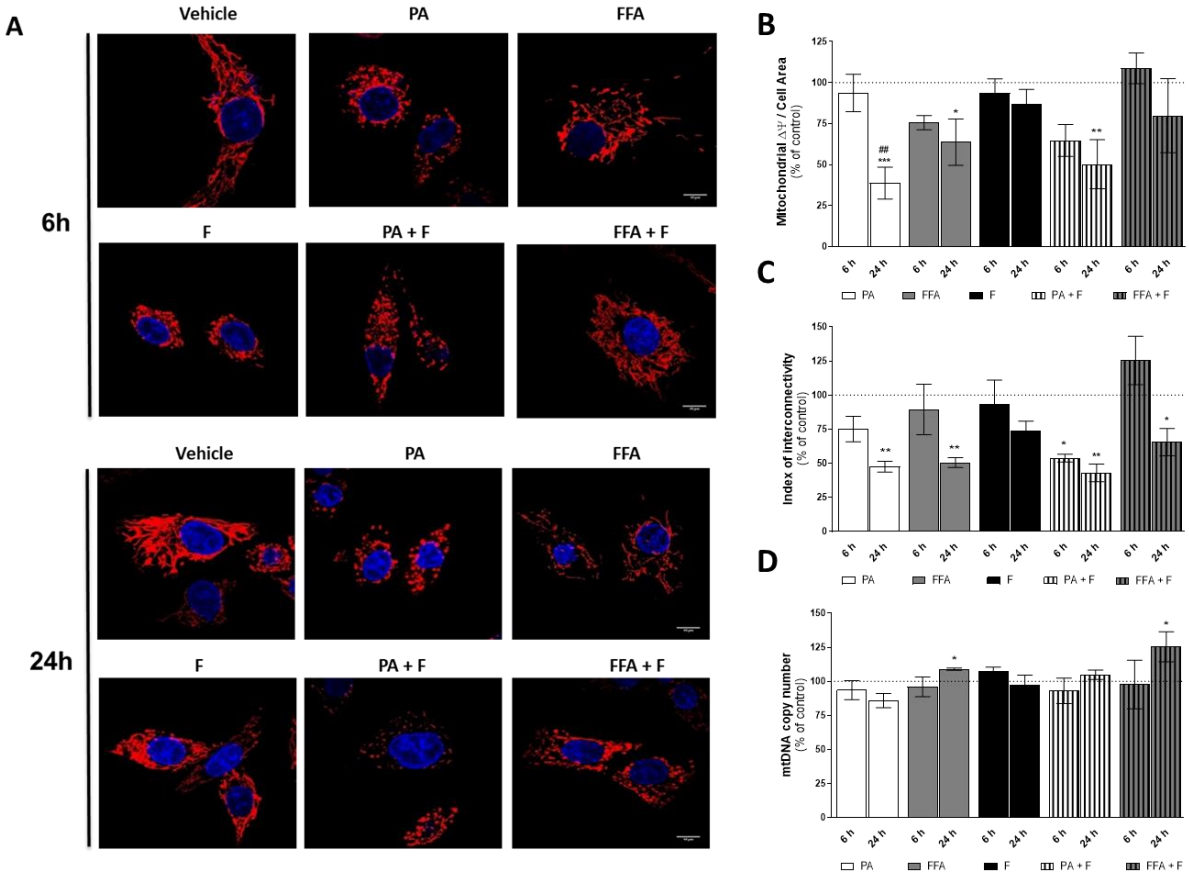

Figure 33. **Effect of supra-physiological concentrations of FA on mitochondrial morphology and mtDNA copy number**. (**A**) Typical background-corrected (COR) image of HepG2 cells stained with the fluorescent cation TMRM and Hoechst 33342 after treatment with palmitic acid (PA, 0.5 mM) or a mix of free fatty

acids (FFA, 0.25 mM) in the presence or absence of fructose (F, 10 mM) for 6 and 24 h. The TMRM and Hoechst fluorescence intensity was color-coded in red and blue, respectively. (**B**) Average mitochondrial TMRM fluorescence intensity calculated from the images. (**C**) Index of mitochondrial interconnectivity calculated from the images. (**D**) mtDNA copy number in HepG2 cells treated with PA or FFA in the presence or absence F for 6 and 24 h. mtDNA copy number was based on the amplification of cytochrome B (encoded on the mitochondrial genome) and -2-microglobulin (encoded on the nuclear genome) ratio. Data are the mean ± SEM of three independent experiments, and the results normalized on the control condition (CTL = 100%, marked by a dotted line). Significance was accepted with * $p < 0.05$, ** $p < 0.01$, *** $p < 0.0005$ for comparisons between treatment vs. CTL (BSA 0.01 g/mL) and $^{\#\#}p < 0.01$ for comparisons during time in the same group (24 and 6 h vs. 1 h).

8.3.6. Supra-physiological concentrations of unsaturated FA significantly increase mtDNA copy number

To understand whether mitochondrial alterations are accompanied by variations in mitochondrial DNA (mtDNA), we next studied the time-dependent impact of the different treatment groups on mtDNA copy number. No changes were observed on mtDNA copy number in cells treated PA ± F (**Figure 33D**). Interestingly, FFA, regardless of F, time-dependently increased mtDNA copy number (**Figure 33D**). Fructose by itself neither increased mtDNA copy number nor aggravated the effects observed for PA- or FFA-treatment regimens (**Figure 33D**). The results suggest that the FFA-treatment regimens lead to different mtDNA content, which could result in or result from different oxidative damage, being the later more severe.

8.3.7. Supra-physiological concentrations of FA altered level of OXPHOS subunits

To determine whether fatty acids overload is implicated with mitochondrial defects in a time-dependent manner, we semi-quantified protein levels for OXPHOS Complex I (NDUFB8), complex II (SDBH), complex III (UQCRC2), complex IV (COXII) and complex V (ATP5A) subunits (**Figure 34A**). PA or PA + F increased the level of complex I NDUFB8 subunit by ≈ 50 % at 6 h followed by a decrease to control levels at the 24 h time point (**Figure 34B**).

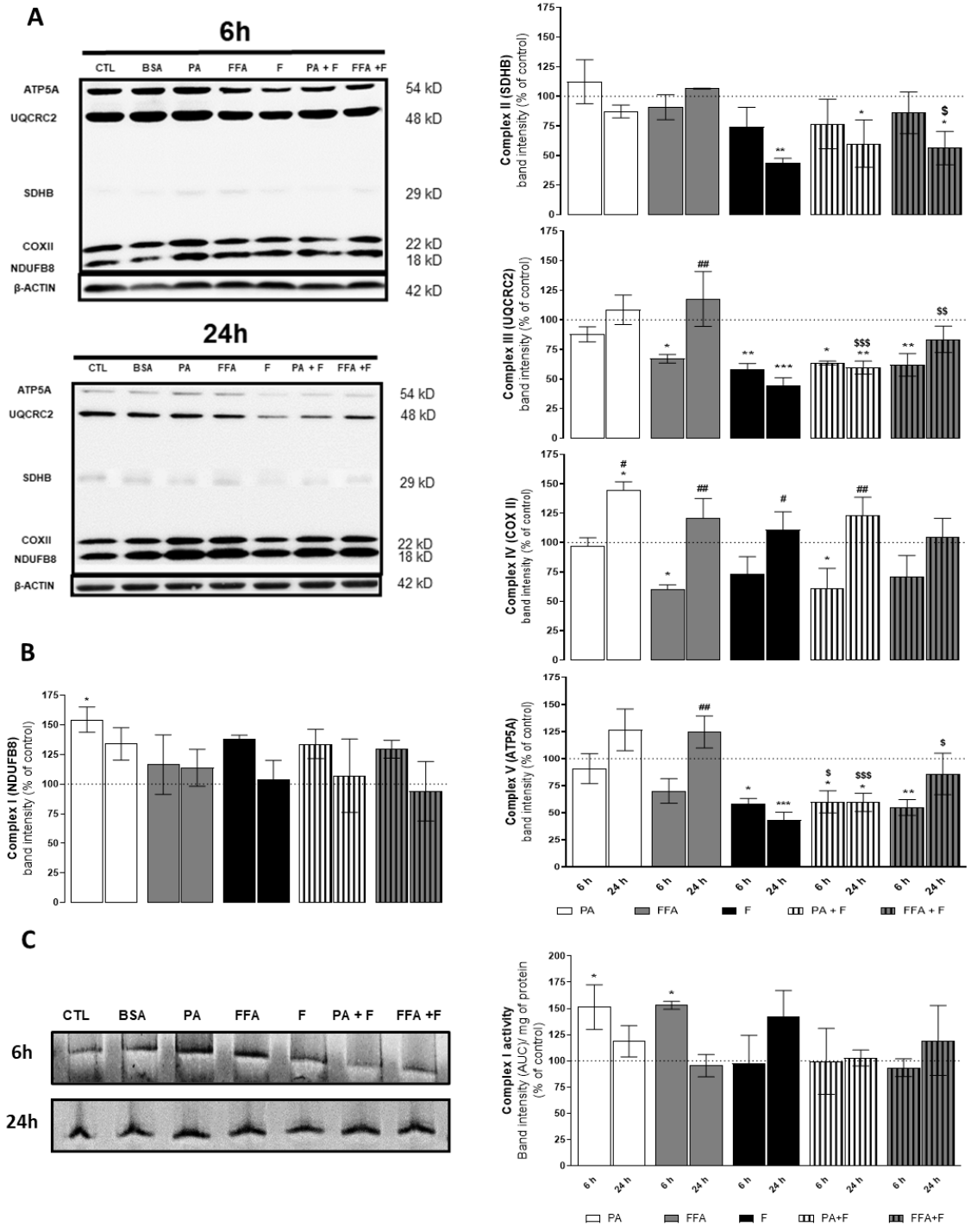

Figure 34. Effect of supra-physiological concentrations of FA on mitochondrial OXPHOS protein levels. (**A**) Typical Western blot result of whole cell homogenates showing the protein level of NDUFB8 (complex I), SDHB (complex II), UQCRC2 (complex III), COXII (complex IV), ATP5A (complex V) subunits, and β-actin (cytosolic marker) in cells treated with palmitic acid (PA, 0.5 mM) or a mix of free fatty acids (FFA, 0.25 mM) in the presence or absence of fructose (F, 10 mM) for 6 and 24 h. This blot was inverted and contrast-optimized for visualization purposes. Quantification of the bands was performed using the original blots. (**B**) Quantification of OXPHOS proteins levels in multiple experiments normalized to β-actin levels and for

the control group (100% marked by a dotted line). (**C**) Typical BN-PAGE in-gel activity result of mitochondrial-enriched fraction homogenates depicting the protein activity of mitochondrial complex I (NADH:ubiquinone oxidoreductase) in cells treated with palmitic acid (PA; 0.5 mM) or a mix of free fatty acids (FFA; 0.25 mM) in the presence or absence of fructose (F; 10 mM) for 6 and 24h. This image was inverted and contrast-optimized for visualization purposes. Quantification of the bands was performed using the original images. Data are the mean ± SEM of four independent experiments, and the results normalized on the control condition (CTL = 100%, marked by a dotted line). Significance was accepted with * $p < 0.05$, ** $p < 0.01$, *** $p < 0.0005$ for comparisons between treatment vs. CTL (BSA 0.01 g/mL) and $^{\#}$ $p < 0.05$, $^{\#\#}$ $p < 0.01$ for comparisons during time in the same group (24 and 6 h vs. 1 h). Significance for additional fructose effect as accepted with $^{\$}$ $p < 0.05$, $^{\$\$}$ $p < 0.01$, $^{\$\$\$}$ $p < 0.0005$.

Although no alterations were found for complex II SDBH subunit at 6 h for any of the treatments, the presence of F in combination with fatty acids (PA or FFA) decreased this subunit at 24 h (**Figure 34B**). The level of complex III UQCRC2 subunit was decreased at 6 h in PA and FFA treatments in the presence of F, while in the absence of this sugar, only the FFA treatment resulted in the same effect. Similarly, F also decreased the protein levels of complex III UQCRC2 subunit.

Interestingly, this effect was also observed at 24 h for F and PA + F treatments, while the levels of this protein recovered to control levels after FFA + F treatment (**Figure 34B**). Except for PA treatment, all the remaining treatments significantly reduced the protein levels of complex IV COXII subunit at 6 h. Interestingly, the levels of COXII subunit were equal in all experimental conditions (**Figure 34B**).

The level of ATP5A subunit was decreased in PA, and FFA treated cells in the presence of F at 6 h, while in the absence of F, no alterations were observed for the same time point. Similarly, F also decreased the level of this subunit of complex V. Interestingly, in F and PA + F treatment, this effect was also observed at 24 h, while in FFA + F treatment, the levels of complex V subunit recovered to control level at the same time-point (**Figure 34B**)

8.3.8. Supra-physiological concentrations of FA altered native mitochondrial electron transport complex I activity

Altered mitochondrial respiration as resulted from impairment of OXPHOS complexes activity has been described as a primary "hit" of NAFLD progression to NASH

[585, 586]. To investigate the contribution of these abnormalities to the final dysfunction outcome, we measured the *in-gel* activity of the major OXPHOS complex (Complex I) using BN-PAGE electrophoresis at 6 and 24 hours. PA- and FFA-treatment showed increased CI activity at 6 h, followed by a decrease to control values at 24 h (**Figure 34C**). Fructose-treatments did not affect complex I activity (**Figure 34C**). These results suggest an early increase of CI activity to overcome the high accumulation of FA, with a later decrease possibly due to the excessive fatty acids β-oxidation and ROS production.

8.3.9. Supra-physiological concentrations of FA time-dependently decrease oxygen consumption rates (OCR) and increased extracellular acidification rates (ECAR)

In order to determine whether fatty acid overload, in the absence or presence of F, affects mitochondrial function, the oxygen consumption rate (OCR) of HepG2 cells was measured by using the Seahorse XF-96 Extracellular Flux Analyzer (**Figure 35A**).

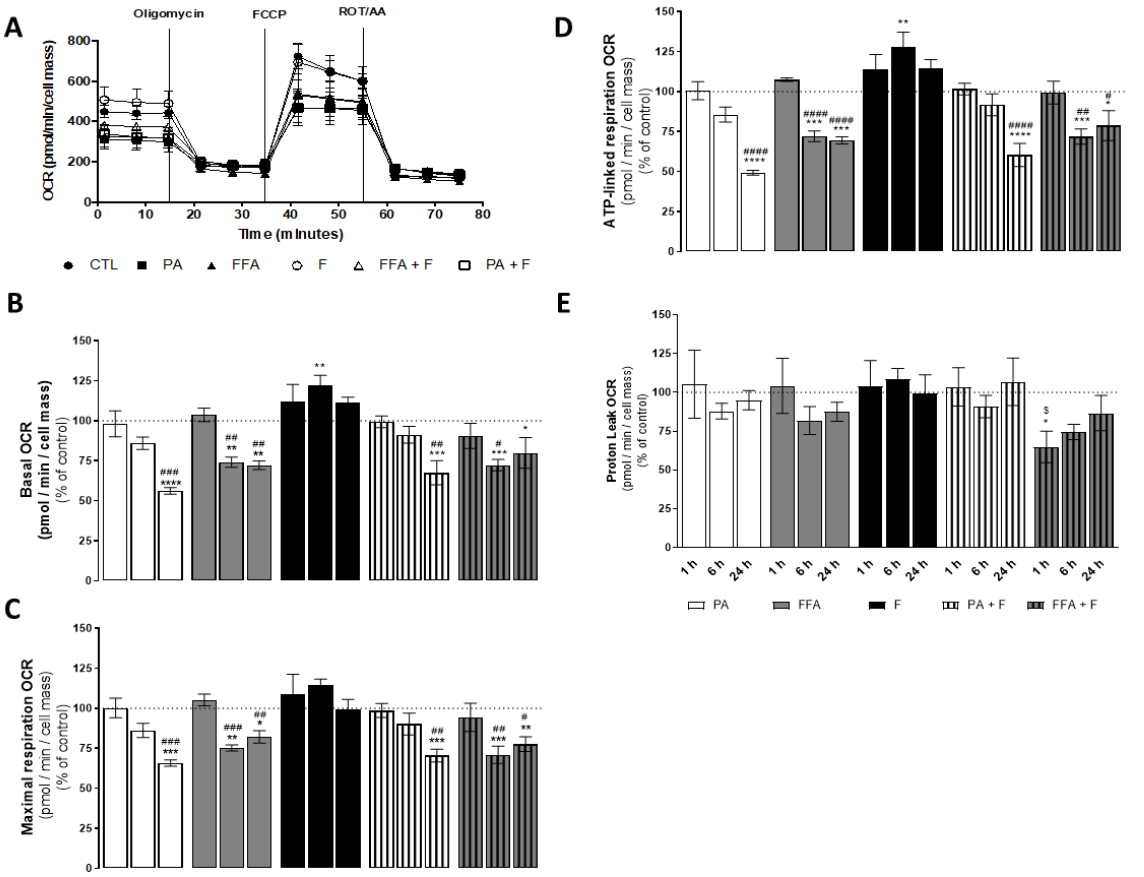

Figure 35. Time-dependent effect of supra-physiological concentration of FA on mitochondrial oxygen consumption. (**A**) Typical representation of oxygen consumption rate (OCR) measurement in HepG2 cells treated with palmitic acid (PA, 0.5 mM) or a mix of free fatty acids (FFA, 0.25 mM) in the presence or absence of fructose (F, 10 mM) for 1, 6 and 24 h. Several respiratory parameters were evaluated: (**B**) cellular basal respiration; (**C**) maximal respiration; (**D**) ATP production-linked respiration; and (**E**) proton leak. Data are mean ± SEM (expressed as pmol O_2/min/cell mass) of four independent experiments, and the results normalized on the control condition (CT = 100%, marked by a dotted line. The data obtained for the different treatments was compared with the control group. Significance was accepted with * $p < 0.05$, ** $p < 0.01$, *** $p < 0.0005$, **** $p < 0.0001$ for comparisons between treatment vs. CTL (BSA 0.01 g/mL) and $^{\#}$ $p < 0.05$, $^{\#\#}$ $p < 0.01$, $^{\#\#\#}$ $p < 0.0005$, $^{\#\#\#\#}$ $p < 0.0001$ for comparisons during time in the same group (24 and 6 h vs. 1 h). Significance for additional fructose effect as accepted with $^{\$}$ $p < 0.05$. Legend: FCCP—carbonyl cyanide 4-(trifluoromethoxy)phenylhydrazone, ROT—rotenone, AA—antimycin A.

PA- and FFA-treatments significantly decreased basal (**Figure. 35B**), ATP-linked (**Figure 35D**), and maximal (**Figure 35C**) OCR respiration in a time-dependent manner, while only FFA + F, for the 6h time-point, affected proton leak respiration (**Figure 35E**). Fructose by itself neither altered mitochondrial OCR nor aggravated the effects observed for PA- or FFA-treatment regimens (**Figure 35**). The extracellular acidification

rate (ECAR), mostly resultant from extrusion of protons to the surrounding medium when lactate is produced, was increased in a time-dependent manner for F-treated cells (**Figure 37A**), although no alterations were observed in PA- or FFA - treated cells (**Figure 37A**). The average data are plotted in **Figure 35B** and **37A**. At the data points tested, cells subjected to PA treatment were shifted for a more quiescent status, while F-treated cells shifted for a more energetic status compared to control data points (**Figure 37B**).

8.3.10. Supra-physiological concentrations of FA induced caspases activation in HepG2 cells which follows ROS and mitochondrial dysfunction

In order to determine whether mitochondrial dysfunction resulting from fatty acid treatment precedes caspase-dependent apoptotic pathways, caspases 8, 9 and 3/7- like activities assays were performed. PA and FFA treatments, in the presence or absence of F significantly decreased caspase 8-like activity at 6 and 24 h. On the other hand, F alone increased caspase 8-like activity at 24 h time-point (**Figure 36A**). Regarding caspase 9-like activity, FFA alone or in combination with F significantly increased its value at 24 h time-point (**Figure 36B**).

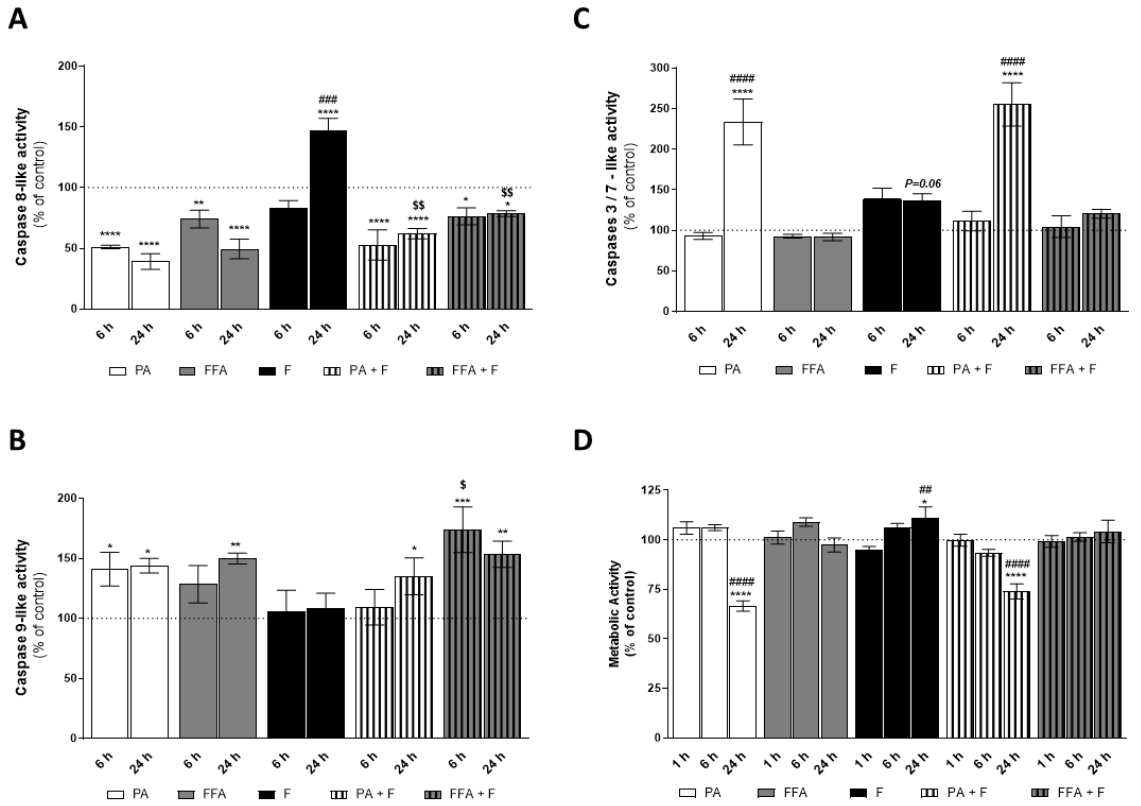

Figure 36. Time-dependent effect of fatty acid excess on caspase activity and cell viability. (**A**) Caspase 8-like activity in HepG2 cells treated with palmitic acid (PA, 0.5 mM) or a mix of free fatty acids (FFA, 0.25 mM) in the presence or absence of fructose (F, 10 mM) for 6 and 24 h. (**B**) Same as panel A but now for caspase 9-like activity. (**C**) Same as panel A but now for caspase 3/7. (D) Cell viability of HepG2 cells cultured in the presence of palmitic acid (PA, 0.5 mM) or a mix of free fatty acids (FFA, 0.25 mM) in the presence or absence of fructose (F, 10 mM) for 6 and 24 h. Data are the mean ± SEM of four independent experiments, and the results normalized on the control condition (CT = 100%, marked by a dotted line). Significance was accepted with * $p < 0.05$, ** $p < 0.01$, *** $p < 0.0005$, **** $p < 0.0001$ for comparisons between treatment vs.CTL (BSA 0.01 g/mL) and $^{\#\#}$ $p < 0.01$, $^{\#\#\#}$ $p < 0.0005$, $^{\#\#\#\#}$ $p < 0.0001$ for comparisons during time in the same group (24 and 6 h vs. 1 h). Significance for additional fructose effect as accepted with $^{\$}$ $p < 0.05$, $^{\$\$}$ $p < 0.01$.

A slight increase was observed in PA treatments alone or in combination at 24h, but only PA-treated cells showed an increased caspase 9-like activity at 6h (**Figure 36B**). On the other hand, PA alone or in combination with F, significantly increased caspases-3/7 activities in a time-dependent manner (**Figure 46C**), while FFA treatment had no effects on caspase 3/7 activity (**Figure 36C**). Taken together, these results suggest that fatty acids induced an early increase in the mitochondrial-independent apoptotic pathway, as observed for the decrease in caspase 8-like activity. Moreover, the

activation of mitochondrial-dependent caspase activation appears to be relevant in PA and FFA treatments. The data reinforce the idea that FFA- and PA-treatments lead to different apoptotic outcomes, being the latter more severe, as observed for the significant increase in caspase 3/7 activities.

8.3.11. Supra-physiological concentrations of saturated FA time-dependently decrease intracellular ATP levels

Considering all observed alterations in the mitochondrial activity, we next measured cellular ATP levels in all treatment groups. PA-treatment (+/- F) significantly decreased ATP levels in a time-dependent manner, while no changes were observed in the case of FFA (**Figure 37C**).

Interestingly, F by itself promoted an initial decrease on intracellular ATP levels, which were restored to control levels after 24 h (**Figure 37C**), a pattern that was also observed for FFA + F treatment (**Figure 37C**). Taken together, these results suggest that the increase in intracellular lipid droplets did not significantly alter intracellular ATP levels. Moreover, the absence of dramatic drop on intracellular ATP levels suggests that FA-induced cell damage trigger apoptotic and not necrotic cell death mechanisms.

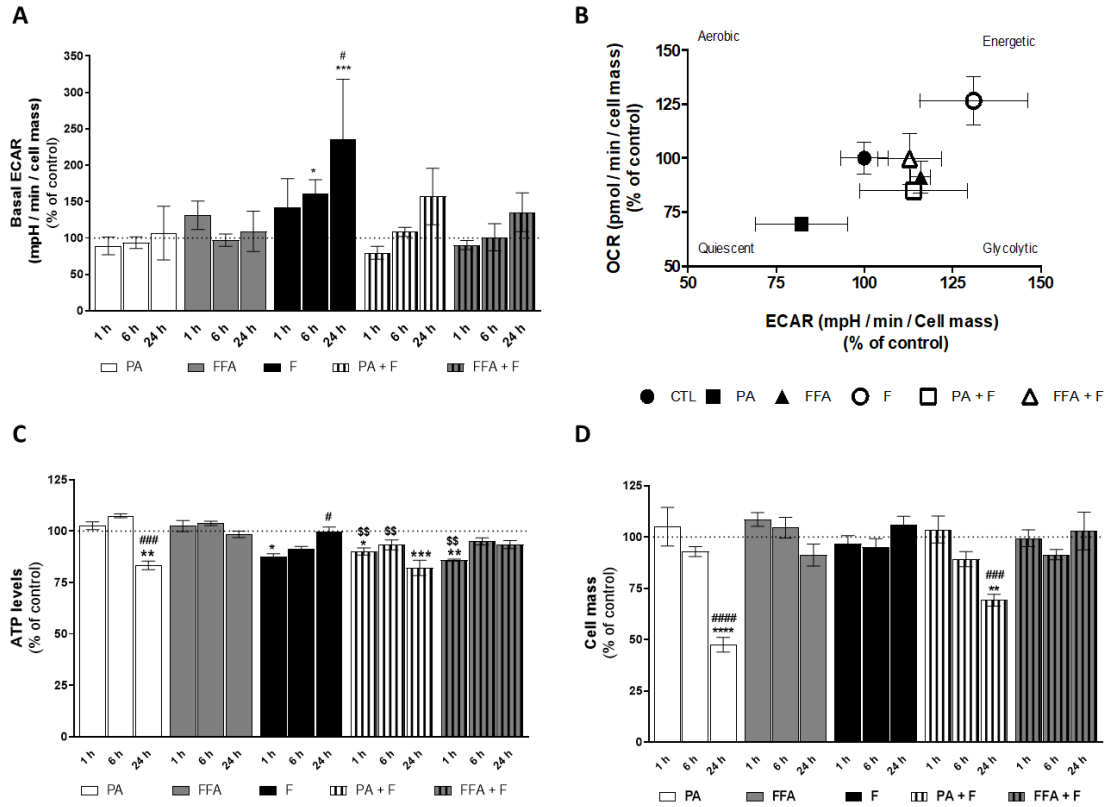

Figure 37. Time-dependent effects of fatty acid excess on extracellular acidification, ATP levels and cell mass. (**A**) Basal extracellular acidification rate of HepG2 cells treated with palmitic acid (PA, 0.5 mM) or a mix of free fatty acids (FFA, 0.25 mM) in the presence or absence of fructose (F, 10 mM) for 1, 6 and 24 h. (**B**) The average mitochondrial basal OCR was plotted against the average basal ECAR (data points taken from Fig. 5b and S2a) in cells submitted to the treatments described above. (**C**) ATP levels in HepG2 cells treated with palmitic acid (PA, 0.5 mM) or a mix of free fatty acids (FFA, 0.25 mM) in the presence or absence of fructose (F, 10 mM) for 6 and 24 h. (**D**) Same as panel A but now for cell mass density. Data are the mean ± SEM of four independent experiments, and the results normalized on the control condition (CT = 100 %, marked by a dotted line). Significance was accepted with *P < 0.05, **P < 0.01, ***P < 0.0005, ****P < 0.0001 for comparisons between treatment vs CTL (BSA 0,01g/mL) and $^{\#}$P < 0.05, $^{\#\#\#}$P < 0.0005, $^{\#\#\#\#}$P < 0.0001 for comparisons during time in the same group (24 and 6 h vs 1 h). Significance for additional fructose effect as accepted with $^{\$\$}$P < 0.01.

8.3.12. Supra-physiological concentrations of FA time dependently decrease cell metabolic activity and mass of human hepatocarcinoma cells

Final endpoints for lipotoxicity were evaluated by measuring cell metabolic activity changes (NADH/NADPH dehydrogenase activity) and mass using the resazurin reduction and sulforhodamine B (SRB) assays, respectively. PA regimens reduced HepG2 metabolic

activity (**Figure 36D**) and mass (**Figure 37D**) in a time-dependent manner, while FFA treatment had no effects on cell metabolic activity (**Figure 36D**) or mass (**Figure 37D**). Fructose by itself increased metabolic activity at 24h (**Figure 36D**), whereas no alterations were observed in cell mass (**Figure 37D**). Moreover, Fructose did not aggravate any of the effects caused by PA- or FFA-treatments alone (**Figure 36D and 37D**). These results demonstrate that different fatty acids treatment regimens (FFA or PA) induced different changes on cell viability and mass, being the later treatment more severe due to hepatic metabolism driven this FA, as observed for the significant decrease in cell viability.

8.3.13. Exploratory data analysis clearly separated PA and FFA regimens by identifying a subset of critical mitochondrial markers

In the present work, we applied exploratory and unsupervised computational data analysis techniques to gain insight into the relations between the biomarkers considered for this study and identify a minimal subset of critical mitochondrial markers can be used to investigate cellular and mitochondrial dysfunction in NAFLD in vitro models. The small number of samples prevents a complete and robust statistical analysis of the results, but it nevertheless allows for identifying relevant hidden patterns and trends.

The 6 matrices from **Figure 38A** present the pairwise correlations for all experimental endpoint measures considered in the study. To enhance clarity and focus the analysis on the most relevant correlations, only absolute values above 0.7 are shown. We present results separately for the PA and FFA treatments, with and without F. For completeness, we also present results obtained in a media without any of the treatments. The analysis of the results unveils the existence of different correlation profiles, regarding PA and FFA treatment groups. While the PA treatment shows a strong positive correlation between PC/PE and caspase 9 activation, the same was not observed in the FFA regimen. Interestingly, a clear negative correlation is observed when comparing ATP levels and basal respiration to caspase 9 activation in FFA treatment.

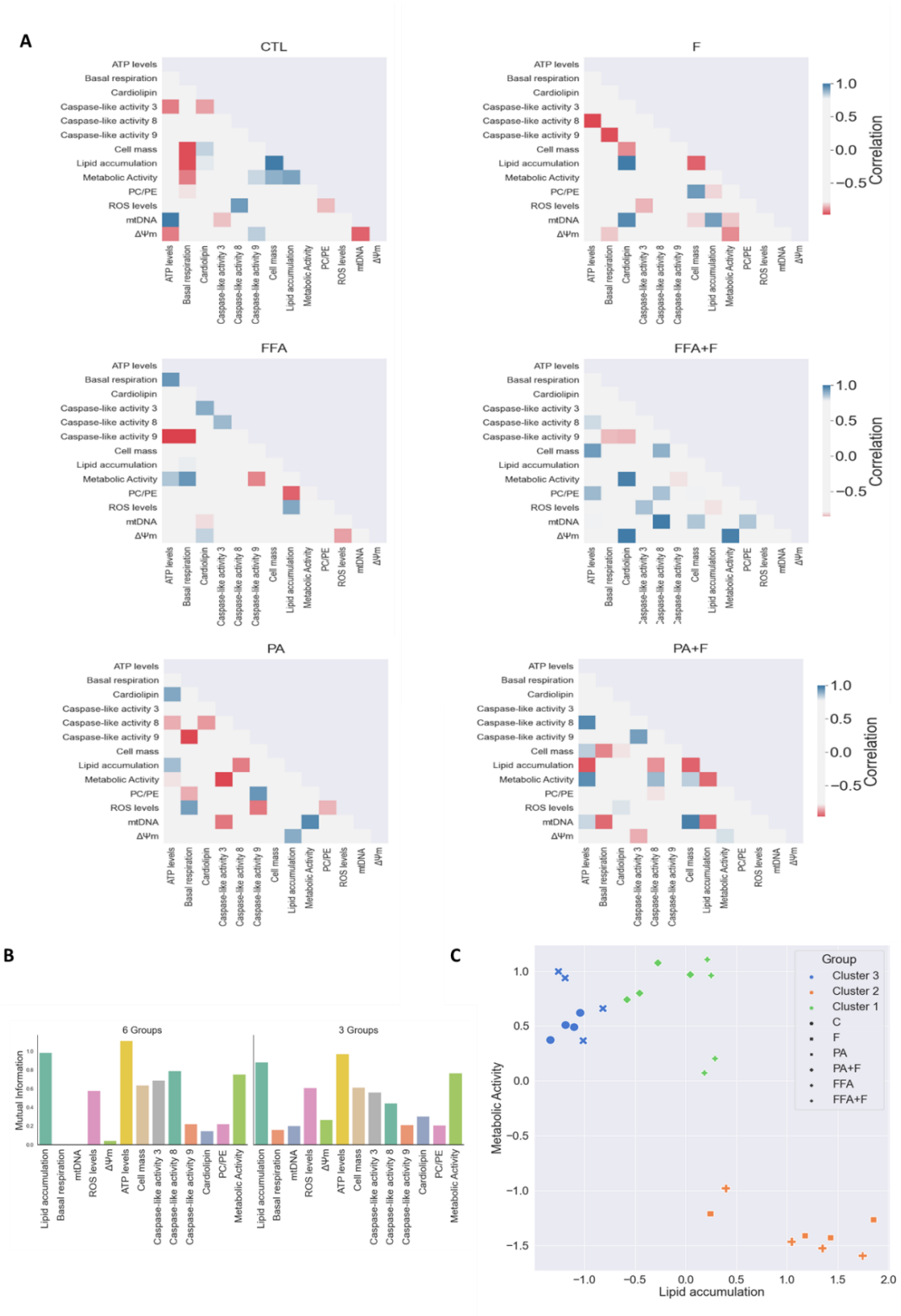

Figure 38. Computational data analysis of all experimental endpoint measures analyzed in different lipotoxicity models on human hepatocytes. (**A**) Correlation matrices of HepG2 cells treated with palmitic acid (PA, 0.5 mM) or a mix of free fatty acids (FFA, 0.25 mM) in the presence or absence of fructose (F, 10 mM). (**B**) Mutual information gain of each individual experimental endpoint (24 h), regarding the existence

of 3 or 6 experimental groups. (**C**) K-means clustering results, for k = 3, using a subset of selected experimental endpoints.

Moreover, metabolic activity correlates negatively with caspase 9 activation, suggesting an important role of these mitochondrial markers in future cell death events for this treatment. Individual mutual information takes every experimental endpoint separately and estimates how relevant this measure is to differentiate targets. It is a relevant step, *e.g.,* in the process of building decision trees [577] and, when considered in the early stages of an exploratory data analysis, it identifies a subset of features that might be particularly relevant to separate experimental samples with different treatments. In this step we consider two alternative target definitions: on the first stage, we consider 6 targets {CTL, F, PA, PA+F, FFA, FFA+F}; on a second approach we aggregate the experimental samples of the original targets two-by-two, ending up with the following groups: {{CTL,F},{ PA, PA+F}, {FFA, FFA+F}}. Charts presented in **Figure 38B** display the individual mutual information for the two scenarios. A brief inspection of the results reveals that the pattern is similar for both situations: ATP levels, lipid accumulation, metabolic activity, ROS levels, cell mass and caspase 3 and 8 are the most relevant features to individually estimate the target, both in the detailed and aggregated scenarios. There are some slight variations, but no single experimental endpoint exhibits a clear different behavior when moving from one situation to the other.

To complete the computational analysis, we applied a non-supervised learning method to verify if it is possible to separate the samples considering just the information provided by a limited subset of experimental endpoints. Building on the analysis of the mutual information, we selected the following endpoints: {Lipid accumulation, ATP levels, Caspase 3, Caspase 9, mtDNA, Metabolic Activity}. All these features exhibit a comparatively high discriminative power of the targets, with the exception of mtDNA.

Nevertheless, we verified that this last endpoint was essential for a good separation. between groups. After standardization, the k-means clustering algorithm was applied to the selected data. The result obtained, when the parameter specifying the number of clusters to form is set to 3, is displayed in **Figure 38C**. Three well-formed clusters, exhibiting good cohesion and separation, are reported by k-means. The clusters

are perfectly homogeneous when considering the aggregated 3 experimental groups previously defined, confirming that the selected subset of features can separate targets. We did some additional experiments and verified that it is not possible to separate the 6 original groups considering any subset of the experimental endpoints. One result from the computational analysis is that the presence or absence of F does not interfere with any separation of the different groups studied, at least in the cell lines used. Indeed, the output of computational analysis strongly correlates with the biological outcomes observed, reinforcing the crucial importance of mitochondria in apoptotic pathways in fatty acid overload scenarios

8.4. Discussion

Supra-physiological accumulation of FA and/or sugars overload in hepatic cells lead to a significant increase in lipid accumulation in the cytoplasm, which can be toxic after a concentration threshold is reached [571]. Here, we investigated time-dependent cellular effects of different in vitro FA overload strategies in the presence or absence of F to understand the chronological events leading to mitochondrial dysfunction upon supra-physiological FA exposure. Exploratory and unsupervised computational approach identified a minimal subset of critical mitochondrial markers that can be used to predict cell death in NAFLD models on human hepatocytes to create a model for high throughput screening of possible therapeutic agents, with particular focus in measuring mitochondrial function. Lipotoxicity driven by high concentrations of lipids and/or carbohydrates exposure has been reported in several *in vitro* studies [548, 549, 587–589]. However, different cellular outcomes were attained depending on lipid composition and/or number of double bonds, which suggest different cellular responses depending on FA composition and time of exposure. We used a well-established human hepatoma cell model (HepG2) owning to the fact that these cells contain major lipid metabolizing enzymes such as triglyceride lipase or 3-hydroxy-3-methyl-glutaryl-coenzyme A reductase (HMG-CoA reductase) [590], which validate that cell line as a proper model for steatotic phenotype studies. To study FA overload, we exposed HepG2 cells to PA, which is the most abundant saturated FFA in mammals and a mixture of FFA (39 % C16:0; 5 % C18:0; 50 % C18:1; 4 % C18:2; 2 % C20:4), in order to mimic FFA

composition in a liver of 24 weeks Western diet- fed mice [572, 573]. The novelty of this work was that we performed initial time-dependent experiments on lipids droplets accumulation and demonstrated that both PA and FFA induced a progressive steatotic phenotype. Although the FFA mixture has been used at half the PA concentration, compared to PA, an identical steatotic phenotype was measured. This result is following previous studies demonstrating that FA structure but also the cellular availability of FA affects lipid droplets accumulation [591]. The addition of F did not result in the accumulation of lipid droplets by itself and did not aggravate the degree of hepatic steatosis when combined with FA. Interestingly, an increased protein amount of hepatic fructokinase was observed in the F group, suggesting that fructolysis may be stimulated by F treatment in this cell model. The small decrease in ATP levels observed at 6h hours for F treatment reinforces the idea of an efficient conversion of Fructose to Fructose-1-P. This result is in accordance with previous studies demonstrating that the initial decreased ATP levels for treatments involving F can be due to the rapid conversion of F to fructose-1-P and later to fructose-1,6-bis P in liver cells, which are both ATP-dependent processes [592]. However, in HepG2 cells, the rate of this process seems to be lower when compared with mouse liver homogenates, as observed by the higher amount of KHK, probably explaining the lack of lipid droplets accumulation in F treatments. Although metabolic effects of F were well documented in these experimental conditions, longer incubation periods should be addressed to reflect TG accumulation in HepG2 cells.

Cellular (phospho)lipid homeostasis is important, particularly for mitochondrial activity, as it plays an important role in coordinating the synthesis of some key membrane phospholipids [593]. The major constituting mitochondrial membrane phospholipids are phosphatidylcholine (PC) (41%) and phosphatidylethanolamine (PE) (32%) [594]. Both PA and FFA treatments showed to induce alterations in phospholipids content with a crucial role in maintaining the structure, integrity, and bioenergetics of mitochondria [595]. On the other hand, F-treated cells showed decreased levels of most of the phospholipids. Phosphatidylinositol (PI) was increased in PA and PA+F treatments, although no difference was observed with FFA (**±** F). Increased PI and phosphoinositides were reported and associated with vacuolar membranes formation and endocytosis [596]. PC/PE ratio alterations may modulate membrane plasticity and bending rigidity

with impact on the conformation dynamics of protein transmembrane domains and regulate the appearance of lipid packing defects influencing fusion phenomena and binding and activity of peripheral membrane properties[597]. PE is highly enriched in mitochondrial inner membranes (~ 40% of total phospholipids) compared to other organelle membranes (15–25% of total phospholipids). In our work, PE was significantly increased on FFA regimens (but not in PA treatments) with no significant alterations for PC, which results in lower PC/PE ratios for FFA treatments, mainly FFA + F. This result, together with higher mtDNA content for the same conditions could indeed mean an increase in mitochondrial mass as an adaptative response to FFA overload. A recent study in hepatocytes from mice showed that lower ratios of PC/PE, a consequence of PE increase, stimulate mitochondrial respiration and activities of proteins of the electron transport chain [598].

Moreover, lower hepatic PC/PE ratios were reported in simple steatosis (SS) patients [599]. In contrast, we observed a decrease in mitochondrial respiration, which may indicate that increase in PE content imposes a curvature stress on the membranes that result not as closely packed as those formed by PC [600], creating lipid-packing defects with deleterious consequences in $\Delta\Psi m$ and O_2 consumption. Interestingly, an increase in mitochondrial PC/PE molar ratio in Chinese hamster ovary cells leads to an impairment in cell survival and growth. In addition, oxygen consumption, cellular ATP levels and the rate of ATP production were markedly reduced, consistent with defects in OXPHOS complexes [601]. Furthermore, a rise in PC/PE ratio has also been found to induce ER stress, leading, in this case, to the unfolding protein response (UPR) through disrupted calcium homoeostasis in leptin-deficient obese mice [309]. As a matter of fact, PA regimens induced a slight increase in PC/PE ratios, as well as a decrease in ATP and OXPHOS complexes, followed by cell death This result is in accordance with previous studies demonstrating that FA overload led to changes in mitochondrial membrane phospholipids profile, possibly with deleterious effects on cellular ROS production and mitochondria function [602].

In our work, supra-physiological levels of FA, in the presence or absence of F, time-dependently increased intracellular ROS levels [548]. In fact, increased mitochondrial β-oxidation of FA, in which FA are repeatedly cleaved to produce acetyl-CoAs that feed the

Krebs cycle and produce reducing equivalents for oxidative phosphorylation [603], is an important source of ROS in NASH [604]. Different levels of steatosis could correlate with stages of mitochondrial health and vice versa. Moreover, altered phospholipids content paralleled by a time-dependent increase in ROS levels support the idea that lipid peroxidation and membrane remodeling could be related. Our work also showed that PA or PA + F treatments resulted in mitochondrial network fragmentation and decreased mitochondrial membrane potential (ΔΨm) The data suggests that the FFA-treatment regimens and PA-treatment led to different oxidative damage status, being the later more severe, and mitochondrial dysfunction, probably due to alterations in mitochondrial structure and integrity. Mitochondria are highly dynamic organelles with constant changes in shape, size and localization around the cell [605]. Mitochondrial shapes vary from small sphere-shaped and oval to extremely interconnected filamentous networks [606]. Altered ΔΨm followed by morphological deformation of mitochondria has been reported in NAFLD, suggesting the involvement of mitochondrial dynamics in the pathogenic progression [607]. This result follows previous studies demonstrating that *in vitro* incubation of cells with saturated fatty acids induces mitochondrial dysfunction, playing a crucial role in NAFLD progression [608].

Mitochondrial dysfunction is commonly associated to mitochondrial fragmentation and loss of mitochondrial DNA (mtDNA) integrity [609]**.** FFA, but not PA, both in the absence or presence of F, time-dependently increased mtDNA copy number. This result is in accordance with previous studies demonstrating that polyunsaturated fatty acids increase mtDNA copy number in human skeletal muscle cells and mouse muscle myoblasts (C2C12) [610, 611], while supra-physiological saturated fatty acid overload treatment reduced mtDNA copy number in C2C12 cells [612]. Although the initial response to high FA import would be an adaptative response to increasing the number of copies of mtDNA [613] and consequently mitochondrial biogenesis, long-term oxidative stress lead to the depletion of mtDNA alongside mitochondrial dysfunction [614]. The data reinforce the idea previously described in the literature that polyunsaturated fatty acids can increase mtDNA copy number as an adaptative response to counteract the initial oxidative stress-induced damage in HepG2 cells [610]. The increase of cardiolipin levels for different treatments also corroborates a possible

adaptation mediated by mitochondrial biogenesis due to CL role in maintaining inner membrane architecture and osmotic stability and the ability to assemble the respiratory supercomplexes [601]. Several studies in rats showed increased levels of CL in the liver as trigger to maintain or boost mitochondrial function in response to the excessive energy substrate availability [615, 616]. However, excess cardiolipin has also been shown to have harmful effects on mitochondria, mainly to its highly susceptible to peroxidation driven by the proximity to respiratory chain proteins, which are the main ROS generators [617].

Mitochondrial dysfunction is commonly associated to mitochondrial fragmentation and alteration of oxidative phosphorylation process [609]. In fact, a defective mitochondrial OXPHOS has been linked to the deleterious effects of FA accumulation and the generation of oxidative stress on hepatocytes during NAFLD [608]. The present results suggested an early increase of complex I NDUFB8 subunit possibly to overcome the excess of supply of fatty acids deposition on the cell and to compensate the decrease of OXPHOS complexes III (UQCR2), IV (COX2) and V (ATP5A) subunits, which is progressively lost with time. The data also suggests a fructose-induced decrease in the level of several OXPHOS subunits, which could be explained by the decrease in phospholipid content [618].

Excess FA critically induces ROS formation, resulting in lipotoxicity associated with ER stress, calcium dysregulation, mitochondrial dysfunction, and bioenergetics failure [619]. PA- and FFA-treatments significantly decreased basal, ATP-linked, and maximal OCR respiration in a time-dependent manner, while no changes were observed on proton leak respiration. Fructose by itself neither decreased mitochondrial function nor aggravated the effects observed for PA- or FFA-treatment regimens. The extracellular acidification rate (ECAR) increased for all treatments involving F, in a time-dependent manner, although no alterations were observed in PA- or FFA- treated cells. Consequently, PA-treated cells' metabolic profile shifted for a more quiescent status, while F-treated cells shifted for a more energetic status compared to control data points. Taken together, these results demonstrate that the increase in intracellular lipid droplets, paralleled by an increase in intracellular ROS levels, led to mitochondrial impairments and consequently, failure of mitochondrial bioenergetics. In most mammalian cells, cellular

energy is generated by the integrated action of the glycolysis pathway in the cytosol, and the tricarboxylic acid (TCA) cycle and OXPHOS system in the mitochondrion [620, 621]. These systems produce energy by catabolizing substrates (e.g. glucose, FA and glutamine) and generate protons (H^+) and lactate during pyruvate metabolism. Alterations in cellular energy metabolism often induce extracellular acidification, the rate and mechanism of which depend on the cell type and used energy substrate [516]. This result agrees with previous studies demonstrating that different FA (PA or FFA) overload progressively led to failure of mitochondrial bioenergetics [622, 623], while sugars (e.g. fructose) may potentiate the glycolytic machinery [624].

Excessive FA accumulation in the liver can trigger oxidative stress, due mainly to early mitochondrial adaptation and further mitochondrial dysfunction, ending with up-regulating of hepatocyte apoptosis via oxidative stress-mediated mechanisms [625]. So far, studies indicate that there are two main apoptotic pathways: the extrinsic or death receptor pathway and the intrinsic or mitochondrial pathway, both resulting from caspase 3 cleavage and dismantling of intracellular components [626].

Our results suggest that FA induced an intrinsic or mitochondrial apoptotic pathway as observed to decrease caspase 8-like activity and time-dependent increase in caspase 9. Indeed, caspase-9 is required for mitochondrial morphological changes and ROS production by cleaving and activating Bid into tBid [627]. Moreover, FFA-treated cells showed a later onset in caspase activation when compared with PA-regimens. The data reinforce the idea described above that FFA-treatment regimens and PA-treatment lead to different oxidative damage status, being the later more severe, as observed for the significant increase in caspase 3/7-like activities. F-treated cells showed increased caspase 8-like activity at 24h with no changes in caspase 9 activation, which suggests that fructose could induce apoptosis by activating extrinsic pathway. When caspase-8 is activated, the execution phase of apoptosis is triggered in this pathway [628]. Furthermore, the presence of fructose in FA treatments increase caspase 8 activity when compared with FA alone, without increase caspase 3/7-like activities or aggravate cell viability.

This result is in accordance with previous studies demonstrating the involvement of caspase-dependent cell death in the lipotoxicity associated with fatty acid overload treatment [629] and that different FA and their cellular availability differentially affected cell's response [549]. Moreover, a link between changes in other mitochondrial lipids and apoptosis events has been described [596]. Concentrations of lysolipids, or ceramides, above their critical micellar concentration can be cytotoxic, as they favor the permeabilization of the outer mitochondrial membrane to release apoptogenic factors into the cytoplasm, acting like detergents [630–633]. In our study, PA-treatment increased LPC levels, corroborating similar results observed in Huh-7 cells [564] and human plasma [634].

Intracellular ATP levels is an *in vitro* and *in vivo* determinant parameter of the cell's decision to die by apoptosis or necroptosis. PA-treatment regimens (in the absence or presence of F) time-dependently significantly decreased ATP levels, while no changes were observed on FFA-treatment regimen. This suggests that the increase of intracellular in intracellular lipid droplet did not significantly alter intracellular ATP levels, probably because in this treatment, cells can still supply ATP demands through glycolysis. Moreover, the absence of a dramatic drop in intracellular ATP levels suggests that FA-induced cell damage triggers apoptotic and not necrotic cell death mechanisms [635], although we did not measure necrosis markers in this work.

Activation of apoptotic caspases results in inactivation or activation of substrates, and the generation of a cascade of signaling events permitting the controlled demolition of cellular components [636]. Hereupon, PA treatment time-dependently reduced HepG2 metabolic activity and mass, while FFA treatment had no effects on cell metabolic activity or mass. Fructose by itself neither reduced cell metabolic activity and mass nor aggravated the effects observed for PA- or FFA-treatment. The FFA regimens displayed similar features regarding PA treatments, such as decreased basal and ATP-linked respiration and $\Delta\Psi m$ reduction and increased ROS levels and CL content but the energetic state of the cell was unaltered with no evidence for caspases 3/7 activation. These data demonstrate that different FA overload (FFA or PA) induced different changes on cell metabolism and death, being the later more severe due to hepatic metabolism driven by PA, as observed for the significant decrease in cell viability. This result is in

accordance with previous studies demonstrating that unsaturated FA showed protective effects against PA-induced toxicity [637–639].

8.5. Conclusions

In summary, we suggest a mechanism of fatty acid overload with a strong association between mitochondria dysfunction and cell death in the HepG2 *in vitro* model (**Figure 39**). Our results confirmed that both FA treatments induce a time-dependent mitochondrial apoptotic pathway, with the deleterious phenotype observed in PA regimens. In agreement, a more comprehensive understanding of how mitochondria chronologically behave in different FA ± fructose incubations in *in vitro* model allowed to attain a feasible model in which mitochondria dysfunction increased in the order: CTL < F < FFA + F≤ FFA < PA ≤ PA + F.

The unsupervised learning algorithms used here created homogeneous and cohesive clusters, with a clear separation between PA and FFA treated samples, identifying a minimal subset of critical mitochondrial experimental endpoints that predict cell dysfunction and death in NAFLD or for high throughput screening of possible therapeutic agents.

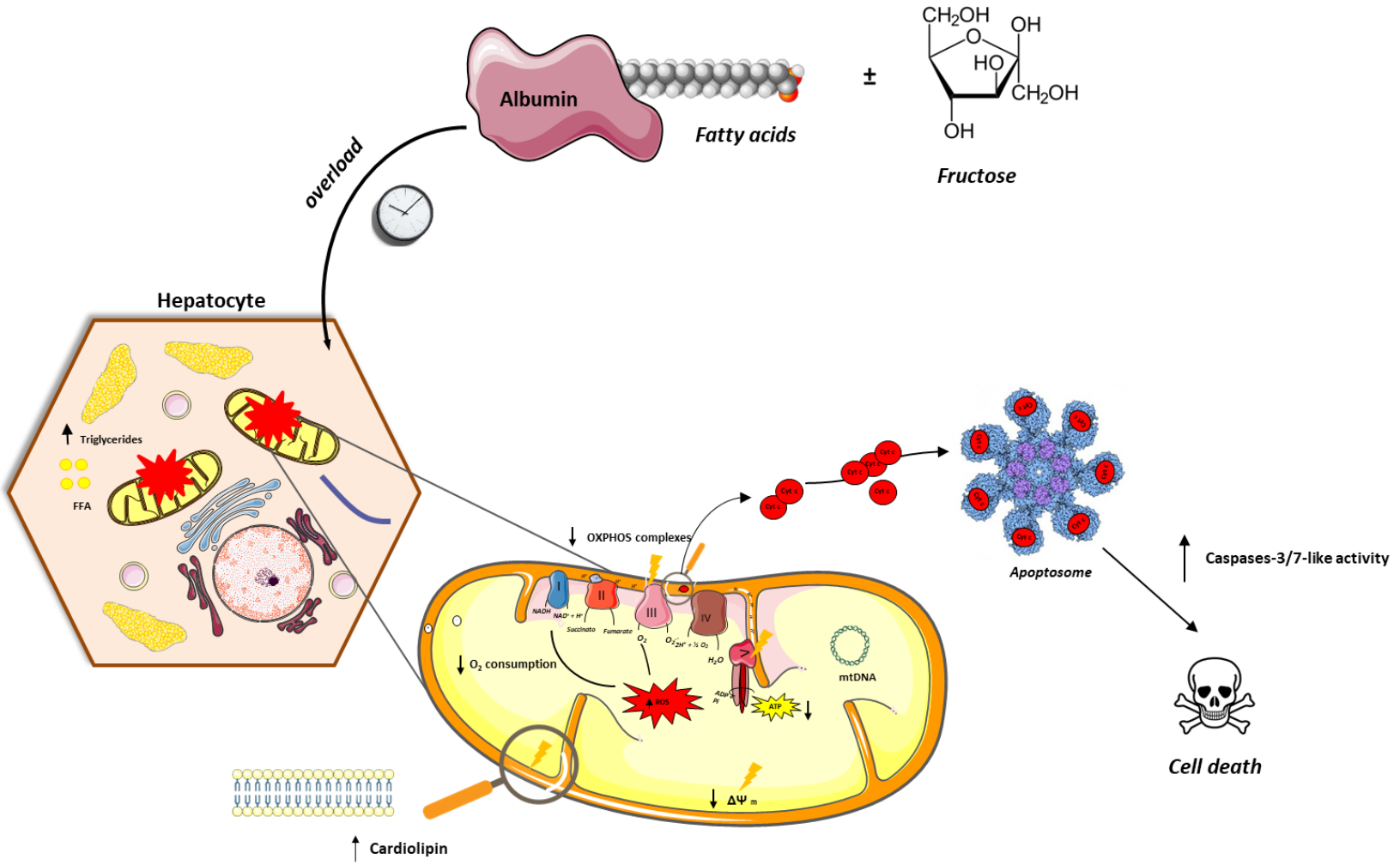

Figure 39. Proposed mechanism for fatty acid overload and mitochondrial dysfunction on human hepatocytes. FA overload are toxic and trigger a time-dependent caspase apoptotic cell death. The progressive increase in neutral lipids content and phospholipid modifications in mitochondria, followed by a large increase in ROS levels compromise mitochondrial function (decrease in ΔΨm, O_2 consumption, and OXPHOS protein levels). Mitochondrial impairment can potentiate even more ROS production. ROS itself, or in conjugation with mitochondrial dysfunction, can lead to activation of caspase-dependent apoptotic cell death pathways. Thus, fatty acid overload led to a time-dependent decrease in cell viability.

9. Chapter

Mitochondria-targeted antioxidant AntiOxCIN$_4$ improved liver steatosis in Western Diet-fed mice by preventing lipid accumulation due to upregulation of fatty acid oxidation, quality control mechanism and antioxidant defense systems

The *in vivo* data presented in this chapter was a collaborative work between the Centre for Neuroscience and Cell Biology (CNC) in Coimbra, Portugal, the University of Porto, Portugal, and the Nencki Institute of Experimental Biology of the Polish Academy of Sciences in Warsaw, Poland. This collaboration work resulted in the already submitted paper, to Redox Biology (REDOX-D-22-00179) entitled "**Mitochondria-targeted antioxidant AntiOxCIN$_4$ improved liver steatosis in Western Diet-fed mice by preventing lipid accumulation due to upregulation of fatty acid oxidation, quality control mechanism and antioxidant defense systems**" and which I am co-first author.

Regarding to this *in vivo* study, I was responsible, together with Inês Simões (at the time a PhD student from Nencki Institute of Experimental Biology of the Polish Academy of Sciences) to daily supplement animals with AntiOxCIN$_4$, the weekly change of water and food in the cages and to weight of the animals at UC-Biotech bioterium, Cantanhede.

9.1. Introduction

NAFLD has become a worldwide public health concern as metabolic syndrome-associated disorders rise. Although the cellular mechanisms behind NAFLD pathogenesis are still controversial, a redox imbalance promoted by exacerbated ROS production seems to contribute to hepatotoxicity and pro-inflammatory processes [372]. These events ultimately culminate in the deleterious progression of the disease from an early stage (NAFL into NASH) and fibrosis. Accumulating evidence of OxS-related phenomena in NAFLD progression fomented antioxidant-based therapies research in NAFLD context.

For instance, vitamin E reduced serum alanine aminotransferase (ALT) levels and hepatic inflammation in NASH patients. However, no improvement in fibrosis was observed [332]. Moreover, in phase II of a clinical trials, silymarin, an extract of milk thistle, known for its antioxidant properties, did not reduce NAFLD activity score (NAS) in NASH patients [640]. More recently, accumulating evidence showing that impairments in mitochondrial function contribute to NAFLD progression spurred active drug discovery efforts focused on mitochondrial pharmacology [641]. Among those, mitochondria-targeted antioxidant MitoQ decreased OxS, cell death and inflammation, reducing liver fibrosis in carbon tetrachloride (CCl_4)-treated mice [642]. Moreover, MitoQ increased liver mitochondrial cardiolipin content in obesogenic diet-fed rats [447]. Nonetheless, MitoQ failed or had minimal beneficial effects in clinical trials of OxS-related disorders, such as Parkinson disease or hepatitis C [449, 450].

As NAFL progresses compromised activation and execution of cellular quality control processes have been widely described [643]. In fact, the blockage of the autophagic pathway contributes to an exacerbation of hepatocyte lipid accumulation and subsequent NAFLD progression, due to impaired regulation of lipophagy [644]. Several polyphenol antioxidants are important autophagic inducers [645, 646]. Caffeic acid improved hepatic steatosis in HFD-fed mice by stimulating autophagy [647] or by alleviating endotoxemia and the proinflammatory response [648]. Notwithstanding, caffeic acid was shown to have poor permeability across human colorectal Caco-2 cells, with low intestinal absorption and low oral bioavailability in rodents [647].

NAFLD is a complex and multifactorial disease, which stimulates diverse therapeutic approaches. Thus, new potential drug candidates presenting target-specific affinity (mitochondria engagement) and the ability to regulate several cellular processes (mitochondrial redox status and quality control mechanisms) to confer cellular protection against oxidative insults are needed. Previously, we demonstrated that the mitochondriotropic antioxidant based on natural dietary caffeic acid (AntiOxCIN$_4$) can prevent OxS-related complications through activation of endogenous ROS-protective pathways in normal primary human fibroblasts (PHSF) [460] and in PHSF from sporadic Parkinson disease patients [461]. AntiOxCIN$_4$ also increases cell stress resistance in human

hepatoma-derived cells (HepG2) by activating the Nrf2-p62-KEAP1 axis, leading to up-regulation of antioxidant defenses, triggering macroautophagy and/or mitochondrial autophagy (mitophagy) and mitochondrial biogenesis, contributing to higher resistance to OxS and lipotoxicity events [649].

In this chapter, we collected clear evidence for the therapeutic benefits of the AntiOxCIN$_4$ supplementation in a Western diet (WD)-induced NAFL mice model. Cellular and molecular evidence in human hepatocytes (HepG2) subjected to supraphysiological FFA were acquired to corroborate the *in vivo* data. Our study shows the beneficial role of AntiOxCIN$_4$ supplementation in NAFL, suggesting the potential mechanism of action for improving steatotic liver phenotype. The remarkable effects of AntiOxCIN$_4$ supplementation on fatty acid oxidation (FAO) and endogenous antioxidant defense stimulation as well as the prevention of obesity-induced autophagic blockage in WD-fed mice highlight AntiOxCIN$_4$ as a great potential candidate for the prevention/treatment of NAFL.

9.2. Material and Methods

9.2.1. Chemicals and reagents

Cell culture medium, medium components, chemicals and reagents were purchased from Sigma-Aldrich (St. Louis, MO, USA) unless otherwise specified.

9.2.2. Synthesis of AntiOxCIN$_4$

The synthetic strategy and procedures used in the synthesis of the mitochondriotropic antioxidant AntiOxCIN$_4$ have been previously described [458]. The structural data is in accordance with the literature [458] and the purity of AntiOxCIN$_4$ was higher than 98%.

9.2.3. Ethics

The animal study was approved by the Animal Welfare Committee at the University of Coimbra (ORBEA_131_2016/24032016) and by the Portuguese Authority of Directorate-General for Food and Veterinary (DGAV - 0421/000/000/2016). All the

procedures were also conducted in accordance with the European Union directive (2010/63/EU) by accredited users.

9.2.4. Animal study

Four-week-old male C57BL/6J mice were obtained from Charles River Laboratories (Charles River, Barcelona, Spain). Animals were housed at the Bioterium of the Center for Neuroscience and Cell Biology, University of Coimbra (UC) – Biotech (Pathogen Free Animal Facility, according to the FELASA agents exclusion list) under controlled 12 h light/dark cycles at 20-24ºC with 45-65% of humidity environment. Upon delivery to the Bioterium, animals acclimatized for 1 week with unlimited access to sterilized water and standard chow diet (SD), composed of 48 % carbohydrate, 14 % protein and 4 % fat (2014S). The chow diet was purchased from ENVIGO Teklad (Madison, MI, USA). At the beginning of the experimental study, animals (n = 20) were divided in 2 experimental groups: in the first one (n = 10), mice were fed with a SD and a vehicle sugar free jelly (daily) (Vehicle + SD), whereas in the other group (n = 10), mice were fed with SD and a sugar free jelly containing AntiOxCIN$_4$ (2.5mg/animal/day) (AntiOxCIN$_4$ + SD). After two weeks, each experimental group was divided into two other groups: half of the mice were maintained in SD while the other half of the mice were fed with “Western Diet” (WD) for sixteen weeks. Therefore, the Vehicle + SD group was divided in Vehicle + SD (n = 5) and Vehicle + WD (n = 5); while AntiOxCIN$_4$ + SD was divided in AntiOxCIN$_4$ + SD (n = 5) and AntiOxCIN$_4$ + WD (n = 5). WD was composed of 35 % carbohydrate, 21 % protein and 3 0% fat (E15126 - Ssniff, Soest, Germany), being supplemented with 30 % sucrose in drinking water. The group of mice fed with Vehicle + SD was established as the control group of the study. After the period of feeding, mice were anesthetized by isoflurane inhalation and then, animal euthanasia by cervical dislocation. Right before cervical dislocation, blood samples were taken by cardiac puncture into EDTA KE-coated microtubes (Sarsted, Nümbrecht, Germany), centrifuged and the plasma was collected and stored for further analysis (−80ºC). The livers were excised, weighed and divided either for mitochondrial isolation, histological staining or stored at -80ºC until further investigations.

The main goal of this study is to evaluate the preventive effects of AntiOxCIN$_4$ on WD-fed animals with an induced NAFL phenotype. Therefore, animals that did not develop the expected phenotype [487] were excluded from the study.

9.2.5. Plasma analysis

Alanine aminotransferase (ALT) and aspartate aminotransferase (AST) activity levels, indicators of hepatocyte function, and cholesterol levels were measured using commercially available kits (A-R0200001001, A-R0200001101 and A-R0100000501, respectively; I.S.E. S.r.l., Guidonia, Italy) according to the manufacturer's protocol in an automated analyzer Miura 200 (I.S.E. S.r.l.).

9.2.6. Liver histology

For hematoxylin and eosin (H&E), Masson trichrome and immunohistological stainings, excised livers were fixed in 10 % neutral buffered formalin (HT 50-1-1, Sigma-Aldrich) for 48 h at room temperature. Then, the tissue was trimmed and processed for paraffin embedding. Briefly, the protocol was as follows: 70 % ethanol (two times, 1 h each), 80 % ethanol (1 h), 95 % ethanol (1 h), 100 % ethanol (three times, 1.5 h each); then xylene (3 times, 1.5 h each); and paraffin wax (two times at 58-60 ºC, for 2 h each) in order to get paraffin blocks.

1) For H&E and Masson trichrome, paraffin blocks were cut into 3 µm slices and mounted on SuperFrost microscope slides (Gerhard Menzel GMBH, Braunschweig, Germany). Liver slices were deparaffinized and rehydrated before H&E and Masson trichrome staining were applied according to the standard protocol [650]. For Masson's staining, Bouin's solution (HT10132, Sigma-Aldrich), Weigert's iron hematoxylin solution (HT1079-1SET, Sigma-Aldrich) and Masson Trichrome Stain kit (HT15-1KT, Sigma-Aldrich) were used.

2) For immunohistochemistry of CD3, CD4 and CD68 inflammatory markers, formalin-fixed embedded paraffin samples were used. Before antigen detection, antigen retrieval was performed using low pH Target Retrieval Solution (DAKO, Glostrup, Denmark) at 99.5°C for 30 min. Then, the following antibodies were used: CD3 (A0452,

Agilent, Santa Clara, USA), CD4 (orb4830, Biorbyt, St Louis, USA) and CD68 (GTX37743, GeneTex, Alton Pkwy Irvine, USA).

3) All the stainings were visualized in a Hamamatsu NanoZoomer 2.0 RS scanner (Hamamatsu Photonics, Hamamatsu, Japan) at the original magnification of 40×.

4) NAFLD activity (NAS) score was firstly described by Kleiner *et al* [650]. This system is based on the histopathological evaluation of four criteria: steatosis, hepatocellular ballooning, lobular inflammation and fibrosis. Steatosis grade comprises: grade 0 = <5 %; grade 1 = 5-33 %; grade 2 = 34-66 %; grade 3 = >66 %. Ballooning grade includes: grade 0 = none; grade 1 = a few ballooned cells; grade 2 = many ballooned cells. Lobular inflammation comprises: grade 0 = none; grade 1 = < 2 foci per field of view (200x magnification); grade 2 = 2-4 foci per field of view; grade 3 = > 4 foci per field of view (note: lipogranulomas are considered in this category). Fibrosis grade includes: grade 0 = none; grade 1a = zone 3, perisinusoidal fibrosis; grade 1b = zone 3, perisinusoidal fibrosis being detected in H&E; grade 1c = only periportal/ portal fibrosis; grade 2 = zone 3 plus periportal/portal fibrosis; grade 3 = zone 3 plus periportal/portal fibrosis with bridging fibrosis; grade 4 = cirrhosis. & - represents the sum of steatosis, hepatocyte ballooning, lobular inflammation and fibrosis grades obtained. This analysis was performed blindly by a pathologist of The Children's Memorial Health Institute (Warsaw, Poland).

9.2.7. Mitochondrial isolation

Livers (without gallbladder) were washed, minced and homogenized in an ice-cold homogenization solution I (50 mM Tris-HCl, pH 7.4, 75 mM sucrose, 225 mM mannitol, 0.5 % fatty acid free bovine serum albumin (BSA), 0.5 mM EGTA). Liver homogenate was centrifuged at 740X*g* at 4 ºC for 3 min. The supernatant was collected and centrifuged again at 740X*g* at 4 ºC for 5 min. Then, supernatant was collected and centrifuged at 10000X*g* at 4 ºC for 10 min. The supernatant was isolated and stored as the cytosolic fraction. The mitochondrial fraction pellet was resuspended in ice-cold solution II (50 mM Tris-HCl, pH 7.4, 75 mM sucrose, 225 mM mannitol, 0.5 % fatty acid free BSA) and centrifuged at 10000x g at 4ºC for 10 min. The resulting pellet was resuspended in ice-cold solution III (50 mM Tris-HCl, pH 7.4, 75 mM sucrose, 225 mM mannitol) and for

the last time centrifuged at 10000X*g* at 4 ºC for 10 min. The final pellet was resuspended in ice-cold solution III. Mitochondrial protein content was quantified according to the bicinchoninic acid (BCA) assay.

9.2.8. Isolated hepatic mitochondria oxygen consumption rate measurement

A XFe96 sensor cartridge placed in a 96-well calibration plate was left to hydrate at 37ºC in the day before the assay. For the coupling assay, XFe96 sensor cartridge was loaded with ADP (4 mM final), oligomycin (2 µg/µL final), FCCP (4 µM final) and antimycin A (2 µM final) in MAS 3x. Plate injections were performed according to: ADP into port A, oligomycin into port B, FCCP into port C and antimycin A into port D. 2.5 µg of fresh liver fresh isolated mitochondria was diluted in mitochondrial assay solution (MAS) 1x (70 mM sucrose, 220 mM mannitol, 10 mM KH_2PO_4, 5 mM $MgCl_2$, 2 mM HEPES, 1.0 mM EGTA and 0.2 % fatty acid-free BSA (pH 7.2)) containing the substrates: succinic acid (10 mM) and rotenone (2 µM); and pyruvic acid (10 mM) and malic acid (5 mM). OCR mitochondrial states: State 2 - basal oxygen consumption; State 3 - ADP-stimulated respiration; State 4o - no-ADP stimulated respiration; State 3u - maximal uncoupled respiration; AA - inhibition of respiration.

For the electron flow assay, inhibitors were prepared in MAS 3x and injected as follows: rotenone (2 µM final) into port A, succinic acid (10 mM final) into port B, antimycin A (2 µM final) into port C and ascorbate (10 mM final)/N,N,N',N'-tetramethyl-p-phenylenediamine (TMPD) (100 µM final) into port D. 2.5 µg of fresh liver fresh isolated mitochondria was diluted in mitochondrial assay solution (MAS) 1x (70 mM sucrose, 220 mM mannitol, 10 mM KH_2PO_4, 5 mM $MgCl_2$, 2 mM HEPES, 1.0 mM EGTA and 0.2 % fatty acid-free BSA (pH 7.2)) containing the substrates: pyruvic acid (10 mM), malic acid (2 mM) and FCCP (2 µM).

After seeding mitochondria in the 96-well assay plate, the plate was centrifuged at 2000X*g* per 20 min at 4ºC followed by 10 min of incubation at 25 ºC. Compounds were pneumatically injected, and three baseline rate measurements of OCR and electron flow assay were performed using a 30 s mix followed by 3 min cycle. Data obtained was analyzed using Software Version Wave Desktop 2.6.

9.2.9. Evaluation of mitochondrial permeability transition pore (mPTP) opening in isolated liver mitochondria

The sensitivity of isolated liver mitochondrial fractions to mitochondrial permeability transition pore (mPTP) opening was measured at 540 nm using a Cytation 3 multi-mode microplate reader (BioTek Instruments, Inc.). The assay was done using 150 µg of mitochondrial protein in the presence of reaction buffer (225 mM mannitol, 75 mM sucrose, 1 mM KH_2PO_4, 3 mM HEPES and 10 µM EGTA), 10 mM succinate and 2 µM rotenone. The reaction was initiated by adding the following mPTP inducers: 200 µM tert-butyl hydroperoxide and 150 µM $CaCl_2$. A negative control for mPTP opening was performed by adding the specific pore de-sensitizer 1 µM cyclosporin-A to the well plate prior to mPTP inducers.

9.2.10. Evaluation of H_2O_2 production in isolated liver mitochondria

Mitochondrial ROS (mtROS) production was measured at an excitation wavelength of 560 nm and emission wavelength of 590 nm using a Cytation 3 multi-mode microplate reader (BioTek Instruments, Inc.) using the Amplex Red kit. The measurement was initiated by adding 100 µg of mitochondrial protein to the reaction buffer (50 mM Tris-HCl, pH 7.4, 75 mM sucrose, 225 mM mannitol) supplemented with 5 µM Amplex Red, 20 U/mL horseradish peroxidase and 40 U/mL superoxide dismutase (SOD) in the presence of 5 mM glutamate/malate or 10 mM succinate/2 µM rotenone as the source of the substrate. mtROS were determined from the slope of the linear regression of experimental values.

9.2.11. Lipidomic analysis

Liver lipids were extracted following the Bligh and Dyer method [651]. 1.8 mg of frozen liver and 500 µg of frozen liver isolated mitochondria were used for neutral lipids and phospholipid analysis of each sample, respectively. Briefly, samples were homogenized in 2:1 mixture of chloroform and methanol with 0.01 % of butylated hydroxytoluene. After, distilled water was added and samples were vortexed before being centrifuged at 1000X*g*, 4ºC for 10 min. A two-phase system composed by the aqueous and

organic phase was obtained. The organic phase was collected and stored at -20 ºC until further analysis.

For mitochondrial phospholipids quantification, the solvents in the organic phase of the samples were evaporated in a N_2 flow. Then, chloroform/methanol (2:1) mixture was added to the lipid extracts, followed by its loading into a pre-activated thin-layer chromatography (TLC) silica gel-60 plate (1003900001, Merck, Darmstadt, Germany) (at 110 ºC for 90 min). Mitochondrial phospholipids content was developed in a TLC tank using chloroform/methanol/acetic acid/water (50/37.5/3.5/2 (v/v/v/v)) as the mobile solvent for approximately 2 h. In order to reveal phospholipids levels, the plate was soaked in a 10 % cupric sulfate/8% phosphoric acid and burned at 140 ºC for 20 min. Different classes of phospholipids were quantified with Image Studio Lite (version 5.2).

For hepatic neutral lipids quantification, the solvents in the organic phase of the samples were evaporated in a N_2 flow. Lipids extracts were then redissolved in chloroform/methanol (2:1) mixture, followed by its loading into a TLC silica gel-60 plate (Merck, Darmstadt, Germany). Neutral lipids were developed in a TLC tank using heptane/isopropyl ether/glacial acetic acid (60/40/3 (v/v/v)) as a mobile phase for 1 h. The neutral lipids bands were revealed by soaking the TLC plate in a 10 % cupric sulfate/8 % phosphoric acid and heated at 140 ºC for 20 min. Different classes of neutral lipids were quantified with Image Studio Lite (version 5.2).

9.2.12. Metabolomic analysis

A metabolomic analysis of livers was obtained from ^{1}H and ^{13}C nuclear magnetic resonance (NMR) spectra. For it, the separation of aqueous and organic phases, containing water soluble metabolites and lipids (TG), respectively, was performed according to the Folch method [652]. Briefly, frozen liver tissue was homogenized in methanol (6.7 mL/g) and mixed with chloroform (13.3 mL/g). Samples were incubated under agitation for 1 h on ice. Next, samples were centrifuged at 13000X*g* for 10 min, 4 ºC, with the pellet saved and supernatant collected for further processing. Separation of phases was induced by addition of distilled water, followed by another centrifugation at 13000X*g* for 10 min, 4 ºC. Aqueous phase was lyophilized and organic phase was left to air dry for two days, before its storage at -80 ºC until further use.

a) Liver TG purification. Organic phase was purified with the use of discovery solid phase extraction DSC-Si silica columns (2 g/12 mL). Columns were washed with 8 mL of hexane/methyl tert-butyl ether (MTBE) (96/4 (v/v)) and with 24 mL of hexane. After washed, columns were loaded with 500 µL of hexane/ MTBE (200/3 (v/v)) of each resuspended sample plus another volume resultant from tube wash. Next, each column was eluted with 32 mL of hexane/ MTBE (96/4 (v/v)) for several dark flasks. Flasks of each sample were then pooled together and afterwards air dried and saved at -20 ºC until running NMR spectra.

b) NMR experiments. NMR spectra of purified TG were obtained at 25 ºC with an Agilent V600 spectrometer (12.1 T, 600 MHz), equipped with a 3 mm broadband probe. TG samples were dissolved in 0.2 mL of $CDCl_3$ and 10 µL of pyrazine standard and placed in 3 mm NMR tubes. Spectra were acquired with a 70 º pulse, 2.5 sec of acquisition time, 0.5 sec of pulse delay, with the collection of 2000-4000 fid. Spectra were processed and peaks were integrated using an ACD/NMR Processor Academic Edition. ^{13}C spectra were set with chloroform as a reference standard (77.36 ppm) while ^{1}H spectra were set with pyrazine as the reference (8.6 ppm). FA profile (in percentage) of SFAs, MUFAs, palmitoleate acid and linoleate acid were estimated from the ^{13}C spectra, while ω-3 FAs and non ω-3 FAs were estimated from ^{1}H spectra described by Duarte *et al* [224].

9.2.13. Measurement of non-enzymatic antioxidants:

9.2.13.1. Measurement of glutathione (GSH) levels

GSH levels were determined following the method proposed by Rahman *et al* [653]. 50 mg of liver tissue was washed in cold 0.9 % NaCl solution. After that, the liver was minced and homogenized in ice-cold working solution (5 % metaphosphoric acid and 0.6% sulfosalicylic acid mixture). Homogenates were centrifuged at 3000X*g* at 4 °C for 10 min. The upper clear aqueous layer was collected and kept at 0–4 °C for the assay (within 1 h). For GSH assessment, reaction of 30 µg of liver lysate and equal volumes of DTNB and GR solutions were combined. After 30 s (conversion of GSSG to GSH), β-NADPH was added, and the absorbance measured every 30 s for 2 min in a Cytation 3 multi-mode microplate reader (BioTek Instruments, Inc.) at 412 nm. The rate of 2-nitro-

5-thiobenzoic acid formation was calculated. Total GSH concentration in the samples was assessed by using linear regression to calculate the values obtained from the standard curve of GSH and expressed as nM/mg protein.

9.2.13.2. Total antioxidant capacity

The determination of antioxidant activity present in cytosolic and mitochondrial fractions was based on an adaptation of the method described by Arnao *et al* [654]. This method measures the antioxidant capacity of each sample by determining the decrease in the amount of the 2,2'-azino-bis (3-ethylbenzothiazoline-6-sulfonic acid) (ABTS) radical. The ABTS radical was prepared by mixing 50 mM phosphate buffer, pH 7.5, 50 mM ABTS, 10 mM hydrogen peroxide (H_2O_2), 1 mM horseradish peroxidase, followed by its incubation in dark, at 4 ºC for 4 h. After, 90-150 µg of cytosol or 150-300 µg of mitochondrial fractions were mixed with stabilized ABTS radical and the absorbance was measured at 730 nm in a microplate reader (Infinite 200Pro, Tecan, Männedorf, Switzerland) for 15 min. Results are expressed per % of Vehicle + SD.

9.2.14. Measurement of antioxidant enzymes activities

9.2.14.1. Catalase activity

The rate of decomposition of H_2O_2 by catalase was calculated following the method proposed by Grilo *et al* [655]. Briefly, 10 mg of frozen liver tissue was homogenized in 50 mM phosphate buffer, pH 7.8. The method was based on the reaction of 10 µg of mitochondria with 50 mM phosphate buffer (pH 7.8) and 10 mM H_2O_2 solution in a 96 well plate, being the absorbance measured at 240 nm for 2 min and 30 s in a Cytation 3 multi-mode microplate reader (BioTek Instruments, Inc.).

9.2.15. Superoxide dismutase activity

The conversion of $O_2^{\bullet -}$ into H_2O_2 by SOD was determined in freshly isolated mitochondria and in total liver lysate. Both samples were prepared according to the manufacturer's protocol of SOD assay kit (ADI-900-157, Enzo Life Sciences, NY, USA). After protein quantification using BCA method, 10 µg of isolated mitochondria were used in a

96 well plate, being the absorbance measured at 450 nm for 10 min at room temperature in a Cytation 3 multi-mode microplate reader (BioTek Instruments, Inc.).

9.2.16. Measurement of glutathione disulfide reductase (GR) activity

50 mg of frozen liver tissue was homogenized in 1 mL of phosphate buffer [50 mM NaH_2PO_4/ Na_2HPO_4, pH 7.5; 1 mM NaF, 1 mM Na_3VO_4, 100mM NaCl, 0.1% Triton X-100, 1 mM phenylmethylsulfonyl fluoride (PMSF)] supplemented with protease and phosphatase inhibitors (1861281, Thermo Fisher Scientific). Homogenates were centrifuged at 1500 x*g* for 6 min at 4ºC. Protein contents were determined by the BCA method [656] using BSA as a standard. GR activity was determined using GSSG as a substrate and monitoring its reduction to GSH through quantification of NADPH oxidation at 340 nm[657] in a Cytation 3 multi-mode microplate reader (BioTek Instruments, Inc.), at 37°C. GR activity was expressed in international units of enzyme per microgram of protein (U/µg prot).

9.2.17. Determination of aconitase activity

Physiological aconitase activity was assessed based on the protocol described by Quirós *et al* [658]. 80 µg of frozen isolated mitochondria was added to 50 mM Tris-HCl, 21.25 mM sodium citrate, 0.60 mM $MnCl_2$, 0.61 mM NADP, 0.2 % Triton X-100 and 2U/mL isocitrate dehydrogenase. Absorbance was measured at 340 nm for 30 min in a Cytation 3 multi-mode microplate reader (BioTek Instruments, Inc.).

Reactivated aconitase activity was performed following the method of Razmara A. *et al*. [659]. Firstly, 60 µg of frozen isolated mitochondria were reduced with 12 mM dithiothreitol (DTT) and 1.2 mM iron chloride for 5 min. Then, the assay above described for measuring physiological aconitase activity was repeated.

Inhibition of aconitase activity was expressed:

$$\%\, inhibition = \; 100 - \frac{physiological\ aconitase\ activity}{reactivated\ aconitase\ activity}$$

9.2.18. Western blot analysis

50 mg of frozen liver tissue was homogenized in 1 mL of phosphate buffer [50 mM NaH_2PO_4/Na_2HPO_4, pH 7.5; 1 mM NaF, 1 mM Na_3VO_4, 100 mM NaCl, 0.1 % Triton X-100, 1 mM phenylmethylsulfonyl fluoride (PMSF)] supplemented with protease and phosphatase inhibitors (1861281, Thermo Fisher Scientific, Waltham, MA, USA). Homogenates were centrifuged at 1500X*g* for 6 min at 4ºC. Mitochondria and cytosol were resuspended in RIPA lysis buffer (50 mM Tris, pH 8.0, 150 mM NaCl, 1% IGEPAL, 0.5 % sodium deoxycholate, 0.1 % SDS) also supplemented with protease and phosphatase inhibitors. After incubation on ice for 30 min, samples were centrifuged at 15000X*g*, at 4 ºC for 15 min. The protein content was determined using the BCA method [660] with BSA as a standard. Then, an equivalent of 20-50 µg of protein was prepared with Laemmli sample buffer and denatured at 95 ºC for 5 min. Protein samples were separated in 7–14 % sodium dodecyl sulfate-polyacrylamide gels followed by transfer to PVDF membranes. Membranes were blocked with 5 % milk or 5 % BSA in TBS-T for 1 h and incubated overnight with primary antibodies. Membranes were further incubated with goat anti-rabbit (1:10000, ab6721, Abcam) and anti-mouse (1:10000, ab216772, Abcam) secondary antibodies for 1 h at room temperature. Membranes were then incubated with ECL Prime Western Blotting System (RPN2232, Sigma-Aldrich) and proteins were visualized using a GBOX Chemi XT4 (Frederik, MD, USA) with GeneSys software (version 1.2.5.0). Protein bands were quantified using Image Studio Lite (version 5.2). The following primary antibodies were used: 4E-BP1 (1:1000; sc9977, Santa Cruz Biotechnology, Dallas, TX, USA), AKT (1:1000; #4691, Cell Signaling, Danvers, TX, USA), AMPKα (1:1000; #2603, Cell Signaling), Beclin1 (1:1000; #3495, Cell Signaling), LC3 (1:1000; #12741, Cell Signaling, USA), mTOR (1:500; #2972, Cell Signaling), p-4E-BP1 (Thr45) (1:1000; sc-271947, Santa Cruz Biotechnology), p62 (1:1000; sc-28359, Santa Cruz Biotechnology), p-AKT (Ser473) (#4060, Cell Signaling), p-AMPKα (Thr172) (1:1000; #2531, Cell Signaling), PGC-1α (1:1000; ST1202, Sigma-Aldrich), p-mTOR (1:500; #2971, Cell Signaling), p-p70 S6K1 (Thr389) (1:1000; #9205, Cell Signaling), p70 S6K1 (1:1000; #sc-8418, Santa Cruz Biotechnology), Parkin (1:1000; #4211, Cell Signaling), PINK1 (1:1000; ab65232, Abcam), SIRT3 (1:1000; #5490, Cell Signaling). The protein in liver

lysates and cytosol was normalized by β-actin (1:5000; A5441, Sigma-Aldrich) or glyceraldehyde 3-phosphate dehydrogenase (GAPDH) (1:1000; #365062, Cell Signaling) while mitochondria protein was normalized by VDAC1 (1:1000; ab34726, Abcam). Once incubation was completed, membranes were washed with TBST and incubated at room temperature with anti-rabbit (1:5000; 1677074S, Cell Signaling) or anti-mouse (1:5000; 1677076S, Cell Signaling) HRP-conjugated secondary antibodies. Clarity™ Western ECL Substrate (1705061, Bio-Rad Laboratories) was used for chemiluminescence detection. The densities of each band were calculated with T Image Studio Lite (version 5.2)

9.2.19. Proteomic analysis

Liquid chromatography-mass spectrometry (LC-MS/MS) was performed at the Thermo Fisher Center for Multiplexed Proteomics (Department of Cell Biology, Harvard Medical School, Cambridge, MA, USA). Liver samples were analysed by application of a LC-MS3 data collection strategy on an Orbitrap Fusion mass spectrometer (Thermo Fisher Scientific Inc., Waltham, MA, USA).

1) Quantitative MS analysis. Liver tissue lysates were prepared in lysis cold buffer (50 mM Tris, pH 8.5, 8 M urea and 1 % SDS) supplemented with protease and phosphatase inhibitors (Roche, Basel, Switzerland). Protein quantification was measured with a micro bicinchoninic acid (BCA) assay (Pierce Biotechnology Inc., Rockford, IL, USA). Protein precipitation was performed by mixing 2-8 mg/mL of liver lysates with four parts of methanol, one part of chloroform and three parts of water. Samples were mixed and centrifuged in order to separate the aqueous phase from chloroform phase. Then, protein was washed with ice-cold methanol, allowed to dry and re-dissolved in 50 mM Tris, pH 8.5 and 4 M urea. Precipitated protein was firstly digested with LysC (1 enzyme:50 protein) for 12 h. After the addition of 1 M urea and 50 mM Tris, pH 8.5, precipitated proteins were digested in the presence of trypsin (1 enzyme:100 protein) for 8 h. Subsequently, the peptide fractions were desalted in C18 solid phase extraction cartridges and peptides were resuspended in 200 mM EPPS, pH 8.0. Peptides quantification was done by a micro BCA assay (Pierce Biotechnology Inc.). Next, peptides were organized in 10-plexes and labelled with tandem mass tag (TMT) reagent (1 peptide:4 TMT)

(Pierce Biotechnology Inc.) for 2 h. The reaction of TMT - tyrosine residues was reversed using 5% hydroxylamine for 15 min. After quenching the reaction with 0.5 % TFA, samples (1:1:1:1:1:1:1:1:1:1 ratio) were ordered in 10-plex experiments, desalted and fractionated offline into 24 fractions according to Weekes *et al*. [661].

2) LC-MS/ MS. 12 of the 24 peptide fractions obtained were examined using a LC-MS3 data collection strategy [662] on an Orbitrap Fusion mass spectrometer (Thermo Fisher Scientific Inc.) containing a Proxeon Easy nLC 1000 for online peptides handling and its separation. 5 µg of peptides were mixed in 5 % formic acid and 5 % acetonitrile (ACN), before its loading into 100 µm inner diameter fused-silica micro capillary in a column with a C18 reversed-phase resin (GP-C18, 1.8 µM, 120 Å, Sepax Technologies Inc., Newark, DE, USA). Samples were separated with a 3 %-25 % gradient of 100 % ACN with 0.125 % formic acid, equilibrated with 3% ACN and 0.125% formic acid, at a flow rate of 600 nL/min for 2 h. The scan order for the Fusion Orbitrap started with a MS1 spectrum (Orbitrap analysis; resolution, 120000; 400−1400 m/z scan range; AGC target, 2 × 105; maximum injection time, 100 ms; dynamic exclusion, 75 sec). 'Top speed' (2 sec) was chosen for MS2 analysis, which consisted of CID (quadrupole isolation set at 0.5 Da and ion trap analysis; AGC, 4 × 103; NCE, 35; maximum injection time, 150 ms). Then, top ten precursors from MS2 scan were used for MS3 investigation, in which precursors were fragmented by HCD prior to Orbitrap analysis (NCE, 55; max AGC, 5 × 104; maximum injection time, 150 ms; isolation window, 2.5 Da; resolution, 60000).

3) LC-MS3 analysis. Raw data was analyzed to control protein false discovery rates, assembled proteins and protein quantification from peptides. Data was identified based in an UniProt mouse database (2014) (both forward and reverse sequences). A set of different criteria was used for the peptides/ protein identification: tryptic with two missed cleavages, a precursor mass tolerance of 50 ppm, fragment ion mass tolerance of 1.0 Da, static cysteine alkylation (57.02146 Da), static TMT labelling of lysine residues and N-terminal of peptides (229.162932 Da), and variable methionine oxidation (15.99491 Da). TMT reporter ion intensities were evaluated with a 0.003 Da window around the theoretical m/z for each reporter ion in the MS3 scan for 10-plex data. Poor quality data were excluded from the analysis.

4) Data analysis. Protein quantification data (ProteinQuant) for 5930 distinct protein IDs (SwissProt/ UniProt ID) consisted of several plexes (groups of 10 samples analyzed per plex), having each plex the same reference sample. In each plex, data was normalized by dividing the quantification value of each protein per sample by the (non-zero) quantification value of the same protein in the reference sample. In the cases when the quantification value of the reference sample was zero or null, the quantification value of the protein in the sample was also set as null. In total, the data with no null values consisted of 5109 rows (distinct protein IDs) and were clustered with the number of significant clusters according with the gap statistics. The mean value (between the group and the respective control group) were loaded in KeggAnim in order to allow the visualization of molecular pathways [663]. Protein abbreviations are detailed in **Table 8**.

9.2.20. Measurement of cathepsin B activity

The sample preparation was performed as described for the catalase assay. Sample aliquots of 50 µL at 0.2 mg/mL protein concentration (10 µg total liver lysate) were incubated at 37 ºC with 70 µL incubation buffer (100 mM sodium acetate, pH 5.5, 1 mM EDTA, 5 mM DTT and 0.05% (v/v) Brij-35). The cathepsin B activity assay was started by the addition of 70 µL of the substrate Z-Arg-Arg-N-methyl-coumarin at 40 µM. Substrate cleavage was followed during 20 min by fluorescence reading at 460 nm emission using 360 nm excitation with the Cytation 3 multi-mode microplate reader (BioTek Instruments, Inc.). A curve with known concentrations of N-methyl-coumarin was used as standard. Cathepsin B activity was determined from the slope of the linear regression of experimental values and the results were normalized using the amount of protein in each sample.

9.2.21. Cell culture and AntiOxCIN$_4$ treatment

Human hepatocellular carcinoma HepG2 cells (85011430, ECACC, UK) were cultured in low-glucose medium composed by Dulbecco's modified Eagle's medium (DMEM; D5030) supplemented with 5 mM glucose, sodium bicarbonate (3.7 g/L), HEPES (1.19 g/L), L-glutamine (0.876 g/L), sodium pyruvate (0.11 g/L), 10 % fetal bovine serum

(FBS), 1 % penicillin-streptomycin 100x solution in a humidified atmosphere (5 % CO_2, 37ºC). HepG2 cells were seeded (4.5 x 10^4 cells/cm^2) and grown for 24 h until reaching 60–70 % confluence. Then, cells were treated for 48 h with the mitochondriotropic antioxidant (AntiOxCIN$_4$, 100 µM) or vehicle (DMSO, 0.1 %) following BSA (0.01 g/mL) or FFAs mixture (250 µM) treatment for 24 h period. Cell condition defined as Vehicle + BSA was established as the control group of the study.

9.2.22. Free fatty acids (FFAs) conjugation

The fatty acid mixtures (FFA) were prepared as saponified 10 mM stock solutions and complexed (1:1) with Free-fatty acid BSA (10 minutes at 50 °C), cooled to room temperature. The Free-fatty acid BSA (0.2 g/mL) was diluted in the same proportion with 25 mM KOH and used as a control. The same ratios of FA dilutions were used for free fatty acid BSA control. The amounts of the different FA in the mixture were: 39 % C16:0 (Catalogue Nº: P0500, Sigma-Aldrich, USA); 5 % C18:0 (Catalogue Nº: 85679, Sigma-Aldrich, USA); 50 % C18:1 (Catalogue Nº: O1008, Sigma-Aldrich, USA); 4 % C18:2 (Catalogue Nº: L1376, Sigma-Aldrich, USA); 2 % C20:4 (Catalogue Nº: A3611, Sigma-Aldrich, USA).

9.2.23. Evaluation of neutral lipid content

Cells were seeded in 96-well plate and subjected to different treatments After incubation, the neutral lipid accumulation was assessed using the Nile Red assay [662]. Briefly, cell culture medium was removed and 100 µL of the Nile red solution was added to each well for 1 h/1.5 h in the dark conditions at 37ºC. Nile Red is freshly diluted 1:200 in medium without FBS from the stock solution (stock: 0.5 mg/mL dissolved in acetone). Nile Red was then removed, and cells were washed twice with PBS 1X. The fat content per well (in 100 µL PBS 1x) was measured fluorimetrically with 520 nm excitation and 620 nm emission wavelengths in a Cytation 3 multi-mode microplate reader (BioTek Instruments, Inc.). Results were normalized for cell mass content at the end of assay, using the SRB method [506].

9.2.24. Lipid Droplet (LD) Staining

Cells were seeded in pre-coated (collagen I 0.15 mg/mL) µ-Slide 8 well ibiTreat Ibidi (2 x 10^4/cm^2) with a final volume of 300 µL per well, and then subjected to the different treatments. Then, cells were fixed with 4 % paraformaldehyde for 20 min at RT and after washing with PBS 1x stained with HCS LipidTOX Green (1:1000, Catalog number: H34475, ThermoFisher Scientific) for 20 min at RT to detect neutral lipid droplets. Subsequently, nuclei were stained using Hoechst 33342 (1 µg/mL, Catalog number: H1399, ThermoFisher Scientific). Images were acquired using a Laser Scanning Confocal Microscope (LSM 710, Zeiss, USA) equipped with an α-Plan-Apochromat 63x/1.4 Oil DIC M27 objective (Zeiss) and analyzed with ImageJ Fiji program (Scion Corporation, USA). LD number, size and area were quantified by using an *MRI_Lipid_Droplets_Tool* Macro [664].

9.2.25. Cell mass measurements

HepG2 cells (4.5 x 10^4 /cm^2) were seeded in 96-well plates and then subjected to the different treatments. After incubation time, the sulforhodamine B (SRB) assay was used for cell mass determination based on the measurement of cellular protein content [506]. Briefly, the cell culture medium was removed and wells rinsed with PBS (1x). Cells were fixed by adding TCA 60 % overnight at 4ºC. Later, the fixation solution was discarded and the plates were dried in an oven at 37ºC. 150 µL of 0.05% SRB in 1 % acetic acid solution was added and incubated at 37°C for 1 h. The wells were then washed with 1 % acetic acid in water and dried. Then, 100 µL of Tris (pH 10) was added and the plates were stirred for 15 min and optical density was measured at 540 nm in a Cytation 3 multi-mode microplate reader (BioTek Instruments, Inc.).

9.2.26. Mitochondrial membrane potential (ΔΨm) measurements

Vital confocal fluorescent microscopy was used to visualize alterations in mitochondrial polarization and network distribution in HepG2 cells. Cells were seeded in pre-coated (collagen I 0.15 mg/mL) µ-Slide 8 well ibiTreat Ibidi (2 x 10^4/cm^2) with a final volume of 300 µL per well, and then subjected to the different treatments. Cells were

incubated with fluorescent dyes MitoTracker Red FM (100 nM, Catalog number: M22425, ThermoFisher Scientific, Waltham, MA, USA) and Hoechst 33342 (1 µg/mL, Catalog number: H1399, ThermoFisher Scientific) for mitochondrial network and nuclei, respectively, 30 min before the end of the treatment time in fresh cell culture medium with no FBS at 37 °C and 5 % CO_2 in dark conditions. Images were acquired using a Laser Scanning Confocal Microscope (LSM 710, Zeiss, USA) equipped with an α-Plan-Apochromat 63x/1.4 Oil DIC M27 objective (Zeiss) and analyzed with ImageJ Fiji program (Scion Corporation, USA). Mitochondrial network was quantified by using a *Mitochondria Morphology Macro* [511].

9.2.27. Cellular ROS detection

Cells were seeded in 96-well plate (flat bottom clear, black polystyrene plate) and then subjected to the different treatments. After incubation time, general ROS levels were assessed through variation in ROS-induced CM-H_2DCFDA fluorescence (C6827, ThermoFisher Scientific). Briefly, cells were loaded with the CM-H_2DCFDA as an indicator of ROS levels, by incubating them with 5 µM of the CM-H_2DCFDA in assay buffer (120 mM NaCl, 3.5 mM KCl, 5 mM $NaHCO_3$, 1.2 mM $NaSO_4$, 0.4 mM KH_2PO_4, 20 mM HEPES) supplemented with 1.3 mM $CaCl_2$, 1.2 mM $MgCl_2$ and 10 mM sodium pyruvate, pH 7.4). After that, the medium was discarded and PBS 1x added. Fluorescence signal was obtained in a Cytation 3 multi-mode microplate reader (BioTek Instruments, Inc.) at 495/527 nm. All treatments were normalized by cell mass, using the SRB method.

9.2.28. Evaluation of cellular fatty acid oxidation (FAO)-linked OCR

HepG2 cells (1 x 10^4 cells/100µl/well) were seeded in Agilent Seahorse XF96 Cell Culture microplates and allowed to grow overnight in typical growth medium. After AntiOxCIN$_4$ treatment, the cell culture medium was replaced with a “starvation medium” composed by glucose (0.5 mM), glutamine (1 mM), and serum (1 % FBS) to deplete endogenous substrates within the cell (glycogen, triglycerides (TG), amino acids), thus priming the cells to oxidize exogenous FAs.

For OCR measurement, 25 µL of 250 µM Palmitoyl-L-carnitine and 25 µL of 1 µM rotenone diluted in low-buffered serum-free DMEM medium (pH 7.4) were pre-loaded

in the XFe96 sensor cartridge. Palmitoyl-L-carnitine was loaded into port A and rotenone into port B. After the calibration of the sensor cartridge and the calibration plate in the XFe96 Extracellular Flux Analyzer, the latter was substituted by the assay plate. Compounds were pneumatically injected, and three baseline rate measurements of OCR were performed using a 3 min mix followed by 5 min cycle. Data obtained was analyzed using Software Version Wave Desktop 2.6.1.

9.2.29. Gene expression measurements

Transcript analysis was assessed by performing quantitative polymerase chain reaction (qPCR). HepG2 cells were seeded in 100 mm cell culture dishes and later subjected to the respective treatments. After 48h AntiOxCIN$_4$ (100 µM) plus 24 h FFA (250 µM), total cellular extracts were obtained by firstly washing the cells with PBS 1x and immediately thereafter through gentle scraping of the bottom of the plates onto 1 mL of PBS 1x. In order to collect the highest number of cells possible, two microtube centrifugation steps were performed at 12000X*g* for 10 min at 4 ºC. Total cellular RNA contents were extracted utilizing the Qiagen RNeasy kit (Qiagen, Hilden, Germany) according to the manufacturer's instructions. RNA was readily quantified, and its purity assessed utilizing Thermo Scientific® NanoDrop 2000™ spectrophotometer (Thermo Fisher Scientific, Waltham, Massachusetts, USA). Upon quantification, the RNA conversion into complementary DNA (cDNA) was performed utilizing the iScript™ cDNA Synthesis Kit, by utilizing Bio-Rad® CFX96™ Real-Time PCR system (Bio-Rad Laboratories, Hercules, California, USA). RT-PCR was performed using the SsoFast Eva Green Supermix, in a CFX96 real time-PCR system (Bio-Rad, Hercules, CA, USA), with the primers defined in **Table 9** at 500 nM. Amplification of 25 ng was performed with an initial cycle of 30 s at 95 ºC, followed by 40 cycles of 5 s at 95 ºC plus 5 s at 60 ºC. At the end of each cycle, Eva Green fluorescence was recorded to enable determination of Cq. After amplification, melting temperature of the PCR products was determined by performing melting curves. One of the negative controls included one sample being subjected to a similar conversion in the absence of the reverse transcriptase enzyme (no reverse transcriptase – NRT). Additionally, for each primer, a second negative control was performed, one in which the DNA

sample was replaced by water (no template control – NTC). Each reaction was performed in triplicate with efficiency between 90 and 110 %. Each sample was run in triplicate. Total gene expression was calculated utilizing the Bio-Rad® CFX96 Manager Software (version 3.1) (Bio-Rad Laboratories, Hercules, California, USA). All primers were designed using the web-based Primer–Basic Local Alignment Search Tool (Primer-BLAST) after obtaining nucleotide accession numbers from the database. Both services are public and supported by the National Center for Biotechnology Information (NCBI). Primers were diluted in RNase-free water to the concentration of 100 µM upon arrival and stored at -20ºC.

9.2.30. Cellular labelled RMN

For carbon labelling experiments on HepG2, DMEM D5030 (with L-glutamine, without glucose and sodium bicarbonate) media was reconstituted with 10 mM 99 % [U-^{13}C] glucose (CLM-1396; Euriso-top). For ^{2}H NMR experiments, regular RPMI media (R6504) was reconstituted with 20 % $^{2}H_2O$ (A2521, Euriso-top). For NMR experiments, cells were grown in Petri dishes and treated for 48 h with AntiOxCIN$_4$. After, medium was discarded and a new one containing FFA (250 µM) with tracers was added for 24 h. Cells were washed twice with ice-cold PBS and 1 mL of ice-cold solution methanol/water 80:20 (containing NaN_3) was directly added. This solution was spread manually throughout the petri dish to swiftly lyse cells. Cells were scraped and collected into 2 mL microtubes. Another 750 µL were added to the Petri dish to properly remove remnant cells and collected to the microtube. Extracts were centrifuged 5 min at 4 ºC, 5000X*g*. The supernatant (aqueous phase) was transferred to another microtube, lyophilized and stored until NMR experiments. One mL of a chloroform/methanol/water 1:1:0.1 (containing NaN3) solution was added to the pellet from the previous extraction. The solution was kept 1 h on ice, with 3-4 vortex mixes. Extract was centrifuged at 5 min at 4 ºC, 5000X*g* and supernatant (organic phase) transferred to another microtube. After lyophilization, extracts were stored until NMR acquisition. The denatured protein pellet was kept and used for normalization purposes.

a) Quantification of TG positional ^{2}H-enrichments and estimation of FA and glycerol concentrations - TG positional ^{2}H-enrichments in the glycerol and FA

moieties were quantified by analysis of ^{1}H and ^{2}H NMR TG spectra as previously described [224].

b) Intracellular metabolism by ^{13}C NMR experiments in HepG2 cells - ^{13}C NMR spectra of the same extracts were used to access intermediary metabolism. By analyzing the glutamate labelling at the C4 and C3, we were able to measure quantitatively some TCA cycle parameters. At glutamate C4 expansion, the peaks were originated by the following isotopomers: [4-^{13}C]glutamate generated a singlet (C4S) at 34.2 ppm; [4,5-$^{13}C2$]glutamate generated a doublet (C4D45) due to the $^{1}J_{C4C5}$=51.3 Hz; and [3,4,5-$^{13}C3$]glutamate generated a doublet of doublets (C4Q) due to the $^{1}J_{C4C5}$ and $^{1}J_{C3C4}$=34.5 Hz, but also an unresolved, multiple bond, $^{2}J_{C3C5}$ ≈1 Hz. HepG2 cells exhibited a C4S, C4D45 and C4Q. The glutamate C3 was also formed by several peaks: a singlet (C3S) at around 27.8 ppm, formed from [3- ^{13}C]glutamate; a doublet from [3,4-$^{13}C2$]glutamate due to $^{1}J_{C3C4}$; and a triplet due to [2,3,4-$^{13}C3$]glutamate. Since $^{1}J_{C2C3}$=34.8 Hz and $^{1}J_{C3C4}$=34.5 Hz were very similar, it was not a true triplet but rather an unresolved center peak. The methyl group of labelled lactate showed a small singlet at around 20.9 ppm and as a doublet from $^{1}J_{C2C3}$=36.9 Hz. **TCA coupling** was calculated by the ratio between the amount of labelling on glutamate C4 isotopomers and [U-^{13}C]lactate (GluC4F/LacC3F). **TCA turnover** is presented as the ratio between [3,4,5-$^{13}C3$]glutamate and [4,5-$^{13}C2$]glutamate (C4Q/C4D45). Finally, **anaplerosis** was assessed by the difference between the unit and the ratio of the amount of labelling on glutamate C3 and glutamate C4 (1-(GluC3/GluC4)).

Every spectrum was processed using ADC lab's 12.0 1D NMR processor software (Advanced Chemistry Development, Inc., Toronto, Ontario, Canada) applying a line broadening of 0.2 Hz, zero-filling to 64k, phasing and baseline correction.

9.2.31. Computational data analysis

Orange 3.27.1 was used for the computational data analysis and visualization. Principal component analysis (PCA), considering the features physiological parameters, is shown in **Figure 42E**, with the two first components explaining 53 % of the variance. Linear projections were generated for the features of physiological parameters (Body weight; Liver weight; AST; ALT; Hepatic lipid accumulation; TG; DAG; SFAs; MUFAs;

Palmitoleate; Linoleate; ω-3 FAs) after application of PCA and evidencing the directions of each individual component.

9.2.32. Statistics

Data were expressed as the mean value ± standard error of the mean (SEM). Statistical analysis was performed using GraphPad Prism version 8.0.2 (GraphPad Software Inc., San Diego, CA, USA). The normality of the data was assessed using the Shapiro-Wilk test. Non-normality data was analyzed using the non-parametric Kruskal-Wallis test while with normal data was used the parametric test two-way ANOVA, followed by Fisher's LSD test for multiple comparisons. The level of significance considered was *P<0.05, **P<0.01, ***P<0.001, ****P<0.0001 for multiple comparisons vs SD or Vehicle + BSA and $^{\#}P < 0.05$, $^{\#\#}P < 0.01$, $^{\#\#\#}P < 0.0005$, $^{\#\#\#\#}P < 0.0001$ vs WD or Vehicle + FFAs.

Table 8. Informative table on proteomic analysis

Proteomics abbreviations	
ABCD1	ATP-binding cassette sub-family D member 1
ABCD2	ATP-binding cassette sub-family D member 2
ACACA	acetyl-CoA carboxylase 1
ACLY	ATP-citrate synthase
ACOT12	acyl-coenzyme A thioesterase 12
ACOT3	acyl-coenzyme A thioesterase 3
ACOT4	acyl-coenzyme A thioesterase 4
ACOT8	acyl-coenzyme A thioesterase 8
ACOX1I1	acyl-coenzyme A oxidase 1, isoform 1
ACOX1I2	acyl-coenzyme A oxidase 1, isoform 2
ACSL4	long-chain-fatty-acid-CoA ligase 4

AGPAT3	glycerol-3-phosphate acyltransferase γ
ATP5L	ATP synthase subunit g, mitochondrial
CAT	catalase
CD36	platelet glycoprotein 4
CTSB	cathepsin B
CTSD	cathepsin D
CTSL	cathepsin L1
CTSO	cathepsin O
CTSS	cathepsin S
DGAT1	diacylglycerol O-acyltransferase 1
DGAT2	diacylglycerol O-acyltransferase 2
ECH1	δ(3,5)-δ(2,4)-dienoyl-CoA isomerase, mitochondrial
ECHDC3	enoyl-CoA hydratase domain-containing protein 3, mitochondrial
ECHS1	enoyl-CoA hydratase, mitochondrial
ELOVL1	elongation of very long chain fatty acids protein 1
ELOVL2	elongation of very long chain fatty acids protein 2
ELOVL5	elongation of very long chain fatty acids protein 5
ELOVL6	elongation of very long chain fatty acids protein 6
FABP2	fatty acid-binding protein, intestinal
FABP4	fatty acid-binding protein, adipocyte
FADS1	fatty acid desaturase 1
FADS2	fatty acid desaturase 2
FASN	fatty acid synthase

G6PC	glucose-6-phosphatase
GK	glycerol kinase
GLRX	glutaredoxin-1
GLRX3	glutaredoxin-3
GPX4	glutathione peroxidase, mitochondrial
HADHA	trifunctional enzyme subunit α, mitochondrial
HMOX1	heme oxygenase 1
LAMP2	lysosomal associated membrane protein 2
LPIN2	phosphatidate phosphatase LPIN2
M6PR	mannose-6-phosphate receptor
MAVS	mitochondrial antiviral-signaling protein
MLXIPL	carbohydrate-responsive element-binding protein
MPO	myeloperoxidase
MSRA	mitochondrial peptide methionine sulfoxide reductase
MTATP8	ATP synthase protein 8
MTCO1	cytochrome c oxidase subunit 1
MTND5	NADH-ubiquinone oxidoreductase chain 5
NDUFA3	NADH dehydrogenase [ubiquinone] 1α subcomplex subunit 3
NDUFB4	NADH dehydrogenase [ubiquinone] 1β subcomplex subunit 4
NDUFS3	NADH dehydrogenase [ubiquinone] iron-sulfur protein 3, mitochondrial
NDUFS8	NADH dehydrogenase [ubiquinone] iron-sulfur protein 8, mitochondrial
NDUFV2	NADH dehydrogenase [ubiquinone] flavoprotein 2, mitochondrial
NQO1	NAD(P)H quinone dehydrogenase 1

PCK2	phosphoenolpyruvate carboxykinase 2, mitochondrial
PGK2	phosphoglycerate kinase 2
PCX	pyruvate carboxylase, mitochondrial
PDIA6	protein disulfide-isomerase A6
PEX14	peroxisomal membrane protein PEX14
PEX19	peroxisomal biogenesis factor 19
PEX26	peroxisome assembly protein 26
PEX3	peroxisomal biogenesis factor 3
PEX5	peroxisomal targeting signal 1 receptor
PEX6	peroxisome assembly factor 2
PEX7	peroxisomal targeting signal 2 receptor
SCAP	sterol regulatory element-binding protein cleavage-activating protein
SCD1	acyl-CoA desaturase 1
SLC27A4	long-chain fatty acid transport protein 4
SLC25A17	solute carrier family 25 member 17
SOAT2	sterol O-acyltransferase 2
SOD1	superoxide dismutase [Cu-Zn]
SOD2	superoxide dismutase [Mn], mitochondrial
SOD3	superoxide dismutase [Mn], mitochondrial
TECR	very-long-chain enoyl-CoA reductase
TXNDC5	thioredoxin domain-containing protein 5
TXNDC17	thioredoxin domain-containing protein 17
UQCR10	cytochrome b-c1 complex subunit 9

UQCRB	cytochrome b-c1 complex subunit 7

Table 9. Informative table on primers used for transcript amplification.

Gene	Accession Number	mRNA Sequence Name	Forward Primer	Reverse Primer
ACOT2	NM_006821	Homo sapiens, acyl-coenzyme A thioesterase 2, mitochondrial, Acyl-CoA thioesterase, transcript variant 1, mRNA	CCATTCAGTTGTTCTCAGGTC	GAACTCTTCAGGCTCCATTG
ACOX1	NM_004035	Homo sapiens Peroxisomal acyl-coenzyme A oxidase 1, transcript variant 1, mRNA	TGAACCAGAACCACAGATT	TGACCAATGCCTTCGTTA
ATP5MC1	NM_001002027	Homo sapiens ATP synthase, H^+ transporting, mitochondrial F_o complex, subunit C1 (subunit 9), transcript variant 2, mRNA	GGCTAAAGCTGGGAGACTGAAA	GTGGGAAGTTGCTGTAGGAAGG
ATP6V1A	NM_001690	Homo sapiens ATPase H^+ Transporting V1 Subunit A, mRNA	GGGTGCAGCCATGTATGAG	TGCGAAGTACAGGATCTCCAA
ATP6V1H	NM_015941	Homo sapiens ATPase H^+ Transporting V1 Subunit H, transcript variant 1, mRNA	GCTGCTGTCCCCACCAATAT	GCTTCTCTTCAGGGCTTCGT
CAT	NM_001752	Homo sapiens catalase, mRNA	CTCAGGTGCGGGCATTCTAT	AGCGGTCAAGAACTTCACTGA
COX4I1	NM_001861	Homo sapiens cytochrome c oxidase subunit IV isoform 1, mRNA	GAGAAAGTCGAGTTGTATCGCA	GCTTCTGCCACATGATAACGA
CPT1A	NM_001876	Homo sapiens carnitine O-palmitoyltransferase 1A, transcript variant 1, mRNA	CAGGAGAGGAGACAGACA	TAGAGCCAGACCTTGAAGTA
ECHS1	NM_004092	Homo sapiens enoyl-CoA hydratase, Short Chain 1l, mRNA	TGACATTAACAGAAGGAAGTAAGT	CCAAGCAGAGGTGTGAAG

GPX1	NM_000581	Homo sapiens glutathione peroxidase 1, transcript variant 1, mRNA	GGAGAACGCCAAGAACGAAG	CCAACTTCATGCTCTTCGAGAA
GPX4	NM_002085	Homo sapiens glutathione peroxidase 4, transcript variant 1,mRNA	AAGATCTGCGTGAACGGGG	CTGGGAAATGCCATCAAGTGG
HMOX1	NM_002133	Homo sapiens heme oxygenase 1, mRNA	CTGCTGACCCATGACACCAA	GGGCAGAATCTTGCACTTTGT
HPRT1	NM_000194	Homo sapiens hypoxanthine phosphori-bosyltransferase 1, mRNA	CCCTGGCGTCGTGATTAGTG	CGAGCAAGACGTTCAGTCCT
LAMP1	NM_005561	Homo sapiens lysosomal associated membrane protein 1, mRNA	CAGATGTGTTAGTGGCACCCA	TTGGAAAGGTACGCCTGGATG
LAMP2	NM_002294	Homo sapiens lysosomal-associated membrane protein 2, transcript variant A, mRNA	CTGCCGTTCTCACACTGCTC	ATGCTGAAAACGGAGCCATTAAC
MT-ATP6	NC_012920 (8527-9207)	Homo sapiens mitochondrially Encoded ATP Synthase Membrane Subunit 6, mRNA	GCGCCACCCTAGCAATATCA	GCTTGGATTAAGGCGACAGC
MT-CO1	NC_012920 (5904-7445)	Homo sapiens mitochondrially encoded cytochrome C oxidase, mRNA	ATACCAAACGCCCCTCTTCG	TGTTGAGGTTGCGGTCTGTT
MT-CYB	NC_012920 (14747-15887)	Homo sapiens mitochondrially encoded cytochrome B, mRNA	CCACCCCATCCAACATCTCC	GCGTCTGGTGAGTAGTGCAT
MT-ND5	NC_012920 (12337-14148)	Homo sapiens mitochondrially encoded NADH: biquinone Oxidoreductase Core Subunit 5, mRNA	AGTTACAATCGGCATCAACCAA	CCCGGAGCACATAAATAGTATGG
NDUFA9	NM_005002	Homo sapiens NADH dehydrogenase (ubiquinone) 1 alpha subcomplex, 9, mRNA	GCCTATCGATGGGTAGCAAGAG	TGAGTTCCAGTGGTGTTGCC

NQO1	NM_000903	Homo sapiens NAD(P)H quinone dehydrogenase 1, transcript variant 1, mRNA	CTGGAGTCGGACCTCTATGC	GGGTCCTTCAGTTTACCTGTGAT
PEX14	NM_004565	Homo sapiens Peroxisomal biogenesis factor 14, mRNA	GGCTTCTTTTAAATCGGAGGCA	CTCGTTGCTGACAGGTGAGA
PPARA	NM_005036	Homo sapiens peroxisome proliferator-activated receptor alpha, trasncript variant 5, mRNA	TCAGGCTATCATTACGGAGTC	CGGTCGCACTTGTCATAC
SDHA	NM_004168	Homo sapiens succinate dehydrogenase complex, subunit A, flavoprotein (Fp), transcript variant 1, mRNA	CGGGTCCATCCATCGCATAAG	TATATGCCTGTAGGGTG-GAACTGAA
SOD1	NM_000454	Homo sapiens superoxide dismutase 1, mRNA	CGAGCAGAAGGAAAGTAATG	GGATAGAGGATTAAAGTGAGGA
SOD2	NM_000636	Homo sapiens superoxide dismutase 2, mitochondrial, transcript variant 1, mRNA	GAAGTTCAATGGTGGTGGTCAT	TTCCAGCAACTCCCCTTTGG
TBP	NM_003194	Homo sapiens TATA box binding protein, transcript variant 1, mRNA	CGAATATAATCCCAAGCGGTTTGC	AGCTGGAAAACCCAACTTCTGT
TFEB	NM_007162	Homo sapiens transcription factor EB, transcript variant1, mRNA	ACCTGTCCGAGACCTATGGG	CGTCCAGACGCATAATGTTGTC
UQCRC2	NM_003366	Homo sapiens ubiquinol-cytochrome c reductase core protein II, mRNA	TTCAGCAATTTAGGAACCACCC	GGTCACACTTAATTTGCCACCAA
YWHAZ	NM_003406	Homo sapiens tyrosine 3-monooxygen-ase/tryptophan 5-monooxygenase activation protein, transcript variant 1, mRNA	TGTAGGAGCCCGTAGGTCATC	GTGAAGCATTGGGGATCAAGA

9.3. Results

9.3.1. AntiOxCIN$_4$ decreased body weight and improved hepatic-related physiological parameters in a WD-fed mice model with a NAFL phenotype

Hypercaloric diets significantly enriched in saturated fat and sucrose are correlated with increased visceral adiposity, thereby contributing to metabolic syndrome-associated disorders [665]. In this study, a rodent diet mimicking WD eating habits induced an increase in body weight (by 74 %) along a sixteen-week feeding period, when compared to the Vehicle + SD mice group (**Figure 40A-B**). AntiOxCIN$_4$ supplementation prevented WD-induced weight gain (**Figure 40B**), being this effect significant from the 15th week of WD feeding until the time of euthanasia (by 43 %). Final body weight, as well as liver, adipose tissue, kidneys, heart and brain weight were collected at euthanasia and provided in **Figure 41A**. Importantly, no alterations were observed in food intake or water consumption (**Figure 41B**), or in the visual inspection of animal welfare upon AntiOxCIN$_4$ supplementation. Noteworthy, WD feeding also induced an increase of liver weight gain (164 %) and size, which was significantly prevented by AntiOxCIN$_4$ supplementation (by 39 %) (**Figure 40C, D**). Plasma from WD-fed mice presented alterations in hepatocyte damage hallmarks such as increased aspartate aminotransferase (AST) (282 %), ALT (763 %) activities (**Figure 40E**), and cholesterol (Chol) (176 %) levels (**Figure 41C**). Interestingly, AntiOxCIN$_4$ decreased WD-induced increase of plasmatic ALT (by 134 %), AST (by 89 %) and cholesterol (by 18 %) circulating levels, when compared with the WD-fed mice without AntiOxCIN$_4$ supplementation (**Figure 40E and 41C**). Histological staining with H&E and Masson's Trichrome revealed that physiological outcomes of WD feeding are associated with the development of simple steatosis (NAFL) (**Figure 40F, G**). The NAFL stage was characterized by mixed steatosis (grade 3), hepatocyte ballooning (grade 2), and the absence of inflammation and fibrosis (**Figure 40G and S41D**).

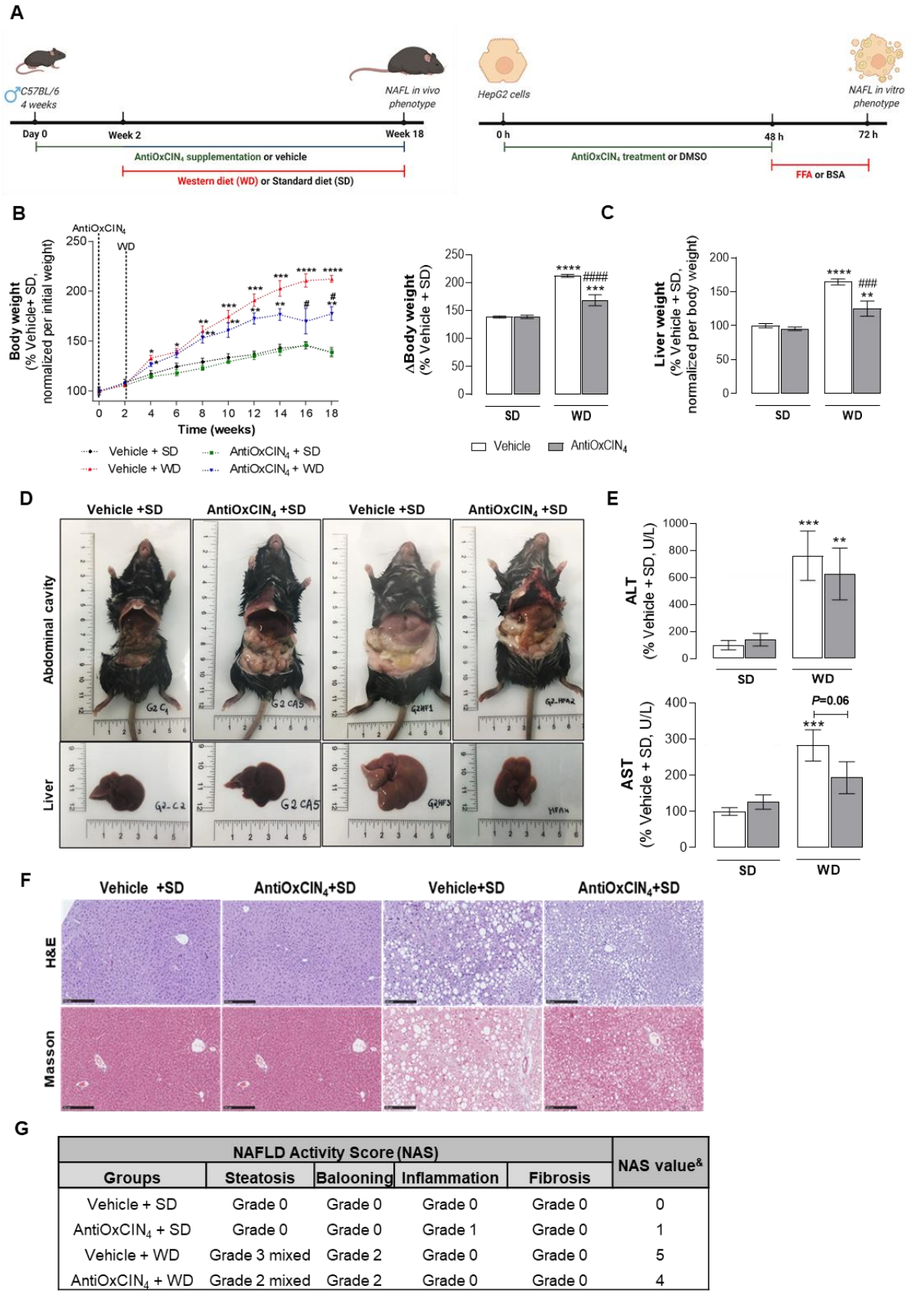

G

NAFLD Activity Score (NAS)					NAS value[&]
Groups	Steatosis	Balooning	Inflammation	Fibrosis	
Vehicle + SD	Grade 0	Grade 0	Grade 0	Grade 0	0
AntiOxCIN$_4$ + SD	Grade 0	Grade 0	Grade 1	Grade 0	1
Vehicle + WD	Grade 3 mixed	Grade 2	Grade 0	Grade 0	5
AntiOxCIN$_4$ + WD	Grade 2 mixed	Grade 2	Grade 0	Grade 0	4

Figure 40. Effects of AntiOxCIN$_4$ on body and liver weight, hepatocellular injury hallmarks and hepatic

histology in a WD-fed mice with NAFL phenotype. (**A**) Animal and human cells study experimental timeline. (**B**) Body weight progression along 18 weeks of antioxidant regimen and 16-weeks of diet (SD or WD) (left). Body weight from euthanized animals at 18th week of intervention (right). (**C**) Wet liver weight from euthanized animals. (**D**) Representative images of body and abdominal cavity (upper) and livers (lower) of euthanized mice. (**E**) Plasma AST and ALT activity levels in WD-fed mice in the absence/presence of AntiOxCIN$_4$ (2.5 mg/day/animal). (**F**) Representative histological images of liver sections stained with H&E and Masson's Trichrome stainings. Scale bar: 250 µm with 10x magnification. (**G**) NAFLD activity score (NAS) evaluation following guidelines provided in SI. ***&*** represents the sum of steatosis, hepatocyte ballooning, lobular inflammation and fibrosis grades obtained. Data are expressed as the mean ± SEM and the results were normalized to the respective control condition (set as 100 %). Statistically significant compared using two-way ANOVA followed by Fisher's LSD test for multiple comparisons (*P<0.05, **P < 0.01,***P < 0.0005, ****P < 0.0001 vs Vehicle + SD); ($^{\#}$P < 0.05, $^{\#\#\#}$P < 0.0005,$^{\#\#\#\#}$P < 0.0001 vs Vehicle + WD). **Contribution to this panel**: I was responsible for the conceptualization, experimental work, and data analysis of **Figure 40A-E.** In the **Figures 40F and G**, I was responsible for liver fixation in 10 % neutral buffered formalin. The tissue was trimmed and processed for paraffin embedding in a paid service at the Instituto Gulbenkian de Ciência (IGC). The histological images and the NAS assessment was realized by our collaborators in the Department of Pathology, The Children's Memorial Health Institute, Warsaw, Poland.

Significantly, AntiOxCIN$_4$ supplementation diminished hepatic lipid accumulation, highlighted by a reduction of the steatotic grade from 3 to 2, while no alterations were observed at hepatocyte ballooning level in comparison with the Vehicle + WD group (**Figure 40F, G**).

A

Parameter (Units, g)	Vehicle + SD	AntiOxCIN$_4$ + SD	Vehicle + WD	AntiOxCIN$_4$ + WD
Body weight initial	21.6 ± 0.9	24.0 ± 0.9	20.6 ± 0.5	22.6 ± 0.8
Body weight final	29.9 ± 1.8	33.4 ± 1.0	43.8 ± 1.4	38.2 ± 3.6
Liver	1.18 ± 0.11	1.25 ± 0.05	2.88 ± 0.03	1.90 ± 0.37
Adipose tissue				
Epididymal[&]	0.50 ± 0.13	0.94 ± 0.30	2.12 ± 0.24	2.00 ± 0.26
Mesenteric[&]	0.21 ± 0.06	0.36 ± 0.09	0.85 ± 0.08	0.63 ± 0.10
Kidneys	0.35 ± 0.04	0.35 ± 0.01	0.36 ± 0.00	0.34 ± 0.02
Heart	0.16 ± 0.02	0.16 ± 0.01	0.17 ± 0.00	0.16 ± 0.01
Brain	0.47 ± 0.01	0.47 ± 0.01	0.43 ± 0.01	0.45 ± 0.02

& - weight does not represent the total tissue from the animal.

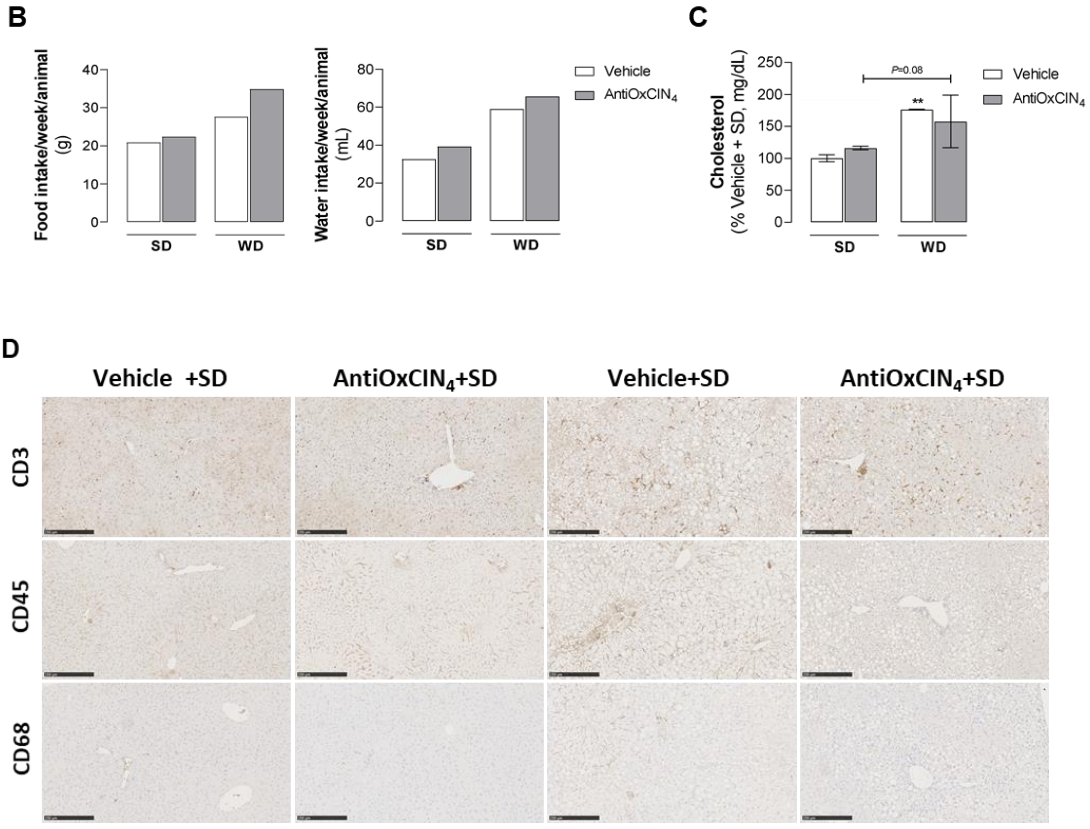

Figure 41. Effects of AntiOxCIN$_4$ on hepatic inflammatory markers and plasma parameters of WD-fed mice induced steatosis. (**A**) Selected physiological parameters of C57BL/6J mice supplemented with Anti-OxCIN$_4$ or vehicle and fed with SD or with WD. (**B**) Average food intake (left) and water consumption (right) in WD-fed mice in the absence/presence of AntiOxCIN$_4$ (2.5 mg/day/animal). (**C**) Plasma levels of cholesterol in WD-fed mice in the absence/presence of AntiOxCIN$_4$ (2.5 mg/day/animal). (**D**) Liver histology of CD3, CD45 and CD68 inflammatory markers. Scale bar: 250 µm, with 10x magnification. Statistically significant compared using two-way ANOVA followed by Fisher's LSD test for multiple comparisons (**P < 0.01 vs Vehicle + SD). **Contribution to this panel:** I was responsible by conceptualization, experimental work, and data analysis of **Figure 41 A-C**. The histological images in **Figure 41D** were realized by our collaborators in the Department of Pathology, The Children's Memorial Health Institute, Warsaw, Poland.

9.3.2. AntiOxCIN$_4$ improved alterations in hepatic lipid profile in the liver of a WD-fed mice model with a NAFL phenotype

In agreement with the histological analysis and NAS score (**Figure 40F, G**), the quantification of LD relative intensity by H&E staining confirmed that Vehicle + WD increased hepatic lipid accumulation (2147 %) when compared to the Vehicle + SD group (**Figure 42A**). These observations align with MS-proteomic data evidencing an increase of DNL and elongation/unsaturation-related proteins in the Vehicle + WD group (**Figure 42D**). The data from TLC analysis revealed that hepatic tissue from WD-fed mice have increased TG (214 %) and cholesteryl esters (CEs) (411 %) content, with an associated increase of diacylglycerols (DAGs) (395 %) and free Chol (119 %) levels (**Figure 42B**). Regarding the saturation/unsaturation of FAs acyl chains, WD feeding induced a decrease of saturated fatty acids (SFAs) levels (23 %) in comparison with the Vehicle + SD group (50 %) (**Figure 42C**). Moreover, WD feeding favored an enrichment of oleate (63 %), while a decrease of linoleate (3 %) and ω-3 FAs (2 %) was noticed in comparison with oleate (17 %), linoleate (15 %) and ω-3 FAs (7 %) of Vehicle + SD group (**Figure 42C**). AntiOxCIN$_4$ *per se* did not alter the hepatic lipid profile of SD-fed mice (**Figure 42A-C**). However, AntiOxCIN$_4$ supplementation induced the expression of proteins involved in DNL but also in elongation/ unsaturation-related pathways (**Figure 42D**). In WD-fed mice, AntiOxCIN$_4$ supplementation partially prevented hepatic lipid accumulation by inducing a decrease (by 570 %) in the LD relative intensity compared to the Vehicle + WD group (**Figure 42A**). Moreover, AntiOxCIN$_4$ also improved the lipid composition profile with a decrease in the TG (by 30 %) and DAGs (by 103 %) levels (**Figure 42B**). Interestingly, AntiOxCIN$_4$ supplementation in WD-fed mice led to higher CEs levels (by 105 %) while no significant differences were found in Chol levels (**Figure 42B**). The data suggested that AntiOxCIN$_4$ can modulate FAs acyl chain composition, as demonstrated by a non-statistically significant decrease of oleate (by 9 %) and a non-statistically significant increase of linoleate (by 4 %) and ω-3 FAs (by 2 %) in the AntiOxCIN$_4$ + WD group, relative to the Vehicle + WD group (**Figure 42C**).

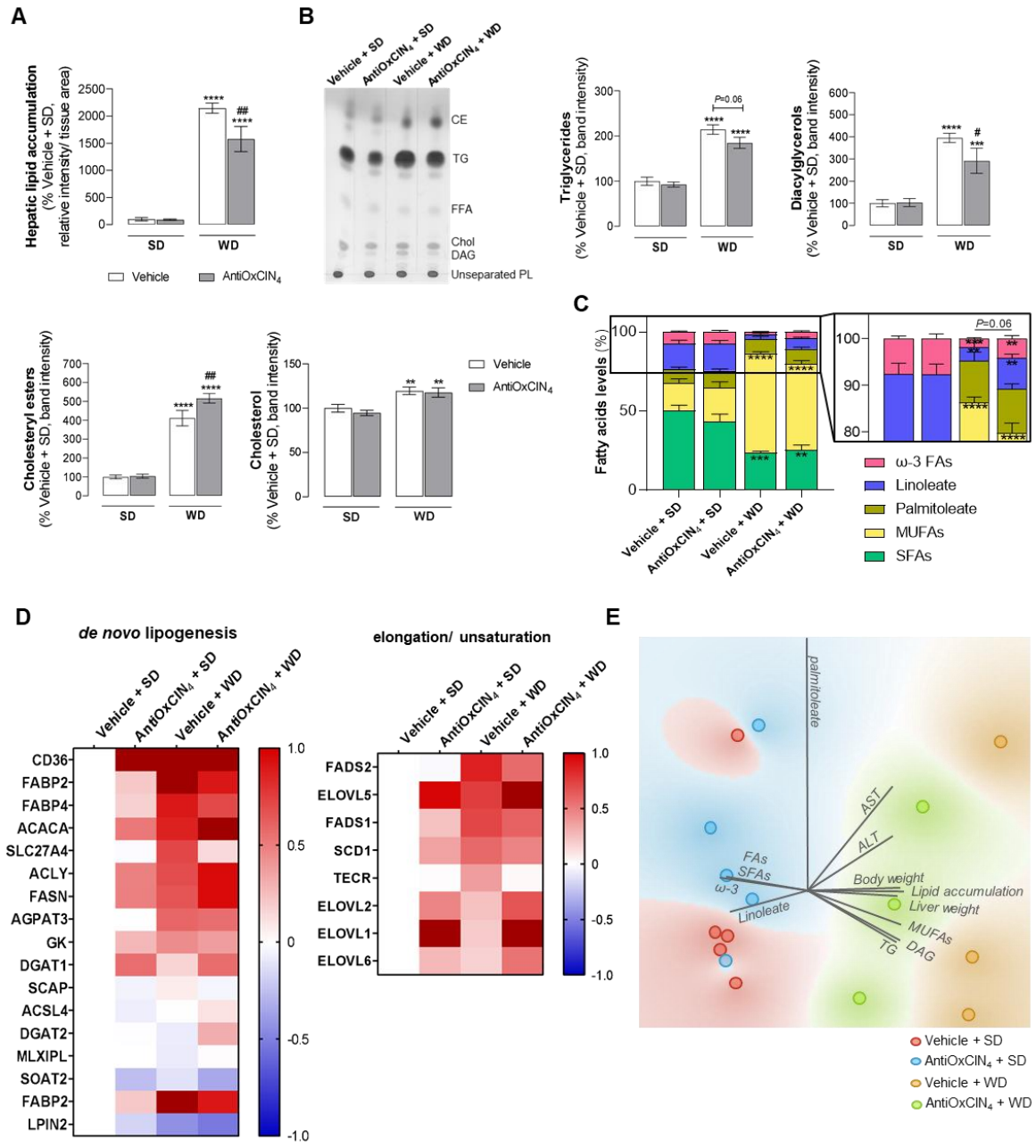

Figure 42. Effects of AntiOxCIN$_4$ on hepatic lipid content and composition of WD-fed mice with NAFL phenotype. (**A**) Hepatic lipid accumulation. Lipid quantification was obtained from three independent images/per animal of each experimental group of H&E staining. (**B**) Representative image of hepatic neutral lipid profile in WD-fed mice in the absence/presence of AntiOxCIN$_4$ (2.5 mg/day/animal) using thin-layer chromatography (TLC). Several parameters were evaluated: triglycerides (TGs), diacylglycerols (DAGs), cholesteryl esters (CEs) and free cholesterol (chol). (**C**) Fatty acyl chain composition of hepatic triglycerides in terms of saturated fatty acids, palmitoleate, oleate, linoleate and ω-3 fatty acids in liver homogenates from WD-fed mice in the absence/presence of AntiOxCIN$_4$ (2.5 mg/day/animal). (**D**) MS-proteomic analysis of hepatic *de novo* lipogenesis and fatty acids elongation/unsaturation-related proteins in WD-fed mice in the absence/presence of AntiOxCIN$_4$ (2.5 mg/day/animal). Blue color represents a decrease, while red

color represents an increase of protein levels. Protein abbreviations are detailed in **Table 8** (**E**) PCA of physiological parameters, hepatocyte damage hallmarks and lipid content with respective composition (data taken from **Figure 41A**, **Figure 40E**, **Figure 42A-C**, respectively). Data are expressed as the mean ± SEM and the results were normalized to the control condition (set as = 100 %). Statistically significant compared using two-way ANOVA followed by Fisher's LSD test for multiple comparisons (**P < 0.01,***P < 0.0005, ****P < 0.0001 vs Vehicle + SD); ($^{\#}$P < 0.05, $^{\#\#\#}$P < 0.0005 Vehicle + WD). **Contribution to this panel**: I was responsible by the conceptualization of **Figure 42A-E**. Team member Teresa Cunha-Oliveira performed the principal component analysis of the data in the **Figure 42E**, which was then analyzed by me.

To identify relevant parameters for the characterization of the experimental groups, we performed principal component analysis (PCA) using the subset of physiological parameters (Body weight; Liver weight; AST; ALT; Hepatic lipid accumulation; TG; DAG; SFAs; MUFAs; Palmitoleate; Linoleate; ω-3 FAs). The measured parameters allow us to discriminate between the experimental groups. In fact, samples belonging to Vehicle + SD and AntiOxCIN$_4$ + SD cluster close to each other while Vehicle + WD sit distant from SD groups. Interestingly, AntiOxCIN$_4$ + WD cluster is more closer to SD groups (**Figure 42E**). These observations point out an amelioration in hepatic lipid profile, which could indicate a healthier liver phenotype when NAFL models were supplemented with AntiOxCIN$_4$.

9.3.3. AntiOxCIN$_4$ decreased LD size of FFAs-treated human HepG2 cells

Cellular and molecular evidences in human hepatocytes (HepG2) were acquired to corroborate the *in vivo* data. AntiOxCIN$_4$ (48 h, 100 µM) counteracted the lipotoxicity of supraphysiological FFA concentrations (24 h, 250 µM). Control (BSA-treated) cells incubated with FFAs showed an increase in neutral lipid content (210 %) without signs of toxicity (**Figure 43A**). AntiOxCIN$_4$ incubation (48h, 100 µM) before FFAs exposure significantly reduced lipid accumulation (by 29 %) (**Figure 43A**). Additionally, AntiOxCIN$_4$ pretreatment showed to significantly reduced LD size while slightly decreased their abundance when compared with vehicle + FFA cells (**Figure 43B**). Nuclear magnetic resonance (NMR) experiments strengthened that AntiOxCIN$_4$ decreased TG and FAs levels in HepG2 cells exposed to FFAs (**Figure 43C**). Altogether, these *in vitro* observations supported the beneficial effects of AntiOxCIN$_4$ in the lipid accumulation of human HepG2 cells.

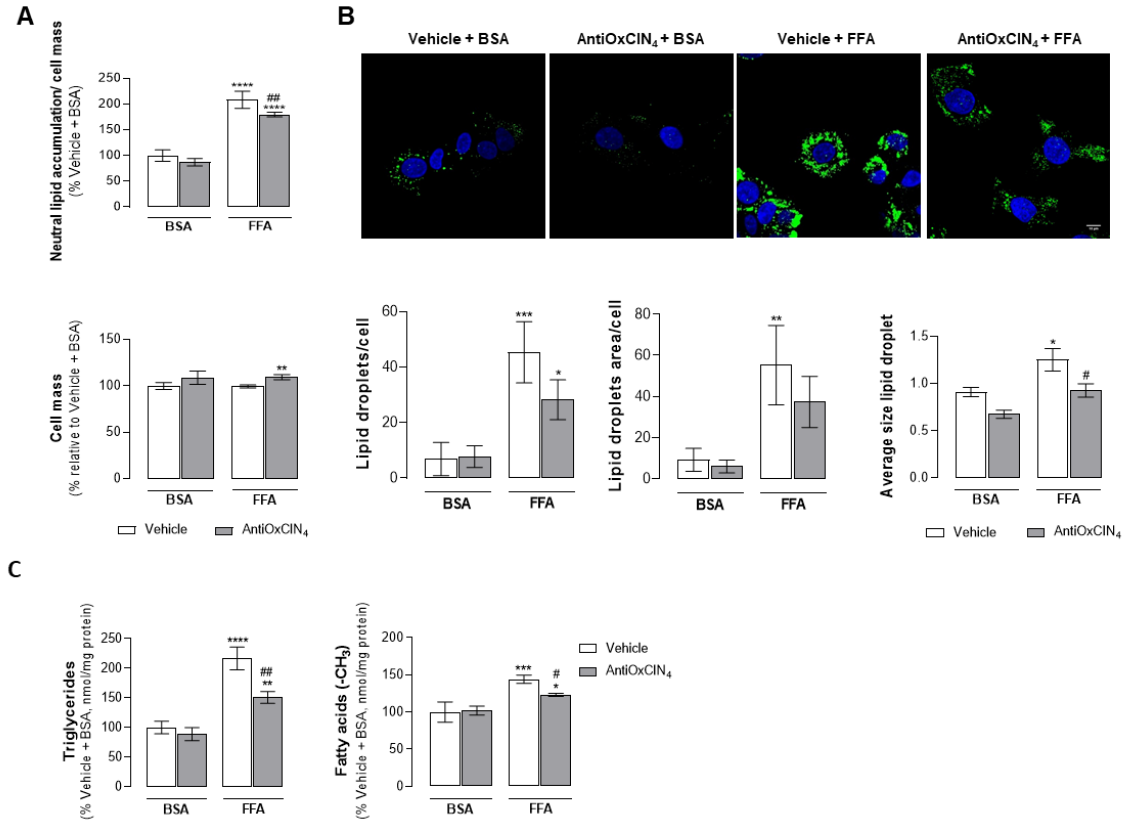

Figure 43. Effects of AntiOxCIN$_4$ on hepatic lipid content and composition of human HepG2 cells. **(A)** Neutral lipid accumulation (upper) and respective cell mass (lower) in human HepG2 cells treated with vehicle (BSA) or FFAs (24 h, 250 µM) in the absence/presence of AntiOxCIN$_4$ (48 h, 100 µM). **(B)** Typical background-corrected images of HepG2 cells stained with the LipidTOX Green (lipids, green) and Hoechst 33342 (nucleus, blue), and treated with vehicle (BSA) or FFAs (24 h, 250 µM) in the absence/presence of AntiOxCIN4 (48 h, 100 µM) (upper). The LipidTOX Green and Hoechst 33342 fluorescence intensity was color-coded to green and blue, respectively. Average lipid droplet number, area and size was calculated from four images in multiple experiments (lower). **(C)** Triglycerides (left) and intracellular fatty acids (right) in cells treated with vehicle (BSA) or FFAs (24h, 250 µM) in the absence/presence of AntiOxCIN$_4$ (48h, 100 µM). Data are expressed as the mean ± SEM and the results were normalized to the respective control condition (set as 100 %). Statistically significant compared using two-way ANOVA followed by Fisher's LSD test for multiple comparisons (*P<0.05, **P < 0.01, ***P < 0.0005, ****P < 0.0001 vs Vehicle + BSA); ($^{\#}$P < 0.05, $^{\#\#}$P < 0.01 vs Vehicle + FFAs).

9.3.4. AntiOxCIN$_4$ increased mitochondrial and peroxisomal fatty acid oxidation (FAO) markers in the liver of WD-fed mice with a NAFL phenotype

As FAO is a major pathway responsible for FAs metabolism in hepatocytes under nutrient overload [259], we evaluate the effects of AntiOxCIN$_4$ in FAO in WD-fed mice Using MS-proteomic analysis, we observed that AntiOxCIN$_4$ + SD mice presented higher levels of mitochondrial-FAO related proteins (ACOT12, ECHS1 and ECHDC3), peroxisomal-FAO related proteins (ACOT3/4, ABCD1/2 transporters and ACOX1i2), and peroxisomal markers (SLC25A17 and MAVS) (**Figure 44**). Although WD feeding can also cause an increase in some of these FAO- and peroxisomal-related proteins, it is important to note that AntiOxCIN$_4$ supplementation had a major impact in mitochondrial- and peroxisomal FAO-related enzymes and peroxisomal-related protein levels (**Figure 44**).

The results suggest that supplementation with AntiOxCIN$_4$ improved both mitochondrial and peroxisomal FAO.

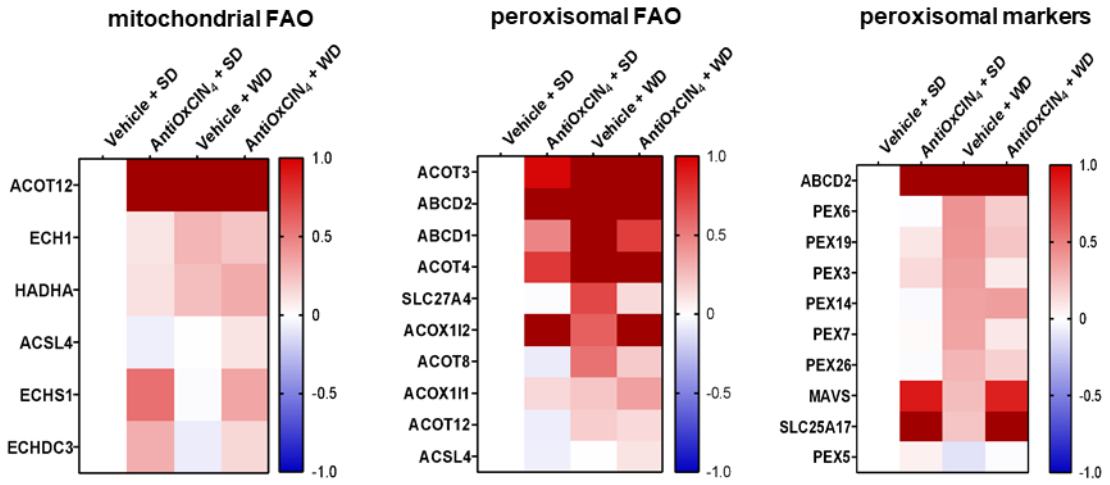

Figure 44. Effects of AntiOxCIN$_4$ on mitochondrial and peroxisomal fatty acid oxidation (FAO) of WD-fed mice with a NAFL phenotype. Mass spectrometry (MS)-proteomic analysis of hepatic mitochondrial, peroxisomal FAO-related proteins, and peroxisomal markers levels in WD-fed mice in the absence/presence of AntiOxCIN$_4$ (2.5 mg/day/animal). Blue color represents a decrease, while red color represents an

increase of the protein levels. Protein abbreviations are detailed in **Table 8**. **Contribution to this panel**: I was responsible by the conceptualization and experimental work of **Figure 44**.

9.3.5. AntiOxCIN$_4$ increased mitochondrial and peroxisomal fatty acid oxidation (FAO) markers and FAO-linked oxygen consumption in FFAs-treated human HepG2 cells

Cellular evidences in human hepatocytes (HepG2) were acquired to corroborate the *in vivo* effects of AntiOxCIN$_4$ in both mitochondrial and peroxisomal FAO. In fact, we observed that AntiOxCIN$_4$ increased mRNA levels of peroxisome proliferator-activated receptor-α (*PPARA*) in both Vehicle + FFAs (169 %) and in Vehicle + BSA (173 %) regimens (**Figure 45A**). PPARα is a master regulator of FAO-related pathways, being its elevated levels correlated with elevated mitochondrial-FAO (*ACOT2*, 169 %; *CPT1A*, 151 %, *ECHS1*, 140 %) and peroxisomal-FAO related genes (*PEX14*, 117 %; *ACOX1*, 174 %) in AntiOxCIN$_4$ + FFAs condition. The markers *CPT1A* (175 %), *ACOT2* (173 %) and *PEX14* (178 %) were also induced in the BSA + AntiOxCIN$_4$ treatment group (**Figure 45A**). The functional cellular oxygen consumption rate (OCR) resulting from palmitoyl-L-carnitine oxidation in human HepG2 cells was analyzed to estimate the mitochondrial contribution for FAO. No significant differences were found between Vehicle + BSA and AntiOxCIN$_4$ + BSA-treated cells (**Figure 45B**). Acute cell treatment with palmitoyl-L-carnitine led to an increase of 33 % in FAO-linked OCR, being this parameter increased by 15 % in AntiOxCIN$_4$ + palmitoyl-L-carnitine cells (**Figure 45B**). Altogether, the observed decrease in hepatic fat accumulation by AntiOxCIN$_4$ supplementation results from an upregulation of both mitochondrial and peroxisomal FAO.

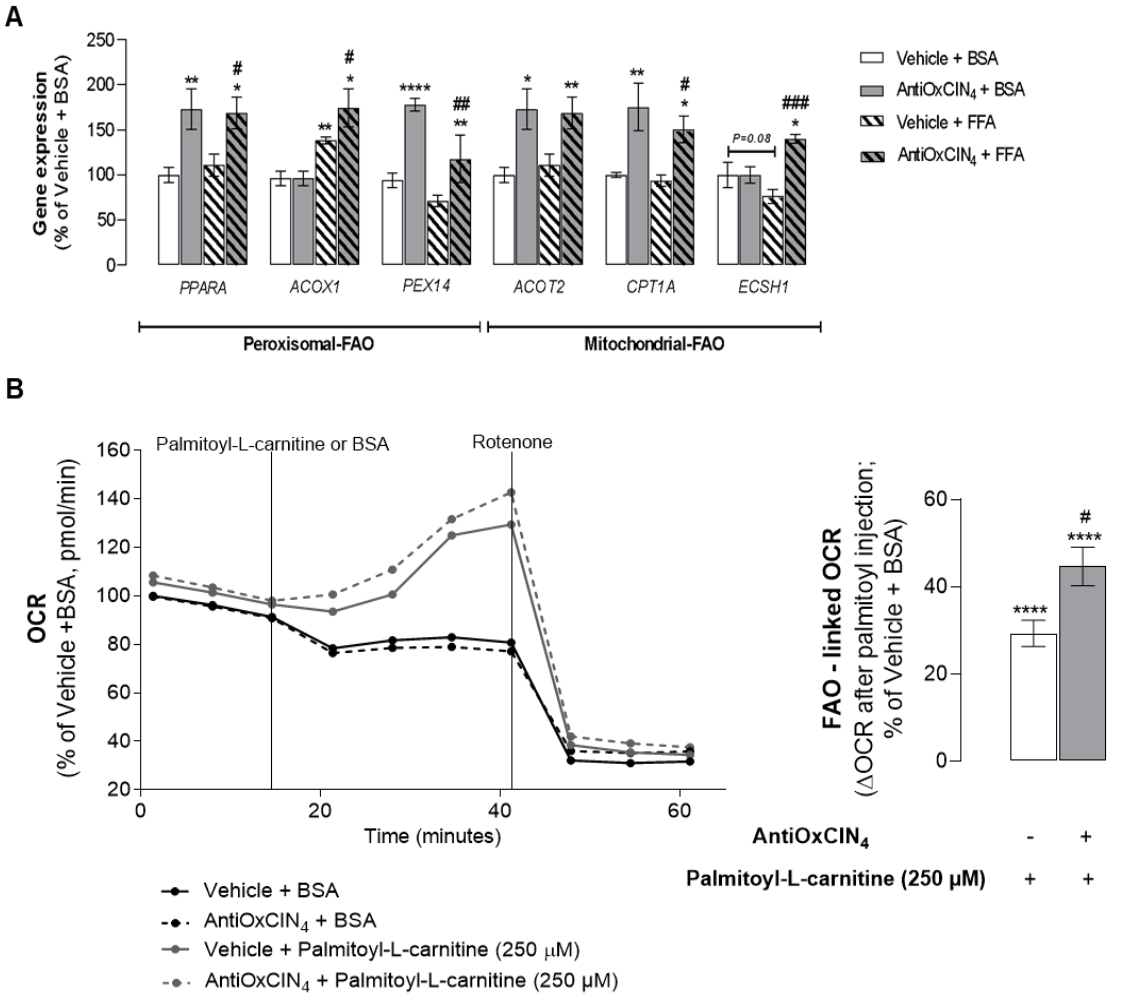

Figure 45. Effects of AntiOxCIN$_4$ on mitochondrial and peroxisomal fatty acid oxidation (FAO) of FFAs-treated human HepG2 cells. (**A**) mRNA transcript levels of FAO-related genes (*PPARA, ACOX1, PEX14, ACOT2, CPT1A, and ECSH1*) in human HepG2 cells treated with vehicle (BSA) or FFAs (24 h, 250 μM) in the absence/presence of AntiOxCIN$_4$ (48 h, 100 μM). (**B**) Representative image of FAO-related oxygen consumption rate (OCR) measurement. BSA or palmitoyl-L-carnitine (250 μM) were acutely injected in HepG2 in the absence/presence of AntiOxCIN$_4$ (48 h, 100 μM). Data are expressed as the mean ± SEM and the results were normalized to the control condition (set as 100 %). Statistically significant compared using

two-way ANOVA followed by Fisher's LSD test for multiple comparisons (*P<0.05, **P < 0.01, ****P < 0.0001 vs Vehicle + BSA); ($^{\#}$P < 0.05, $^{\#\#}$P < 0.01, $^{\#\#\#}$P < 0.0005 vs Vehicle + FFAs).

9.3.6. AntiOxCIN$_4$ improved mitochondrial oxygen consumption and decreased the susceptibility to mitochondrial permeability transition pore (mPTP) opening in the liver of WD-fed mice with NAFL phenotype

Considering the observed stimulation of the mitochondrial FAO pathway, we investigated whether AntiOxCIN$_4$ also impacts the mitochondrial oxygen consumption. This was assessed by using isolated hepatic mitochondrial fractions from the experimental mice groups. Liver mitochondria from Vehicle + WD energized with pyruvate/malate showed an increase in ADP-stimulated respiration (st3) and maximal uncoupled respiration (st3u) OCR (**Figure 46A**). AntiOxCIN$_4$ supplementation significantly prevented the WD-induced increase in st3u OCR (**Figure 46A**). Moreover, AntiOxCIN$_4$ promoted a decrease in st3u in SD-fed mice (**Figure 4A**). The respiratory control ratio (RCR, state 3/state 4o), a measure of OXPHOS-coupling efficiency, was decreased in liver mitochondria from Vehicle + WD, an effect that was partially prevented by AntiOxCIN$_4$ supplementation in WD (**Figure 46C**). Although similar results were observed for succinate-energized mitochondria (**Figure 46B**), RCR was not affected in complex II-driven respiration (**Figure 46D**). Notwithstanding, we observed no differences in the transport of electrons through complex I, II and III between both WD-fed groups (Vehicle + WD vs. AntiOxCIN$_4$ + WD), despite an increase in the Vehicle + SD mice group (**Figure 46F**). Next, we evaluated the susceptibility of the hepatic mitochondria to mPTP opening in the presence of Ca^{2+} and *t*BHP. Isolated mitochondria from Vehicle + WD mice had higher susceptibility to mPTP opening (150 %), while AntiOxCIN$_4$ supplementation showed a non-statistically significant protection against mPTP opening (by 18 %) in this group (**Figure 46E**). These results suggest that AntiOxCIN$_4$ improves overall liver mitochondrial function of WD-fed mice.

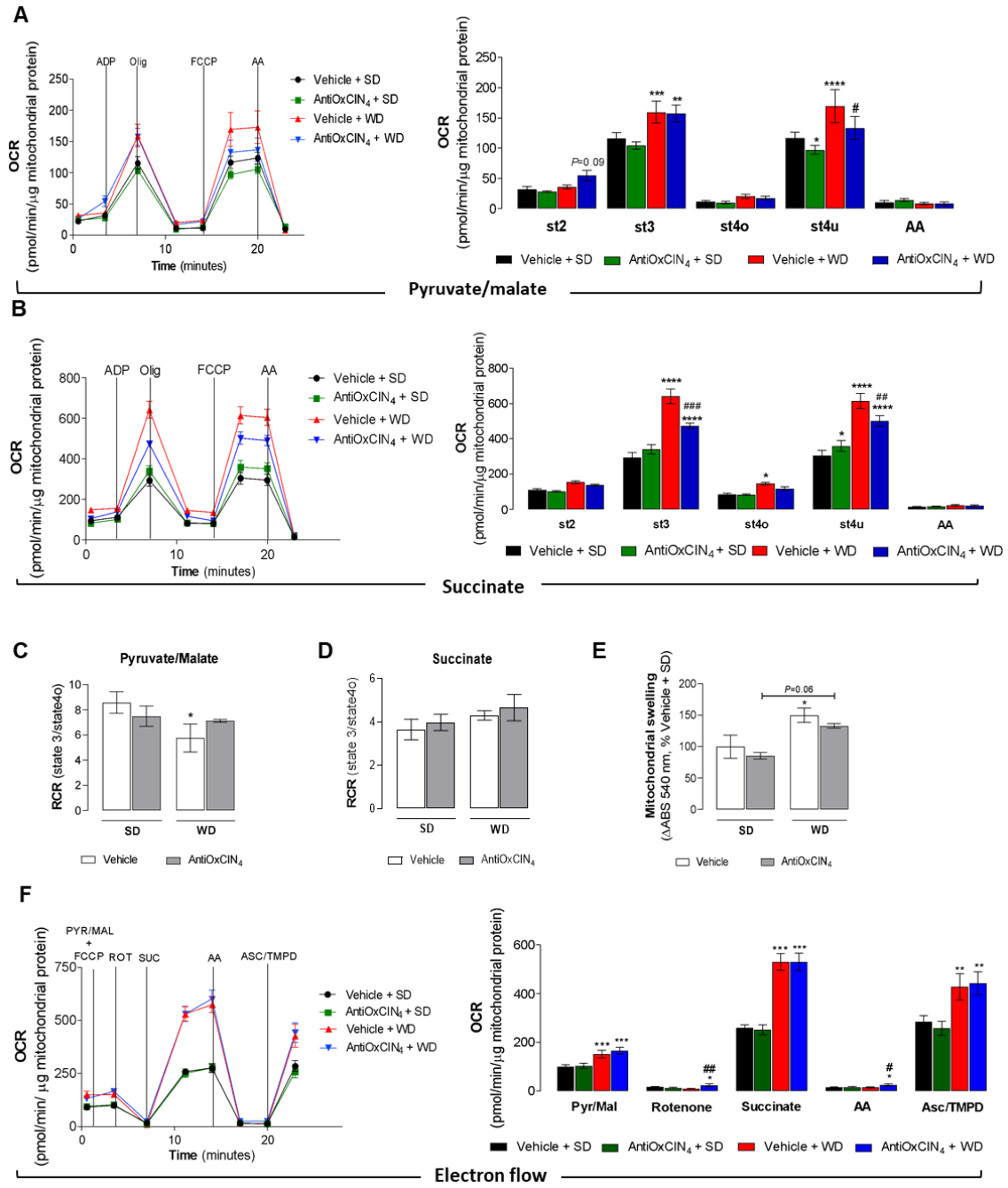

Figure 46. Effects of AntiOxCIN$_4$ on mitochondrial function in a WD-fed mice with NAFL phenotype. (**A**) Oxygen consumption rate (OCR) of Complex I-linked respiration (pyruvate/malate, 10 mM/5 mM) in isolated liver mitochondria from WD-fed mice in the absence/presence of AntiOxCIN$_4$ (2.5 mg/day/animal). Adenosine di-phosphate (ADP) (4 mM), oligomycin (olig) (2 µg/µL), carbonyl cyanide-p-trifluoromethoxyphenylhydrazone (FCCP) (4 µM) and antimycin A (AA) (2 µM) were sequentially added to modulate mitochondrial function as described in the **section 9.2.8**. (**B**) Oxygen consumption rate (OCR) of Complex II-linked respiration (succinate, 10 mM) in isolated liver mitochondria of WD-fed mice in the absence/presence of AntiOxCIN$_4$ (2.5

mg/day/animal). ADP (4 mM), olig (2 µg/µL), FCCP (4 µM) and AA (2 µM) were sequentially added to modulate mitochondrial function. (**C**) Respiratory control ratio (RCR) (state 3/state 4o) of pyruvate/malate-energized isolated liver mitochondria of WD-fed mice in the absence/presence of AntiOxCIN$_4$ (2.5 mg/day/animal). (**D**) Respiratory control ratio (RCR) (state 3/state 4o) of succinate-energized isolated liver mitochondria of WD-fed mice in the absence/presence of AntiOxCIN$_4$ (2.5 mg/day/animal). (**E**) Mitochondrial swelling after induction of mitochondrial permeability transition pore opening in succinate-energized isolated liver mitochondria of WD-fed mice in the absence/presence of AntiOxCIN$_4$ (2.5 mg/day/animal), in the presence of *t*BHP and $CaCl_2$. (**F**) Mitochondrial electron flow-associated OCR measurement in pyruvate/malate-energized isolated liver mitochondria, supplemented with FCCP (2 µM), of WD-fed mice in the absence/presence of AntiOxCIN$_4$ (2.5 mg/day/animal). Rotenone (2 µM), succinate (10 mM), antimycin A (2 µM) and Asc/TMPD (10 mM/100 µM) were sequentially added to modulate mitochondrial function. Data are expressed as mean ± SEM and the results were normalized to the control condition (set as = 100%). Statistically significant compared using two-way ANOVA followed by Fisher's LSD test for multiple comparisons (*P<0.05, **P < 0.01, ***P < 0.0005, ****P < 0.0001 vs Vehicle + SD); ($^{\#}$P < 0.05, $^{\#\#}$P < 0.01, $^{\#\#\#}$P < 0.0005 vs Vehicle + WD). **Contribution to this panel**: I was responsible by the conceptualization, experimental work and data analysis of **Figure 46 A-F.**

9.3.7. AntiOxCIN$_4$ avoided alterations in mitochondrial phospholipid profile in the liver of WD-fed mice with NAFL phenotype

Phospholipid composition in mitochondrial membranes is crucial for the architecture and functionality of mitochondria [666]. So, we analyzed the mitochondrial phospholipid composition of steatotic livers in the absence/presence of AntiOxCIN$_4$. Vehicle + WD mice showed decreased levels of sphingomyelin (62 %) and phosphatidylethanolamine (PE) (77 %), with the latter contributing to an increase of phosphatidylcholine (PC)/PE ratio (126 %) (**Figure 47**). Importantly, AntiOxCIN$_4$ supplementation decreased cardiolipin levels (85 %) when compared with Vehicle + WD (110 %), while maintaining PC/PE ratio to levels similar to the SD-fed groups (93 %) (**Figure 47**). AntiOxCIN$_4$ *per se* (SD group) did not affect mitochondrial phospholipid levels (**Figure 4D and S2D**). The data reinforced the indication that AntiOxCIN$_4$ supplementation can prevent mitochondrial membrane composition alterations in WD-fed mice. Modifications in mitochondrial

membrane composition may determine alterations on parameters such as fluidity and stability which modulate mitochondrial bioenergetics.

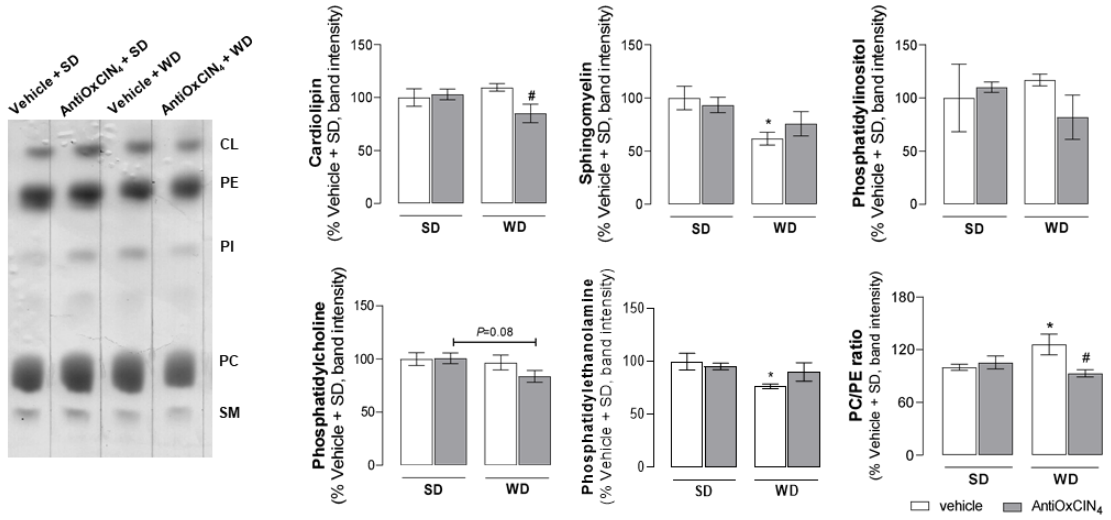

Figure 47. Effects of AntiOxCIN$_4$ on mitochondrial phospholipid profile in a WD-fed mice with NAFL phenotype Mitochondrial phospholipid profile in isolated liver mitochondria from WD-fed mice in the absence/presence of AntiOxCIN$_4$ (2.5 mg/day/animal) using TLC. Several parameters were evaluated: cardiolipin (CL), phosphatidylethanolamine (PE), phosphatidylcholine (PC), phosphatidylinositol (PI) and sphingomyelin (SM), PC/PE ratio levels. Data are expressed as mean ± SEM and the results were normalized to the control condition (set as = 100%). Statistically significant compared using two-way ANOVA followed by Fisher's LSD test for multiple comparisons (*P<0.05 vs Vehicle + SD); ($^{\#}$P < 0.05 vs Vehicle + WD). **Contribution to this panel**: I was responsible by the conceptualization of **Figure 47.**

9.3.8. AntiOxCIN$_4$ upregulated mitochondrial OXPHOS subunits by increasing PGC-1α and mitochondrial SIRT3 protein levels in the liver of WD-fed mice with NAFL phenotype

SIRT3, a member of NAD$^+$-dependent deacetylases mainly localized in mitochondria, modulates mitochondrial ROS and biogenesis in a NAFLD context [276, 667]. To unravel the origin of the mitochondrial bioenergetics alteration induced by WD, we analyzed SIRT3 and peroxisome proliferator-activated receptor-gamma coactivator (PGC-1α) protein levels. Vehicle + WD group showed a non-statistically significant increase of SIRT3 (5-fold) and PGC-1α (173 %) protein levels (**Figure 48A**). Interestingly, AntiOxCIN$_4$ supplementation in WD-fed mice further amplified that effect by 53 % in PGC-1α and 603 % in SIRT3 (**Figure 48A**). Moreover, PGC-1α protein expression in both AntiOxCIN$_4$-

treated groups (SD or WD) was correlated with a higher protein expression of OXPHOS complexes subunits, mainly at Complex I level (MT-ND5, NDUFA3, NDUFV2, NDUFB4, NDUFS8, NDUFS3) (**Figure 48B**). These findings indicate that AntiOxCIN$_4$ modulates mitochondrial metabolism by increasing protein levels of OXPHOS complexes subunits through PGC-1α-SIRT3 pathway in the liver of WD-fed mice with NAFL phenotype.

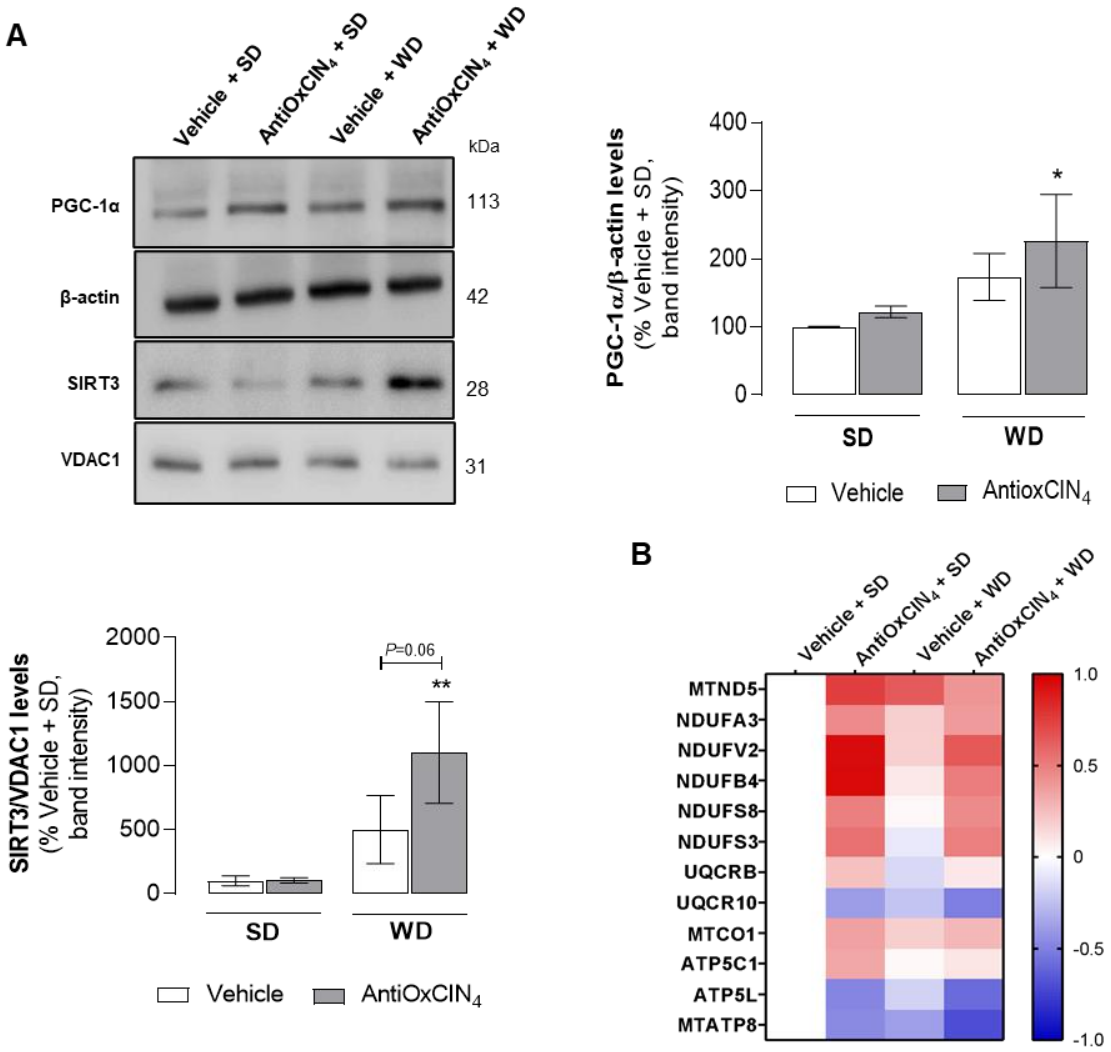

Figure 48. Effects of AntiOxCIN$_4$ on SIRT3-PGC-1α axis and mitochondrial OXPHOS subunits in a WD-fed mice with NAFL phenotype. (**A**) Typical Western blot result of whole-liver homogenates depicting the cytosolic protein levels of PGC-1α and mitochondrial protein levels of SIRT3 from WD-fed mice in the absence/presence of AntiOxCIN$_4$ (2.5 mg/day/animal). These blots were inverted and contrast-optimized for visualization purposes. Quantification of the bands was performed using the original blots. Quantification of protein levels in multiple experiments were normalized to β- actin (cytosol) or VDAC (mitochondria) levels. (**B**) MS-proteomic analysis of mitochondrial OXPHOS complexes subunits protein levels in liver homogenates from WD-fed mice in the absence/presence of AntiOxCIN$_4$ (2.5 mg/day/animal). Blue color

represents a decrease, while red color represents an increase of protein levels. Blue color represents a decrease, while red color represents an increase of protein levels. Protein abbreviations are detailed in **Table 8**. Data are expressed as the mean ± SEM and the results were normalized to the control condition (set as 100 %). Statistically significant compared using two-way ANOVA followed by Fisher's LSD test for multiple comparisons (*P<0.05, **P < 0.01 vs Vehicle + SD). **Contribution to this panel**: I was responsible by the conceptualization, experimental work, and data analysis of **Figure 48A-B.**

9.3.9. AntiOxCIN$_4$ improved mitochondrial morphology and function of FFAs-treated human HepG2 cells

To assess the mice-to-human translation of the mitochondrial implications, we evaluated the effects of AntiOxCIN$_4$ in ΔΨm by incubating BSA- or FFAs-treated human HepG2 cells with the fluorescent cation Mitotracker Red. (**Figure 49A**) FFA-treated cells showed a decreased ΔΨm (65 %), but the pre-incubation with AntiOxCIN$_4$ (48 h, 100 μM) not only prevented FFAs alterations but increased ΔΨm (160 %) when compared to control cells (**Figure 49B**). AntiOxCIN$_4$ induced a ΔΨm hyperpolarization (130 %) in BSA-treated HepG2 cells (**Figure 49B**). The cellular consequences of AntiOxCIN$_4$ and/or FFAs treatments on gene expression of mitochondrial OXPHOS-related genes was also determined. The mRNA transcripts levels were significantly increased in the presence of AntiOxCIN$_4$ (**Figure 49C**). Human HepG2 cells treated with FFAs (24 h, 250 μM) showed decreased mRNA levels of the mitochondrial DNA-encoded NADH dehydrogenase subunit 5 of respiratory complex I gene (*MT-ND5*, 64 %) and the nuclear DNA-encoded succinate dehydrogenase subunit A of respiratory complex II gene (*SDHA*, 32 %) (**Figure 49C**). Pre-incubation with AntiOxCIN$_4$ prevented a FFAs-induced *MT-ND5* gene mRNA depletion. However, no differences were observed in the mRNA level of *SDHA* gene (**Figure 49C**). AntiOxCIN$_4$ also increased mRNA levels of other mitochondrial OXPHOS subunits genes (*e.g., NDUFA9*, *UQCRC2*, *COX4I1*, *MT-ATP6* and *ATG5MC1*) in the FFAs treated cells (**Figure 49C**). These results propose that in HepG2 cells AntiOxCIN$_4$ induced a mitochondrial membrane potential hyperpolarization due to an increased mitochondrial OXPHOS content in human HepG2 cells.

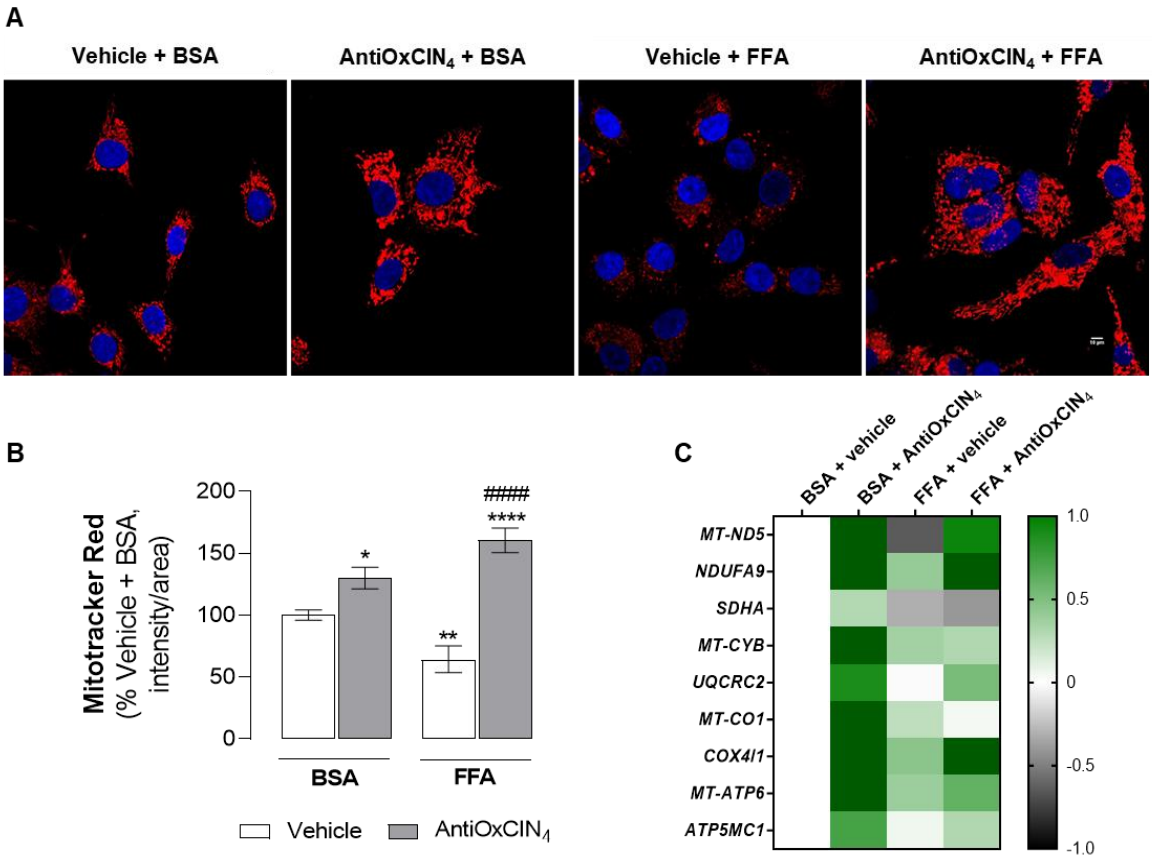

Figure 49. Effects of AntiOxCIN$_4$ on mitochondrial morphology and function of FFAs-treated human HepG2 cells. (**A**) Typical background-corrected images of HepG2 cells stained with the fluorescent cation MitoTracker Red FM (red) and Hoechst 33342 (blue) and treated with vehicle (BSA) or FFAs (24h, 250 µM) in the absence/presence of AntiOxCIN$_4$ (48h, 100 µM). The MitoTracker Red FM and Hoechst 33342 fluorescence intensity was color-coded to red and blue, respectively. (**B**) Average mitochondrial MitoTracker Red fluorescence intensity was calculated from four imagens of each independent experiment (n=3). (**C**) mRNA transcript levels of mitochondrial OXPHOS complexes subunits genes (*MT-ND5, NDUFA9, SDHA, MT-CYB, UQCRC2, MT-CO1, COX4I1, MT-ATP6 and ATP5MC1*) in cells treated with vehicle (BSA) or FFA (24h, 250 µM) in the absence/presence of AntiOxCIN$_4$ (48h, 100 µM). Data are expressed as the mean ± SEM and the results were normalized to the control condition (set as = 100%). Statistically significant

compared using two-way ANOVA followed by Fisher's LSD test for multiple comparisons (*P<0.05, **P < 0.01, ****P < 0.0001 vs Vehicle + BSA); ($^{\#\#\#\#}$P < 0.0001 vs Vehicle + FFA).

9.3.10. AntiOxCIN$_4$ increased tricarboxylic acid cycle (TCA) coupling and anaplerotic processes while decreased the TCA turnover in human FFAs-treated HepG2 cells

Alterations in mitochondrial morphology and function have been associated with exacerbated TCA cycle function due to excessive substrate influx, a widely described observation in the pathogenesis of diet-induced fatty liver [240]. To determine the AntiOxCIN$_4$ effect on TCA cycle rates, we used ^{13}C NMR isotopomer analysis for monitoring TCA cycle intermediates. AntiOxCIN$_4$-treated human HepG2 cells in the presence of FFAs/BSA and [1,6-^{13}C2]glucose will generate [3-^{13}C]pyruvate, which can either generate [3-^{13}C]lactate by lactate dehydrogenase or [4-13C]glutamate through the TCA cycle. Briefly, TCA coupling is a ratio between the amount of labelling on glutamate C4 isotopomers and [U-^{13}C]lactate. We observed that TCA coupling is increased in AntiOxCIN$_4$ + BSA-treated human HepG2 cells (252 %) (**Figure 50A**). Moreover, FFAs treatment also increases TCA coupling (254 %), being this effect counteracted when HepG2 were pre-incubated with AntiOxCIN$_4$ (by 121 %) (**Figure 50A**). TCA turnover, a ratio between [3,4,5-^{13}C3]glutamate and [4,5- ^{13}C2]glutamate, was decreased in both AntiOxCIN$_4$ regimens (70 % in both cases), while no alteration was observed in FFAs treatment (**Figure 50B**). Anaplerosis, a process responsible for replenishing TCA cycle intermediates, showed higher values in AntiOxCIN$_4$-treated human HepG2 cells (143% in BSA and 135% in FFA conditions) (**Figure 50C**), while FFAs exposure by itself did not alter this process. These results suggest that the presence of AntiOxCIN$_4$ causes a higher oxidation of pyruvate by the TCA cycle. Moreover, reduced TCA turnover and increased anaplerosis in AntiOxCIN$_4$ treatment may indicate an up-regulation of the biosynthetic precursors.

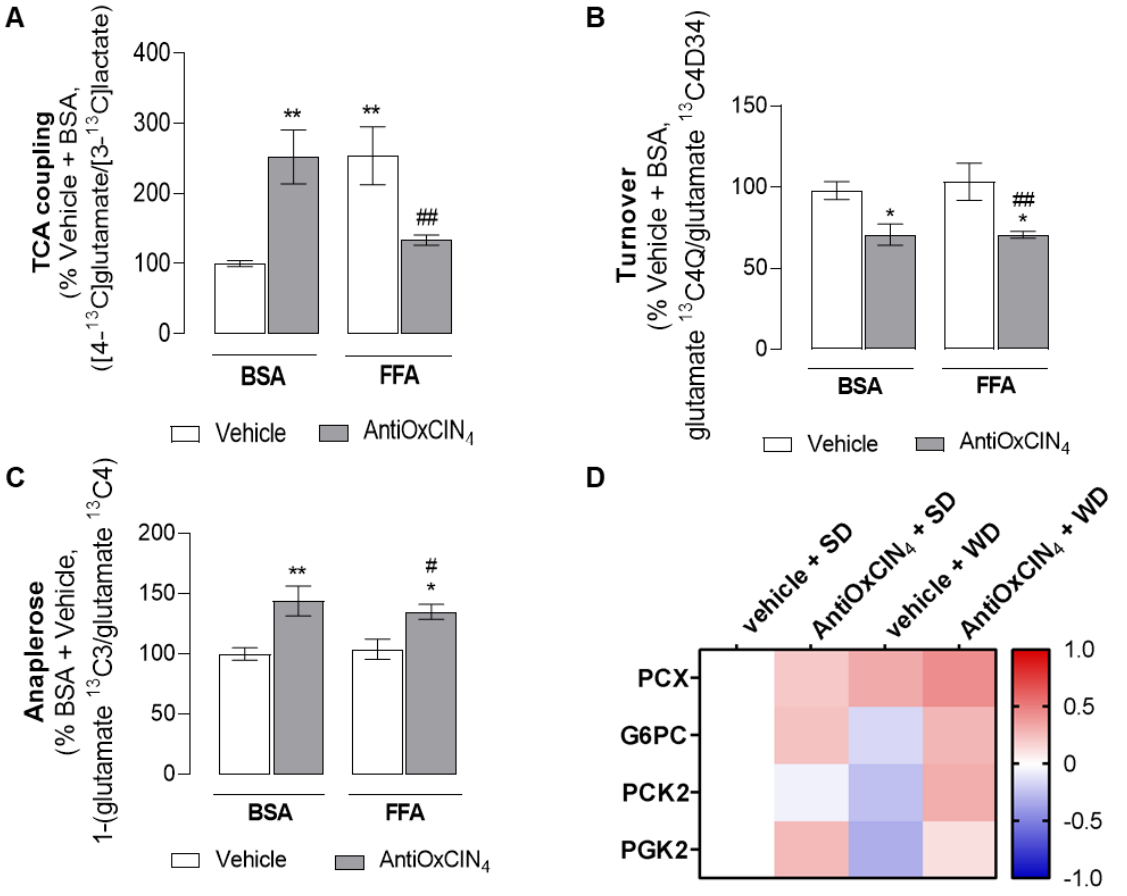

Figure 50. Effects of AntiOxCIN$_4$ on tricarboxylic acid cycle (TCA) coupling and anaplerotic processes in human FFAs-treated HepG2 cells and gluconeogenic-related proteins in the liver of WD-fed mice with NAFL phenotype (A) TCA coupling - [1,6-^{13}C2]glucose consumption coupled to TCA cycle ([4-^{13}C]glutamate/[3-^{13}C]lactate). (**B**) TCA cycle turnover (glutamate ^{13}C4Q/glutamate ^{13}C4D34). (**C**) Anaplerosis [1-(glutamate ^{13}C3/glutamate ^{13}C4)]. (**D**) MS-proteomic analysis of gluconeogenic-related protein levels in WD-fed mice in the absence/presence of AntiOxCIN$_4$ (2.5 mg/day/animal). Blue color represents a decrease, while red color represents an increase of protein levels. Protein abbreviations are detailed in **Table 8.** Data are expressed as the mean ± SEM and the results were normalized to the control condition (set as 100 %). Statistically significant compared using two-way ANOVA followed by Fisher's LSD test for multiple comparisons (*P<0.05, **P < 0.01 vs Vehicle + BSA); ($^{\#}$P < 0.05, $^{\#\#}$P < 0.01, vs Vehicle + FFA).

9.3.11. AntiOxCIN$_4$ increased levels of gluconeogenic-related proteins in the liver of WD-fed mice with NAFL phenotype

Anaplerosis is catalyzed in the liver by the combined action of mitochondrial pyruvate carboxylase (PCX) and phosphoenolpyruvate carboxykinase (PCK2), the two first enzymes of the gluconeogenic pathway [218]. In our NAFL mice model, PCK2 protein was diminished, while AntiOxCIN$_4$ supplementation increased both PCX and PCK2 levels (**Figure 50D**). Moreover, other gluconeogenic enzymes such as phosphoglycerate kinase 2 (PGK2) and glucose-6-phosphatase (G6PC) were increased in AntiOxCIN$_4$ + WD group (**Figure 50D**). AntiOxCIN$_4$ also increased PCX, G6PC and PGK2 protein levels in SD-fed mice (**Figure 50D**).

9.3.12. AntiOxCIN$_4$ stimulated endogenous antioxidant defenses in the liver of WD-fed mice with NAFL phenotype

Hepatic OxS is considered a contributing factor in NAFLD pathogenesis [668], we next evaluated the redox status of steatotic livers from WD-fed mice. In our study, no alterations in hepatic mitochondrial H_2O_2 levels were observed in mice from Vehicle + WD and AntiOxCIN$_4$ + WD (**Figure 51A**). As we previously described AntiOxCIN$_4$ as a redox modulator [460], we decided to investigate whether AntiOxCIN$_4$ impacted the mitochondrial and/or cytosolic enzymatic antioxidant defenses system. Consequently, mitochondria and cytosol subcellular fractions from SD- and WD-fed mice in the presence or absence of AntiOxCIN$_4$ were prepared (**Figure 51B)**. Aconitase is a known mitochondrial enzyme whose activity is compromised in the presence of mtROS. In our study, we observed that AntiOxCIN$_4$ prevented the hepatic de-activation of aconitase in SD-fed mice (**Figure 52C**). In accordance, major antioxidants enzymes such as superoxide dismutase (SOD) and (299 %) and catalase (159 %) activities were increased in isolated hepatic mitochondria from AntiOxCIN$_4$ + SD mice (**Figure 52D**).

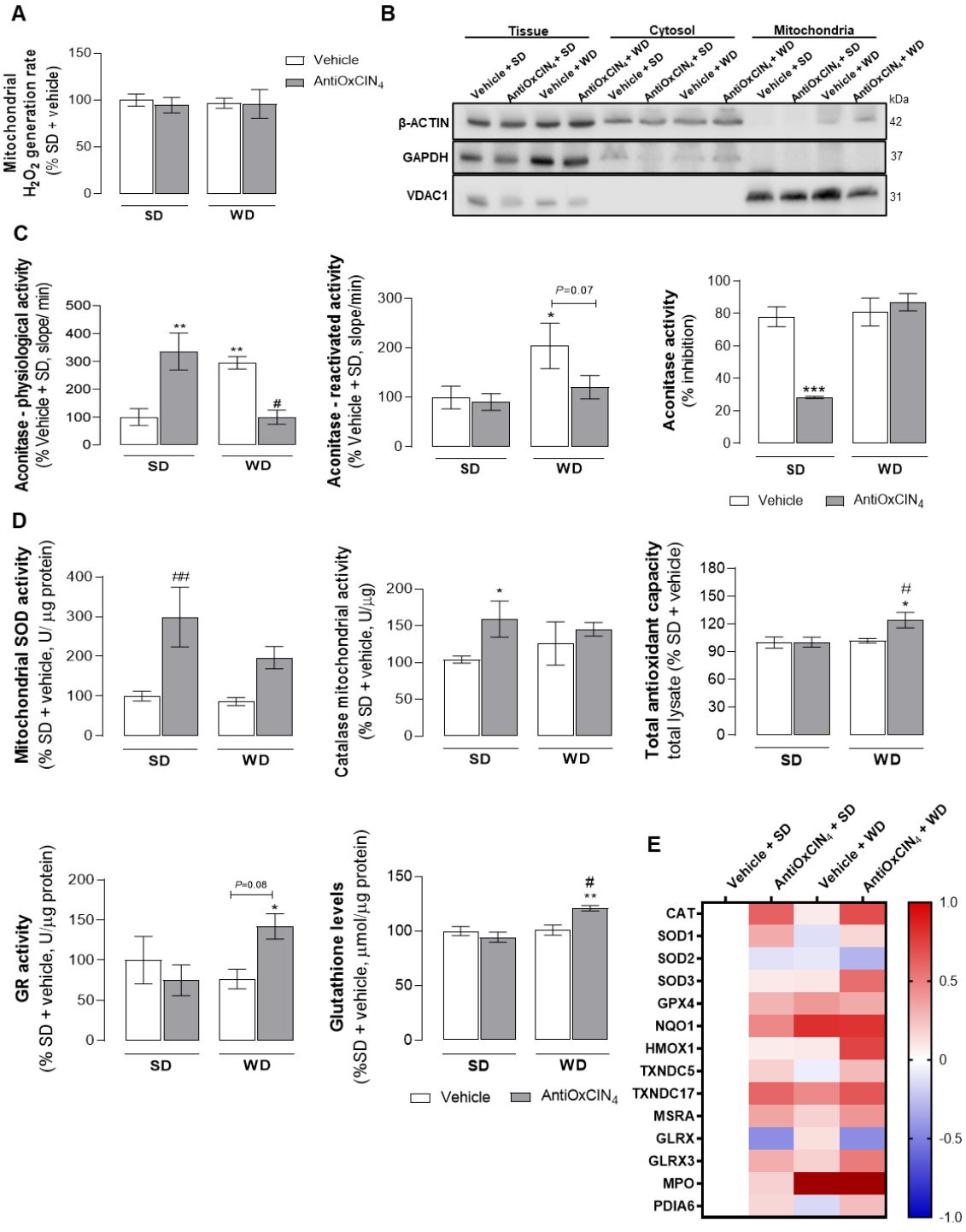

Figure 51. Effects of AntiOxCIN$_4$ on oxidative stress hallmarks and antioxidant defenses in a WD-fed mice with NAFL phenotype. (A) H_2O_2 production rate in isolated liver mitochondria from WD-fed mice in the absence/presence of AntiOxCIN$_4$ (2.5 mg/day/animal). **(B)** Typical Western blot results showing the purity of cytosolic and mitochondrial fractions by using β-actin, GAPDH and VDAC1 levels. **(C)** Physiological and reactivated aconitase activity in isolated liver mitochondria from WD-fed mice in the absence/presence of AntiOxCIN$_4$ (2.5 mg/day/animal). Aconitase activity inhibition was measured as

described in the **section 9.2.15**. (**D**) Antioxidant defense enzymes. Superoxide dismutase (SODs) and catalase activity in isolated liver mitochondrial fraction from WD-fed mice in the absence/presence of AntiOxCIN$_4$ (2.5 mg/day/animal). Total antioxidant capacity, glutathione reductase (GR) activity, and glutathione (GSH) levels in whole liver homogenate from WD-fed mice in the absence/presence of AntiOxCIN$_4$ (2.5 mg/day/animal). **(E)** MS-proteomic analysis of hepatic antioxidant-related enzymes levels in WD-fed mice in the absence/presence of AntiOxCIN$_4$ (2.5 mg/day/animal). The blue color represents a decrease, while the red color represents an increase in protein levels. Protein abbreviations are detailed in **Table 8.** Data are expressed as the mean ± SEM, and the results were normalized to the control condition (set as 100%). Statistically significant compared using two-way ANOVA followed by Fisher's LSD test for multiple comparisons (*P<0.05, **P < 0.01, ***P < 0.0005 vs Vehicle + SD); ($^{\#}$P < 0.05, $^{\#\#}$P < 0.01 vs Vehicle + WD). **Contribution to this panel:** I was responsible by the conceptualization, experimental work, and data analysis of **Figure 51A, C, D, E.**

In total mice liver homogenates, total antioxidant capacity was increased in the AntiOxCIN$_4$ + WD group (**Figure 51D**). Moreover, a higher glutathione reductase (GR) activity (by 67 %) and increment of glutathione (GSH) levels (by 27 %) were observed in the AntiOxCIN$_4$ + WD group, when compared with Vehicle + SD group (**Figure 51D**). We also detected increased protein levels of several antioxidant defense enzymes (e.g., CAT, SOD1, TXNDC5, MSRA, GLRX3) in WD + AntiOxCIN$_4$ (**Figure 51E**). These findings strengthened the redox modulator role of AntiOxCIN$_4$, which impacted the endogenous antioxidant defense system with positive outcomes in the liver of WD-fed mice.

9.3.13. AntiOxCIN$_4$ decreases FFAs-induced ROS in human HepG2 cells by rising endogenous antioxidant defense gene expression

HepG2 cells were used to corroborate the *in vivo* effects of AntiOxCIN$_4$ in the hepatic antioxidant defense system through the measurement of mRNA levels of antioxidant defense enzymes in cells exposed to supraphysiological concentrations of FFAs. Although AntiOxCIN$_4$ *per se* (AntiOxCIN$_4$ + BSA) increased mRNA transcripts of *CAT*, *SOD1, SOD2, GPX1, GPX4, NQO1*, and *HMOX1* genes mRNA transcripts, in the presence of FFA (AntiOxCIN4 + FFA) only mRNA transcripts of *CAT, SOD1, GPX1, GPX4* and *NQO1* genes mRNA transcripts were augmented by AntiOxCIN$_4$ treatment (**Figure 52A**). Oxidation of the cellular OxS indicator CM-H$_2$DCFDA was augmented in FFAs incubation (24 h, 250 μM) in human HepG2 cells (143 %) (**Figure 52B**), an effect that was remarkably

prevented by AntiOxCIN$_4$ (48h, 100 µM) (by 24 %) (**Figure 52B**). These findings in human HepG2 cells corroborated the redox modulator role of AntiOxCIN$_4$ by increasing endogenous antioxidant defense system.

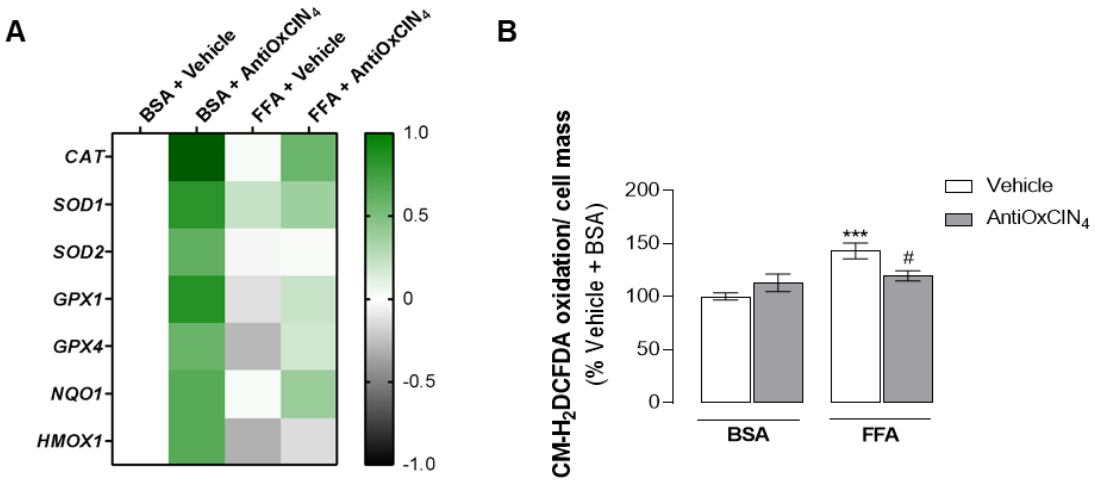

Figure 52. Effects of AntiOxCIN$_4$ on oxidative stress hallmarks and antioxidant defenses in human FFAs-treated HepG2 cells. (B) mRNA transcript levels of antioxidant-related genes (*CAT*, *SOD1*, *SOD2*, *GPX1*, *GPX4*, *NQO1* and *HMOX1*) in cells treated with vehicle (BSA) or FFA (24h, 250 µM) in the absence/presence of AntiOxCIN$_4$ (48h, 100 µM) (right). The grey color represents a decrease, while the green color represents an increase of gene expression levels. **(C)** Cellular reactive oxygen species (ROS) on HepG2 cells treated with vehicle (BSA) or FFA (24h, 250 µM) in the absence/presence of AntiOxCIN$_4$ (48h, 100 µM). (***P < 0.0005 vs Vehicle + BSA); ($^{\#}$P < 0.05 vs Vehicle + FFA).

9.3.14. AntiOxCIN$_4$ did not alter the AKT/mTOR/S6K1/4E-BP1 pathway in the liver of WD-fed mice with a NAFL phenotype

AMP-activated protein kinase (AMPK) and mammalian target of rapamycin complex (mTOR) are major cellular energy sensors, which may contribute to the cellular metabolic adaptation under stress conditions [669, 670]. In the presence of growth factors/insulin or nutrients such as glucose or amino acids, there is a stimulation of PI3K-AKT-mTOR pathway.

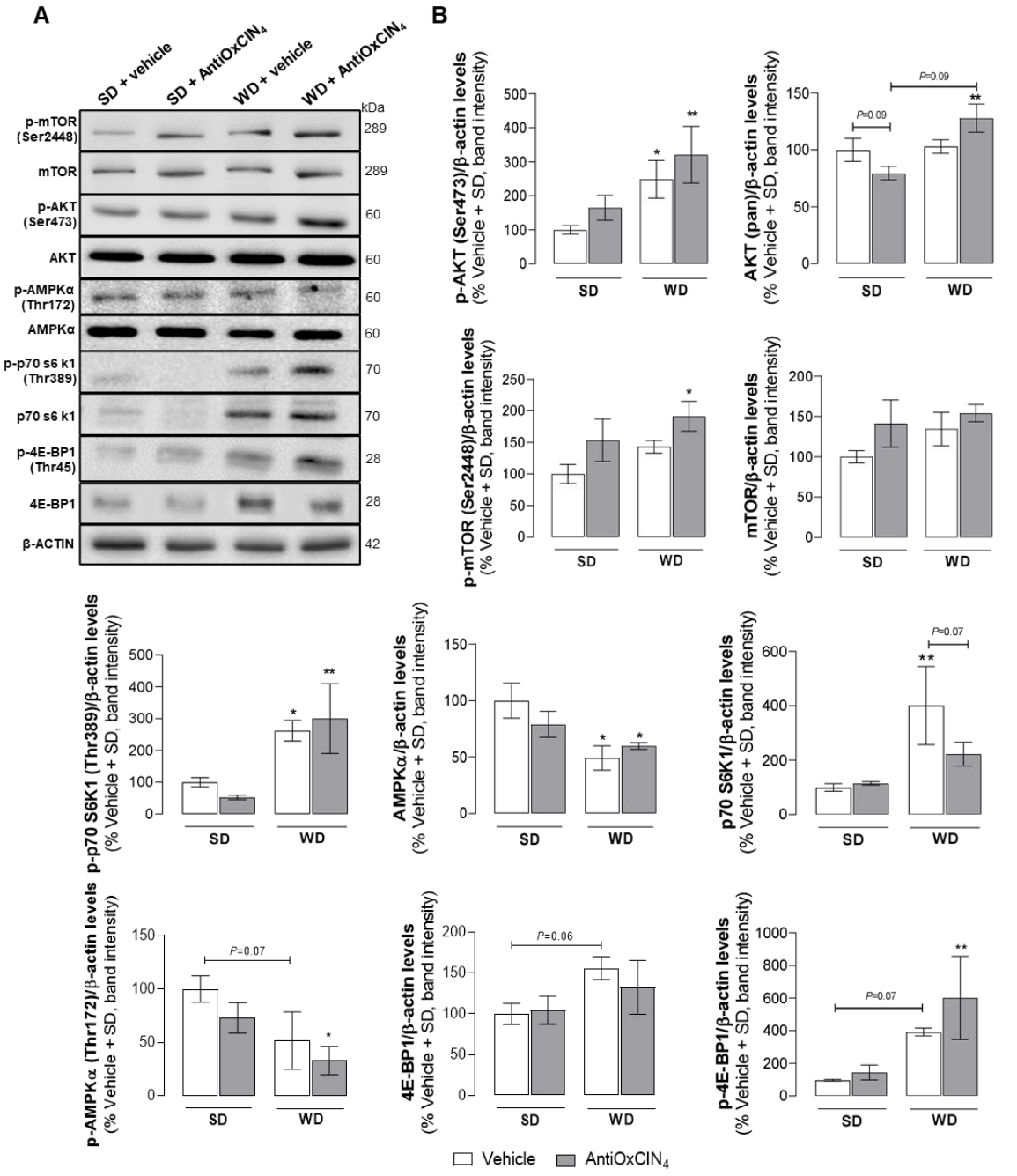

Figure 53. Effects of AntiOxCIN$_4$ on AKT/mTOR axis pathway of WD-fed mice with a NAFL phenotype. (**A**) Typical Western blot result of whole liver homogenates depicting the protein level of p-AKT (Ser473), AKT, p-mTOR (Ser2448), mTOR, p-AMPKalpha (Thr172), AMPKalpha, p-p70 S6K1 (Thr389), p70 S6K1, p-4E-BP1 (Thr46), 4E-BP1 and β-actin (cytosolic marker) from WD-fed mice in the absence/presence of AntiOxCIN$_4$ (2.5 mg/day/animal). These blots were inverted and contrast-optimized for visualization purposes. Quantification of the bands was performed using the original blots. (**B**) Protein expression levels in liver homogenates from WD-fed mice in the absence/presence of AntiOxCIN$_4$ (2.5 mg/day/animal). Quantification of proteins described above in multiple experiments was normalized to β- actin levels. Data are expressed as mean ± SEM and the results were normalized to the control condition (set as = 100%).

Statistically significant compared using two-way ANOVA followed by Fisher's LSD test for multiple comparisons (*P<0.05, **P < 0.01 vs Vehicle + SD). **Contribution to this panel**: I was responsible by the conceptualization, experimental work, and data analysis of **Figure 53** (except p-mTOR/mTOR WB).

In fact, we observed that the WD induced increased phosphorylation at Ser473 (248 %) of the protein kinase B complex (AKT) and a non-significant increase in mTOR phosphorylation at Ser2448 (143 %) (**Figure 53A, B**). A decrease of AMPKα phosphorylation (Thr172) (51 %) reinforced the activation of AKT/mTOR pathway with subsequent phosphorylation of downstream proteins responsible for the induction of protein synthesis: p-p70 S6K1 (Thr389) (262 %) and p-eIF4E-binding protein 1(4E-BP1) (Thr45) (392 %) (**Figure 53A, B**). Similar results were observed when mice fed with WD were supplemented with AntiOxCIN$_4$, with increased levels of p-AKT (320 %), p-mTOR (192 %), p-p70 S6K1 (300 %) and p-4EBP1 (601 %), and decreased levels of p-AMPKα (33 %) (Figure S4A, B). AntiOxCIN$_4$ had no significant effect in AKT/mTOR axis and related downstream pathways in SD-fed mice (**Figure 53A, B**). These results suggest that the high availability of nutrients in WD-fed groups decreases AMPKα activation while increases AKT/mTOR and protein synthesis activation.

9.3.15. AntiOxCIN$_4$ prevented autophagy impairment in the liver of WD-fed mice with a NAFL phenotype

Autophagy is a downstream pathway under AKT/mTOR axis regulation [671]. A decrease in autophagic flux has been described to contribute to NAFLD pathophysiology and disease progression [285]. To determine if and whether AntiOxCIN$_4$ counteracts WD-induced autophagy blockage, several autophagic markers were evaluated. Vehicle + WD treatment increased LC3II/LC3I ratio (225 %) and p62 (267 %), and decreased Beclin1 protein levels (54 %), thereby indicating autophagosome accumulation (**Figure 54A, B**).

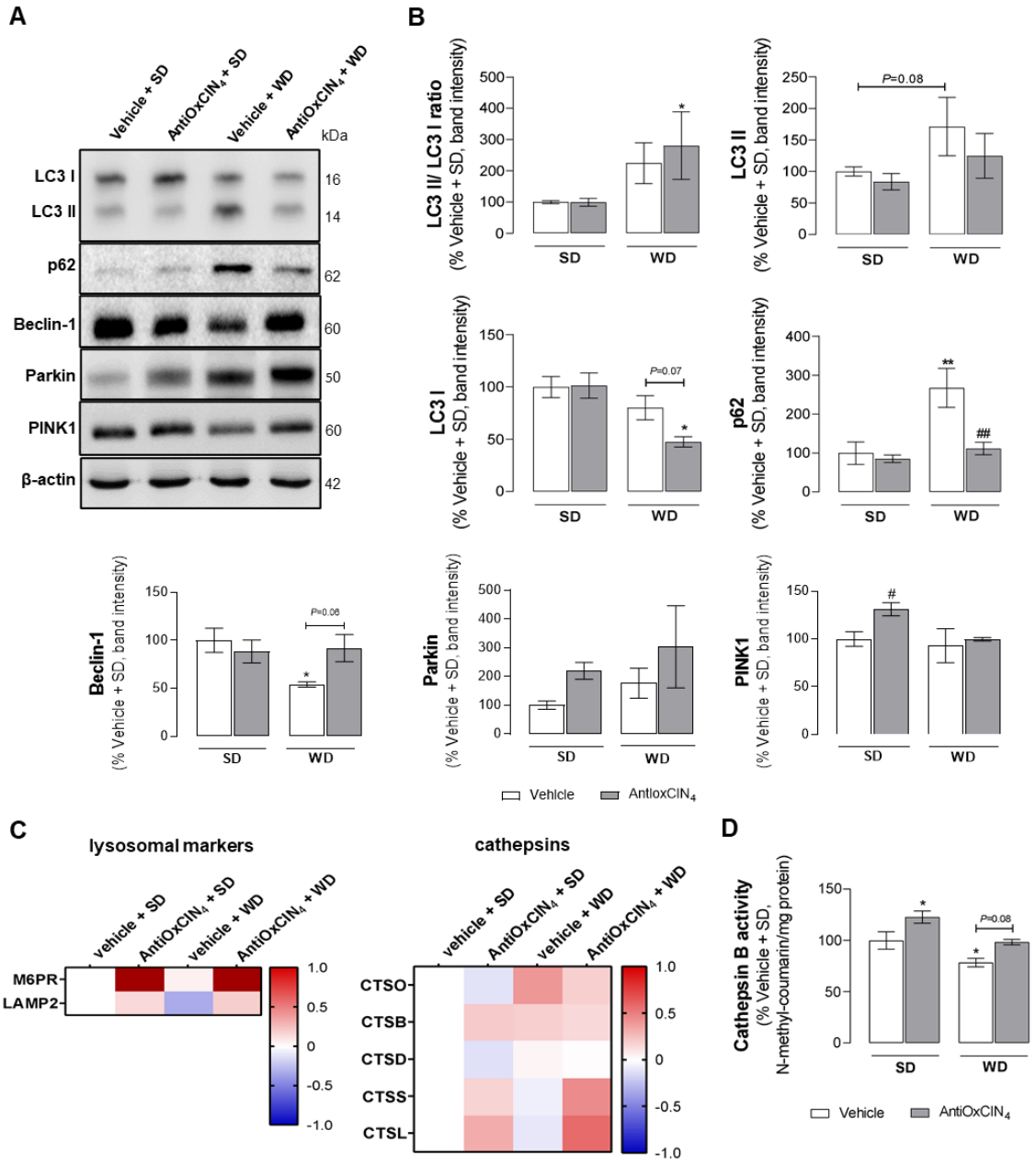

Figure 54. Effects of AntiOxCIN$_4$ on auto(mito)phagy markers in WD-fed mice with NAFL phenotype. (**A**) Typical Western blot result of whole-liver homogenates depicting the protein levels of LC3BI, LC3BII, p62, Beclin-1, Parkin, PINK1 and β-actin (cytosolic marker) in liver homogenates from WD-fed mice in the absence/presence of AntiOxCIN$_4$ (2.5 mg/day/animal). **(B)** Protein expression levels of several autophagic and/or mitophagic markers from WD-fed mice in the absence/presence of AntiOxCIN$_4$ (2.5 mg/day/animal). These blots were inverted and contrast-optimized for visualization purposes. Quantification of the bands was performed using the original blots. Quantification of proteins described above in multiple experiments was normalized to β- actin levels. Data are expressed as mean ± SEM. (**C**) MS-proteomic analysis of hepatic lysosomal-associated markers and cathepsins-related proteins in WD-fed mice in the absence/presence of AntiOxCIN$_4$ (2.5 mg/day/animal). The blue color represents a decrease, while the red

color represents an increase in protein levels. Protein abbreviations are detailed in **Table 8**. (**D**) Cathepsin B activity in the whole liver homogenate from WD-fed mice in the absence/presence of AntiOxCIN$_4$ (2.5 mg/day/animal). Data are expressed as the mean ± SEM and the results were normalized to the control condition (set as = 100%). Statistically significant compared using two-way ANOVA followed by Fisher's LSD test for multiple comparisons (*P<0.05, **P < 0.01 vs Vehicle + SD); ($^{\#}$P < 0.05, $^{\#\#}$P < 0.01 vs Vehicle + WD). **Contribution to this panel**: I was responsible by the conceptualization, experimental work, and data analysis of **Figure 54** (except LC3BI/II WB).

AntiOxCIN$_4$ supplementation in WD-fed mice prevented autophagosome accumulation as measured by the increase in LC3II/LC3I ratio (by 55 %) and the maintenance of p62 (112 %) and Beclin-1 (92 %) protein levels similar to the SD groups (**Figure 54A, B**). Mitophagy constitutes an important cellular process for mitochondrial quality control by eliminating dysfunctional mitochondria, maintaining a mitochondrial homeostasis [672]. WD-fed mice showed a non-statistically significant increase of Parkin (176 %), while no alterations were observed in PINK1 (93 %) protein levels (**Figure 54A, B**). AntiOxCIN$_4$ increased Parkin (219 %) and PINK1 (130 %) protein levels in SD-fed mice, but its supplementation in WD-fed mice only induced an upward trend in PARKIN levels (by 126 %) (**Figure 54A, B**). A decreased autophagic flux was correlated with a reduction of the associated lysosomal membrane protein 2 (LAMP2) protein level (**Figure 54C**) and cathepsin B activity (78%) (**Figure 54D**) in the Vehicle + WD group. AntiOxCIN$_4$ supplementation prevented a WD-induced decrease in LAMP2 and increased the levels of M6PR (**Figure 54C**), a receptor responsible for the binding and transport of acid hydrolases from Golgi apparatus to inside lysosomes. These findings are supported by the higher protein levels of lysosomal hydrolases such as CTSS and CTSL, and higher cathepsin B activity (increased by 20 %) observed in WD + AntiOxCIN$_4$ mice group (**Figure 54C, D**). AntiOxCIN$_4$ also increased cathepsin B activity in the SD-fed group (122 %) (**Figure 54D**). Altogether, these results indicate that AntiOxCIN$_4$ prevents WD-induced autophagy blockage, conceivably by increasing lysosomal proteolytic capacity.

9.3.16. AntiOxCIN$_4$ upregulated gene expression of lysosomal markers in FFAs-treated human HepG2 cells

HepG2 cells exposed to supraphysiological concentrations of FFAs were used to corroborate the *in vivo* observed AntiOxCIN$_4$-induced increased lysosomal capacity. Consequently, mRNA levels of lysosomal markers in FFA-treated cells in the presence or absence of AntiOxCIN$_4$ (48 h, 100 µM) were evaluated. Transcription factor EB (TFEB) is a master transcriptional factor of lysosomal biogenesis, thereby coordinating the gene expression of lysosomal hydrolases, lysosomal membrane proteins, and other proteins involved in autophagy [38]. FFAs-treated cells exhibited increased mRNA levels of *TFEB* gene (172 %) **(Figure 55**). However, no alterations were observed in mRNA levels of lysosomal associated membrane proteins encoding genes such as *LAMP1*, *LAMP2* and *ATP6V1A* (**Figure 55**). FFAs regimen decreased mRNA levels of *ATP6V1H* gene (76 %) (**Figure 55**).

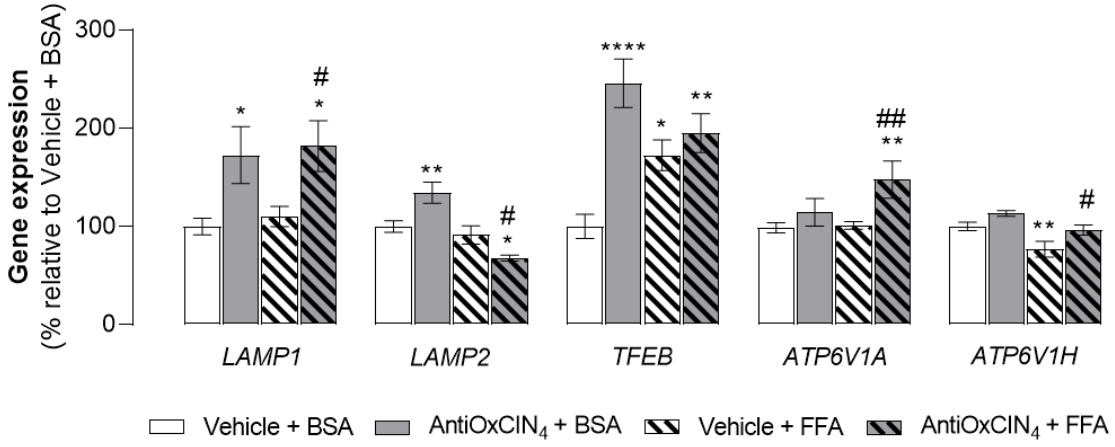

Figure 55. Effects of AntiOxCIN$_4$ on lysosomal markers expression in FFAs-treated human HepG2 cells. mRNA transcript levels of autophagy-related genes (*LAMP1, LAMP2, TFEB, ATP6V1A, ATP6V1H*) in cells treated with vehicle (BSA) or FFA (24h, 250 µM) in the absence/presence of AntiOxCIN$_4$ (48h, 100 µM). Data are expressed as the mean ± SEM and the results were normalized to the control condition (set as 100 %). Statistically significant compared using two-way ANOVA followed by Fisher's LSD test for multiple comparisons (*P<0.05, **P < 0.01, ****P < 0.0001 vs Vehicle + BSA); ($^{\#}$P < 0.05, $^{\#\#}$P < 0.01 vs Vehicle + FFA).

Outstandingly, AntiOxCIN$_4$-treated cells in the presence of FFAs (24 h, 250 µM) showed an increase in mRNA levels of *TFEB* (by 25 %), *LAMP1* (by 72 %), *ATP6V1a* (by 47

%) and *ATP6V1h* (by 20 %), when compared to FFAs - vehicle cells (**Figure 55**). Moreover, pre-incubation with AntiOxCIN$_4$ (48 h, 100 µM) also increased mRNA levels of *TFEB* (245 %), *LAMP1* (172 %) and *LAMP2* (134 %) genes in BSA-treated cells (**Figure 55**). The data reinforced our previous *in vivo* findings supporting the role of AntiOxCIN$_4$ in the prevention of autophagic flux blockage by upregulating lysosomal-related markers and function

9.4. Discussion

NAFLD has become a worldwide public health concern as metabolic syndrome-associated disorders rise. Although the cellular mechanisms behind NAFLD pathogenesis are still controversial, mitochondrial dysfunction plays a determinant role in disease progression. Mitochondria, key organelles involved in energy supply and cellular survival, are particularly affected in NAFL/NAFLD patients [300] and animal models due to FFAs overload and subsequent higher FAO demand [673].

Consequently, development of pharmacologic strategies targeting mitochondria can be seen as potential candidates for the prevention/treatment of NAFLD. Recently, we described that the mitochondria-targeted antioxidant AntiOxCIN$_4$ improved mitochondrial function by upregulating antioxidant defense systems and cellular quality control mechanisms (mitophagy/autophagy) [460, 649]. Activation of endogenous ROS-protective pathways, such as the Nrf2/KEAP1 pathway, by AntiOxCIN$_4$ [649] can explain the preventive effects towards iron and H_2O_2-induced cell damage in human hepatoma-derived HepG2 cells [458] and the cell death induced by H_2O_2 or 6-hydroxydopamine (6-OHDA) in human neuroblastoma (SH-SY5Y) cells [459]. Moreover, AntiOxCIN$_4$ also improved several mitochondrial functional parameters in PHSF and in PHSF from sporadic Parkinson's disease patients [460, 461].

Herein, we hypothesize that daily supplementation with a mitochondria-targeted agent based on natural dietary caffeic acid (AntiOxCIN$_4$) would prevent NAFLD phenotype development in a WD-fed mice. To mimic a WD, C57BL/6 mice were fed a high-fat (30 %) plus high-sucrose (30 %) diet for 16 weeks [487]. WD feeding induced abnormal body weight gain and visceral adiposity, with increased plasmatic AST and ALT levels suggesting hepatocyte damage. Moreover, the absence of evident inflammatory markers and signs of fibrosis confirmed the presence of NAFL, an early NAFLD stage

development. AntiOxCIN$_4$ supplementation prevented body weight gain in WD-fed mice, reducing liver weight and its fat deposition, with improved ALT and AST levels. Similarly, another mitochondrially-targeted antioxidant (MitoQ) improved hepatic-related parameters in a metabolic syndrome mice model, namely reducing fat accumulation and hepatic damage [448].

The reduction of hepatic steatosis is correlated with a lower TG content, being the LD number and size decreased in our in vitro model. The effects of AntiOxCIN$_4$ appear not to be correlated with significant alterations in protein hallmarks of FFAs influx and the DNL pathway. Even so, we have found higher protein levels of elongases ELOVL1 and 5. In fact, higher ELOVL5 activity has been shown to decrease TG levels by increasing TG catabolism and reducing ER stress in obese mice [674]. Notwithstanding, MUFA/PUFA synthesis can also protect hepatocytes from FFAs-induced toxicity [675].

A dysregulation between FA synthesis and FAO has been associated with NAFLD progression. Decreased mitochondrial FAO capacity is described to be at the origin of more advanced steatotic phenotypes [676]. Despite that, our NAFL mice model showed up-regulation of mitochondrial and peroxisomal FAO-related protein levels, which indicated an adaptive response to FAs overload. Nevertheless, we observed that WD feeding caused TG accumulation, which presented higher content in oleate, and reduced amounts of linoleate and ω-3 FAs. Notably, AntiOxCIN$_4$ supplementation prevented the above-described alterations, mainly regarding ω-3 FAs. Studies exploring ω-3 PUFA supplementation showed beneficial effects on decreasing blood TG levels [677], and activation of PPARs, which in turn increases hepatic FAO [678], and autophagic degradation [679].

In AntiOxCIN$_4$-treated human HepG2 cells, up-regulation of *PPARA* gene expression was paralleled by downstream FAO-related genes (*CPT1A*, *ACOX1* and *ESCH1*), and O_2 consumption increased upon FA acute exposure. These effects culminate in a reduction of TG accumulation and LD number. Increased mitochondrial and peroxisomal FAO-related protein levels were also observed in AntiOxCIN$_4$-supplemented SD-fed mice supporting the hypothesis that AntiOxCIN$_4$ can restrain lipotoxicity by boosting FAO. Since elevated microvesicular steatosis is correlated with more severe NAFLD histology and

bad prognosis of the disease [680], an augmented FAO favors the clearance of lipid accumulation, thereby preventing lipotoxicity-associated injury.

NAFLD pathophysiology is associated with altered lipid homeostasis that together with other unbalanced processes such as increased OxS or autophagic blockage may lead to a progression towards a more severe phenotype. Besides mitochondria, peroxisomes are also an important site for the generation of ROS through β-oxidation and the activities of numerous oxidases generating H_2O_2 [238]. In fact, increased mtROS levels or mitochondrial-associated OxS were not observed in WD-fed mice. Recent studies supported our data as they have suggested that peroxisomal H_2O_2 rather than mitochondrial H_2O_2 contributed for ROS production in the early stages of NAFLD [681, 682]. Insights in human hepatoma-derived HepG2 cells detailed the overall ROS origin within the cell. In fact, supraphysiological concentrations of FFAs increased total cellular (mainly peroxisomal) ROS in human HepG2 cells. Nevertheless, AntiOxCIN$_4$ pre-treatment significantly attenuated cellular increased ROS production.

Interestingly, in the absence of abnormal mitochondrial H_2O_2, WD feeding induced mitochondrial remodeling with augmented respiration and had a strong impact on mitochondrial membrane composition with a decreased RCR and a higher sensitivity of mPTP to open. AntiOxCIN$_4$ supplementation plays a role in mitochondrial homeostasis by up-regulating OXPHOS complexes subunits (mainly at complex I) gene/protein expression levels, thereby preventing WD-induced abnormalities in PC/PE ratio and RCR, and slightly protecting mitochondria from mPTP opening episodes by Ca^{2+}/tBHP. Our data indicate that PGC-1α-SIRT3 axis interplay regulates these processes. Sirtuins are energetic sensors that play an essential role in pathophysiological conditions. SIRT3 showed to control global mitochondrial protein acetylation level, mitochondrial redox status, epigenetic regulation, and lipid homeostasis in the liver [683]. Li *et al* showed that SIRT3 overexpression prevents HFD-induced NAFLD by blocking hepatocyte mitochondrial apoptosis and promoting Bnip3-mediated mitophagy [667]. In agreement, HFD-fed Sirt3$^{-/-}$ mice presented marked hyperacetylation of gluconeogenic and mitochondrial-related proteins which exacerbates fatty liver [242, 684]. Moreover, PGC-1α, the main regulator of mitochondrial biogenesis, stimulates SIRT3 expression in a

regulatory pathway that drives mtROS generation and mitochondrial biogenesis [685]. The effect on the PGC-1α-SIRT3 axis increased the antioxidant power of AntiOxCIN$_4$-treated animals and/or cells. In fact, both in vivo and in vitro corroborated this observation as AntiOxCIN$_4$ stimulated the endogenous antioxidant defense system, particularly GSH, mitochondrial SOD, and peroxisomal catalase. Upregulation of the endogenous antioxidant defense system by AntiOxCIN$_4$ treatment can attenuate the overall OxS.

Studies in NAFLD animal models and patients using liver mitochondria showed increased TCA cycle function [218, 240] but impaired respiratory coupling [241, 242]. By using our *in vitro* model [525], we observed that FFAs-treated human HepG2 cells also showed increased TCA coupling. As mitochondrial TCA cycle intermediates are not stored, the pathways of anaplerosis and cataplerosis operate continuously at the same rate. Interestingly, AntiOxCIN$_4$-treated human HepG2 cells increased anaplerotic fluxes and β-oxidation processes, which corroborate the observation that β-oxidation and the generation of acetyl-CoA increase anaplerotic capacity [686]. Anaplerosis is also indispensable for urea cycle function and antioxidant defenses, by maintaining NADPH pool [49]. In our *in vivo* model, WD-fed mice showed decrease in some gluconeogenic-related proteins (G6PC; PGK2), an effect that was prevented by AntiOxCIN$_4$ supplementation. Moreover, AntiOxCIN$_4$ supplementation also increased PCX and mitochondrial isoform of PCK2 protein levels in WD-fed mice. PCX is essential not only to fuel TCA cycle but also to provide substrates for non-enzymatic antioxidant defense system build-up, such as NADPH pool [687]. Insights in HepG2 cells showed that AntiOxCIN$_4$ decrease TCA cycle turnover in human hepatoma-derived cells, which could limit citrate cataplerosis used in lipogenesis, possibly explaining the decrease in TG content in the whole liver form WD-fed mice supplemented with AntiOxCIN$_4$. *In vivo* and *in vitro* observations strongly support that mitochondria-targeted dietary polyphenolic antioxidant AntiOxCIN$_4$ improved mitochondrial function by up-regulating antioxidant defense systems and cellular quality control mechanisms (mitophagy/autophagy) [460]. AntiOxCIN$_4$ supplementation on WD-fed mice ameliorate mitochondrial functional parameters, even in the absence of marked OxS-associated damage. Moreover, AntiOxCIN$_4$ induces mitochondrial biogenesis and upregulates the endogenous antioxidant defense system, which

strengthen hepatic mitochondria make them less prone to further oxidative damage in the later NAFLD stages.

Diet-induced obesity/NAFLD is associated with AKT/mTORC signaling activation. Therefore, activation of mTORC1 produces phosphorylation of S6K1, resulting in cellular translation and cell growth mediated by 4E-BP1 [688]. In our *in vivo* model we observed that WD feeding upregulated the AKT/mTOR/S6K1/4E-BP1 pathway. Moreover, mTORC activation can block autophagic flux. In fact, it has been reported a decline of autophagic response in NAFLD patients [285, 289] and in NAFL mice model induced by WD [487]. Herein, we confirmed our previous observation of impaired autophagic flux and a possible WD-induced blocked autophagy, reflected by increased p62 levels and LC3-II/LC3-I ratio and decreased Beclin-1 levels. Remarkably, AntiOxCIN$_4$ supplementation in WD-fed mice prevented p62 accumulation and maintained Beclin-1 levels comparable to SD-fed mice. Although autophagy can contribute to hepatocyte adaptation due to the specific degradation of LD in NAFL, increased p62 levels have been linked to NASH progression [689]. AntiOxCIN$_4$ maintains or increases normal autophagic flux, which can counteract the accumulation of damaged mitochondria or other subcellular structures and protect hepatocytes from lipotoxicity insults in NAFLD-associated conditions.

In vivo and *in vivo* observations showed that AntiOxCIN$_4$ treatment augmented expression and protein levels of lysosomal markers, namely proteins responsible for the acidification of lysosomes/autophagolysosomes and cathepsins. We propose that AntiOxCIN$_4$ overcomes autophagic blockage that can result from defective lysosomal acidification [288], by improving the lysosomal number and proteolytic activity. In fact, AntiOxCIN$_4$ pre-treatment increased lysosomal content in both fibroblasts from Parkinson disease patients [461] and human hepatoma-derived HepG2 cells [649]. Mitophagy has also been implicated in NAFLD progression [690]. Although no single parameter is sufficient to demonstrate mitophagy unequivocally, we observed up-regulation of the PINK1-Parkin protein levels axis in SD-fed mice supplemented with AntiOxCIN$_4$. In accordance, our previous work showed that AntiOxCIN$_4$-treated HepG2 cells increased lysosomes co-localized with the mitochondria [649]. These results suggest that

AntiOxCIN$_4$ could also remove functionally damaged mitochondria, maintaining mitochondrial homeostasis by improving proteolytic activity.

9.5. Conclusions

In summary, our pioneering study has shown for the first time the beneficial role of AntiOxCIN$_4$ supplementation *in vivo* in the early NAFL stage (**Figure 56**). Using a WD-fed mice model, and mechanistically complementing and translating the data with human hepatic HepG2 cells, we pointed out the potential mechanism of action for the improvement of steatotic liver phenotype. In addition to a decrease in body weight gain, AntiOxCIN$_4$ decreased hepatic steatosis by decreasing LD number/size and its composition. Importantly, these effects were correlated with increased cellular FAO activity. The mitochondriotropic antioxidant AntiOxCIN$_4$ upregulates the endogenous antioxidant defense system in hepatocytes exposed to FA insults in WD-fed mice and causes mitochondrial remodeling of OXPHOS and phospholipid membrane composition. Finally, AntiOxCIN$_4$ supplementation prevented the blockage of proper recycling/elimination of damaged protein/organelles by increasing proteolytic activity.

The amelioration of whole-body mouse parameters and especially, a healthier phenotype of hepatocytes support the use of AntiOxCIN$_4$ as a great potential candidate for the prevention/treatment of NAFLD (**Figure 56**).

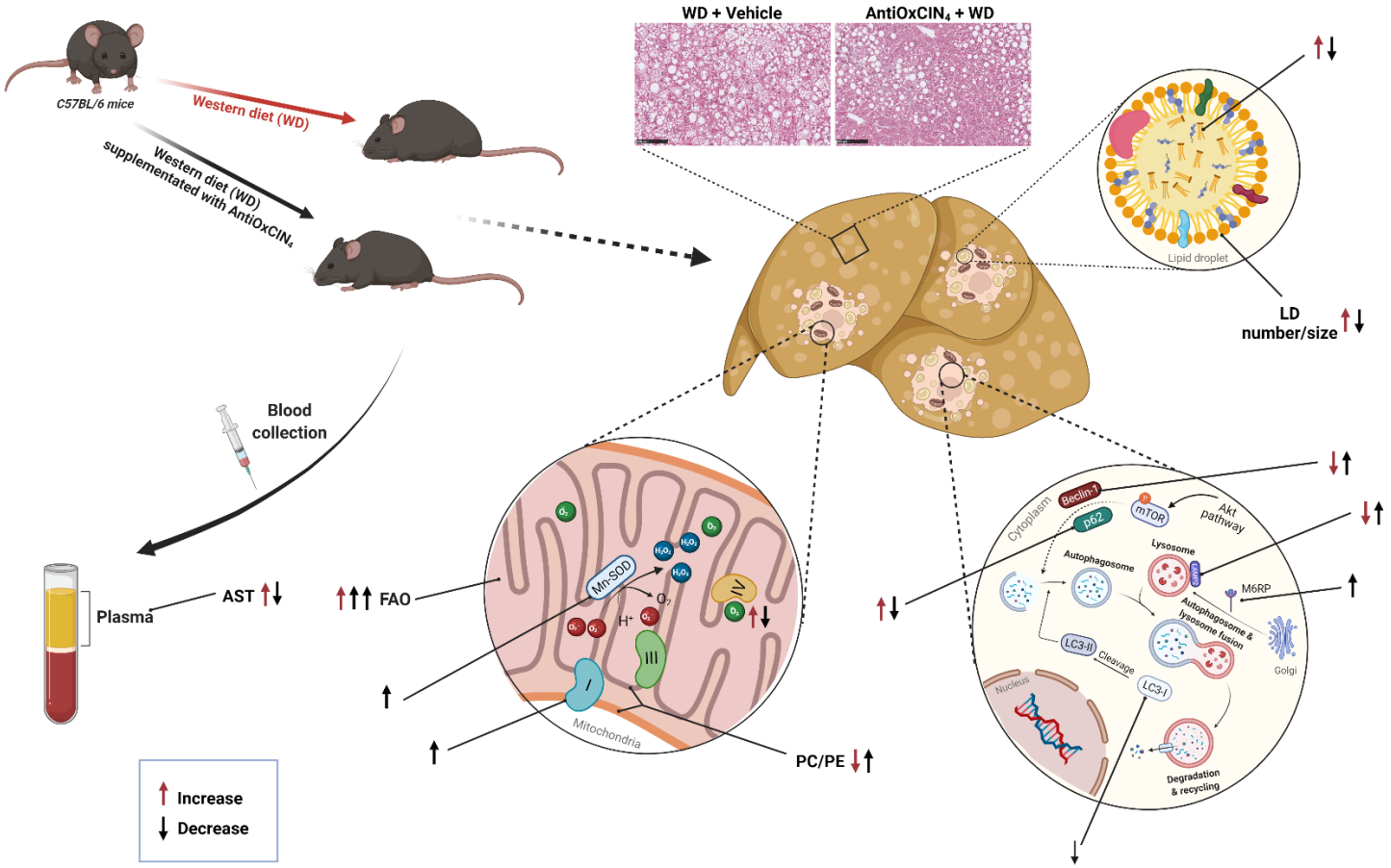

Figure 56. Schematic diagram summarizing the effects of mitochondriotropic antioxidant AntiOxCIN$_4$ supplementation in a WD-fed mice with NAFL phenotype. AntiOxCIN$_4$ supplementation reduced body weight gain of mice fed with a Western diet (WD) for 16 weeks. AntiOxCIN$_4$ also decreased liver weight with amelioration of hepatic damage markers (aspartate aminotransferase (AST)) and decreased steatosis with a reduction in the number/size of lipid droplets. These effects were shown to be partly attributed to increased fatty acid oxidation (FAO). AntiOxCIN$_4$ supplementation promoted a mitochondrial remodeling, which resulted in increased protein levels of Complex I subunits, prevention of WD modification on phosphatidylcholine/phosphatidylethanolamine (PC/PE) levels. Additionally, an induction of endogenous antioxidant defense system was

also observed, with higher activity of mitochondrial superoxide dismutase (SOD). Furthermore, AntiOxCIN$_4$ prevented WD-induced impairment of autophagy quality control mechanism as shown by the avoidance of p62 accumulation and the maintenance of Beclin-1 and LC3-II protein levels. Moreover, AntiOxCIN$_4$ additionally increased lysosomal proteolytic activity as shown by higher lysosome-associated membrane glycoprotein 2 (LAMP2) and mannose-6-phosphate receptor (M6PR) levels. The amelioration of whole-body mouse parameters and especially, a healthier phenotype of hepatocytes support the use of AntiOxCIN$_4$ as a great potential agent for the prevention/treatment of NAFLD (**details in Discussion**).

PART IV

Final Conclusion and Future Perspectives

10. Chapter
Final conclusion

NAFLD is a worldwide public health concern as it affects approximately one-quarter of the global adult population, causing a significant morbidity burden with widespread social and economic implications. NAFLD is a multifactorial disease and is considered the hepatic component of metabolic syndrome. Although the cellular mechanisms behind NAFLD pathogenesis are still under focus of debate, mitochondrial dysfunction plays a determinant role in disease progression as demonstrated in several *in vivo* models as well as in NAFLD/NASH patients. In this context, and in the absence of drugs directly targeting NAFLD, development of pharmacologic strategies targeting mitochondria can be seen as potential candidates for the prevention/treatment of NAFLD.

Previously studies showed that the mitochondriotropic antioxidant AntiOxCIN$_4$ (100 μM; 48 h) presented significant cytoprotective effect against OxS insults without affecting the viability of human hepatoma-derived (HepG2) cells [458]. Based on this observation, the main goal of this dissertation was to study the beneficial effects of the hydroxycinnamic-derived mitochondriotropic antioxidant AntiOxCIN$_4$ in *in vitro* and *in vivo* models NAFLD models, while obtaining mechanistic insights behind AntiOxCIN$_4$ effects.

First, we unraveled the Nrf2-dependent antioxidant mechanism behind the beneficial effects of mitochondriotropic antioxidant AntiOxCIN$_4$ in human HepG2 cells. AntiOxCIN$_4$ induced a Nrf2-dependent cellular adaptative response mediated by a sustainable increase in mtROS, which resulted in the stimulation of critical antioxidant systems, such as SOD and GR activities and higher GSH content. AntiOxCIN$_4$ increased mitochondria biogenesis, suggested by increased PGC-1α protein levels and mtDNA copy number. Additionally, AntiOxCIN$_4$ induced a ROS-dependent Nrf2 activation mediated by Nrf2-KEAP1-p62 axis and triggered an efficient removal of potentially damaged mitochondria by cellular quality control mechanisms, such as autophagy and/or mitophagy. The work carried out in **chapter 7** showed also that AntiOxCIN$_4$ protected HepG2 cells against

lipotoxic insults such as palmitic acid (PA), opening a new possibility to extend its potential application in the context of a NAFLD/NASH.

In order to validate an *in vitro* NAFLD model that better mimic a NAFL stage and which could be used as a screening tool for novel therapies, we investigate time-dependent cellular and mitochondrial effects of different supra-physiological fatty acids treatment protocols, in the presence or absence of fructose, on human hepatoma-derived HepG2 cells (**chapter 8**). Herein, we provided evidence that fatty acids induced a time-dependent increase in the intracellular neutral lipids, which was paralleled by an increase in OxS and altered mitochondrial phospholipid profile. Furthermore, mitochondrial dysfunction comprises not only alterations in ΔΨm and morphology but also a decrease in oxygen consumption rate and oxidative phosphorylation protein content. Alterations in mitochondria were observed early after treatment and these changes precede cell death in human HepG2 cells. Interestingly, we observed no lipogenic effect of fructose overload in this cell model, which was explained by lower levels of hepatic fructokinase (KHK) in human HepG2 cells. The FFA steatotic protocol (250 μM. 24h) was established as more reliable NAFL model when compared with PA, since this model had a huge increase in intracellular lipid accumulation without stimulated cell death pathways, such as apoptosis. As observed in PA treatment (**chapter 7**), AntiOxCIN$_4$ provided the best protection against lipid accumulation.

Finally, we validated for the first-time the beneficial effects of hydroxycinnamic-derived mitochondriotropic antioxidant supplementation in a mouse NAFL model (**chapter 9**). By using a WD-fed mice model, while investigating mechanism of action by using human hepatic HepG2 cells, we dissected the potential mechanism of action for the improvement of steatotic liver phenotype. AntiOxCIN$_4$ supplementation improved NAFL-related physiological parameters, such as body and liver weight gain, lowering LD number/size and modulating their composition. Importantly, these effects were correlated with increased cellular FAO activity. The mitochondriotropic antioxidant AntiOxCIN$_4$ upregulated the endogenous antioxidant defense system in hepatocytes exposed to FA insults in WD-fed mice and causes mitochondrial remodeling of OXPHOS and phospholipid membrane composition. Finally, AntiOxCIN$_4$ supplementation prevented the blockage

of proper recycling/elimination of damaged protein/organelles by increasing proteolytic activity.

The results obtained in this thesis added knowledge to the dual role of mitochondria in NAFLD development. Mitochondria early adaptations were observed in the NAFL mouse model, including O_2 consumption and higher levels of β-oxidation-associated proteins. Notwithstanding, the decreased RCR and the altered mitochondrial phospholipid composition anticipate a deleterious contribution of mitochondrial impairment to NAFLD progression. More important, this thesis described for the first-time AnitOxCIN$_4$ mechanisms of action, namely mediated by Nfr2 activation, mitochondrial remodeling, and induction of the cell repair mechanisms in NAFL and non-NAFL conditions, stimulating the use of this approach in several contexts, from other liver diseases to neurodegenerative conditions.

Food insecurity defined as 'limited or uncertain availability of nutritionally adequate and safe foods or limited or uncertain ability to acquire acceptable foods in socially acceptable ways' has been associated with an amplified risk of NAFLD among adults in low-income households [691]. Alongside with the estimation that NAFLD will be the most frequent indication for liver transplantation by 2030, projection models based on health insurance beneficiaries estimate a rise in annual US economic burden to 103 billion dollars from direct medical care costs alone and another 188 billion dollars in societal costs related to NAFLD [692].

The ground-breaking nature of the AntiOxCIN$_4$ approach was the improvement of mitochondrial oxidative damage and bioenergetic capacity through the specific modulation of mtROS production in a validated and comprehensive preclinical liver model, attenuating the signaling pathways responsible to disease progression. This validation is one step forward towards overcoming the absence of FDA-approved effective therapies for NAFLD, contributing decisively to minimizing the worldwide NAFLD-associated ill health and social burden, decreasing the amount of time of work absence and increasing healthy lifespan. In fact, this can be translated in improved quality of life, social interactions as well as reduced NAFLD-associated healthcare costs.

Importantly, associations between cardiometabolic risk factors and NAFLD are well reported. The use of AntiOxCIN$_4$ strategy may reduce the morbidity and mortality associated with CVD, the main cause of global death.

Alongside with the important social impact, the economic revenues of the results obtained in this document are real as they can be used to stimulate AntiOxCIN$_4$ translation to clinical trials and, later, to a pharmaceutical market. It estimated that by 2025, the drug market for NAFLD will be worth 20 billion to 35 billion dollars per year [693]. AntiOxCIN$_4$ is already protected by intellectual property (N. º: PCT/IB2017/056412/WO/2018/069904), which allow a quick path from bench to market and attract future investors, speeding up the drug development process. Commercial exploitation has been licensed already to a CNC and University of Porto spin-off, Mito-TAG.

Although the several positive effects observed through this dissertation regarding the use of AntiOxCIN$_4$ in NAFLD context, this work presented some limitations. The low sample size, the lack of genetic and gender heterogeneity in the *in vivo* study warrant future more robust *in vivo* studies.

11. Chapter
Future perspectives

Although this dissertation has clarified some questions regarding AntiOxCIN$_4$-induced lipid lowering ability and has provided new clues with respect to its mechanism of action, it has also opened several doors to be further explored. For example, and not in any particular order:

We demonstrated that AntiOxCIN$_4$ induced an Nrf2-dependent cellular adaptative response (**chapter 7**). Nevertheless, it would be important to understand the Nfr2-dependence of AntiOxCIN$_4$ protective mechanisms in a more complex system using, for instance, a Nrf2 $^{-/-}$ mutant mice.

In the search for a more relevant *in vitro* NAFL model, we provided news insights how mitochondria chronologically behave in different models of fatty acid overload (**chapter 8**). In fact, we implement a feasible *in vitro* model in which mitochondria dysfunction is latent and that can be used in pharmacological screening approaches. Additionally, we separated the different treatments by using a computational analysis considering just the information provided by a limited subset of experimental endpoints. However, a larger sample size should be considered to create a more robust method to predict cell death in NAFLD models on human hepatocytes. It would be also relevant to check if this computational approach can also be translated to human samples, more specially by evaluating OxS markers in plasma. In fact, the revolutionary nature of this approach is that the bioinformatic tools will help to elucidated proteins and metabolites related to mitochondrial and peroxisomal oxidative stress relevant for disease progression that could refine disease characterization, uncover pathways to monitor therapeutic efficacy, and/or delineate disease-modifying targets.

AntiOxCIN$_4$ supplementation prevented WD-induced autophagic blockage in our study. However, the role of AntiOxCIN$_4$ on lipophagy was not studied, which could give important insights on how of AntiOxCIN$_4$ in prevented lipid accumulation. Moreover, a

more detail study how autophagy, more specially mitophagy, is achieved upon AntiOxCIN$_4$ treatment is required. Understanding the involvement of AntiOxCIN$_4$ in the mTOR-ULK1 pathway should also be taken in consideration.

AntiOxCIN$_4$ has been showed remarkably antioxidant properties in studies published so far [458, 459, 461]. Importantly, AntiOxCIN$_4$ also demonstrated to have an important capacity in iron chelation [458], which could be also an interestingly approach since ferroptosis is observed in later stages of NAFLD.

Proteomic analysis provided other indications that were not discussed in this thesis. For instance, AntiOxCIN$_4$ showed to prevent a WD-induced decrease in liver glycogen phosphorylase (PYGL) (data not shown). In fact, PYGL deficiency leads to profibrogenic phenotype in a mice model [694], opening other potential target of AntiOxCIN$_4$ treatment.

Although we confirmed the beneficial effects of AntiOxCIN$_4$ in NAFL prevention in **chapter 9**, an increase the animal sample size would be advisable, as well as the study the effects of AntiOxCIN$_4$ supplementation in later stages of NAFLD, such as NASH.

Although TPP$^+$-attached molecules showed good accumulation in several organs, AntiOxCIN$_4$ accumulation in the liver was not accessed [695]. Further studies using liquid chromatography–tandem mass spectrometry (LC/MS/MS) to quantify AntiOxCIN$_4$ in liver and other tissues should be addressed. Moreover, the next steps will also include obtaining pharmacokinetic and pharmacodynamic data for AntiOxCIN$_4$, as well as investigating the potential interactions of the compound with gut microbiota.

Although not the goal of our work, several considerations about OxS in NAFLD progression were raised. For instance, our mice model did not present mitochondrial OxS or major alterations in antioxidant enzymes, which is in accordance with the absence of OxS in mitochondrial adaptation in simples steatosis [696]. Interestingly, recent findings showed that mitochondrial H_2O_2 decreased from 16 to 24 weeks of WD feeding [681]. Following these observations, it would be relevant to check time-dependent peroxisomal H_2O_2 generation in the same mice model and how it contributes to the simple steatosis transition to NASH.

PART V

Bibliography

12. Chapter
Bibliographic references

[1] Lonardo A, Leoni S, Alswat KA, et al. History of Nonalcoholic Fatty Liver Disease. *Int J Mol Sci*; 2020;21(16):5888.

[2] LEEVY CM. Fatty liver: a study of 270 patients with biopsy proven fatty liver and review of the literature. *Medicine (Baltimore)* 1962; 41: 249–276.

[3] THALER H. [The fatty liver and its pathogenetic relation to liver cirrhosis]. *Virchows Arch Pathol Anat Physiol Klin Med* 1962; 335: 180–210.

[4] Adler M, Schaffner F. Fatty liver hepatitis and cirrhosis in obese patients. *Am J Med* 1979; 67: 811–816.

[5] Ludwig J, Viggiano TR, McGill DB, et al. Nonalcoholic steatohepatitis: Mayo Clinic experiences with a hitherto unnamed disease. *Mayo Clin Proc* 1980; 55: 434–438.

[6] Schaffner F, Thaler H. Nonalcoholic fatty liver disease. *Prog Liver Dis* 1986; 8: 283–298.

[7] Lee RG. Nonalcoholic steatohepatitis: a study of 49 patients. *Hum Pathol* 1989; 20: 594–598.

[8] Brunt EM, Janney CG, Di Bisceglie AM, et al. Nonalcoholic steatohepatitis: a proposal for grading and staging the histological lesions. *Am J Gastroenterol* 1999; 94: 2467–2474.

[9] Cortez-Pinto H, Camilo ME, Baptista A, et al. Non-alcoholic fatty liver: another feature of the metabolic syndrome? *Clin Nutr* 1999; 18: 353–358.

[10] Marceau P, Biron S, Hould FS, et al. Liver pathology and the metabolic syndrome X in severe obesity. *J Clin Endocrinol Metab* 1999; 84: 1513–1517.

[11] Knobler H, Schattner A, Zhornicki T, et al. Fatty liver--an additional and treatable feature of the insulin resistance syndrome. *QJM* 1999; 92: 73–79.

[12] Romeo S, Kozlitina J, Xing C, et al. Genetic variation in PNPLA3 confers susceptibility to nonalcoholic fatty liver disease. *Nat Genet* 2008; 40: 1461–1465.

[13] Eslam M, Newsome PN, Sarin SK, et al. A new definition for metabolic dysfunction-associated fatty liver disease: An international expert consensus statement. *J Hepatol* 2020; 73: 202–209.

[14] Adams LA, Lymp JF, St Sauver J, et al. The natural history of nonalcoholic fatty liver disease: a population-based cohort study. *Gastroenterology* 2005; 129: 113–121.

[15] White DL, Kanwal F, El-Serag HB. Association between nonalcoholic fatty liver disease and risk for hepatocellular cancer, based on systematic review. *Clin Gastroenterol Hepatol Off Clin Pract J Am Gastroenterol Assoc* 2012; 10: 1342-1359.e2.

[16] Singh S, Allen AM, Wang Z, et al. Fibrosis progression in nonalcoholic fatty liver vs nonalcoholic steatohepatitis: a systematic review and meta-analysis of paired-biopsy studies. *Clin Gastroenterol Hepatol Off Clin Pract J Am Gastroenterol Assoc* 2015; 13: 640–643.

[17] Younossi ZM, Koenig AB, Abdelatif D, et al. Global epidemiology of nonalcoholic fatty liver disease-Meta-analytic assessment of prevalence, incidence, and outcomes. *Hepatology* 2016; 64: 73–84.

[18] Li J, Zou B, Yeo YH, et al. Prevalence, incidence, and outcome of non-alcoholic fatty liver disease in Asia, 1999-2019: a systematic review and meta-analysis. *lancet Gastroenterol Hepatol* 2019; 4: 389–398.

[19] Younossi ZM. Non-alcoholic fatty liver disease – A global public health perspective. *J Hepatol* 2019; 70: 531–544.

[20] Zois C-D, Baltayiannis G-H, Bekiari A, et al. Steatosis and steatohepatitis in postmortem material from Northwestern Greece. *World J Gastroenterol* 2010; 16: 3944–3949.

[21] Leitão J, Carvalhana S, Cochicho J, et al. Prevalence and risk factors of fatty liver

in Portuguese adults. *Eur J Clin Invest* 2020; 50: e13235.

[22] Ye Q, Zou B, Yeo YH, et al. Global prevalence, incidence, and outcomes of non-obese or lean non-alcoholic fatty liver disease: a systematic review and meta-analysis. *lancet Gastroenterol Hepatol* 2020; 5: 739–752.

[23] Sayiner M, Koenig A, Henry L, et al. Epidemiology of Nonalcoholic Fatty Liver Disease and Nonalcoholic Steatohepatitis in the United States and the Rest of the World. *Clin Liver Dis* 2016; 20: 205–214.

[24] Paik JM, Golabi P, Younossi Y, et al. The Growing Burden of Disability Related to Nonalcoholic Fatty Liver Disease: Data From the Global Burden of Disease 2007-2017. *Hepatol Commun* 2020; 4: 1769–1780.

[25] Estes C, Anstee QM, Arias-Loste MT, et al. Modeling NAFLD disease burden in China, France, Germany, Italy, Japan, Spain, United Kingdom, and United States for the period 2016-2030. *J Hepatol* 2018; 69: 896–904.

[26] Cholankeril G, Patel R, Khurana S, et al. Hepatocellular carcinoma in non-alcoholic steatohepatitis: Current knowledge and implications for management. *World J Hepatol* 2017; 9: 533–543.

[27] Flemming JA, Djerboua M, Groome PA, et al. NAFLD and alcohol-related liver disease will be responsible for almost all new diagnoses of cirrhosis in Canada by 2040. *Hepatology*. 2021 Dec;74(6):3330-3344.

[28] Simon TG, Roelstraete B, Hartjes K, et al. Non-alcoholic fatty liver disease in children and young adults is associated with increased long-term mortality. *J Hepatol*. 021 Nov;75(5):1034-1041.

[29] Younossi Z, Tacke F, Arrese M, et al. Global Perspectives on Nonalcoholic Fatty Liver Disease and Nonalcoholic Steatohepatitis. *Hepatology* 2019; 69: 2672–2682.

[30] Camhi SM, Bray GA, Bouchard C, et al. The relationship of waist circumference and BMI to visceral, subcutaneous, and total body fat: sex and race differences.

Obesity (Silver Spring) 2011; 19: 402–408.

[31] Zhao Y-C, Zhao G-J, Chen Z, et al. Nonalcoholic Fatty Liver Disease: An Emerging Driver of Hypertension. *Hypertens (Dallas, Tex 1979)* 2020; 75: 275–284.

[32] Lorbeer R, Bayerl C, Auweter S, et al. Association between MRI-derived hepatic fat fraction and blood pressure in participants without history of cardiovascular disease. *J Hypertens* 2017; 35: 737–744.

[33] López-Suárez A, Guerrero JMR, Elvira-González J, et al. Nonalcoholic fatty liver disease is associated with blood pressure in hypertensive and nonhypertensive individuals from the general population with normal levels of alanine aminotransferase. *Eur J Gastroenterol Hepatol* 2011; 23: 1011–1017.

[34] Zhou D, Xi B, Zhao M, et al. Uncontrolled hypertension increases risk of all-cause and cardiovascular disease mortality in US adults : the NHANES III Linked Mortality Study. 2018; 1–7.

[35] Cui J, Chen C-H, Lo M-T, et al. Shared genetic effects between hepatic steatosis and fibrosis: A prospective twin study. *Hepatology* 2016; 64: 1547–1558.

[36] Kozlitina J, Smagris E, Stender S, et al. Exome-wide association study identifies a TM6SF2 variant that confers susceptibility to nonalcoholic fatty liver disease. *Nat Genet* 2014; 46: 352–356.

[37] Jonas W, Schürmann A. Genetic and epigenetic factors determining NAFLD risk. *Mol Metab* 2021; 50: 101111.

[38] Pirazzi C, Valenti L, Motta BM, et al. PNPLA3 has retinyl-palmitate lipase activity in human hepatic stellate cells. *Hum Mol Genet* 2014; 23: 4077–4085.

[39] Sookoian S, Pirola CJ. Meta-analysis of the influence of I148M variant of patatin-like phospholipase domain containing 3 gene (PNPLA3) on the susceptibility and histological severity of nonalcoholic fatty liver disease. *Hepatology* 2011; 53: 1883–1894.

[40] Zain SM, Mohamed Z, Mohamed R. Common variant in the glucokinase regulatory

gene rs780094 and risk of nonalcoholic fatty liver disease: a meta-analysis. *J Gastroenterol Hepatol* 2015; 30: 21–27.

[41] Beer NL, Tribble ND, McCulloch LJ, et al. The P446L variant in GCKR associated with fasting plasma glucose and triglyceride levels exerts its effect through increased glucokinase activity in liver. *Hum Mol Genet* 2009; 18: 4081–4088.

[42] Sparsø T, Andersen G, Nielsen T, et al. The GCKR rs780094 polymorphism is associated with elevated fasting serum triacylglycerol, reduced fasting and OGTT-related insulinaemia, and reduced risk of type 2 diabetes. *Diabetologia* 2008; 51: 70–75.

[43] Liu Y-L, Reeves HL, Burt AD, et al. TM6SF2 rs58542926 influences hepatic fibrosis progression in patients with non-alcoholic fatty liver disease. *Nat Commun* 2014; 5: 4309.

[44] Mahdessian H, Taxiarchis A, Popov S, et al. TM6SF2 is a regulator of liver fat metabolism influencing triglyceride secretion and hepatic lipid droplet content. *Proc Natl Acad Sci U S A* 2014; 111: 8913–8918.

[45] Luukkonen PK, Zhou Y, Nidhina Haridas PA, et al. Impaired hepatic lipid synthesis from polyunsaturated fatty acids in TM6SF2 E167K variant carriers with NAFLD. *J Hepatol* 2017; 67: 128–136.

[46] Pirola CJ, Garaycoechea M, Flichman D, et al. Splice variant rs72613567 prevents worst histologic outcomes in patients with nonalcoholic fatty liver disease. *J Lipid Res* 2019; 60: 176–185.

[47] Luukkonen PK, Tukiainen T, Juuti A, et al. Hydroxysteroid 17-β dehydrogenase 13 variant increases phospholipids and protects against fibrosis in nonalcoholic fatty liver disease. *JCI insight*; 5. Epub ahead of print March 2020. DOI: 10.1172/jci.insight.132158.

[48] Helsley RN, Varadharajan V, Brown AL, et al. Obesity-linked suppression of membrane-bound O-acyltransferase 7 (MBOAT7) drives non-alcoholic fatty liver

disease. *Elife*; 2019 Oct 17;8:e49882.

[49] Mancina RM, Dongiovanni P, Petta S, et al. The MBOAT7-TMC4 Variant rs641738 Increases Risk of Nonalcoholic Fatty Liver Disease in Individuals of European Descent. *Gastroenterology* 2016; 150: 1219-1230.e6.

[50] Berger D, Desai V, Janardhan S. Con: Liver Biopsy Remains the Gold Standard to Evaluate Fibrosis in Patients With Nonalcoholic Fatty Liver Disease. *Clin liver Dis* 2019; 13: 114–116.

[51] Alkhouri N, McCullough AJ. Noninvasive Diagnosis of NASH and Liver Fibrosis Within the Spectrum of NAFLD. *Gastroenterol Hepatol (N Y)* 2012; 8: 661–668.

[52] Noureddin M, Loomba R. Nonalcoholic fatty liver disease: Indications for liver biopsy and noninvasive biomarkers. *Clin liver Dis* 2012; 1: 104—107.

[53] Neuman MG, Malnick S, Maor Y, et al. Alcoholic liver disease: Clinical and translational research. *Exp Mol Pathol* 2015; 99: 596—610.

[54] Rinella ME. Nonalcoholic fatty liver disease: a systematic review. *JAMA* 2015; 313: 2263–2273.

[55] Hagström H, Nasr P, Bottai M, et al. Elevated serum ferritin is associated with increased mortality in non-alcoholic fatty liver disease after 16 years of follow-up. *Liver Int Off J Int Assoc Study Liver* 2016; 36: 1688–1695.

[56] Zhang H, Niu Y, Gu H, et al. Low serum adiponectin is a predictor of progressing to nonalcoholic fatty liver disease. 2019; 1–6.

[57] Feldstein AE, Wieckowska A, Lopez AR, et al. Cytokeratin-18 fragment levels as noninvasive biomarkers for nonalcoholic steatohepatitis: a multicenter validation study. *Hepatology* 2009; 50: 1072–1078.

[58] Castera L, Friedrich-Rust M, Loomba R. Noninvasive Assessment of Liver Disease in Patients With Nonalcoholic Fatty Liver Disease. *Gastroenterology* 2019; 156: 1264-1281.e4.

[59] Hernaez R, Lazo M, Bonekamp S, et al. Diagnostic accuracy and reliability of

ultrasonography for the detection of fatty liver: a meta-analysis. *Hepatology* 2011; 54: 1082–1090.

[60] Strauss S, Gavish E, Gottlieb P, et al. Interobserver and intraobserver variability in the sonographic assessment of fatty liver. *AJR Am J Roentgenol* 2007; 189: W320-3.

[61] Sasso M, Beaugrand M, de Ledinghen V, et al. Controlled attenuation parameter (CAP): a novel VCTE™ guided ultrasonic attenuation measurement for the evaluation of hepatic steatosis: preliminary study and validation in a cohort of patients with chronic liver disease from various causes. *Ultrasound Med Biol* 2010; 36: 1825–1835.

[62] Tada T, Kumada T, Toyoda H, et al. Utility of Attenuation Coefficient Measurement Using an Ultrasound-Guided Attenuation Parameter for Evaluation of Hepatic Steatosis: Comparison With MRI-Determined Proton Density Fat Fraction. *AJR Am J Roentgenol* 2019; 212: 332–341.

[63] Han A, Andre MP, Deiranieh L, et al. Repeatability and Reproducibility of the Ultrasonic Attenuation Coefficient and Backscatter Coefficient Measured in the Right Lobe of the Liver in Adults With Known or Suspected Nonalcoholic Fatty Liver Disease. *J ultrasound Med Off J Am Inst Ultrasound Med* 2018; 37: 1913–1927.

[64] Pirmoazen AM, Khurana A, El Kaffas A, et al. Quantitative ultrasound approaches for diagnosis and monitoring hepatic steatosis in nonalcoholic fatty liver disease. *Theranostics* 2020; 10: 4277–4289.

[65] Postic C, Girard J. Contribution of de novo fatty acid synthesis to hepatic steatosis and insulin resistance: lessons from genetically engineered mice. *J Clin Invest* 2008; 118: 829–838.

[66] Samuel VT, Shulman GI. Nonalcoholic Fatty Liver Disease as a Nexus of Metabolic and Hepatic Diseases. *Cell Metab* 2018; 27: 22–41.

[67] Chaurasia B, Summers SA. Ceramides - Lipotoxic Inducers of Metabolic Disorders. *Trends Endocrinol Metab* 2015; 26: 538–550.

[68] Donnelly KL, Smith CI, Schwarzenberg SJ, et al. Sources of fatty acids stored in liver and secreted via lipoproteins in patients with nonalcoholic fatty liver disease. *J Clin Invest* 2005; 115: 1343–1351.

[69] Day CP, James OF. Steatohepatitis: a tale of two 'hits'? *Gastroenterology* 1998; 114: 842–845.

[70] Tilg H, Moschen AR. Evolution of inflammation in nonalcoholic fatty liver disease: the multiple parallel hits hypothesis. *Hepatology* 2010; 52: 1836–1846.

[71] Degli Esposti D, Hamelin J, Bosselut N, et al. Mitochondrial roles and cytoprotection in chronic liver injury. *Biochem Res Int* 2012; 2012: 387626.

[72] Sena LA, Chandel NS. Physiological roles of mitochondrial reactive oxygen species. *Mol Cell* 2012; 48: 158–167.

[73] Osellame LD, Blacker TS, Duchen MR. Cellular and molecular mechanisms of mitochondrial function. *Best Pract Res Clin Endocrinol Metab* 2012; 26: 711–723.

[74] Scatena R, Bottoni P, Botta G, et al. The role of mitochondria in pharmacotoxicology: a reevaluation of an old, newly emerging topic. *Am J Physiol Cell Physiol* 2007; 293: C12-21.

[75] Montero J, Mari M, Colell A, et al. Cholesterol and peroxidized cardiolipin in mitochondrial membrane properties, permeabilization and cell death. *Biochim Biophys Acta* 2010; 1797: 1217–1224.

[76] Nicholls DG, Ferguson SJ. Introduction to Part 2. In: Nicholls DG, Ferguson SJBT-B (Fourth E (eds). Boston: Academic Press, p. 89.

[77] Pernas L, Scorrano L. Mito-Morphosis: Mitochondrial Fusion, Fission, and Cristae Remodeling as Key Mediators of Cellular Function. *Annu Rev Physiol* 2016; 78: 505–531.

[78] Rossignol R, Gilkerson R, Aggeler R, et al. Energy substrate modulates

mitochondrial structure and oxidative capacity in cancer cells. *Cancer Res* 2004; 64: 985–993.

[79] Anderson S, Bankier AT, Barrell BG, et al. Sequence and organization of the human mitochondrial genome. *Nature* 1981; 290: 457–465.

[80] Robin ED, Wong R. Mitochondrial DNA molecules and virtual number of mitochondria per cell in mammalian cells. *J Cell Physiol* 1988; 136: 507–513.

[81] Schatz G. The protein import system of mitochondria. *J Biol Chem* 1996; 271: 31763–31766.

[82] Rich PR, Maréchal A. The mitochondrial respiratory chain. *Essays Biochem* 2010; 47: 1–23.

[83] Minasyan L, Sreekumar PG, Hinton DR, et al. Protective Mechanisms of the Mitochondrial-Derived Peptide Humanin in Oxidative and Endoplasmic Reticulum Stress in RPE Cells. *Oxid Med Cell Longev* 2017; 2017: 1675230.

[84] Hashimoto Y, Niikura T, Tajima H, et al. A rescue factor abolishing neuronal cell death by a wide spectrum of familial Alzheimer's disease genes and Abeta. *Proc Natl Acad Sci U S A* 2001; 98: 6336–6341.

[85] Lee C, Zeng J, Drew BG, et al. The mitochondrial-derived peptide MOTS-c promotes metabolic homeostasis and reduces obesity and insulin resistance. *Cell Metab* 2015; 21: 443–454.

[86] Cobb LJ, Lee C, Xiao J, et al. Naturally occurring mitochondrial-derived peptides are age-dependent regulators of apoptosis, insulin sensitivity, and inflammatory markers. *Aging (Albany NY)* 2016; 8: 796–809.

[87] Kim S-J, Mehta HH, Wan J, et al. Mitochondrial peptides modulate mitochondrial function during cellular senescence. *Aging (Albany NY)* 2018; 10: 1239–1256.

[88] Nicholls DG, Ferguson SJ. 5 - Respiratory Chains. In: Nicholls DG, Ferguson SJBT-B (Fourth E (eds). Boston: Academic Press, pp. 91–157.

[89] Bezawork-Geleta A, Rohlena J, Dong L, et al. Mitochondrial Complex II: At the Crossroads. *Trends Biochem Sci* 2017; 42: 312–325.

[90] Nicholls DG, Ferguson SJ. 7 - ATP Synthases and Bacterial Flagella Rotary Motors. In: Nicholls DG, Ferguson SJBT-B (Fourth E (eds). Boston: Academic Press, pp. 197–220.

[91] Nicholls DG. Mitochondrial ion circuits. *Essays Biochem* 2010; 47: 25–35.

[92] Schägger H, Pfeiffer K. Supercomplexes in the respiratory chains of yeast and mammalian mitochondria. *EMBO J* 2000; 19: 1777–1783.

[93] Gu J, Wu M, Guo R, et al. The architecture of the mammalian respirasome. *Nature* 2016; 537: 639–643.

[94] Claypool SM. Cardiolipin, a critical determinant of mitochondrial carrier protein assembly and function. *Biochim Biophys Acta* 2009; 1788: 2059–2068.

[95] Maranzana E, Barbero G, Falasca AI, et al. Mitochondrial respiratory supercomplex association limits production of reactive oxygen species from complex I. *Antioxid Redox Signal* 2013; 19: 1469–1480.

[96] Peyta L, Jarnouen K, Pinault M, et al. Reduced cardiolipin content decreases respiratory chain capacities and increases ATP synthesis yield in the human HepaRG cells. *Biochim Biophys Acta* 2016; 1857: 443—453.

[97] Rahal A, Kumar A, Singh V, et al. Oxidative stress, prooxidants, and antioxidants: the interplay. *Biomed Res Int* 2014; 2014: 761264.

[98] Lü J-M, Lin PH, Yao Q, et al. Chemical and molecular mechanisms of antioxidants: experimental approaches and model systems. *J Cell Mol Med* 2010; 14: 840–860.

[99] Halliwell B, Gutteridge JM. Oxygen free radicals and iron in relation to biology and medicine: some problems and concepts. *Arch Biochem Biophys* 1986; 246: 501–514.

[100] Martindale JL, Holbrook NJ. Cellular response to oxidative stress: signaling for suicide and survival. *J Cell Physiol* 2002; 192: 1–15.

[101] Brown GC, Borutaite V. There is no evidence that mitochondria are the main source of reactive oxygen species in mammalian cells. *Mitochondrion* 2012; 12: 1–4.

[102] Cichoż-Lach H, Michalak A. Oxidative stress as a crucial factor in liver diseases. *World J Gastroenterol* 2014; 20: 8082–8091.

[103] Chance B, Sies H, Boveris A. Hydroperoxide metabolism in mammalian organs. *Physiol Rev* 1979; 59: 527–605.

[104] Sies H, Jones DP. Reactive oxygen species (ROS) as pleiotropic physiological signalling agents. *Nat Rev Mol Cell Biol* 2020; 21: 363–383.

[105] Forrester SJ, Kikuchi DS, Hernandes MS, et al. Reactive Oxygen Species in Metabolic and Inflammatory Signaling. *Circ Res* 2018; 122: 877–902.

[106] Kausar S, Wang F, Cui H. The Role of Mitochondria in Reactive Oxygen Species Generation and Its Implications for Neurodegenerative Diseases. *Cells*; 7. Epub ahead of print December 2018. DOI: 10.3390/cells7120274.

[107] Carreras MC, Franco MC, Peralta JG, et al. Nitric oxide, complex I, and the modulation of mitochondrial reactive species in biology and disease. *Mol Aspects Med* 2004; 25: 125–139.

[108] Forkink M, Smeitink JAM, Brock R, et al. Detection and manipulation of mitochondrial reactive oxygen species in mammalian cells. *Biochim Biophys Acta* 2010; 1797: 1034–1044.

[109] Brand MD. The sites and topology of mitochondrial superoxide production. *Exp Gerontol* 2010; 45: 466–472.

[110] Murphy MP. How mitochondria produce reactive oxygen species. *Biochem J* 2009; 417: 1–13.

[111] Kudin AP, Bimpong-Buta NY-B, Vielhaber S, et al. Characterization of superoxide-producing sites in isolated brain mitochondria. *J Biol Chem* 2004; 279: 4127–4135.

[112] Kussmaul L, Hirst J. The mechanism of superoxide production by NADH:ubiquinone oxidoreductase (complex I) from bovine heart mitochondria. *Proc Natl Acad Sci U S A* 2006; 103: 7607–7612.

[113] Aon MA, Cortassa S, O'Rourke B. Redox-optimized ROS balance: a unifying hypothesis. *Biochim Biophys Acta* 2010; 1797: 865–877.

[114] Jastroch M, Divakaruni AS, Mookerjee S, et al. Mitochondrial proton and electron leaks. *Essays Biochem* 2010; 47: 53–67.

[115] Venditti P, Di Stefano L, Di Meo S. Mitochondrial metabolism of reactive oxygen species. *Mitochondrion* 2013; 13: 71–82.

[116] Rhee SG, Bae YS, Lee SR, et al. Hydrogen peroxide: a key messenger that modulates protein phosphorylation through cysteine oxidation. *Sci STKE* 2000; 2000: pe1.

[117] Sies H. Oxidative eustress: On constant alert for redox homeostasis. *Redox Biol* 2021; 41: 101867.

[118] Kirkman HN, Rolfo M, Ferraris AM, et al. Mechanisms of protection of catalase by NADPH. Kinetics and stoichiometry. *J Biol Chem* 1999; 274: 13908–13914.

[119] Andreyev AY, Kushnareva YE, Murphy AN, et al. Mitochondrial ROS Metabolism: 10 Years Later. *Biochemistry (Mosc)* 2015; 80: 517–531.

[120] Starkov AA. The role of mitochondria in reactive oxygen species metabolism and signaling. *Ann N Y Acad Sci* 2008; 1147: 37–52.

[121] Chen Y, Dong H, Thompson DC, et al. Glutathione defense mechanism in liver injury: insights from animal models. *Food Chem Toxicol an Int J Publ Br Ind Biol Res Assoc* 2013; 60: 38–44.

[122] Go Y-M, Jones DP. Redox compartmentalization in eukaryotic cells. *Biochim Biophys Acta* 2008; 1780: 1273–1290.

[123] Chouchani ET, Kazak L, Spiegelman BM. Mitochondrial reactive oxygen species and adipose tissue thermogenesis: Bridging physiology and mechanisms. *J Biol*

Chem 2017; 292: 16810–16816.

[124] Chen Z, Tian R, She Z, et al. Role of oxidative stress in the pathogenesis of nonalcoholic fatty liver disease. *Free Radic Biol Med* 2020; 152: 116–141.

[125] van der Vliet A, Janssen-Heininger YMW, Anathy V. Oxidative stress in chronic lung disease: From mitochondrial dysfunction to dysregulated redox signaling. *Mol Aspects Med* 2018; 63: 59–69.

[126] Vercesi AE, Castilho RF, Kowaltowski AJ, et al. Mitochondrial calcium transport and the redox nature of the calcium-induced membrane permeability transition. *Free Radic Biol Med* 2018; 129: 1–24.

[127] Finkel T. Signal transduction by mitochondrial oxidants. *J Biol Chem* 2012; 287: 4434–4440.

[128] Forman HJ, Maiorino M, Ursini F. Signaling functions of reactive oxygen species. *Biochemistry* 2010; 49: 835–842.

[129] Serviddio G, Bellanti F, Vendemiale G. Free radical biology for medicine: learning from nonalcoholic fatty liver disease. *Free Radic Biol Med* 2013; 65: 952–968.

[130] Ore A, Akinloye OA. Oxidative Stress and Antioxidant Biomarkers in Clinical and Experimental Models of Non-Alcoholic Fatty Liver Disease. *Medicina (Kaunas)*; 2019 Jan 24;55(2):26.

[131] Hauck AK, Bernlohr DA. Oxidative stress and lipotoxicity. *J Lipid Res* 2016; 57: 1976–1986.

[132] Castro L, Tórtora V, Mansilla S, et al. Aconitases: Non-redox Iron-Sulfur Proteins Sensitive to Reactive Species. *Acc Chem Res* 2019; 52: 2609–2619.

[133] Braymer JJ, Stümpfig M, Thelen S, et al. Depletion of thiol reducing capacity impairs cytosolic but not mitochondrial iron-sulfur protein assembly machineries. *Biochim Biophys acta Mol cell Res* 2019; 1866: 240–251.

[134] Kondadi AK, Anand R, Reichert AS. Functional Interplay between Cristae

Biogenesis, Mitochondrial Dynamics and Mitochondrial DNA Integrity. *Int J Mol Sci*; 2020 Aug 26;10(9):164.

[135] Bulthuis EP, Adjobo-Hermans MJW, Willems PHGM, et al. Mitochondrial Morphofunction in Mammalian Cells. *Antioxid Redox Signal* 2019; 30: 2066–2109.

[136] Detmer SA, Chan DC. Functions and dysfunctions of mitochondrial dynamics. *Nat Rev Mol Cell Biol* 2007; 8: 870–879.

[137] Hoppins S, Lackner L, Nunnari J. The machines that divide and fuse mitochondria. *Annu Rev Biochem* 2007; 76: 751–780.

[138] Sebastián D, Hernández-Alvarez MI, Segalés J, et al. Mitofusin 2 (Mfn2) links mitochondrial and endoplasmic reticulum function with insulin signaling and is essential for normal glucose homeostasis. *Proc Natl Acad Sci U S A* 2012; 109: 5523–5528.

[139] Wang L, Ishihara T, Ibayashi Y, et al. Disruption of mitochondrial fission in the liver protects mice from diet-induced obesity and metabolic deterioration. *Diabetologia* 2015; 58: 2371–2380.

[140] Baker MJ, Tatsuta T, Langer T. Quality control of mitochondrial proteostasis. *Cold Spring Harb Perspect Biol*; 3. 2011 Jul 1;3(7):a007559.

[141] Nargund AM, Pellegrino MW, Fiorese CJ, et al. Mitochondrial import efficiency of ATFS-1 regulates mitochondrial UPR activation. *Science* 2012; 337: 587–590.

[142] Wong E, Cuervo AM. Autophagy gone awry in neurodegenerative diseases. *Nat Neurosci* 2010; 13: 805–811.

[143] Mathew R, Karantza-Wadsworth V, White E. Role of autophagy in cancer. *Nature reviews. Cancer* 2007; 7: 961–967.

[144] Khambu B, Yan S, Huda N, et al. Autophagy in non-alcoholic fatty liver disease and alcoholic liver disease. *Liver Res* 2018; 2: 112–119.

[145] Egan DF, Shackelford DB, Mihaylova MM, et al. Phosphorylation of ULK1 (hATG1) by AMP-activated protein kinase connects energy sensing to mitophagy. *Science*

2011; 331: 456–461.

[146] Twig G, Elorza A, Molina AJA, et al. Fission and selective fusion govern mitochondrial segregation and elimination by autophagy. *EMBO J* 2008; 27: 433–446.

[147] Ashrafi G, Schwarz TL. The pathways of mitophagy for quality control and clearance of mitochondria. *Cell Death Differ* 2013; 20: 31–42.

[148] Guardia-Laguarta C, Liu Y, Lauritzen KH, et al. PINK1 Content in Mitochondria is Regulated by ER-Associated Degradation. *J Neurosci* 2019; 39: 7074–7085.

[149] Greene AW, Grenier K, Aguileta MA, et al. Mitochondrial processing peptidase regulates PINK1 processing, import and Parkin recruitment. *EMBO Rep* 2012; 13: 378–385.

[150] Kane LA, Lazarou M, Fogel AI, et al. PINK1 phosphorylates ubiquitin to activate Parkin E3 ubiquitin ligase activity. *J Cell Biol* 2014; 205: 143–153.

[151] Kitada T, Asakawa S, Hattori N, et al. Mutations in the parkin gene cause autosomal recessive juvenile parkinsonism. *Nature* 1998; 392: 605–608.

[152] Lazarou M. Keeping the immune system in check: a role for mitophagy. *Immunol Cell Biol* 2015; 93: 3–10.

[153] Narendra D, Tanaka A, Suen D-F, et al. Parkin-induced mitophagy in the pathogenesis of Parkinson disease. *Autophagy* 2009; 5: 706–708.

[154] Liu L, Feng D, Chen G, et al. Mitochondrial outer-membrane protein FUNDC1 mediates hypoxia-induced mitophagy in mammalian cells. *Nat Cell Biol* 2012; 14: 177–185.

[155] Zhang H, Bosch-Marce M, Shimoda LA, et al. Mitochondrial autophagy is an HIF-1-dependent adaptive metabolic response to hypoxia. *J Biol Chem* 2008; 283: 10892–10903.

[156] Lieber T, Jeedigunta SP, Palozzi JM, et al. Mitochondrial fragmentation drives

selective removal of deleterious mtDNA in the germline. *Nature* 2019; 570: 380–384.

[157] Ott M, Gogvadze V, Orrenius S, et al. Mitochondria, oxidative stress and cell death. *Apoptosis* 2007; 12: 913–922.

[158] Rizzuto R, Pinton P, Carrington W, et al. Close contacts with the endoplasmic reticulum as determinants of mitochondrial Ca2+ responses. *Science* 1998; 280: 1763–1766.

[159] Gunter TE, Gunter KK. Uptake of calcium by mitochondria: transport and possible function. *IUBMB Life* 2001; 52: 197–204.

[160] Morciano G, Naumova N, Koprowski P, et al. The mitochondrial permeability transition pore: an evolving concept critical for cell life and death. *Biol Rev Camb Philos Soc*. 2021 Dec;96(6):2489-2521.

[161] Li Y, Sun J, Wu R, et al. Mitochondrial MPTP: A Novel Target of Ethnomedicine for Stroke Treatment by Apoptosis Inhibition. *Front Pharmacol* 2020; 11: 352.

[162] Halestrap AP, Clarke SJ, Javadov SA. Mitochondrial permeability transition pore opening during myocardial reperfusion--a target for cardioprotection. *Cardiovasc Res* 2004; 61: 372–385.

[163] Feissner RF, Skalska J, Gaum WE, et al. Crosstalk signaling between mitochondrial Ca2+ and ROS. *Front Biosci (Landmark Ed* 2009; 14: 1197–1218.

[164] Halestrap AP. Mitochondria and reperfusion injury of the heart--a holey death but not beyond salvation. *J Bioenerg Biomembr* 2009; 41: 113–121.

[165] Dykens JA, Will Y. The significance of mitochondrial toxicity testing in drug development. *Drug Discov Today* 2007; 12: 777–785.

[166] Shi Y. Mechanisms of caspase activation and inhibition during apoptosis. *Mol Cell* 2002; 9: 459–470.

[167] Nagata S. Apoptosis and Clearance of Apoptotic Cells. *Annu Rev Immunol* 2018; 36: 489–517.

[168] Kang M, Li S, Zhong D, et al. [Hepatocyte apoptosis and mitochondrial permeability transition pore opening in rats with nonalcoholic fatty liver]. *Nan Fang Yi Ke Da Xue Xue Bao* 2013; 33: 1062–1066.

[169] Häcker G. The morphology of apoptosis. *Cell Tissue Res* 2000; 301: 5–17.

[170] Kamata H, Honda S-I, Maeda S, et al. Reactive oxygen species promote TNFalpha-induced death and sustained JNK activation by inhibiting MAP kinase phosphatases. *Cell* 2005; 120: 649–661.

[171] Wang C, Youle RJ. The role of mitochondria in apoptosis*. *Annu Rev Genet* 2009; 43: 95–118.

[172] Shi Y, Nikulenkov F, Zawacka-Pankau J, et al. ROS-dependent activation of JNK converts p53 into an efficient inhibitor of oncogenes leading to robust apoptosis. *Cell Death Differ* 2014; 21: 612–623.

[173] Kekulandara DN, Nagi S, Seo H, et al. Redox-Inactive Peptide Disrupting Trx1-Ask1 Interaction for Selective Activation of Stress Signaling. *Biochemistry* 2018; 57: 772–780.

[174] Soga M, Matsuzawa A, Ichijo H. Oxidative Stress-Induced Diseases via the ASK1 Signaling Pathway. *Int J Cell Biol* 2012; 2012: 439587.

[175] Circu ML, Aw TY. Glutathione and apoptosis. *Free Radic Res* 2008; 42: 689–706.

[176] Linkermann A, Bräsen JH, Darding M, et al. Two independent pathways of regulated necrosis mediate ischemia-reperfusion injury. *Proc Natl Acad Sci U S A* 2013; 110: 12024–12029.

[177] Cho YS, Challa S, Moquin D, et al. Phosphorylation-driven assembly of the RIP1-RIP3 complex regulates programmed necrosis and virus-induced inflammation. *Cell* 2009; 137: 1112–1123.

[178] Afonso MB, Rodrigues PM, Mateus-Pinheiro M, et al. RIPK3 acts as a lipid metabolism regulator contributing to inflammation and carcinogenesis in non-

alcoholic fatty liver disease. *Gut*. 2021 Dec;70(12):2359-2372.

[179] Wei J, Chen L, Wang D, et al. Upregulation of RIP3 promotes necroptosis via a ROS-dependent NF-κB pathway to induce chronic inflammation in HK-2 cells. *Mol Med Rep*; 2021 Nov;24(5):783.

[180] Poli V, Camporeale A. STAT3-Mediated Metabolic Reprograming in Cellular Transformation and Implications for Drug Resistance. *Front Oncol* 2015; 5: 121.

[181] Sun W, Wu X, Gao H, et al. Cytosolic calcium mediates RIP1/RIP3 complex-dependent necroptosis through JNK activation and mitochondrial ROS production in human colon cancer cells. *Free Radic Biol Med* 2017; 108: 433–444.

[182] Zhang Y, Su SS, Zhao S, et al. RIP1 autophosphorylation is promoted by mitochondrial ROS and is essential for RIP3 recruitment into necrosome. *Nat Commun*; 2017 Feb 8;8:14329.

[183] Zhang D-W, Shao J, Lin J, et al. RIP3, an energy metabolism regulator that switches TNF-induced cell death from apoptosis to necrosis. *Science* 2009; 325: 332–336.

[184] Yang Z, Wang Y, Zhang Y, et al. RIP3 targets pyruvate dehydrogenase complex to increase aerobic respiration in TNF-induced necroptosis. *Nat Cell Biol* 2018; 20: 186–197.

[185] Vaz FM, Wanders RJA. Carnitine biosynthesis in mammals. *Biochem J* 2002; 361: 417–429.

[186] Houten SM, Violante S, Ventura F V, et al. The Biochemistry and Physiology of Mitochondrial Fatty Acid β-Oxidation and Its Genetic Disorders. *Annu Rev Physiol* 2016; 78: 23–44.

[187] Kersten S, Seydoux J, Peters JM, et al. Peroxisome proliferator-activated receptor alpha mediates the adaptive response to fasting. *J Clin Invest* 1999; 103: 1489–1498.

[188] Tapia PC. Sublethal mitochondrial stress with an attendant stoichiometric augmentation of reactive oxygen species may precipitate many of the beneficial

alterations in cellular physiology produced by caloric restriction, intermittent fasting, exercise and dietary . *Med Hypotheses* 2006; 66: 832–843.

[189] Ristow M, Schmeisser K. Mitohormesis: Promoting Health and Lifespan by Increased Levels of Reactive Oxygen Species (ROS). *Dose Response* 2014; 12: 288–341.

[190] Zarse K, Schmeisser S, Groth M, et al. Impaired insulin/IGF1 signaling extends life span by promoting mitochondrial L-proline catabolism to induce a transient ROS signal. *Cell Metab* 2012; 15: 451–465.

[191] Irrcher I, Adhihetty PJ, Joseph A-M, et al. Regulation of mitochondrial biogenesis in muscle by endurance exercise. *Sports Med* 2003; 33: 783–793.

[192] Martel C, Wang Z, Brenner C. VDAC phosphorylation, a lipid sensor influencing the cell fate. *Mitochondrion* 2014; 19 Pt A: 69–77.

[193] Herzig S, Shaw RJ. AMPK: guardian of metabolism and mitochondrial homeostasis. *Nat Rev Mol Cell Biol* 2018; 19: 121–135.

[194] Katsyuba E, Auwerx J. Modulating NAD(+) metabolism, from bench to bedside. *EMBO J* 2017; 36: 2670–2683.

[195] Fang EF, Lautrup S, Hou Y, et al. NAD(+) in Aging: Molecular Mechanisms and Translational Implications. *Trends Mol Med* 2017; 23: 899–916.

[196] Niu B, He K, Li P, et al. SIRT1 upregulation protects against liver injury induced by a HFD through inhibiting CD36 and the NF-κB pathway in mouse kupffer cells. *Mol Med Rep* 2018; 18: 1609–1615.

[197] Wang R-H, Kim H-S, Xiao C, et al. Hepatic Sirt1 deficiency in mice impairs mTorc2/Akt signaling and results in hyperglycemia, oxidative damage, and insulin resistance. *J Clin Invest* 2011; 121: 4477–4490.

[198] Shpilka T, Haynes CM. The mitochondrial UPR: mechanisms, physiological functions and implications in ageing. *Nat Rev Mol Cell Biol* 2018; 19: 109–120.

[199] Nargund AM, Fiorese CJ, Pellegrino MW, et al. Mitochondrial and nuclear accumulation of the transcription factor ATFS-1 promotes OXPHOS recovery during the UPR(mt). *Mol Cell* 2015; 58: 123–133.

[200] Chung HK, Kim JT, Kim H-W, et al. GDF15 deficiency exacerbates chronic alcohol- and carbon tetrachloride-induced liver injury. *Sci Rep* 2017; 7: 17238.

[201] Gariani K, Menzies KJ, Ryu D, et al. Eliciting the mitochondrial unfolded protein response by nicotinamide adenine dinucleotide repletion reverses fatty liver disease in mice. *Hepatology* 2016; 63: 1190–1204.

[202] Carotti S, Aquilano K, Zalfa F, et al. Lipophagy Impairment Is Associated With Disease Progression in NAFLD. *Front Physiol* 2020; 11: 850.

[203] Ferrín G, Guerrero M, Amado V, et al. Activation of mTOR Signaling Pathway in Hepatocellular Carcinoma. *Int J Mol Sci*; 2020 Feb 13;21(4):1266.

[204] Lee JH, Khor TO, Shu L, et al. Dietary phytochemicals and cancer prevention: Nrf2 signaling, epigenetics, and cell death mechanisms in blocking cancer initiation and progression. *Pharmacol Ther* 2013; 137: 153–171.

[205] Upadhyay S, Dixit M. Role of Polyphenols and Other Phytochemicals on Molecular Signaling. *Oxid Med Cell Longev* 2015; 2015: 504253.

[206] Espinosa-Diez C, Miguel V, Mennerich D, et al. Antioxidant responses and cellular adjustments to oxidative stress. *Redox Biol* 2015; 6: 183–197.

[207] Perlemuter G, Davit-Spraul A, Cosson C, et al. Increase in liver antioxidant enzyme activities in non-alcoholic fatty liver disease. *Liver Int Off J Int Assoc Study Liver* 2005; 25: 946–953.

[208] Lee L-Y, Köhler UA, Zhang L, et al. Activation of the Nrf2-ARE pathway in hepatocytes protects against steatosis in nutritionally induced non-alcoholic steatohepatitis in mice. *Toxicol Sci* 2014; 142: 361–374.

[209] Wang C, Cui Y, Li C, et al. Nrf2 deletion causes 'benign' simple steatosis to develop into nonalcoholic steatohepatitis in mice fed a high-fat diet. *Lipids Health Dis*

2013; 12: 165.

[210] Mantena SK, Vaughn DP, Andringa KK, et al. High fat diet induces dysregulation of hepatic oxygen gradients and mitochondrial function in vivo. *Biochem J* 2009; 417: 183–193.

[211] Eccleston HB, Andringa KK, Betancourt AM, et al. Chronic exposure to a high-fat diet induces hepatic steatosis, impairs nitric oxide bioavailability, and modifies the mitochondrial proteome in mice. *Antioxid Redox Signal* 2011; 15: 447–459.

[212] Arab JP, Arrese M, Trauner M. Recent Insights into the Pathogenesis of Nonalcoholic Fatty Liver Disease. *Annu Rev Pathol* 2018; 13: 321–350.

[213] Pessayre D, Fromenty B, Berson A, et al. Central role of mitochondria in drug-induced liver injury. *Drug Metab Rev* 2012; 44: 34–87.

[214] Hirschey MD, Shimazu T, Goetzman E, et al. SIRT3 regulates mitochondrial fatty-acid oxidation by reversible enzyme deacetylation. *Nature* 2010; 464: 121–125.

[215] Serra D, Mera P, Malandrino MI, et al. Mitochondrial fatty acid oxidation in obesity. *Antioxid Redox Signal* 2013; 19: 269–284.

[216] Gusdon AM, Song K-X, Qu S. Nonalcoholic Fatty liver disease: pathogenesis and therapeutics from a mitochondria-centric perspective. *Oxid Med Cell Longev* 2014; 2014: 637027.

[217] Lim CY, Jun DW, Jang SS, et al. Effects of carnitine on peripheral blood mitochondrial DNA copy number and liver function in non-alcoholic fatty liver disease. *Korean J Gastroenterol* 2010; 55: 384–389.

[218] Sunny NE, Parks EJ, Browning JD, et al. Excessive hepatic mitochondrial TCA cycle and gluconeogenesis in humans with nonalcoholic fatty liver disease. *Cell Metab* 2011; 14: 804–810.

[219] Iozzo P, Bucci M, Roivainen A, et al. Fatty acid metabolism in the liver, measured by positron emission tomography, is increased in obese individuals.

Gastroenterology 2010; 139: 846–56, 856.e1–6.

[220] Fletcher JA, Deja S, Satapati S, et al. Impaired ketogenesis and increased acetyl-CoA oxidation promote hyperglycemia in human fatty liver. *JCI insight*; 2019 Apr 23;5(11):e127737.

[221] Gray LR, Sultana MR, Rauckhorst AJ, et al. Hepatic Mitochondrial Pyruvate Carrier 1 Is Required for Efficient Regulation of Gluconeogenesis and Whole-Body Glucose Homeostasis. *Cell Metab* 2015; 22: 669–681.

[222] Rauckhorst AJ, Gray LR, Sheldon RD, et al. The mitochondrial pyruvate carrier mediates high fat diet-induced increases in hepatic TCA cycle capacity. *Mol Metab* 2017; 6: 1468–1479.

[223] McCommis KS, Chen Z, Fu X, et al. Loss of Mitochondrial Pyruvate Carrier 2 in the Liver Leads to Defects in Gluconeogenesis and Compensation via Pyruvate-Alanine Cycling. *Cell Metab* 2015; 22: 682–694.

[224] Duarte JAG, Carvalho F, Pearson M, et al. A high-fat diet suppresses de novo lipogenesis and desaturation but not elongation and triglyceride synthesis in mice. *J Lipid Res* 2014; 55: 2541–2553.

[225] Smith GI, Shankaran M, Yoshino M, et al. Insulin resistance drives hepatic de novo lipogenesis in nonalcoholic fatty liver disease. *J Clin Invest* 2020; 130: 1453–1460.

[226] Kim C-W, Addy C, Kusunoki J, et al. Acetyl CoA Carboxylase Inhibition Reduces Hepatic Steatosis but Elevates Plasma Triglycerides in Mice and Humans: A Bedside to Bench Investigation. *Cell Metab* 2017; 26: 394-406.e6.

[227] Aharoni-Simon M, Hann-Obercyger M, Pen S, et al. Fatty liver is associated with impaired activity of PPARγ-coactivator 1α (PGC1α) and mitochondrial biogenesis in mice. *Lab Invest* 2011; 91: 1018–1028.

[228] Zhang Y, Bharathi SS, Beck ME, et al. The fatty acid oxidation enzyme long-chain acyl-CoA dehydrogenase can be a source of mitochondrial hydrogen peroxide. *Redox Biol* 2019; 26: 101253.

[229] Cardoso AR, Kakimoto PAHB, Kowaltowski AJ. Diet-sensitive sources of reactive oxygen species in liver mitochondria: role of very long chain acyl-CoA dehydrogenases. *PLoS One* 2013; 8: e77088.

[230] Pessayre D. Role of mitochondria in non-alcoholic fatty liver disease. *J Gastroenterol Hepatol* 2007; 22 Suppl 1: S20-7.

[231] Chavin KD, Yang S, Lin HZ, et al. Obesity induces expression of uncoupling protein-2 in hepatocytes and promotes liver ATP depletion. *J Biol Chem* 1999; 274: 5692–5700.

[232] Lin HZ, Yang SQ, Chuckaree C, et al. Metformin reverses fatty liver disease in obese, leptin-deficient mice. *Nat Med* 2000; 6: 998–1003.

[233] Lee K, Haddad A, Osme A, et al. Hepatic Mitochondrial Defects in a Nonalcoholic Fatty Liver Disease Mouse Model Are Associated with Increased Degradation of Oxidative Phosphorylation Subunits. *Mol Cell Proteomics* 2018; 17: 2371–2386.

[234] Bellanti F, Villani R, Facciorusso A, et al. Lipid oxidation products in the pathogenesis of non-alcoholic steatohepatitis. *Free Radic Biol Med* 2017; 111: 173–185.

[235] Albano E, Mottaran E, Vidali M, et al. Immune response towards lipid peroxidation products as a predictor of progression of non-alcoholic fatty liver disease to advanced fibrosis. *Gut* 2005; 54: 987–993.

[236] Liu S, Shi W, Li G, et al. Plasma reactive carbonyl species levels and risk of non-alcoholic fatty liver disease. *J Gastroenterol Hepatol* 2011; 26: 1010–1015.

[237] Marette A. Molecular mechanisms of inflammation in obesity-linked insulin resistance. *Int J Obes Relat Metab Disord J Int Assoc Study Obes* 2003; 27 Suppl 3: S46-8.

[238] Begriche K, Igoudjil A, Pessayre D, et al. Mitochondrial dysfunction in NASH: causes, consequences and possible means to prevent it. *Mitochondrion* 2006; 6: 1–28.

[239] Begriche K, Massart J, Fromenty B. Effects of β-aminoisobutyric acid on leptin production and lipid homeostasis: mechanisms and possible relevance for the prevention of obesity. *Fundam Clin Pharmacol* 2010; 24: 269–282.

[240] Satapati S, Sunny NE, Kucejova B, et al. Elevated TCA cycle function in the pathology of diet-induced hepatic insulin resistance and fatty liver. *J Lipid Res* 2012; 53: 1080–1092.

[241] Rector RS, Thyfault JP, Uptergrove GM, et al. Mitochondrial dysfunction precedes insulin resistance and hepatic steatosis and contributes to the natural history of non-alcoholic fatty liver disease in an obese rodent model. *J Hepatol* 2010; 52: 727–736.

[242] Morris EM, McCoin CS, Allen JA, et al. Aerobic capacity mediates susceptibility for the transition from steatosis to steatohepatitis. *J Physiol* 2017; 595: 4909–4926.

[243] Meakin PJ, Chowdhry S, Sharma RS, et al. Susceptibility of Nrf2-null mice to steatohepatitis and cirrhosis upon consumption of a high-fat diet is associated with oxidative stress, perturbation of the unfolded protein response, and disturbance in the expression of metabolic enzymes but not with . *Mol Cell Biol* 2014; 34: 3305–3320.

[244] Win S, Than TA, Zhang J, et al. New insights into the role and mechanism of c-Jun-N-terminal kinase signaling in the pathobiology of liver diseases. *Hepatology* 2018; 67: 2013–2024.

[245] Win S, Than TA, Min RWM, et al. c-Jun N-terminal kinase mediates mouse liver injury through a novel Sab (SH3BP5)-dependent pathway leading to inactivation of intramitochondrial Src. *Hepatology* 2016; 63: 1987–2003.

[246] Vernia S, Cavanagh-Kyros J, Garcia-Haro L, et al. The PPARα-FGF21 hormone axis contributes to metabolic regulation by the hepatic JNK signaling pathway. *Cell Metab* 2014; 20: 512–525.

[247] Li J, Romestaing C, Han X, et al. Cardiolipin remodeling by ALCAT1 links oxidative stress and mitochondrial dysfunction to obesity. *Cell Metab* 2010; 12: 154–165.

[248] Turpin SM, Nicholls HT, Willmes DM, et al. Obesity-induced CerS6-dependent C16:0 ceramide production promotes weight gain and glucose intolerance. *Cell Metab* 2014; 20: 678–686.

[249] Apostolopoulou M, Gordillo R, Koliaki C, et al. Specific Hepatic Sphingolipids Relate to Insulin Resistance, Oxidative Stress, and Inflammation in Nonalcoholic Steatohepatitis. *Diabetes Care* 2018; 41: 1235–1243.

[250] Krishnan KJ, Reeve AK, Samuels DC, et al. What causes mitochondrial DNA deletions in human cells? *Nat Genet* 2008; 40: 275–279.

[251] Tanaka S, Miyanishi K, Kobune M, et al. Increased hepatic oxidative DNA damage in patients with nonalcoholic steatohepatitis who develop hepatocellular carcinoma. *J Gastroenterol* 2013; 48: 1249–1258.

[252] Perfield JW 2nd, Ortinau LC, Pickering RT, et al. Altered hepatic lipid metabolism contributes to nonalcoholic fatty liver disease in leptin-deficient Ob/Ob mice. *J Obes* 2013; 2013: 296537.

[253] Matsuzawa-Nagata N, Takamura T, Ando H, et al. Increased oxidative stress precedes the onset of high-fat diet-induced insulin resistance and obesity. *Metabolism* 2008; 57: 1071–1077.

[254] Knebel B, Hartwig S, Haas J, et al. Peroxisomes compensate hepatic lipid overflow in mice with fatty liver. *Biochim Biophys Acta* 2015; 1851: 965–976.

[255] Collins JC, Scheinberg IH, Giblin DR, et al. Hepatic peroxisomal abnormalities in abetalipoproteinemia. *Gastroenterology* 1989; 97: 766–770.

[256] De Craemer D, Pauwels M, Van den Branden C. Alterations of peroxisomes in steatosis of the human liver: a quantitative study. *Hepatology* 1995; 22: 744–752.

[257] Hall D, Poussin C, Velagapudi VR, et al. Peroxisomal and microsomal lipid pathways associated with resistance to hepatic steatosis and reduced pro-inflammatory state. *J Biol Chem* 2010; 285: 31011–31023.

[258] Natarajan SK, Eapen CE, Pullimood AB, et al. Oxidative stress in experimental liver microvesicular steatosis: role of mitochondria and peroxisomes. *J Gastroenterol Hepatol* 2006; 21: 1240–1249.

[259] Begriche K, Massart J, Robin M-A, et al. Mitochondrial adaptations and dysfunctions in nonalcoholic fatty liver disease. *Hepatology* 2013; 58: 1497–1507.

[260] Maulik N, McFadden D, Otani H, et al. Antioxidants in longevity and medicine. *Oxidative medicine and cellular longevity* 2013; 2013: 820679.

[261] Kumar A, Sharma A, Duseja A, et al. Patients with Nonalcoholic Fatty Liver Disease (NAFLD) have Higher Oxidative Stress in Comparison to Chronic Viral Hepatitis. *J Clin Exp Hepatol* 2013; 3: 12–18.

[262] Koruk M, Taysi S, Savas MC, et al. Oxidative stress and enzymatic antioxidant status in patients with nonalcoholic steatohepatitis. *Ann Clin Lab Sci* 2004; 34: 57–62.

[263] Delli Bovi AP, Marciano F, Mandato C, et al. Oxidative Stress in Non-alcoholic Fatty Liver Disease. An Updated Mini Review. *Front Med* 2021; 8: 595371.

[264] Song L, Qu D, Zhang Q, et al. Phytosterol esters attenuate hepatic steatosis in rats with non-alcoholic fatty liver disease rats fed a high-fat diet. *Sci Rep* 2017; 7: 41604.

[265] Gan LT, Van Rooyen DM, Koina ME, et al. Hepatocyte free cholesterol lipotoxicity results from JNK1-mediated mitochondrial injury and is HMGB1 and TLR4-dependent. *J Hepatol* 2014; 61: 1376–1384.

[266] Yang S, Zhu H, Li Y, et al. Mitochondrial adaptations to obesity-related oxidant stress. *Arch Biochem Biophys* 2000; 378: 259–268.

[267] Laurent A, Nicco C, Tran Van Nhieu J, et al. Pivotal role of superoxide anion and beneficial effect of antioxidant molecules in murine steatohepatitis. *Hepatology* 2004; 39: 1277–1285.

[268] von Montfort C, Matias N, Fernandez A, et al. Mitochondrial GSH determines the

toxic or therapeutic potential of superoxide scavenging in steatohepatitis. *J Hepatol* 2012; 57: 852–859.

[269] Merry TL, Tran M, Dodd GT, et al. Hepatocyte glutathione peroxidase-1 deficiency improves hepatic glucose metabolism and decreases steatohepatitis in mice. *Diabetologia* 2016; 59: 2632–2644.

[270] Delibegovic M, Zimmer D, Kauffman C, et al. Liver-specific deletion of protein-tyrosine phosphatase 1B (PTP1B) improves metabolic syndrome and attenuates diet-induced endoplasmic reticulum stress. *Diabetes* 2009; 58: 590–599.

[271] Owen C, Lees EK, Grant L, et al. Inducible liver-specific knockdown of protein tyrosine phosphatase 1B improves glucose and lipid homeostasis in adult mice. *Diabetologia* 2013; 56: 2286–2296.

[272] Jais A, Einwallner E, Sharif O, et al. Heme oxygenase-1 drives metaflammation and insulin resistance in mouse and man. *Cell* 2014; 158: 25–40.

[273] Menken M, Waggoner JG, Berlin NI. The influence of bilirubin on oxidative phosphorylation and related reactions in brain and liver mitochondria: effects of protein-binding. *J Neurochem* 1966; 13: 1241–1248.

[274] Vasavda C, Kothari R, Malla AP, et al. Bilirubin Links Heme Metabolism to Neuroprotection by Scavenging Superoxide. *Cell Chem Biol* 2019; 26: 1450-1460.e7.

[275] Park J-S, Nam E, Lee H-K, et al. In Cellulo Mapping of Subcellular Localized Bilirubin. *ACS Chem Biol* 2016; 11: 2177–2185.

[276] Li R, Xin T, Li D, et al. Therapeutic effect of Sirtuin 3 on ameliorating nonalcoholic fatty liver disease: The role of the ERK-CREB pathway and Bnip3-mediated mitophagy. *Redox Biol* 2018; 18: 229–243.

[277] Gong L-L, Yang S, Zhang W, et al. Akebia saponin D alleviates hepatic steatosis through BNip3 induced mitophagy. *J Pharmacol Sci* 2018; 136: 189–195.

[278] Yu X, Hao M, Liu Y, et al. Liraglutide ameliorates non-alcoholic steatohepatitis by inhibiting NLRP3 inflammasome and pyroptosis activation via mitophagy. *Eur J Pharmacol* 2019; 864: 172715.

[279] Ma X, McKeen T, Zhang J, et al. Role and Mechanisms of Mitophagy in Liver Diseases. *Cells*; 2020 Mar 31;9(4):837. doi: 10.3390/cells9040837.

[280] Edmunds LR, Xie B, Mills AM, et al. Liver-specific Prkn knockout mice are more susceptible to diet-induced hepatic steatosis and insulin resistance. *Mol Metab* 2020; 41: 101051.

[281] Kim K-Y, Stevens M V, Akter MH, et al. Parkin is a lipid-responsive regulator of fat uptake in mice and mutant human cells. *J Clin Invest* 2011; 121: 3701–3712.

[282] Kim K-Y, Sack MN. Parkin in the regulation of fat uptake and mitochondrial biology: emerging links in the pathophysiology of Parkinson's disease. *Curr Opin Lipidol* 2012; 23: 201–205.

[283] Glick D, Zhang W, Beaton M, et al. BNip3 regulates mitochondrial function and lipid metabolism in the liver. *Mol Cell Biol* 2012; 32: 2570–2584.

[284] Zhao Q, Guo Z, Deng W, et al. Calpain 2-mediated autophagy defect increases susceptibility of fatty livers to ischemia-reperfusion injury. *Cell Death Dis* 2016; 7: e2186.

[285] González-Rodríguez A, Mayoral R, Agra N, et al. Impaired autophagic flux is associated with increased endoplasmic reticulum stress during the development of NAFLD. *Cell Death Dis* 2014; 5: e1179.

[286] Willy JA, Young SK, Mosley AL, et al. Function of inhibitor of Bruton's tyrosine kinase isoform α (IBTKα) in nonalcoholic steatohepatitis links autophagy and the unfolded protein response. *J Biol Chem* 2017; 292: 14050–14065.

[287] Zhou T, Chang L, Luo Y, et al. Mst1 inhibition attenuates non-alcoholic fatty liver disease via reversing Parkin-related mitophagy. *Redox Biol* 2019; 21: 101120.

[288] Inami Y, Yamashina S, Izumi K, et al. Hepatic steatosis inhibits autophagic

proteolysis via impairment of autophagosomal acidification and cathepsin expression. *Biochem Biophys Res Commun* 2011; 412: 618–625.

[289] Fukuo Y, Yamashina S, Sonoue H, et al. Abnormality of autophagic function and cathepsin expression in the liver from patients with non-alcoholic fatty liver disease. *Hepatol Res* 2014; 44: 1026–1036.

[290] Koga H, Kaushik S, Cuervo AM. Altered lipid content inhibits autophagic vesicular fusion. *FASEB J Off Publ Fed Am Soc Exp Biol* 2010; 24: 3052–3065.

[291] Tanaka S, Hikita H, Tatsumi T, et al. Rubicon inhibits autophagy and accelerates hepatocyte apoptosis and lipid accumulation in nonalcoholic fatty liver disease in mice. *Hepatology* 2016; 64: 1994–2014.

[292] Park H-W, Park H, Semple IA, et al. Pharmacological correction of obesity-induced autophagy arrest using calcium channel blockers. *Nat Commun* 2014; 5: 4834.

[293] Zubiete-Franco I, García-Rodríguez JL, Martínez-Uña M, et al. Methionine and S-adenosylmethionine levels are critical regulators of PP2A activity modulating lipophagy during steatosis. *J Hepatol* 2016; 64: 409–418.

[294] Hernández-Alvarez MI, Sebastián D, Vives S, et al. Deficient Endoplasmic Reticulum-Mitochondrial Phosphatidylserine Transfer Causes Liver Disease. *Cell* 2019; 177: 881-895.e17.

[295] Lee DH, Jung YY, Park MH, et al. Peroxiredoxin 6 Confers Protection Against Nonalcoholic Fatty Liver Disease Through Maintaining Mitochondrial Function. *Antioxid Redox Signal* 2019; 31: 387–402.

[296] Sanyal AJ, Campbell-Sargent C, Mirshahi F, et al. Nonalcoholic steatohepatitis: Association of insulin resistance and mitochondrial abnormalities. *Gastroenterology* 2001; 120: 1183–1192.

[297] Sunny NE, Bril F, Cusi K. Mitochondrial Adaptation in Nonalcoholic Fatty Liver Disease: Novel Mechanisms and Treatment Strategies. *Trends Endocrinol Metab* 2017; 28: 250–260.

[298] Lee J, Park J-S, Roh YS. Molecular insights into the role of mitochondria in non-alcoholic fatty liver disease. *Arch Pharm Res* 2019; 42: 935–946.

[299] Pérez-Carreras M, Del Hoyo P, Martín MA, et al. Defective hepatic mitochondrial respiratory chain in patients with nonalcoholic steatohepatitis. *Hepatology* 2003; 38: 999–1007.

[300] Koliaki C, Szendroedi J, Kaul K, et al. Adaptation of Hepatic Mitochondrial Function in Humans with Non-Alcoholic Fatty Liver Is Lost in Steatohepatitis. *Cell Metab* 2015; 21: 739–746.

[301] Serviddio G, Bellanti F, Tamborra R, et al. Alterations of hepatic ATP homeostasis and respiratory chain during development of non-alcoholic steatohepatitis in a rodent model. *Eur J Clin Invest* 2008; 38: 245–252.

[302] Carmiel-Haggai M, Cederbaum AI, Nieto N. A high-fat diet leads to the progression of non-alcoholic fatty liver disease in obese rats. *FASEB J Off Publ Fed Am Soc Exp Biol* 2005; 19: 136–138.

[303] Jiang Y, Zhao M, An W. Increased hepatic apoptosis in high-fat diet-induced NASH in rats may be associated with downregulation of hepatic stimulator substance. *J Mol Med (Berl)* 2011; 89: 1207–1217.

[304] Serviddio G, Bellanti F, Tamborra R, et al. Uncoupling protein-2 (UCP2) induces mitochondrial proton leak and increases susceptibility of non-alcoholic steatohepatitis (NASH) liver to ischaemia-reperfusion injury. *Gut* 2008; 57: 957–965.

[305] Tell G, Vascotto C, Tiribelli C. Alterations in the redox state and liver damage: hints from the EASL Basic School of Hepatology. *J Hepatol* 2013; 58: 365–374.

[306] Pessayre D, Mansouri A, Fromenty B. Nonalcoholic steatosis and steatohepatitis. V. Mitochondrial dysfunction in steatohepatitis. *Am J Physiol Gastrointest Liver Physiol* 2002; 282: G193-9.

[307] Carter-Kent C, Zein NN, Feldstein AE. Cytokines in the pathogenesis of fatty liver and disease progression to steatohepatitis: implications for treatment. *Am J*

Gastroenterol 2008; 103: 1036–1042.

[308] Henkel A, Green RM. The unfolded protein response in fatty liver disease. *Semin Liver Dis* 2013; 33: 321–329.

[309] Fu S, Yang L, Li P, et al. Aberrant lipid metabolism disrupts calcium homeostasis causing liver endoplasmic reticulum stress in obesity. *Nature* 2011; 473: 528–531.

[310] Lee S, Kim S, Hwang S, et al. Dysregulated expression of proteins associated with ER stress, autophagy and apoptosis in tissues from nonalcoholic fatty liver disease. *Oncotarget* 2017; 8: 63370–63381.

[311] Willy JA, Young SK, Stevens JL, et al. CHOP links endoplasmic reticulum stress to NF-κB activation in the pathogenesis of nonalcoholic steatohepatitis. *Mol Biol Cell* 2015; 26: 2190–2204.

[312] Afonso MB, Rodrigues PM, Carvalho T, et al. Necroptosis is a key pathogenic event in human and experimental murine models of non-alcoholic steatohepatitis. *Clin Sci (Lond)* 2015; 129: 721–739.

[313] Islam T, Afonso MB, Rodrigues CMP. The role of RIPK3 in liver mitochondria bioenergetics and function. *Eur J Clin Invest* 2021; e13648.

[314] Qiu X, Zhang Y, Han J. RIP3 is an upregulator of aerobic metabolism and the enhanced respiration by necrosomal RIP3 feeds back on necrosome to promote necroptosis. *Cell Death Differ* 2018; 25: 821–824.

[315] Elsheikh A, Lavergne SN, Castrejon JL, et al. Drug antigenicity, immunogenicity, and costimulatory signaling: evidence for formation of a functional antigen through immune cell metabolism. *J Immunol* 2010; 185: 6448–6460.

[316] Marques PE, Oliveira AG, Pereira RV, et al. Hepatic DNA deposition drives drug-induced liver injury and inflammation in mice. *Hepatology* 2015; 61: 348–360.

[317] Garcia-Martinez I, Santoro N, Chen Y, et al. Hepatocyte mitochondrial DNA drives nonalcoholic steatohepatitis by activation of TLR9. *J Clin Invest* 2016; 126: 859–

864.

[318] Veena J, Muragundla A, Sidgiddi S, et al. Non-alcoholic fatty liver disease: need for a balanced nutritional source. *Br J Nutr* 2014; 112: 1858–1872.

[319] Vilar-Gomez E, Martinez-Perez Y, Calzadilla-Bertot L, et al. Weight Loss Through Lifestyle Modification Significantly Reduces Features of Nonalcoholic Steatohepatitis. *Gastroenterology* 2015; 149: 365–367.

[320] Pugliese N, Plaz Torres MC, Petta S, et al. Is there an 'ideal' diet for patients with NAFLD? *Eur J Clin Invest* 2021; e13659.

[321] Conlon BA, Beasley JM, Aebersold K, et al. Nutritional management of insulin resistance in nonalcoholic fatty liver disease (NAFLD). *Nutrients* 2013; 5: 4093–4114.

[322] Romero-Gómez M, Zelber-Sagi S, Trenell M. Treatment of NAFLD with diet, physical activity and exercise. *J Hepatol* 2017; 67: 829–846.

[323] Kistler KD, Brunt EM, Clark JM, et al. Physical activity recommendations, exercise intensity, and histological severity of nonalcoholic fatty liver disease. *Am J Gastroenterol* 2011; 106: 460–8; quiz 469.

[324] Keating SE, Hackett DA, George J, et al. Exercise and non-alcoholic fatty liver disease: a systematic review and meta-analysis. *J Hepatol* 2012; 57: 157–166.

[325] Wong VW-S, Wong GL-H, Chan RS-M, et al. Beneficial effects of lifestyle intervention in non-obese patients with non-alcoholic fatty liver disease. *J Hepatol* 2018; 69: 1349–1356.

[326] Belfort R, Harrison SA, Brown K, et al. A placebo-controlled trial of pioglitazone in subjects with nonalcoholic steatohepatitis. *N Engl J Med* 2006; 355: 2297–2307.

[327] Aithal GP, Thomas JA, Kaye P V, et al. Randomized, placebo-controlled trial of pioglitazone in nondiabetic subjects with nonalcoholic steatohepatitis. *Gastroenterology* 2008; 135: 1176–1184.

[328] Cusi K, Orsak B, Bril F, et al. Long-Term Pioglitazone Treatment for Patients With

Nonalcoholic Steatohepatitis and Prediabetes or Type 2 Diabetes Mellitus: A Randomized Trial. *Ann Intern Med* 2016; 165: 305–315.

[329] Marchesini G, Day CP, Dufour JF, et al. EASL-EASD-EASO Clinical Practice Guidelines for the management of non-alcoholic fatty liver disease. *J Hepatol* 2016; 64: 1388–1402.

[330] Erhardt A, Stahl W, Sies H, et al. Plasma levels of vitamin E and carotenoids are decreased in patients with Nonalcoholic Steatohepatitis (NASH). *Eur J Med Res* 2011; 16: 76–78.

[331] Hasegawa T, Yoneda M, Nakamura K, et al. Plasma transforming growth factor-beta1 level and efficacy of alpha-tocopherol in patients with non-alcoholic steatohepatitis: a pilot study. *Aliment Pharmacol Ther* 2001; 15: 1667–1672.

[332] Sanyal AJ, Chalasani N, Kowdley K V., et al. Pioglitazone, Vitamin E, or Placebo for Nonalcoholic Steatohepatitis. *N Engl J Med* 2010; 362: 1675–1685.

[333] Sato K, Gosho M, Yamamoto T, et al. Vitamin E has a beneficial effect on nonalcoholic fatty liver disease: a meta-analysis of randomized controlled trials. *Nutrition* 2015; 31: 923–930.

[334] Sumida Y, Naito Y, Tanaka S, et al. Long-term (>=2 yr) efficacy of vitamin E for non-alcoholic steatohepatitis. *Hepatogastroenterology* 2013; 60: 1445–1450.

[335] Sumida Y, Yoneda M. Current and future pharmacological therapies for NAFLD/NASH. *J Gastroenterol* 2018; 53: 362–376.

[336] Wang W, Zhao C, Zhou J, et al. Simvastatin ameliorates liver fibrosis via mediating nitric oxide synthase in rats with non-alcoholic steatohepatitis-related liver fibrosis. *PLoS One* 2013; 8: e76538.

[337] Schierwagen R, Maybüchen L, Hittatiya K, et al. Statins improve NASH via inhibition of RhoA and Ras. *Am J Physiol Gastrointest Liver Physiol* 2016; 311: G724–G733.

[338] Park HS, Jang JE, Ko MS, et al. Statins Increase Mitochondrial and Peroxisomal Fatty Acid Oxidation in the Liver and Prevent Non-Alcoholic Steatohepatitis in Mice. *Diabetes Metab J* 2016; 40: 376–385.

[339] Bril F, Portillo Sanchez P, Lomonaco R, et al. Liver Safety of Statins in Prediabetes or T2DM and Nonalcoholic Steatohepatitis: Post Hoc Analysis of a Randomized Trial. *J Clin Endocrinol Metab* 2017; 102: 2950–2961.

[340] Ratziu V, Harrison SA, Francque S, et al. Elafibranor, an Agonist of the Peroxisome Proliferator-Activated Receptor-α and -δ, Induces Resolution of Nonalcoholic Steatohepatitis Without Fibrosis Worsening. *Gastroenterology* 2016; 150: 1147-1159.e5.

[341] Sven M F, Pierre B, Manal F A, et al. A randomised, double-blind, placebo-controlled, multi-centre, dose-range, proof-of-concept, 24-week treatment study of lanifibranor in adult subjects with non-alcoholic steatohepatitis: Design of the NATIVE study. *Contemp Clin Trials* 2020; 98: 106170.

[342] Gawrieh S, Noureddin M, Loo N, et al. Saroglitazar, a PPAR-α/γ Agonist, for Treatment of NAFLD: A Randomized Controlled Double-Blind Phase 2 Trial. *Hepatology*. 2021 Oct;74(4):1809-1824..

[343] Ikeda S, Sugihara T, Hoshino Y, et al. Pemafibrate Dramatically Ameliorated the Values of Liver Function Tests and Fibrosis Marker in Patients with Non-Alcoholic Fatty Liver Disease. *Yonago Acta Med* 2020; 63: 188–197.

[344] Eguchi Y, Kitajima Y, Hyogo H, et al. Pilot study of liraglutide effects in non-alcoholic steatohepatitis and non-alcoholic fatty liver disease with glucose intolerance in Japanese patients (LEAN-J). *Hepatol Res* 2015; 45: 269–278.

[345] Armstrong MJ, Gaunt P, Aithal GP, et al. Liraglutide safety and efficacy in patients with non-alcoholic steatohepatitis (LEAN): a multicentre, double-blind, randomised, placebo-controlled phase 2 study. *Lancet (London, England)* 2016; 387: 679–690.

[346] Newsome PN, Buchholtz K, Cusi K, et al. A Placebo-Controlled Trial of

Subcutaneous Semaglutide in Nonalcoholic Steatohepatitis. *N Engl J Med* 2021; 384: 1113–1124.

[347] Safadi R, Konikoff FM, Mahamid M, et al. The fatty acid-bile acid conjugate Aramchol reduces liver fat content in patients with nonalcoholic fatty liver disease. *Clin Gastroenterol Hepatol Off Clin Pract J Am Gastroenterol Assoc* 2014; 12: 2085–91.e1.

[348] Loomba R, Kayali Z, Noureddin M, et al. GS-0976 Reduces Hepatic Steatosis and Fibrosis Markers in Patients With Nonalcoholic Fatty Liver Disease. *Gastroenterology* 2018; 155: 1463-1473.e6.

[349] Lawitz EJ, Coste A, Poordad F, et al. Acetyl-CoA Carboxylase Inhibitor GS-0976 for 12 Weeks Reduces Hepatic De Novo Lipogenesis and Steatosis in Patients With Nonalcoholic Steatohepatitis. *Clin Gastroenterol Hepatol Off Clin Pract J Am Gastroenterol Assoc* 2018; 16: 1983-1991.e3.

[350] Loomba R, Noureddin M, Kowdley K V, et al. Combination Therapies Including Cilofexor and Firsocostat for Bridging Fibrosis and Cirrhosis Attributable to NASH. *Hepatology* 2021; 73: 625–643.

[351] Neuschwander-Tetri BA, Loomba R, Sanyal AJ, et al. Farnesoid X nuclear receptor ligand obeticholic acid for non-cirrhotic, non-alcoholic steatohepatitis (FLINT): a multicentre, randomised, placebo-controlled trial. *Lancet (London, England)* 2015; 385: 956–965.

[352] Ogawa Y, Yoneda M, Kobayashi T, et al. Present and emerging pharmacotherapies for non-alcoholic steatohepatitis in adults. *Expert Opin Pharmacother* 2019; 20: 69–82.

[353] Harrison SA, Bashir MR, Guy CD, et al. Resmetirom (MGL-3196) for the treatment of non-alcoholic steatohepatitis: a multicentre, randomised, double-blind, placebo-controlled, phase 2 trial. *Lancet (London, England)* 2019; 394: 2012–2024.

[354] Harrison SA, Wong VW-S, Okanoue T, et al. Selonsertib for patients with bridging fibrosis or compensated cirrhosis due to NASH: Results from randomized phase III STELLAR trials. *J Hepatol* 2020; 73: 26–39.

[355] Harrison SA, Goodman Z, Jabbar A, et al. A randomized, placebo-controlled trial of emricasan in patients with NASH and F1-F3 fibrosis. *J Hepatol* 2020; 72: 816–827.

[356] Garcia-Tsao G, Bosch J, Kayali Z, et al. Randomized placebo-controlled trial of emricasan for non-alcoholic steatohepatitis-related cirrhosis with severe portal hypertension. *J Hepatol* 2020; 72: 885–895.

[357] Friedman SL, Ratziu V, Harrison SA, et al. A randomized, placebo-controlled trial of cenicriviroc for treatment of nonalcoholic steatohepatitis with fibrosis. *Hepatology* 2018; 67: 1754–1767.

[358] Traber PG, Zomer E. Therapy of experimental NASH and fibrosis with galectin inhibitors. *PLoS One* 2013; 8: e83481.

[359] Chalasani N, Abdelmalek MF, Garcia-Tsao G, et al. Effects of Belapectin, an Inhibitor of Galectin-3, in Patients With Nonalcoholic Steatohepatitis With Cirrhosis and Portal Hypertension. *Gastroenterology* 2020; 158: 1334-1345.e5.

[360] Sanyal A, Charles ED, Neuschwander-Tetri BA, et al. Pegbelfermin (BMS-986036), a PEGylated fibroblast growth factor 21 analogue, in patients with non-alcoholic steatohepatitis: a randomised, double-blind, placebo-controlled, phase 2a trial. *Lancet (London, England)* 2019; 392: 2705–2717.

[361] Wah Kheong C, Nik Mustapha NR, Mahadeva S. A Randomized Trial of Silymarin for the Treatment of Nonalcoholic Steatohepatitis. *Clin Gastroenterol Hepatol Off Clin Pract J Am Gastroenterol Assoc* 2017; 15: 1940-1949.e8.

[362] Yan H-M, Xia M-F, Wang Y, et al. Efficacy of Berberine in Patients with Non-Alcoholic Fatty Liver Disease. *PLoS One* 2015; 10: e0134172.

[363] Pasternack RF, Skowronek WRJ. Catalysis of the disproportionation of superoxide by metalloporphyrins. *J Inorg Biochem* 1979; 11: 261–267.

[364] Batinic-Haberle I, Spasojevic I, Tse HM, et al. Design of Mn porphyrins for treating oxidative stress injuries and their redox-based regulation of cellular transcriptional activities. *Amino Acids* 2012; 42: 95–113.

[365] Coudriet GM, Delmastro-Greenwood MM, Previte DM, et al. Treatment with a Catalytic Superoxide Dismutase (SOD) Mimetic Improves Liver Steatosis, Insulin Sensitivity, and Inflammation in Obesity-Induced Type 2 Diabetes. *Antioxidants (Basel, Switzerland)*; 2017 Nov 1;6(4):85.

[366] Forman HJ, Zhang H. Targeting oxidative stress in disease: promise and limitations of antioxidant therapy. *Nat Rev Drug Discov* 2021; 1–21.

[367] Wasser S, Lim GY, Ong CN, et al. Anti-oxidant ebselen causes the resolution of experimentally induced hepatic fibrosis in rats. *J Gastroenterol Hepatol* 2001; 16: 1244–1253.

[368] Raftos JE, Whillier S, Chapman BE, et al. Kinetics of uptake and deacetylation of N-acetylcysteine by human erythrocytes. *Int J Biochem Cell Biol* 2007; 39: 1698–1706.

[369] Rushworth GF, Megson IL. Existing and potential therapeutic uses for N-acetylcysteine: the need for conversion to intracellular glutathione for antioxidant benefits. *Pharmacol Ther* 2014; 141: 150–159.

[370] Tsai C-C, Chen Y-J, Yu H-R, et al. Long term N-acetylcysteine administration rescues liver steatosis via endoplasmic reticulum stress with unfolded protein response in mice. *Lipids Health Dis* 2020; 19: 105.

[371] Khoshbaten M, Aliasgarzadeh A, Masnadi K, et al. N-acetylcysteine improves liver function in patients with non-alcoholic Fatty liver disease. *Hepat Mon* 2010; 10: 12–16.

[372] Masarone M, Rosato V, Dallio M, et al. Role of Oxidative Stress in Pathophysiology of Nonalcoholic Fatty Liver Disease. *Oxid Med Cell Longev* 2018; 2018: 9547613.

[373] Tsurusaki S, Tsuchiya Y, Koumura T, et al. Hepatic ferroptosis plays an important

role as the trigger for initiating inflammation in nonalcoholic steatohepatitis. *Cell Death Dis* 2019; 10: 449.

[374] Mao L, Zhao T, Song Y, et al. The emerging role of ferroptosis in non-cancer liver diseases: hype or increasing hope? *Cell Death Dis* 2020; 11: 518.

[375] Qi J, Kim J-W, Zhou Z, et al. Ferroptosis Affects the Progression of Nonalcoholic Steatohepatitis via the Modulation of Lipid Peroxidation-Mediated Cell Death in Mice. *Am J Pathol* 2020; 190: 68–81.

[376] Cuadrado A, Rojo AI, Wells G, et al. Therapeutic targeting of the NRF2 and KEAP1 partnership in chronic diseases. *Nat Rev Drug Discov* 2019; 18: 295–317.

[377] Forman HJ, Davies KJA, Ursini F. How do nutritional antioxidants really work: nucleophilic tone and para-hormesis versus free radical scavenging in vivo. *Free Radic Biol Med* 2014; 66: 24–35.

[378] Culbreth M, Aschner M. GSK-3β, a double-edged sword in Nrf2 regulation: Implications for neurological dysfunction and disease. *F1000Research* 2018; 7: 1043.

[379] Jain A, Lamark T, Sjøttem E, et al. p62/SQSTM1 is a target gene for transcription factor NRF2 and creates a positive feedback loop by inducing antioxidant response element-driven gene transcription. *J Biol Chem* 2010; 285: 22576–22591.

[380] Chen W, Sun Z, Wang X-J, et al. Direct interaction between Nrf2 and p21(Cip1/WAF1) upregulates the Nrf2-mediated antioxidant response. *Mol Cell* 2009; 34: 663–673.

[381] Gorrini C, Baniasadi PS, Harris IS, et al. BRCA1 interacts with Nrf2 to regulate antioxidant signaling and cell survival. *J Exp Med* 2013; 210: 1529–1544.

[382] Bloom DA, Jaiswal AK. Phosphorylation of Nrf2 at Ser40 by protein kinase C in response to antioxidants leads to the release of Nrf2 from INrf2, but is not required for Nrf2 stabilization/accumulation in the nucleus and transcriptional activation of antioxidant response elemen. *J Biol Chem* 2003; 278: 44675–44682.

[383] Zhang X, Guo J, Wei X, et al. Bach1: Function, Regulation, and Involvement in Disease. *Oxid Med Cell Longev* 2018; 2018: 1347969.

[384] Robledinos-Antón N, Fernández-Ginés R, Manda G, et al. Activators and Inhibitors of NRF2: A Review of Their Potential for Clinical Development. *Oxid Med Cell Longev* 2019; 2019: 9372182.

[385] Hu Y, Yin F, Liu Z, et al. Acerola polysaccharides ameliorate high-fat diet-induced non-alcoholic fatty liver disease through reduction of lipogenesis and improvement of mitochondrial functions in mice. *Food Funct* 2020; 11: 1037–1048.

[386] Feng X, Yu W, Li X, et al. Apigenin, a modulator of PPARγ, attenuates HFD-induced NAFLD by regulating hepatocyte lipid metabolism and oxidative stress via Nrf2 activation. *Biochem Pharmacol* 2017; 136: 136–149.

[387] Zhao M-G, Sheng X-P, Huang Y-P, et al. Triterpenic acids-enriched fraction from Cyclocarya paliurus attenuates non-alcoholic fatty liver disease via improving oxidative stress and mitochondrial dysfunction. *Biomed Pharmacother* 2018; 104: 229–239.

[388] Yan C, Zhang Y, Zhang X, et al. Curcumin regulates endogenous and exogenous metabolism via Nrf2-FXR-LXR pathway in NAFLD mice. *Biomed Pharmacother* 2018; 105: 274–281.

[389] Qu L-L, Yu B, Li Z, et al. Gastrodin Ameliorates Oxidative Stress and Proinflammatory Response in Nonalcoholic Fatty Liver Disease through the AMPK/Nrf2 Pathway. *Phytother Res* 2016; 30: 402–411.

[390] Li J, Sapper TN, Mah E, et al. Green tea extract provides extensive Nrf2-independent protection against lipid accumulation and NFκB pro- inflammatory responses during nonalcoholic steatohepatitis in mice fed a high-fat diet. *Mol Nutr Food Res* 2016; 60: 858–870.

[391] Kim J, Lee H, Lim J, et al. The lemon balm extract ALS-L1023 inhibits obesity and

nonalcoholic fatty liver disease in female ovariectomized mice. *Food Chem Toxicol* 2017; 106: 292–305.

[392] Du J, Zhang M, Lu J, et al. Osteocalcin improves nonalcoholic fatty liver disease in mice through activation of Nrf2 and inhibition of JNK. *Endocrine* 2016; 53: 701–709.

[393] Hosseini H, Teimouri M, Shabani M, et al. Resveratrol alleviates non-alcoholic fatty liver disease through epigenetic modification of the Nrf2 signaling pathway. *Int J Biochem Cell Biol* 2020; 119: 105667.

[394] Zhang X, Ji R, Sun H, et al. Scutellarin ameliorates nonalcoholic fatty liver disease through the PPARγ/PGC-1α-Nrf2 pathway. *Free Radic Res* 2018; 52: 198–211.

[395] Ou Q, Weng Y, Wang S, et al. Silybin Alleviates Hepatic Steatosis and Fibrosis in NASH Mice by Inhibiting Oxidative Stress and Involvement with the Nf-κB Pathway. *Dig Dis Sci* 2018; 63: 3398–3408.

[396] Yang Y, Li J, Wei C, et al. Amelioration of nonalcoholic fatty liver disease by swertiamarin in fructose-fed mice. *Phytomedicine* 2019; 59: 152782.

[397] Altenhöfer S, Kleikers PWM, Radermacher KA, et al. The NOX toolbox: validating the role of NADPH oxidases in physiology and disease. *Cell Mol Life Sci* 2012; 69: 2327–2343.

[398] Ichimura M, Masuzumi M, Kawase M, et al. A diet-induced Sprague-Dawley rat model of nonalcoholic steatohepatitis-related cirrhosis. *J Nutr Biochem* 2017; 40: 62–69.

[399] Jiang JX, Chen X, Fukada H, et al. Advanced glycation endproducts induce fibrogenic activity in nonalcoholic steatohepatitis by modulating TNF-α-converting enzyme activity in mice. *Hepatology* 2013; 58: 1339–1348.

[400] Matsumoto M, Zhang J, Zhang X, et al. The NOX1 isoform of NADPH oxidase is involved in dysfunction of liver sinusoids in nonalcoholic fatty liver disease. *Free Radic Biol Med* 2018; 115: 412–420.

[401] Bettaieb A, Jiang JX, Sasaki Y, et al. Hepatocyte Nicotinamide Adenine Dinucleotide Phosphate Reduced Oxidase 4 Regulates Stress Signaling, Fibrosis, and Insulin Sensitivity During Development of Steatohepatitis in Mice. *Gastroenterology* 2015; 149: 468–80.e10.

[402] Meng R, Zhu D-L, Bi Y, et al. Apocynin improves insulin resistance through suppressing inflammation in high-fat diet-induced obese mice. *Mediators Inflamm* 2010; 2010: 858735.

[403] Aoyama T, Paik Y-H, Watanabe S, et al. Nicotinamide adenine dinucleotide phosphate oxidase in experimental liver fibrosis: GKT137831 as a novel potential therapeutic agent. *Hepatology* 2012; 56: 2316–2327.

[404] Obrenovich ME, Nair NG, Beyaz A, et al. The role of polyphenolic antioxidants in health, disease, and aging. *Rejuvenation Res* 2010; 13: 631–643.

[405] Barrajón-Catalán E, Herranz-López M, Joven J, et al. Molecular promiscuity of plant polyphenols in the management of age-related diseases: far beyond their antioxidant properties. *Adv Exp Med Biol* 2014; 824: 141–159.

[406] Mladěnka P, Macáková K, Filipský T, et al. In vitro analysis of iron chelating activity of flavonoids. *J Inorg Biochem* 2011; 105: 693–701.

[407] Wu L, Noyan Ashraf MH, Facci M, et al. Dietary approach to attenuate oxidative stress, hypertension, and inflammation in the cardiovascular system. *Proc Natl Acad Sci U S A* 2004; 101: 7094–7099.

[408] Mattson MP, Cheng A. Neurohormetic phytochemicals: Low-dose toxins that induce adaptive neuronal stress responses. *Trends Neurosci* 2006; 29: 632–639.

[409] Soobrattee MA, Bahorun T, Aruoma OI. Chemopreventive actions of polyphenolic compounds in cancer. *Biofactors* 2006; 27: 19–35.

[410] Ferramosca A, Di Giacomo M, Zara V. Antioxidant dietary approach in treatment of fatty liver: New insights and updates. *World J Gastroenterol* 2017; 23: 4146–4157.

[411] Desquiret-Dumas V, Gueguen N, Leman G, et al. Resveratrol induces a mitochondrial complex I-dependent increase in NADH oxidation responsible for sirtuin activation in liver cells. *J Biol Chem* 2013; 288: 36662–36675.

[412] Chen C, Liu Q, Liu L, et al. Potential Biological Effects of (-)-Epigallocatechin-3-gallate on the Treatment of Nonalcoholic Fatty Liver Disease. *Mol Nutr Food Res*; 2018 Jan;62(1):1700483..

[413] Oliveira MR de, Nabavi SF, Daglia M, et al. Epigallocatechin gallate and mitochondria-A story of life and death. *Pharmacol Res* 2016; 104: 70–85.

[414] Jiang X, Tang X, Zhang P, et al. Cyanidin-3-O-β-glucoside protects primary mouse hepatocytes against high glucose-induced apoptosis by modulating mitochondrial dysfunction and the PI3K/Akt pathway. *Biochem Pharmacol* 2014; 90: 135–144.

[415] Vecchione G, Grasselli E, Cioffi F, et al. The Nutraceutic Silybin Counteracts Excess Lipid Accumulation and Ongoing Oxidative Stress in an In Vitro Model of Non-Alcoholic Fatty Liver Disease Progression. *Front Nutr* 2017; 4: 42.

[416] Hasnain BI, Mooradian AD. Recent trials of antioxidant therapy: what should we be telling our patients? *Cleve Clin J Med* 2004; 71: 327–334.

[417] M Davies A, G Holt A. Why antioxidant therapies have failed in clinical trials. *J Theor Biol* 2018; 457: 1–5.

[418] Murphy MP. Antioxidants as therapies: can we improve on nature? *Free Radic Biol Med* 2014; 66: 20–23.

[419] Yang CS, Sang S, Lambert JD, et al. Bioavailability issues in studying the health effects of plant polyphenolic compounds. *Mol Nutr Food Res* 2008; 52 Suppl 1: S139-51.

[420] Manach C, Scalbert A, Morand C, et al. Polyphenols: food sources and bioavailability. *Am J Clin Nutr* 2004; 79: 727–747.

[421] Firuzi O, Miri R, Tavakkoli M, et al. Antioxidant therapy: current status and future

prospects. *Curr Med Chem* 2011; 18: 3871–3888.

[422] Schmidt HHHW, Stocker R, Vollbracht C, et al. Antioxidants in Translational Medicine. *Antioxid Redox Signal* 2015; 23: 1130–1143.

[423] Teixeira J, Gaspar A, Garrido EM, et al. Hydroxycinnamic acid antioxidants: an electrochemical overview. *Biomed Res Int* 2013; 2013: 251754.

[424] Rice-Evans CA, Miller NJ, Paganga G. Structure-antioxidant activity relationships of flavonoids and phenolic acids. *Free Radic Biol Med* 1996; 20: 933–956.

[425] Perron NR, Brumaghim JL. A review of the antioxidant mechanisms of polyphenol compounds related to iron binding. *Cell Biochem Biophys* 2009; 53: 75–100.

[426] da Cunha FM, Duma D, Assreuy J, et al. Caffeic acid derivatives: in vitro and in vivo anti-inflammatory properties. *Free Radic Res* 2004; 38: 1241–1253.

[427] Jung UJ, Lee M-K, Park YB, et al. Antihyperglycemic and antioxidant properties of caffeic acid in db/db mice. *J Pharmacol Exp Ther* 2006; 318: 476–483.

[428] Celik S, Erdogan S, Tuzcu M. Caffeic acid phenethyl ester (CAPE) exhibits significant potential as an antidiabetic and liver-protective agent in streptozotocin-induced diabetic rats. *Pharmacol Res* 2009; 60: 270–276.

[429] Bezerra RMN, Veiga LF, Caetano AC, et al. Caffeic acid phenethyl ester reduces the activation of the nuclear factor κB pathway by high-fat diet-induced obesity in mice. *Metabolism* 2012; 61: 1606–1614.

[430] Huang D-W, Shen S-C, Wu JS-B. Effects of caffeic acid and cinnamic acid on glucose uptake in insulin-resistant mouse hepatocytes. *J Agric Food Chem* 2009; 57: 7687–7692.

[431] Alam MA, Subhan N, Hossain H, et al. Hydroxycinnamic acid derivatives: a potential class of natural compounds for the management of lipid metabolism and obesity. *Nutr Metab (Lond)* 2016; 13: 27.

[432] Eid HM, Thong F, Nachar A, et al. Caffeic acid methyl and ethyl esters exert

potential antidiabetic effects on glucose and lipid metabolism in cultured murine insulin-sensitive cells through mechanisms implicating activation of AMPK. *Pharm Biol* 2017; 55: 2026–2034.

[433] Lee HJ, Cha KH, Kim CY, et al. Bioavailability of hydroxycinnamic acids from Crepidiastrum denticulatum using simulated digestion and Caco-2 intestinal cells. *J Agric Food Chem* 2014; 62: 5290–5295.

[434] Hurko O. Drug development for rare mitochondrial disorders. *Neurother J Am Soc Exp Neurother* 2013; 10: 286–306.

[435] Kanabus M, Heales SJ, Rahman S. Development of pharmacological strategies for mitochondrial disorders. *Br J Pharmacol* 2014; 171: 1798–1817.

[436] Suomalainen A, Battersby BJ. Mitochondrial diseases: the contribution of organelle stress responses to pathology. *Nat Rev Mol Cell Biol* 2018; 19: 77–92.

[437] Sorriento D, Pascale AV, Finelli R, et al. Targeting mitochondria as therapeutic strategy for metabolic disorders. *ScientificWorldJournal* 2014; 2014: 604685.

[438] Smith RAJ, Hartley RC, Cochemé HM, et al. Mitochondrial pharmacology. *Trends Pharmacol Sci* 2012; 33: 341–352.

[439] Gerő D, Torregrossa R, Perry A, et al. The novel mitochondria-targeted hydrogen sulfide (H(2)S) donors AP123 and AP39 protect against hyperglycemic injury in microvascular endothelial cells in vitro. *Pharmacol Res* 2016; 113: 186–198.

[440] Apostolova N, Victor VM. Molecular strategies for targeting antioxidants to mitochondria: therapeutic implications. *Antioxid Redox Signal* 2015; 22: 686–729.

[441] Murphy MP, Smith RAJ. Targeting antioxidants to mitochondria by conjugation to lipophilic cations. *Annu Rev Pharmacol Toxicol* 2007; 47: 629–656.

[442] Anders MW. Exploiting endobiotic metabolic pathways to target xenobiotic antioxidants to mitochondria. *Mitochondrion* 2013; 13: 454–463.

[443] Ross MF, Kelso GF, Blaikie FH, et al. Lipophilic triphenylphosphonium cations as

tools in mitochondrial bioenergetics and free radical biology. *Biochemistry (Mosc)* 2005; 70: 222–230.

[444] Zielonka J, Joseph J, Sikora A, et al. Mitochondria-Targeted Triphenylphosphonium-Based Compounds: Syntheses, Mechanisms of Action, and Therapeutic and Diagnostic Applications. *Chem Rev* 2017; 117: 10043–10120.

[445] Murphy MP. Understanding and preventing mitochondrial oxidative damage. *Biochem Soc Trans* 2016; 44: 1219–1226.

[446] Chacko BK, Srivastava A, Johnson MS, et al. Mitochondria-targeted ubiquinone (MitoQ) decreases ethanol-dependent micro and macro hepatosteatosis. *Hepatology* 2011; 54: 153–163.

[447] Fouret G, Tolika E, Lecomte J, et al. The mitochondrial-targeted antioxidant, MitoQ, increases liver mitochondrial cardiolipin content in obesogenic diet-fed rats. *Biochim Biophys Acta* 2015; 1847: 1025–1035.

[448] Mercer JR, Yu E, Figg N, et al. The mitochondria-targeted antioxidant MitoQ decreases features of the metabolic syndrome in ATM+/-/ApoE-/- mice. *Free Radic Biol Med* 2012; 52: 841–849.

[449] Snow BJ, Rolfe FL, Lockhart MM, et al. A double-blind, placebo-controlled study to assess the mitochondria-targeted antioxidant MitoQ as a disease-modifying therapy in Parkinson's disease. *Mov Disord* 2010; 25: 1670–1674.

[450] Gane EJ, Weilert F, Orr DW, et al. The mitochondria-targeted anti-oxidant mitoquinone decreases liver damage in a phase II study of hepatitis C patients. *Liver Int Off J Int Assoc Study Liver* 2010; 30: 1019–1026.

[451] Trnka J, Blaikie FH, Smith RAJ, et al. A mitochondria-targeted nitroxide is reduced to its hydroxylamine by ubiquinol in mitochondria. *Free Radic Biol Med* 2008; 44: 1406–1419.

[452] Lim S, Rashid MA, Jang M, et al. Mitochondria-targeted antioxidants protect pancreatic β-cells against oxidative stress and improve insulin secretion in

glucotoxicity and glucolipotoxicity. *Cell Physiol Biochem Int J Exp Cell Physiol Biochem Pharmacol* 2011; 28: 873–886.

[453] Liang HL, Sedlic F, Bosnjak Z, et al. SOD1 and MitoTEMPO partially prevent mitochondrial permeability transition pore opening, necrosis, and mitochondrial apoptosis after ATP depletion recovery. *Free Radic Biol Med* 2010; 49: 1550–1560.

[454] Pung YF, Rocic P, Murphy MP, et al. Resolution of mitochondrial oxidative stress rescues coronary collateral growth in Zucker obese fatty rats. *Arterioscler Thromb Vasc Biol* 2012; 32: 325–334.

[455] Wu J, Zheng L, Mo J, et al. Protective Effects of MitoTEMPO on Nonalcoholic Fatty Liver Disease via Regulating Myeloid-Derived Suppressor Cells and Inflammation in Mice. *Biomed Res Int* 2020; 2020: 9329427.

[456] Amorim R, Benfeito S, Teixeira J, et al. Targeting Mitochondria: The Road to Mitochondriotropic Antioxidants and Beyond. *Mitochondrial Biology and Experimental Therapeutics*. 2018, 978-3-319-73343-2

[457] Pfeffer G, Horvath R, Klopstock T, et al. New treatments for mitochondrial disease-no time to drop our standards. *Nat Rev Neurol* 2013; 9: 474–481.

[458] Teixeira J, Cagide F, Benfeito S, et al. Development of a Mitochondriotropic Antioxidant Based on Caffeic Acid: Proof of Concept on Cellular and Mitochondrial Oxidative Stress Models. *J Med Chem* 2017; 60: 7084–7098.

[459] Benfeito S, Oliveira C, Fernandes C, et al. Fine-tuning the neuroprotective and blood-brain barrier permeability profile of multi-target agents designed to prevent progressive mitochondrial dysfunction. *Eur J Med Chem*. 2019 Apr 1;167:525-545.

[460] Teixeira J, Basit F, Willems PHGM, et al. Mitochondria-targeted phenolic antioxidants induce ROS-protective pathways in primary human skin fibroblasts. *Free Radic Biol Med* 2021; 163: 314–324.

[461] Deus CM, Pereira SP, Cunha-Oliveira T, et al. A mitochondria-targeted caffeic acid derivative reverts cellular and mitochondrial defects in human skin fibroblasts

from male sporadic Parkinson's disease patients. *Redox Biol* 2021; 102037.

[462] Pinti M, Troiano L, Nasi M, et al. Hepatoma HepG2 cells as a model for in vitro studies on mitochondrial toxicity of antiviral drugs: which correlation with the patient? *J Biol Regul Homeost Agents* 2003; 17: 166–171.

[463] Choi JM, Oh SJ, Lee SY, et al. HepG2 cells as an in vitro model for evaluation of cytochrome P450 induction by xenobiotics. *Arch Pharm Res* 2015; 38: 691–704.

[464] Marroquin LD, Hynes J, Dykens JA, et al. Circumventing the Crabtree effect: replacing media glucose with galactose increases susceptibility of HepG2 cells to mitochondrial toxicants. *Toxicol Sci* 2007; 97: 539–547.

[465] Lin Y, Ding D, Huang Q, et al. Downregulation of miR-192 causes hepatic steatosis and lipid accumulation by inducing SREBF1: Novel mechanism for bisphenol A-triggered non-alcoholic fatty liver disease. *Biochim Biophys acta Mol cell Biol lipids* 2017; 1862: 869–882.

[466] Bai X, Hong W, Cai P, et al. Valproate induced hepatic steatosis by enhanced fatty acid uptake and triglyceride synthesis. *Toxicol Appl Pharmacol* 2017; 324: 12–25.

[467] Gómez-Lechón MJ, Donato MT, Martínez-Romero A, et al. A human hepatocellular in vitro model to investigate steatosis. *Chem Biol Interact* 2007; 165: 106–116.

[468] Cui W, Chen SL, Hu K-Q. Quantification and mechanisms of oleic acid-induced steatosis in HepG2 cells. *Am J Transl Res* 2010; 2: 95–104.

[469] Donato MT, Tolosa L, Jiménez N, et al. High-content imaging technology for the evaluation of drug-induced steatosis using a multiparametric cell-based assay. *J Biomol Screen* 2012; 17: 394–400.

[470] Hintze KJ, Benninghoff AD, Cho CE, et al. Modeling the Western Diet for Preclinical Investigations. *Adv Nutr* 2018; 9: 263–271.

[471] Hosseini Z, Whiting SJ, Vatanparast H. Current evidence on the association of the

metabolic syndrome and dietary patterns in a global perspective. *Nutr Res Rev* 2016; 29: 152–162.

[472] Wiernsperger N. Hepatic function and the cardiometabolic syndrome. *Diabetes Metab Syndr Obes* 2013; 6: 379–388.

[473] Wang D, Wei Y, Pagliassotti MJ. Saturated fatty acids promote endoplasmic reticulum stress and liver injury in rats with hepatic steatosis. *Endocrinology* 2006; 147: 943–951.

[474] Vergnes L, Phan J, Strauss M, et al. Cholesterol and cholate components of an atherogenic diet induce distinct stages of hepatic inflammatory gene expression. *J Biol Chem* 2003; 278: 42774–42784.

[475] Tsuchiya M, Ji C, Kosyk O, et al. Interstrain differences in liver injury and one-carbon metabolism in alcohol-fed mice. *Hepatology* 2012; 56: 130–139.

[476] Tryndyak V, de Conti A, Kobets T, et al. Interstrain differences in the severity of liver injury induced by a choline- and folate-deficient diet in mice are associated with dysregulation of genes involved in lipid metabolism. *FASEB J Off Publ Fed Am Soc Exp Biol* 2012; 26: 4592–4602.

[477] Shpyleva S, Pogribna M, Cozart C, et al. Interstrain differences in the progression of nonalcoholic steatohepatitis to fibrosis in mice are associated with altered hepatic iron metabolism. *J Nutr Biochem* 2014; 25: 1235–1242.

[478] Schierwagen R, Maybüchen L, Zimmer S, et al. Seven weeks of Western diet in apolipoprotein-E-deficient mice induce metabolic syndrome and non-alcoholic steatohepatitis with liver fibrosis. *Sci Rep* 2015; 5: 12931.

[479] Sorbi D, Boynton J, Lindor KD. The ratio of aspartate aminotransferase to alanine aminotransferase: potential value in differentiating nonalcoholic steatohepatitis from alcoholic liver disease. *Am J Gastroenterol* 1999; 94: 1018–1022.

[480] Lian J, Wei E, Groenendyk J, et al. Ces3/TGH Deficiency Attenuates Steatohepatitis. *Sci Rep* 2016; 6: 25747.

[481] Machado M V, Michelotti GA, Jewell ML, et al. Caspase-2 promotes obesity, the metabolic syndrome and nonalcoholic fatty liver disease. *Cell Death Dis* 2016; 7: e2096.

[482] Lim JS, Mietus-Snyder M, Valente A, et al. The role of fructose in the pathogenesis of NAFLD and the metabolic syndrome. *Nat Rev Gastroenterol Hepatol* 2010; 7: 251–264.

[483] Wang D, Wei Y, Pagliassotti MJ. Saturated fatty acids promote endoplasmic reticulum stress and liver injury in rats with hepatic steatosis. *Endocrinology* 2006; 147: 943–951.

[484] Grande F, Anderson JT, Keys A. Sucrose and various carbohydrate-containing foods and serum lipids in man. *Am J Clin Nutr* 1974; 27: 1043–1051.

[485] Dorn C, Engelmann JC, Saugspier M, et al. Increased expression of c-Jun in nonalcoholic fatty liver disease. *Lab Invest* 2014; 94: 394–408.

[486] Gariani K, Ryu D, Menzies KJ, et al. Inhibiting poly ADP-ribosylation increases fatty acid oxidation and protects against fatty liver disease. *J Hepatol* 2017; 66: 132–141.

[487] Simoes ICM, Karkucinska-Wieckowska A, Janikiewicz J, et al. Western Diet Causes Obesity-Induced Nonalcoholic Fatty Liver Disease Development by Differentially Compromising the Autophagic Response. *Antioxidants (Basel, Switzerland)*, 2020 Oct 15;9(10):995.

[488] Schattenberg JM, Galle PR. Animal models of non-alcoholic steatohepatitis: of mice and man. *Dig Dis* 2010; 28: 247–254.

[489] Kasahara A, Scorrano L. Mitochondria: From cell death executioners to regulators of cell differentiation. *Trends Cell Biol* 2014; 24: 761–770.

[490] Bulthuis EP, Adjobo-Hermans MJW, Willems PHGM, et al. Mitochondrial Morphofunction in Mammalian Cells. 2019 Jun 20;30(18):2066-2109.

[491] Willems PHGM, Rossignol R, Dieteren CEJ, et al. Redox Homeostasis and Mitochondrial Dynamics. *Cell Metab* 2015; 22: 207–218.

[492] Palmeira CM, Teodoro JS, Amorim JA, et al. Mitohormesis and metabolic health: The interplay between ROS, cAMP and sirtuins. *Free Radic Biol Med* 2019; 141: 483–491.

[493] Bohovych I, Khalimonchuk O. Sending out an SOS: Mitochondria as a signaling hub. *Front Cell Dev Biol*; 2016 Oct 13;4:109.

[494] Kotrys A V., Szczesny RJ. Mitochondrial Gene Expression and Beyond-Novel Aspects of Cellular Physiology. *Cells*; 2019 Dec 19;9(1):17.

[495] Brand RM, Wipf P, Durham A, et al. Targeting mitochondrial oxidative stress to mitigate UV-induced skin damage. *Front Pharmacol* 2018; 9: 1–10.

[496] Sanchez MC, Lancel S, Boulanger E, et al. Targeting oxidative stress and mitochondrial dysfunction in the treatment of impaired wound healing: A systematic review. *Antioxidants* 2018; 7: 1–14.

[497] Kiyuna LA, Albuquerque RP e., Chen CH, et al. Targeting mitochondrial dysfunction and oxidative stress in heart failure: Challenges and opportunities. *Free Radic Biol Med* 2018; 129: 155–168.

[498] Tsai SJ, Chao CY, Yin MC. Preventive and therapeutic effects of caffeic acid against inflammatory injury in striatum of MPTP-treated mice. *Eur J Pharmacol* 2011; 670: 441–447.

[499] Kanagaraj VV, Panneerselvam L, Govindarajan V, et al. Caffeic acid, a phyto polyphenol mitigates fluoride induced hepatotoxicity in rats: A possible mechanism. *BioFactors* 2015; 41: 90–100.

[500] Teixeira J, Chavarria D, Borges F, et al. Dietary Polyphenols and Mitochondrial Function: Role in Health and Disease. *Curr Med Chem* 2019; 26: 3376–3406.

[501] Sandoval-Acuña C, Ferreira J, Speisky H. Polyphenols and mitochondria: an update on their increasingly emerging ROS-scavenging independent actions. *Arch*

Biochem Biophys 2014; 559: 75–90.

[502] Taofiq O, González-Paramás AM, Barreiro MF, et al. Hydroxycinnamic Acids and Their Derivatives: Cosmeceutical Significance, Challenges and Future Perspectives, a Review. *Molecules*; 2017 Feb 13;22(2):281.

[503] Mateos R, Goya L, Bravo L. Uptake and metabolism of hydroxycinnamic acids (chlorogenic, caffeic, and ferulic acids) by HepG2 cells as a model of the human liver. *J Agric Food Chem* 2006; 54: 8724–8732.

[504] Kamalian L, Chadwick AE, Bayliss M, et al. The utility of HepG2 cells to identify direct mitochondrial dysfunction in the absence of cell death. *Toxicol Vitr* 2015; 29: 732–740.

[505] McMillian MK, Grant ER, Zhong Z, et al. Nile red binding to HepG2 cells: An improved assay for in vitro studies of hepatosteatosis. *Vitr Mol Toxicol J Basic Appl Res* 2001; 14: 177–190.

[506] Vichai V, Kirtikara K. Sulforhodamine B colorimetric assay for cytotoxicity screening. *Nat Protoc* 2006; 1: 1112–1116.

[507] Silva FSG, Starostina IG, Ivanova V V., et al. Determination of metabolic viability and cell mass using a tandem resazurin/sulforhodamine B assay. *Curr Protoc Toxicol* 2016; 2016: 1–15.

[508] Bradford MM. A rapid and sensitive method for the quantitation of microgram quantities of protein utilizing the principle of protein-dye binding. *Anal Biochem* 1976; 72: 248–254.

[509] Smith PK, Krohn RI, Hermanson GT, et al. Measurement of protein using bicinchoninic acid. *Anal Biochem* 1985; 150: 76–85.

[510] Grilo LF, Martins JD, Cavallaro CH, et al. Development of a 96-well based assay for kinetic determination of catalase enzymatic-activity in biological samples. *Toxicol In Vitro* 2020; 69: 104996.

[511] Valente AJ, Maddalena LA, Robb EL, et al. A simple ImageJ macro tool for analyzing mitochondrial network morphology in mammalian cell culture. *Acta Histochem* 2017; 119: 315–326.

[512] O Lt E SB, C O R D E L I È R E S FP. A guided tour into subcellular colocalization analysis in light microscopy. *J Microsc* 2006; 224: 213–232.

[513] Hissin PJ HR. A fluorometric method for determination of oxidized and reduced glutathione in tissues. *Anal Biochem* 1967; 74: 214–226.

[514] Vatassery GT, Younoszai R. Alpha tocopherol levels in various regions of the central nervous systems of the rat and guinea pig. *Lipids* 1978; 13: 828–831.

[515] Dettmer K, Nürnberger N, Kaspar H, et al. Metabolite extraction from adherently growing mammalian cells for metabolomics studies: optimization of harvesting and extraction protocols. *Anal Bioanal Chem* 2011; 399: 1127–1139.

[516] Mookerjee SA, Goncalves RLS, Gerencser AA, et al. Biochimica et Biophysica Acta The contributions of respiration and glycolysis to extracellular acid production. *BBA - Bioenerg* 2015; 1847: 171–181.

[517] Zorov DB, Juhaszova M, Sollott SJ. Mitochondrial reactive oxygen species (ROS) and ROS-induced ROS release. *Physiol Rev* 2014; 94: 909–950.

[518] Bellezza I, Giambanco I, Minelli A, et al. Nrf2-Keap1 signaling in oxidative and reductive stress. *Biochim Biophys Acta - Mol Cell Res* 2018; 1865: 721–733.

[519] Jornayvaz FR, Shulman GI. Regulation of mitochondrial biogenesis. *Essays Biochem* 2010; 47: 69–84.

[520] Lee HC, Wei YH. Mitochondrial biogenesis and mitochondrial DNA maintenance of mammalian cells under oxidative stress. *Int J Biochem Cell Biol* 2005; 37: 822–834.

[521] Zorova LD, Popkov VA, Plotnikov EY, et al. Mitochondrial membrane potential. *Anal Biochem* 2018; 552: 50–59.

[522] Nimse SB, Pal D. Free radicals, natural antioxidants, and their reaction

mechanisms. *RSC Adv* 2015; 5: 27986–28006.

[523] Berliner LJ, Parinandi NL. *Measuring Oxidants and Oxidative Stress in Biological Systems*.

[524] Loor G, Kondapalli J, Schriewer JM, et al. Menadione triggers cell death through ROS-dependent mechanisms involving PARP activation without requiring apoptosis. *Free Radic Biol Med* 2010; 49: 1925–1936.

[525] Amorim R, Simões ICM, Veloso C, et al. Exploratory Data Analysis of Cell and Mitochondrial High-Fat, High-Sugar Toxicity on Human HepG2 Cells. *Nutrients*; 2021 May 19;13(5):1723.

[526] Parinandi NL, Maulik N, Thirunavukkarasu M, et al. Antioxidants in longevity and medicine 2014. *Oxid Med Cell Longev*; 2015;2015:739417.

[527] Zhang J, Wang X, Vikash V, et al. ROS and ROS-Mediated Cellular Signaling. *Oxid Med Cell Longev*; 2016;2016:4350965.

[528] Siquet C, Paiva-Martins F, Lima JLFC, et al. Antioxidant profile of dihydroxy- and trihydroxyphenolic acids--a structure-activity relationship study. *Free Radic Res* 2006; 40: 433–442.

[529] Rungratanawanich W, Memo M, Uberti D. Redox Homeostasis and Natural Dietary Compounds: Focusing on Antioxidants of Rice (Oryza sativa L.). *Nutrients*; 2018 Nov 1;10(11):1605.

[530] He X, Ma Q. NRF2 cysteine residues are critical for oxidant/electrophile-sensing, Kelch-like ECH-associated protein-1-dependent ubiquitination-proteasomal degradation, and transcription activation. *Mol Pharmacol* 2009; 76: 1265–1278.

[531] Mokhtari V, Afsharian P, Shahhoseini M, et al. A Review on Various Uses of N-Acetyl Cysteine Citation: Mokhtari V, Afsharian P, Shahhoseini M, Kalantar SM, Moini A. A review on various uses of N-acetyl. *CELL JOURNAL(Yakhteh) Cell Journal(Yakhteh) Cell J* 2017; 19: 11–17.

[532] Sirota R, Gibson D, Kohen R. The role of the catecholic and the electrophilic moieties of caffeic acid in Nrf2/Keap1 pathway activation in ovarian carcinoma cell lines. *Redox Biol* 2015; 4: 48–59.

[533] Tonelli C, Chio IIC, Tuveson DA. Transcriptional Regulation by Nrf2. *Antioxidants Redox Signal* 2018; 29: 1727–1745.

[534] Ross D, Siegel D. The diverse functionality of NQO1 and its roles in redox control. *Redox Biol* 2021; 41: 101950.

[535] Palikaras K, Lionaki E, Tavernarakis N. Balancing mitochondrial biogenesis and mitophagy to maintain energy metabolism homeostasis. *Cell Death Differ* 2015; 22: 1399–1401.

[536] Ravikumar B, Duden R, Rubinsztein DC. Aggregate-prone proteins with polyglutamine and polyalanine expansions are degraded by autophagy. *Hum Mol Genet* 2002; 11: 1107–1117.

[537] Ravikumar B, Vacher C, Berger Z, et al. Inhibition of mTOR induces autophagy and reduces toxicity of polyglutamine expansions in fly and mouse models of Huntington disease. *Nat Genet* 2004; 36: 585–595.

[538] Takeuchi H, Kondo Y, Fujiwara K, et al. Synergistic augmentation of rapamycin-induced autophagy in malignant glioma cells by phosphatidylinositol 3-kinase/protein kinase B inhibitors. *Cancer Res* 2005; 65: 3336–3346.

[539] Lin X, Han L, Weng J, et al. Rapamycin inhibits proliferation and induces autophagy in human neuroblastoma cells. *Biosci Rep*; 2018 Nov 30;38(6):BSR20181822.

[540] Johansen T, Lamark T. Selective autophagy mediated by autophagic adapter proteins. *Autophagy* 2011; 7: 279–296.

[541] Mo C, Wang L, Zhang J, et al. The crosstalk between Nrf2 and AMPK signal pathways is important for the anti-inflammatory effect of berberine in LPS-stimulated macrophages and endotoxin-shocked mice. *Antioxid Redox Signal* 2014; 20: 574–588.

[542] Li X, Wang H, Gao Y, et al. Protective Effects of Quercetin on Mitochondrial Biogenesis in Experimental Traumatic Brain Injury via the Nrf2 Signaling Pathway. *PLoS One* 2016; 11: e0164237.

[543] Aguiar ASJ, Duzzioni M, Remor AP, et al. Moderate-Intensity Physical Exercise Protects Against Experimental 6-Hydroxydopamine-Induced Hemiparkinsonism Through Nrf2-Antioxidant Response Element Pathway. *Neurochem Res* 2016; 41: 64–72.

[544] Holmström KM, Baird L, Zhang Y, et al. Nrf2 impacts cellular bioenergetics by controlling substrate availability for mitochondrial respiration. *Biol Open* 2013; 2: 761–770.

[545] Dinkova-Kostova AT, Abramov AY. The emerging role of Nrf2 in mitochondrial function. *Free Radic Biol Med* 2015; 88: 179–188.

[546] Younossi ZM, Marchesini G, Pinto-Cortez H, et al. Epidemiology of Nonalcoholic Fatty Liver Disease and Nonalcoholic Steatohepatitis: Implications for Liver Transplantation. *Transplantation* 2019; 103: 22–27.

[547] Anstee QM, Targher G, Day CP. Progression of NAFLD to diabetes mellitus, cardiovascular disease or cirrhosis. *Nat Rev Gastroenterol Hepatol* 2013; 10: 330–344.

[548] Park EJ, Lee AY, Park S, et al. Multiple pathways are involved in palmitic acid-induced toxicity. *Food Chem Toxicol* 2014; 67: 26–34.

[549] Ricchi M, Odoardi MR, Carulli L, et al. Differential effect of oleic and palmitic acid on lipid accumulation and apoptosis in cultured hepatocytes. *J Gastroenterol Hepatol* 2009; 24: 830–840.

[550] Wei Y, Wang D, Topczewski F, et al. Saturated fatty acids induce endoplasmic reticulum stress and apoptosis independently of ceramide in liver cells. *Am J Physiol - Endocrinol Metab*; 2006 Aug;291(2):E275-81.

[551] Šrámek J, Němcová-Fürstová V, Kovář J. Kinase signaling in apoptosis induced by

saturated fatty acids in pancreatic β-cells. *Int J Mol Sci*; 2016 Sep 12;17(9):1400.

[552] Egnatchik RA, Leamy AK, Jacobson DA, et al. ER calcium release promotes mitochondrial dysfunction and hepatic cell lipotoxicity in response to palmitate overload. *Mol Metab* 2014; 3: 544–553.

[553] Li ZZ, Berk M, McIntyre TM, et al. The lysosomal-mitochondrial axis in free fatty acid-induced hepatic lipotoxicity. *Hepatology* 2008; 47: 1495–1503.

[554] Cazanave SC, Elmi NA, Akazawa Y, et al. CHOP and AP-1 cooperatively mediate PUMA expression during lipoapoptosis. *Am J Physiol - Gastrointest Liver Physiol*; 2010 Jul;299(1):G236-43.

[555] Egnatchik RA, Leamy AK, Noguchi Y, et al. Palmitate-induced activation of mitochondrial metabolism promotes oxidative stress and apoptosis in H4IIEC3 rat hepatocytes. *Metabolism* 2014; 63: 283–295.

[556] Pardo V, González-Rodríguez Á, Guijas C, et al. Opposite cross-talk by oleate and palmitate on insulin signaling in hepatocytes through macrophage activation. *J Biol Chem* 2015; 290: 11663–11677.

[557] Wu HT, Chen W, Cheng KC, et al. Oleic acid activates peroxisome proliferator-activated receptor δ to compensate insulin resistance in steatotic cells. *J Nutr Biochem* 2012; 23: 1264–1270.

[558] Yang J, Fernández-Galilea M, Martínez-Fernández L, et al. Oxidative stress and non-alcoholic fatty liver disease: Effects of omega-3 fatty acid supplementation. *Nutrients* 2019; 11: 1–37.

[559] Zhang Y, Dong L, Yang X, et al. α-Linolenic acid prevents endoplasmic reticulum stress-mediated apoptosis of stearic acid lipotoxicity on primary rat hepatocytes. *Lipids Health Dis* 2011; 10: 2–7.

[560] Zhang K, Chang Y, Shi Z, et al. ω-3 PUFAs ameliorate liver fibrosis and inhibit hepatic stellate cells proliferation and activation by promoting YAP/TAZ degradation. *Sci Rep* 2016; 6: 1–14.

[561] Schultz Moreira AR, Rüschenbaum S, Schefczyk S, et al. 9-PAHSA Prevents Mitochondrial Dysfunction and Increases the Viability of Steatotic Hepatocytes. *Int J Mol Sci*; 2020 Nov 5;21(21):8279.

[562] Neuschwander-Tetri BA. Carbohydrate intake and nonalcoholic fatty liver disease. *Curr Opin Clin Nutr Metab Care* 2013; 16: 446–452.

[563] Agoun H, Semiane N, Mallek A, et al. High-carbohydrate diet-induced metabolic disorders in Gerbillus tarabuli (a new model of non-alcoholic fatty-liver disease). Protective effects of 20-hydroxyecdysone. *Arch Physiol Biochem* 2019; 0: 1–9.

[564] Kakisaka K, Cazanave SC, Fingas CD, et al. Mechanisms of lysophosphatidylcholine-induced hepatocyte lipoapoptosis. *Am J Physiol - Gastrointest Liver Physiol* 2012; 302: 77–84.

[565] Kurek K, Piotrowska DM, Wiesiołek-Kurek P, et al. Inhibition of ceramide de novo synthesis reduces liver lipid accumulation in rats with nonalcoholic fatty liver disease. *Liver Int* 2014; 34: 1074–1083.

[566] Pagadala M, Kasumov T, McCullough AJ, et al. Role of ceramides in nonalcoholic fatty liver disease. *Trends Endocrinol Metab* 2012; 23: 365–371.

[567] Arguello G, Balboa E, Arrese M, et al. Recent insights on the role of cholesterol in non-alcoholic fatty liver disease. *Biochim Biophys Acta - Mol Basis Dis* 2015; 1852: 1765–1778.

[568] Ferreira DMS, Afonso MB, Rodrigues PM, et al. c-Jun N-Terminal Kinase 1/c-Jun Activation of the p53/MicroRNA 34a/Sirtuin 1 Pathway Contributes to Apoptosis Induced by Deoxycholic Acid in Rat Liver. *Mol Cell Biol* 2014; 34: 1100–1120.

[569] Kohli R, Kirby M, Xanthakos SA, et al. High-fructose, medium chain trans fat diet induces liver fibrosis and elevates plasma coenzyme Q9 in a novel murine model of obesity and nonalcoholic steatohepatitis. *Hepatology* 2010; 52: 934–944.

[570] Sobrecases H, Lê KA, Bortolotti M, et al. Effects of short-term overfeeding with fructose, fat and fructose plus fat on plasma and hepatic lipids in healthy men.

Diabetes Metab 2010; 36: 244–246.

[571] Yao H-R, Liu J, Plumeri D, et al. Lipotoxicity in HepG2 cells triggered by free fatty acids. *Am J Transl Res* 2011; 3: 284–291.

[572] Vecchione G, Grasselli E, Cioffi F, et al. The Nutraceutic Silybin Counteracts Excess Lipid Accumulation and Ongoing Oxidative Stress in an In Vitro Model of Non-Alcoholic Fatty Liver Disease Progression. 2017 Sep 19;4:42.

[573] Einer C, Hohenester S, Wimmer R, et al. Data on chow, liver tissue and mitochondrial fatty acid compositions as well as mitochondrial proteome changes after feeding mice a western diet for 6–24 weeks. *Data Br* 2017; 15: 163–169.

[574] Bligh, E.G. and Dyer WJ. Canadian Journal of Biochemistry and Physiology. *Can J Biochem Physiol*; 37.

[575] Rouser G, Fleischer S, Yamamoto A. Two dimensional thin layer chromatographic separation of polar lipids and determination of phospholipids by phosphorus analysis of spots. *Lipids* 1970; 5: 494–496.

[576] Nijtmans LGJ, Henderson NS, Holt IJ. Blue Native electrophoresis to study mitochondrial and other protein complexes. *Methods* 2002; 26: 327–334.

[577] Ross BC. Mutual Information between Discrete and Continuous Data Sets. 9. Epub ahead of print 2014. DOI: 10.1371/journal.pone.0087357.

[578] MacQueen J. Some methods for classification and analysis of multivariate observations. In: *Proceedings of the Fifth Berkeley Symposium on Mathematical Statistics and Probability, Volume 1: Statistics*. Berkeley, Calif.: University of California Press, pp. 281–297.

[579] Mckinney W. Data Structures for Statistical Computing in Python. 2010; 1: 56–61.

[580] Walt S Van Der, Colbert SC, Varoquaux G, et al. The NumPy array : a structure for efficient numerical computation To cite this version : HAL Id : inria-00564007 The NumPy array : a structure for efficient numerical computation.

[581] Jones E, Oliphant T, Peterson P. SciPy: Open Source Scientific Tools for Python.

[582] Pedregosa F, Weiss R, Brucher M. Scikit-learn : Machine Learning in Python. 2011; 12: 2825–2830.

[583] Jensen T, Abdelmalek MF, Sullivan S, et al. Fructose and Sugar: A Major Mediator of Nonalcoholic Fatty Liver Disease. *J Hepatol*. 2018 May;68(5):1063-1075.

[584] Schultz A, Neil D, Aguila MB, et al. Hepatic Adverse Effects of Fructose Consumption Independent of Overweight / Obesity. *Int J Mol Sci.* 2013 Nov 5;14(11):21873-86.

[585] Sun Q, Zhong W, Zhang W, et al. Defect of mitochondrial respiratory chain is a mechanism of ROS overproduction in a rat model of alcoholic liver disease: Role of zinc deficiency. *Am J Physiol - Gastrointest Liver Physiol* 2016; 310: G205–G214.

[586] Pérez-Carreras M, Del Hoyo P, Martín MA, et al. Defective hepatic mitochondrial respiratory chain in patients with nonalcoholic steatohepatitis. *Hepatology* 2003; 38: 999–1007.

[587] Gómez-Lechón MJ, Donato MT, Martínez-Romero A, et al. A human hepatocellular in vitro model to investigate steatosis. *Chem Biol Interact* 2007; 165: 106–116.

[588] Zhao L, Guo X, Wang O, et al. Fructose and glucose combined with free fatty acids induce metabolic disorders in HepG2 cell : A new model to study the impacts of high-fructose / sucrose and high-fat diets in vitro. *Mol Nutr Food Res*. 2016 Apr;60(4):909-21.

[589] Nishi H, Higashihara T, Inagi R. Lipotoxicity in Kidney, Heart, and Skeletal Muscle Dysfunction. Nutrients. 2019 Jul 20;11(7):1664..

[590] Busch SJ, Jackson L, Barnhart L, et al. Differential Regulation of Hepatic Triglyceride Lipase and Reductase Gene Expression in a Human Hepatoma Cell Line , HepGZ *. 1990; 265: 22474–22479.

[591] Shi X, Li J, Zou X, et al. Regulation of lipid droplet size and phospholipid composition by stearoyl-CoA desaturase. *Lipid Res*. 2013 Sep;54(9):2504-14.

[592] Hannou SA, Mckeown NM, Herman MA, et al. Fructose metabolism and metabolic disease. *J Clin Invest*. 2018 Feb 1;128(2):545-555.

[593] Mesmin B. Mitochondrial lipid transport and biosynthesis: A complex balance. *J Cell Biol* 2016; 214: 9–11.

[594] Benga G, Hodârnău A, Böhm B, et al. Human liver mitochondria: relation of a particular lipid composition to the mobility of spin-labelled lipids. *Eur J Biochem* 1978; 84: 625–633.

[595] Osman C, Voelker DR, Langer T. Making heads or tails of phospholipids in mitochondria. *Cell Biol*. 2011 Jan 10;192(1):7-16.

[596] Crimi M, Esposti MD. Apoptosis-induced changes in mitochondrial lipids. *Biochim Biophys Acta - Mol Cell Res* 2011; 1813: 551–557.

[597] Li Z, Agellon LB, Allen TM, et al. The ratio of phosphatidylcholine to phosphatidylethanolamine influences membrane integrity and steatohepatitis. *Cell Metab.* 2006 May;3(5):321-31.

[598] Veen JN Van Der, Lingrell S, Robin P, et al. The Concentration of Phosphatidylethanolamine in Mitochondria Can Modulate ATP Production and Glucose Metabolism in Mice. *Diabetes*. 2014 Aug;63(8):2620-30.

[599] Arendt BM, Ma DWL, Simons B, et al. Nonalcoholic fatty liver disease is associated with lower hepatic and erythrocyte ratios of phosphatidylcholine to phosphatidylethanolamine. *Appl Physiol Nutr Metab* 2013; 38: 334–340.

[600] van Meer G, de Kroon AIPM. Lipid map of the mammalian cell. *J Cell Sci* 2011; 124: 5 LP – 8.

[601] Tasseva G, Bai HD, Davidescu M, et al. Phosphatidylethanolamine Deficiency in Mammalian Mitochondria Impairs Oxidative Phosphorylation and Alters Mitochondrial Morphology *. 2013; 288: 4158–4173.

[602] Cohen G, Shamni O, Avrahami Y, et al. Beta cell response to nutrient overload involves phospholipid remodelling and lipid peroxidation. *Diabetologia*. 2015

Jun;58(6):1333-43.

[603] Yao, H.-R.; Liu, J.; Plumeri, D.; Cao, Y.-B.; He, T.; Lin, L.; Li, Y.; Jiang, Y.-Y.; Li, J.; Shang, J. Lipotoxicity in HepG2 cells triggered by free fatty acids. Am. J. Transl. Res. 2011, 3, 284–291

[604] Wu X, Zhang L, Gurley E, et al. Prevention of free fatty acid-induced hepatic lipotoxicity by 18β-glycyrrhetinic acid through lysosomal and mitochondrial pathways. *Hepatology* 2008; 47: 1905–1915.

[605] Bereiter-Hahn and Voth M. Dynamics of mitochondria in living cells. *Microsc res Tech* 1994; 219: 198–219.

[606] Wai T, Langer T. Mitochondrial Dynamics and Metabolic Regulation. *Trends Endocrinol Metab* 2016; 27: 105–117.

[607] Galloway CA, Yoon Y. Mitochondrial morphology in metabolic diseases. *Antioxidants Redox Signal* 2013; 19: 415–430.

[608] García-Ruiz I, Solís-Muñoz P, Fernández-Moreira D, et al. In vitro treatment of HepG2 cells with saturated fatty acids reproduces mitochondrial dysfunction found in nonalcoholic steatohepatitis. *DMM Dis Model Mech* 2015; 8: 183–191.

[609] Suárez-rivero JM, Villanueva-paz M, Cruz-ojeda P De, et al. Mitochondrial Dynamics in Mitochondrial Diseases. *Diseases*. 2017; 1–15.

[610] Vaughan RA, Garcia-Smith R, Bisoffi M, et al. Conjugated linoleic acid or omega 3 fatty acids increase mitochondrial biosynthesis and metabolism in skeletal muscle cells. *Lipids Health Dis* 2012; 11: 1.

[611] Lee MS, Shin Y, Moon S, et al. Effects of eicosapentaenoic acid and docosahexaenoic acid on mitochondrial DNA replication and PGC-1α gene expression in C 2 C 12 muscle cells. *Prev Nutr Food Sci* 2016; 21: 317–322.

[612] Patková J, Anděl M, Trnka J. Palmitate-induced cell death and mitochondrial respiratory dysfunction in myoblasts are not prevented by mitochondria-targeted

antioxidants. *Cell Physiol Biochem* 2014; 33: 1439–1451.

[613] Carabelli J, Burgueño AL, Soledad M, et al. High fat diet-induced liver steatosis promotes an increase in liver mitochondrial biogenesis in response to hypoxia. *J Cell Mol Med*. 2011 Jun;15(6):1329-38

[614] Malik AN, Czajka A. Is mitochondrial DNA content a potential biomarker of mitochondrial dysfunction? *Mitochondrion* 2013; 13: 481–492.

[615] Aoun M, Fouret G, Michel F, et al. Dietary fatty acids modulate liver mitochondrial cardiolipin content and its fatty acid composition in rats with non alcoholic fatty liver disease. *J Bioenerg Biomembr.* 2012 Aug;44(4):439-52.

[616] Fouret G, Gaillet S, Lecomte J, et al. 20-Week follow-up of hepatic steatosis installation and liver mitochondrial structure and activity and their interrelation in rats fed a high-fat – high-fructose diet. *Br J Nutr*. 2018 Feb;119(4):368-380..

[617] Petrosillo G, Ruggiero FM, Pistolese M, et al. Reactive oxygen species generated from the mitochondrial electron transport chain induce cytochrome c dissociation from beef-heart submitochondrial particles via cardiolipin peroxidation . Possible role in the apoptosis. *FEBS Lett*. 2001 Dec 14;509(3):435-8..

[618] Adams SH, Fiehn O. Temporal metabolomic responses of cultured HepG2 liver cells to high fructose and high glucose exposures. *Metabolomics*. 2015 Jun 1;11(3):707-721..

[619] Ly LD, Xu S, Choi SK, et al. Oxidative stress and calcium dysregulation by palmitate in type 2 diabetes. *Exp Mol Med* 2017; 49: e291-12.

[620] Bonora M, Patergnani S, Rimessi A, et al. ATP synthesis and storage. *Purinergic Signal*. 2012 Sep;8(3):343-57.

[621] Osellame LD, Hons BS, Ph D, et al. Best Practice & Research Clinical Endocrinology & Metabolism Cellular and molecular mechanisms of mitochondrial function. *Best Pract Res Clin Endocrinol Metab* 2012; 26: 711–723.

[622] Spitz DR, Kinter MT, Kehrer JP, et al. The Effect of Monosaturated and Polyunsaturated Fatty Acids on Oxygen Toxicity in Cultured Cells. *Pediatr Res*. 1992 Sep;32(3):366-72.

[623] Joseph LC, Barca E, Subramanyam P, et al. Inhibition of NAPDH Oxidase 2 (NOX2) Prevents Oxidative Stress and Mitochondrial Abnormalities Caused by Saturated Fat in Cardiomyocytes. *PLoS One*. 2016 Jan 12;11(1):e0145750.

[624] Hun S, Wolfgang M, Tokutake Y, et al. Differential effects of central fructose and glucose on hypothalamic malonyl – CoA and food intake. *Proc Natl Acad Sci U S A*. 2008; 105: 16871–16875.

[625] Schwabe RF, Luedde T. Apoptosis and necroptosis in the liver: a matter of life and death. *Nat Rev Gastroenterol Hepatol* 2018; 15: 738–752.

[626] Elmore S. Apoptosis: a review of programmed cell death. *Toxicol Pathol* 2007; 35: 495–516.

[627] Brentnall M, Rodriguez-menocal L, Guevara RL De, et al. Caspase-9 , caspase-3 and caspase-7 have distinct roles during intrinsic apoptosis. *BMC Cell Biol*. 2013 Jul 9;14:32. doi: 10.1186/1471-2121-14-32.

[628] Kominami K, Nakabayashi J, Nagai T, et al. Biochimica et Biophysica Acta The molecular mechanism of apoptosis upon caspase-8 activation : Quantitative experimental validation of a mathematical model. *BBA - Mol Cell Res* 2012; 1823: 1825–1840.

[629] Hirsova P, Ibrahim SH, Gores GJ, et al. Lipotoxic lethal and sublethal stress signaling in hepatocytes: relevance to NASH pathogenesis. *J Lipid Res* 2016; 57: 1758–1770.

[630] Sorice M, Circella A, Cristea IM, et al. Cardiolipin and its metabolites move from mitochondria to other cellular membranes during death receptor-mediated apoptosis. *Cell Death Differ* 2004; 11: 1133–1145.

[631] Goonesinghe A, Mundy ES, Smith M, et al. Pro-apoptotic Bid induces membrane

perturbation by inserting selected lysolipids into the bilayer. *Biochem J* 2005; 387: 109–118.

[632] Henriksen JR, Andresen TL, Feldborg LN, et al. Understanding detergent effects on lipid membranes: A model study of lysolipids. *Biophys J* 2010; 98: 2199–2205.

[633] Lauber K, Bohn E, Kröber SM, et al. Apoptotic cells induce migration of phagocytes via caspase-3-mediated release of a lipid attraction signal. *Cell* 2003; 113: 717–730.

[634] Lehmann R, Franken H, Dammeier S, et al. Circulating Lysophosphatidylcholines Are Markers of a Metabolically Benign Nonalcoholic Fatty Liver. *Diabetes Care* 2013; 36: 2331 LP – 2338.

[635] Li H, Xiao Y, Tang L, et al. Adipocyte Fatty Acid-Binding Protein Promotes Palmitate-Induced Mitochondrial Dysfunction and Apoptosis in Macrophages. *Front Immunol.* 2018 Jan 30;9:81.

[636] Mcilwain DR, Berger T, Mak TW. Caspase Functions in Cell Death and Disease Caspase Functions in Cell Death and Disease. *Cold Spring Harb Perspect Biol.* 2013 Apr 1;5(4):a008656.

[637] Kučera O, Lotková H, Sobotka O, et al. The effect of D-galactosamine on lean and steatotic rat hepatocytes in primary culture. *Physiol Res* 2015; 64: S637–S646.

[638] Chen X, Li L, Liu X, et al. Oleic acid protects saturated fatty acid mediated lipotoxicity in hepatocytes and rat of non-alcoholic steatohepatitis. *Life Sci* 2018; 203: 291–304.

[639] Vinciguerra M, Sgroi A, Veyrat-Durebex C, et al. Unsaturated fatty acids inhibit the expression of tumor suppressor phosphatase and tensin homolog(PTEN) via microRNA-21 up-regulation in hepatocytes. *Hepatology* 2009; 49: 1176–1184.

[640] Navarro VJ, Belle SH, D'Amato M, et al. Silymarin in non-cirrhotics with non-alcoholic steatohepatitis: A randomized, double-blind, placebo controlled trial. *PLoS One* 2019; 14: e0221683.

[641] Grattagliano I, Montezinho LP, Oliveira PJ, et al. Targeting mitochondria to oppose the progression of nonalcoholic fatty liver disease. *Biochem Pharmacol* 2019; 160: 34–45.

[642] Rehman H, Liu Q, Krishnasamy Y, et al. The mitochondria-targeted antioxidant MitoQ attenuates liver fibrosis in mice. *Int J Physiol Pathophysiol Pharmacol* 2016; 8: 14–27.

[643] Singh R, Kaushik S, Wang Y, et al. Autophagy regulates lipid metabolism. *Nature* 2009; 458: 1131–1135.

[644] Carotti S, Aquilano K, Zalfa F, et al. Lipophagy Impairment Is Associated With Disease Progression in NAFLD. *Front Physiol* 2020; 11: 1–12.

[645] Lin K-L, Lin K-J, Wang P-W, et al. Resveratrol provides neuroprotective effects through modulation of mitochondrial dynamics and ERK1/2 regulated autophagy. *Free Radic Res* 2018; 52: 1371–1386.

[646] Wang S-F, Wu M-Y, Cai C-Z, et al. Autophagy modulators from traditional Chinese medicine: Mechanisms and therapeutic potentials for cancer and neurodegenerative diseases. *J Ethnopharmacol* 2016; 194: 861–876.

[647] Kim HM, Kim Y, Lee ES, et al. Caffeic acid ameliorates hepatic steatosis and reduces ER stress in high fat diet-induced obese mice by regulating autophagy. *Nutrition* 2018; 55–56: 63–70.

[648] Mu H-N, Zhou Q, Yang R-Y, et al. Caffeic acid prevents non-alcoholic fatty liver disease induced by a high-fat diet through gut microbiota modulation in mice. *Food Res Int* 2021; 143: 110240.

[649] Amorim R, Cagide F, Tavares LC, et al. Mitochondriotropic antioxidant based on caffeic acid AntiOxCIN4 activates Nrf2-dependent antioxidant defenses and quality control mechanisms to antagonize oxidative stress-induced cell damage. *Free Radic Biol Med* 2022; 179: 119–132.

[650] Szymanska-Debinska T, Karkucinska-Wieckowska A, Piekutowska-Abramczuk D,

et al. Leigh disease due to SCO2 mutations revealed at extended autopsy. *J Clin Pathol* 2015; 68: 397–399.

[651] BLIGH EG, DYER WJ. A rapid method of total lipid extraction and purification. *Can J Biochem Physiol* 1959; 37: 911–917.

[652] FOLCH J, LEES M, SLOANE STANLEY GH. A simple method for the isolation and purification of total lipides from animal tissues. *J Biol Chem* 1957; 226: 497–509.

[653] Rahman I, Kode A, Biswas SK. Assay for quantitative determination of glutathione and glutathione disulfide levels using enzymatic recycling method. *Nat Protoc* 2007; 1: 3159–3165.

[654] Arnao MB, Cano A, Acosta M. The hydrophilic and lipophilic contribution to total antioxidant activity. *Food Chem* 2001; 73: 239–244.

[655] Grilo LF, Martins JD, Cavallaro CH, et al. Development of a 96-well based assay for kinetic determination of catalase enzymatic-activity in biological samples. *Toxicol Vitr* 2020; 69: 104996.

[656] Burk RF, Trumble MJ, Lawrence RA. Rat hepatic cytosolic glutathione-dependent enzyme protection against lipid peroxidation in the NADPH-microsomal lipid peroxidation system. *Biochim Biophys Acta* 1980; 618: 35–41.

[657] Mannervik B. Measurement of glutathione reductase activity. *Curr Protoc Toxicol* 2001; Chapter 7: Unit7.2.

[658] Quirós PM. Determination of Aconitase Activity: A Substrate of the Mitochondrial Lon Protease. *Methods Mol Biol* 2018; 1731: 49–56.

[659] Razmara A, Sunday L, Stirone C, et al. Mitochondrial effects of estrogen are mediated by estrogen receptor alpha in brain endothelial cells. *J Pharmacol Exp Ther* 2008; 325: 782–790.

[660] Walker JM. The bicinchoninic acid (BCA) assay for protein quantitation. *Methods Mol Biol* 1994; 32: 5–8.

[661] Weekes MP, Tomasec P, Huttlin EL, et al. Quantitative temporal viromics: an

approach to investigate host-pathogen interaction. *Cell* 2014; 157: 1460–1472.

[662] McAlister GC, Nusinow DP, Jedrychowski MP, et al. MultiNotch MS3 enables accurate, sensitive, and multiplexed detection of differential expression across cancer cell line proteomes. *Anal Chem* 2014; 86: 7150–7158.

[663] Adler P, Reimand J, Jänes J, et al. KEGGanim: pathway animations for high-throughput data. *Bioinformatics* 2008; 24: 588–590.

[664] Hammel JH, Bellas E. Endothelial cell crosstalk improves browning but hinders white adipocyte maturation in 3D engineered adipose tissue. *Integr Biol (Camb)* 2020; 12: 81–89.

[665] Yki-Järvinen H, Luukkonen PK, Hodson L, et al. Dietary carbohydrates and fats in nonalcoholic fatty liver disease. *Nat Rev Gastroenterol Hepatol* 2021; 18: 770–786.

[666] van der Veen JN, Kennelly JP, Wan S, et al. The critical role of phosphatidylcholine and phosphatidylethanolamine metabolism in health and disease. *Biochim Biophys acta Biomembr* 2017; 1859: 1558–1572.

[667] Kong X, Wang R, Xue Y, et al. Sirtuin 3, a new target of PGC-1alpha, plays an important role in the suppression of ROS and mitochondrial biogenesis. *PLoS One* 2010; 5: e11707.

[668] Simões ICM, Fontes A, Pinton P, et al. Mitochondria in non-alcoholic fatty liver disease. *Int J Biochem Cell Biol* 2018; 95: 93–99.

[669] Hardie DG. AMP-activated protein kinase: an energy sensor that regulates all aspects of cell function. *Genes Dev* 2011; 25: 1895–1908.

[670] Mihaylova MM, Shaw RJ. The AMPK signalling pathway coordinates cell growth, autophagy and metabolism. *Nat Cell Biol* 2011; 13: 1016–1023.

[671] Kim YC, Guan K-L. mTOR: a pharmacologic target for autophagy regulation. *J Clin Invest* 2015; 125: 25–32.

[672] Lemasters JJ. Selective mitochondrial autophagy, or mitophagy, as a targeted defense against oxidative stress, mitochondrial dysfunction, and aging. *Rejuvenation Res* 2005; 8: 3–5.

[673] Patterson RE, Kalavalapalli S, Williams CM, et al. Lipotoxicity in steatohepatitis occurs despite an increase in tricarboxylic acid cycle activity. *Am J Physiol Endocrinol Metab* 2016; 310: E484-94.

[674] Tripathy S, Lytle KA, Stevens RD, et al. Fatty acid elongase-5 (Elovl5) regulates hepatic triglyceride catabolism in obese C57BL/6J mice. *J Lipid Res* 2014; 55: 1448–1464.

[675] Pardo V, González-Rodríguez Á, Muntané J, et al. Role of hepatocyte S6K1 in palmitic acid-induced endoplasmic reticulum stress, lipotoxicity, insulin resistance and in oleic acid-induced protection. *Food Chem Toxicol an Int J Publ Br Ind Biol Res Assoc* 2015; 80: 298–309.

[676] Naguib G, Morris N, Yang S, et al. Dietary fatty acid oxidation is decreased in non-alcoholic fatty liver disease: A palmitate breath test study. *Liver Int Off J Int Assoc Study Liver* 2020; 40: 590–597.

[677] Parker HM, Johnson NA, Burdon CA, et al. Omega-3 supplementation and non-alcoholic fatty liver disease: a systematic review and meta-analysis. *J Hepatol* 2012; 56: 944–951.

[678] Lu W, Li S, Li J, et al. Effects of Omega-3 Fatty Acid in Nonalcoholic Fatty Liver Disease: A Meta-Analysis. *Gastroenterol Res Pract* 2016; 2016: 1459790.

[679] Chen Y, Xu C, Yan T, et al. ω-3 Fatty acids reverse lipotoxity through induction of autophagy in nonalcoholic fatty liver disease. *Nutrition* 2015; 31: 1423-1429.e2.

[680] Tandra S, Yeh MM, Brunt EM, et al. Presence and significance of microvesicular steatosis in nonalcoholic fatty liver disease. *J Hepatol* 2011; 55: 654–659.

[681] Simões ICM, Amorim R, Teixeira J, et al. The Alterations of Mitochondrial Function during NAFLD Progression—An Independent Effect of Mitochondrial ROS Production. *Int J Mol Sci* 2021; 22: 6848.

[682] Einer C, Hohenester S, Wimmer R, et al. Mitochondrial adaptation in steatotic mice. *Mitochondrion* 2018; 40: 1–12.

[683] Zhang J, Xiang H, Liu J, et al. Mitochondrial Sirtuin 3: New emerging biological function and therapeutic target. *Theranostics* 2020; 10: 8315–8342.

[684] Kendrick AA, Choudhury M, Rahman SM, et al. Fatty liver is associated with reduced SIRT3 activity and mitochondrial protein hyperacetylation. *Biochem J* 2011; 433: 505–514.

[685] Barroso E, Rodríguez-Rodríguez R, Zarei M, et al. SIRT3 deficiency exacerbates fatty liver by attenuating the HIF1α-LIPIN 1 pathway and increasing CD36 through Nrf2. *Cell Commun Signal* 2020; 18: 147.

[686] White HM. The Role of TCA Cycle Anaplerosis in Ketosis and Fatty Liver in Periparturient Dairy Cows. *Anim an open access J from MDPI* 2015; 5: 793–802.

[687] Cappel DA, Deja S, Duarte JAG, et al. Pyruvate-Carboxylase-Mediated Anaplerosis Promotes Antioxidant Capacity by Sustaining TCA Cycle and Redox Metabolism in Liver. *Cell Metab* 2019; 29: 1291-1305.e8.

[688] Dowling RJO, Topisirovic I, Fonseca BD, et al. Dissecting the role of mTOR: lessons from mTOR inhibitors. *Biochim Biophys Acta* 2010; 1804: 433–439.

[689] Wang X, Zhang X, Chu ESH, et al. Defective lysosomal clearance of autophagosomes and its clinical implications in nonalcoholic steatohepatitis. *FASEB J Off Publ Fed Am Soc Exp Biol* 2018; 32: 37–51.

[690] Li R, Toan S, Zhou H. Role of mitochondrial quality control in the pathogenesis of nonalcoholic fatty liver disease. *Aging (Albany NY)* 2020; 12: 6467–6485.

[691] Golovaty I, Tien PC, Price JC, et al. Food Insecurity May Be an Independent Risk Factor Associated with Nonalcoholic Fatty Liver Disease among Low-Income Adults in the United States. *J Nutr* 2020; 150: 91–98.

[692] Younossi ZM, Blissett D, Blissett R, et al. The economic and clinical burden of

nonalcoholic fatty liver disease in the United States and Europe. *Hepatology* 2016; 64: 1577–1586.

[693] Drew L. Drug development: Sprint finish. *Nature* 2017; 551: S86–S89.

[694] Wilson LH, Cho J-H, Estrella A, et al. Liver Glycogen Phosphorylase Deficiency Leads to Profibrogenic Phenotype in a Murine Model of Glycogen Storage Disease Type VI. *Hepatol Commun* 2019; 3: 1544–1555.

[695] Le Gal K, Wiel C, Ibrahim MX, et al. Mitochondria-Targeted Antioxidants MitoQ and MitoTEMPO Do Not Influence BRAF-Driven Malignant Melanoma and KRAS-Driven Lung Cancer Progression in Mice. *Antioxidants (Basel, Switzerland)*; 2021 Jan 22;10(2):163.

[696] Einer C, Hohenester S, Wimmer R, et al. Mitochondrial adaptation in steatotic mice. *Mitochondrion* 2018; 40: 1–12.

PART VI

Copy Rights License Agreements

Appendix A

SPRINGER NATURE LICENSE
TERMS AND CONDITIONS

Oct 28, 2021

This Agreement between Mr. Ricardo Fernando Santos Amorim ("You") and Springer Nature ("Springer Nature") consists of your license details and the terms and conditions provided by Springer Nature and Copyright Clearance Center.

License Number	5177600230481
License date	Oct 28, 2021
Licensed Content Publisher	Springer Nature
Licensed Content Publication	Nature Reviews Gastroenterology & Hepatology
Licensed Content Title	Global epidemiology of NAFLD-related HCC: trends, predictions, risk factors and prevention
Licensed Content Author	Daniel Q. Huang et al
Licensed Content Date	Dec 21, 2020